



HAL
open science

Bioinspired materials: Optimization of the mechanical behavior using Discrete Element Method

Kaoutar Radi

► **To cite this version:**

Kaoutar Radi. Bioinspired materials: Optimization of the mechanical behavior using Discrete Element Method. Solid mechanics [physics.class-ph]. Université Grenoble Alpes, 2019. English. NNT: 2019GREAI066 . tel-02446727

HAL Id: tel-02446727

<https://theses.hal.science/tel-02446727>

Submitted on 21 Jan 2020

HAL is a multi-disciplinary open access archive for the deposit and dissemination of scientific research documents, whether they are published or not. The documents may come from teaching and research institutions in France or abroad, or from public or private research centers.

L'archive ouverte pluridisciplinaire **HAL**, est destinée au dépôt et à la diffusion de documents scientifiques de niveau recherche, publiés ou non, émanant des établissements d'enseignement et de recherche français ou étrangers, des laboratoires publics ou privés.



THÈSE

Pour obtenir le grade de

DOCTEUR DE LA COMMUNAUTÉ UNIVERSITÉ GRENOBLE ALPES

Spécialité : 2MGE : Matériaux, Mécanique, Génie civil,
Electrochimie

Arrêté ministériel : 25 mai 2016

Présentée par

Kaoutar RADI

Thèse dirigée par **Christophe MARTIN**, Directeur de recherche ,
Communauté Université Grenoble Alpes
et codirigée par **David JAUFFRES**, Grenoble INP

préparée au sein du **Laboratoire Science et Ingénierie des
Matériaux et Procédés**
dans l'**École Doctorale I-MEP2 - Ingénierie - Matériaux,
Mécanique, Environnement, Energétique, Procédés,
Production**

**Matériaux bio-inspirés : Optimisation du
comportement mécanique en utilisant la
méthode des éléments discrets**

**Bioinspired materials: Optimization of the
mechanical behavior using Discrete Element
Method**

Thèse soutenue publiquement le **12 novembre 2019**,
devant le jury composé de :

Monsieur FRANÇOIS BARTHELAT

Professeur, Université de MCGILL, Rapporteur

Monsieur IVAN IORDANOFF

Professeur, ENSAM PARIS, Président du jury

Monsieur FLORIAN BOUVILLE

Maitre de Conférences, Imperial College, Examineur

Monsieur DOMINIQUE LEGUILLON

Directeur de Recherche Emérite, CNRS DELEGATION PARIS, Examineur

Monsieur SYLVAIN DEVILLE

Directeur de Recherche, CNRS/Saint-Gobain CREE, Invité

Monsieur CHRISTOPHE MARTIN

Directeur de Recherche, CNRS délégation Alpes, Directeur de thèse

Monsieur DAVID JAUFFRES

Maître de Conférences, Univ. Grenoble Alpes G-INP, Co-encadrant de thèse

“We know very little, and yet it is astonishing that we know so much, and still more astonishing that so little knowledge can give us so much power.”

— **Bertrand Russell**

Abstract

Natural materials such as bone and the nacre of some seashells are made of relatively weak building blocks and yet often exhibit remarkable combinations of stiffness, strength, and toughness. Such performances are due in large part to their brick and mortar architectures. Many efforts are devoted to translate these design principles into synthetic materials. However, much of the progress is based on trial-and-error approaches, which are time consuming and do not guarantee that an optimum is achieved. Modeling is an appealing alternative to guide the design and processing routes of such materials. In this work, we develop a numerical model based on Discrete Element Method (DEM) to understand the reinforcement mechanisms and optimize the mechanical properties of nacre-like materials based on their microstructural parameters. The model follows the crack propagation, accounts for different reinforcement mechanisms, and quantitatively assess stiffness, strength, and toughness. An interesting approach, based on EBSD imaging, is presented to model the real material and its different microstructural variations. Results are then combined to provide design guidelines for synthetic brick-and-mortar composites comprising with only brittle constituents.

Key words: Discrete simulations, bio-inspired materials, brick and mortar materials, strength, toughness.

Acknowledgments

The past three years have been rich in emotions, joy, motivation, but also stress and despair. Not to demotivate any future PhD students, but completing a PhD takes a lot of courage, perseverance, and motivation. Before you start reading this PhD, I would like to say a few words and thank a few people. A PhD is not just another degree, it is a journey at which you try to do your best to find original solutions and test your limits. To do so, a lot of motivation is needed, which must remain intact throughout the whole three years. However, it is not so obvious. Small snags bring us back to reality. These little snags are the ups and downs of any PhD: equipment problems, simulations problems or even social problems that one may encounter eventually.

Luckily to resolve these problems I was surrounded by a lot of people on both the scientific and the personal levels. First, I would like to thank my supervisors Christophe Martin and David Jauffrès for choosing me for this PhD. I remember the first time I had a Skype interview with Christophe when he described the subject to me, I was so excited and curious about bio-inspiration to the point that I immediately decided to take this PhD offer. Working on this project that was also new for my supervisors was interesting because we all had a fresh vision on the ensemble. It was exciting and also scary to start working on something from scratch and not having anyone around who worked on something similar. But thanks to a lot of dedication and the help of my supervisors, everything worked out well and we succeeded to achieve important and interesting results. Thanks to your guidance, and precious advises a - Christophe and David - I was able to overcome a lot of difficulties during these three years. I would also like to thank the members of the Bicult project, with who also helped a lot during our meetings. A big thank you to Sylvain Deville from Saint Gobain research center, who started and coordinated the project. Sylvain was so inspiring, always encouraging and motivating everyone in the project and I honestly enjoyed working with him. Hassan Saad was also an important person who contributed to this PhD. I appreciated our discussions during the meetings and especially on Instagram. I wish you good luck for the end of your PhD. I am sure you will do great. I would also like to thank all the other members of the project, Sylvain Meille from MATEIS laboratory, Frabrice Rossignol from ICER and their teams. Without forgetting the Association Nationale à la recherche (ANR) and le pôle PEM for their financial support without which I would have been very poor during this PhD.

Many thanks to the members of the committee of my PhD who were chosen for their expertise and contributions in the different fields of this PhD (bio-inspiration, fracture mechanics, discrete elements modeling). Thank you, professor Ivan Iordanoff, for your nice and encouraging report, it was a real honor to receive your compliments, thank you for your good mood and the nice words at the end of the presentation, it was appreciated

by all my friends and family. Thank you professor Barthelat, your work was the basis that helped me to develop my model, it was a real honor to have you in my committee. I would also like to thank professor Dominique Leguillon, your expertise in fracture mechanics made the discussion captivating. A big thanks to Florian Bouville, who developed the first nacre-like alumina, I have been reading about your work and hearing a lot of good things about you from Sylvain. I was very honored that you accepted our invitation and I was even more honored talking to you. I understand now what Sylvain was talking about.

A crucial part of this PhD journey is the GPM2-SIMaP laboratory, what could I say about this amazing group? The three years I spent there will be forever unforgettable. Thanks to all the professors who were always present to help and to have great discussions. A special thanks to Elisabeth Lussi who always helped me with the administrative issues since the day I arrived, she will be truly missed after her retirement. Because of the numerical aspect of this PhD, I had numerous issues -of course- with the servers and the different software, thank you Yannick Le port and Alain Mouny for your help and good mood.

Now we get to the most important part of the laboratory, the PhD students. Over time, we became more than colleagues, we became friends and I will always cherish this friendship. First, I would like to thank all the members of the blue room, especially Pauline Gravier, Alexis Burr, Tristan Garnault, Shrey Joshi, Julia Bonaldo, Corentin Velard, H el ene Gomez, Elena Jover and Thibault Dissolier for all the interesting discussions we had either about work, politics, travels and of course the non-conventional subjects. A lot of thanks also to Etienne Guesnet who was very helpful at the beginning of my PhD. Without forgetting, of course, Zo e Roulon, Mathilde Labonne, Guillaume Crousot, Sara Abraham, Xavier Bataillon, Eliott Guerin, and Jessica Muzzy, for all the good times we had together. I think that having the parties, the ski weekends and the mountain trips helped a lot with overcoming the stressful times of this PhD.

Coming to Grenoble and doing this PhD was one of the best decisions I made in my life, I feel very blessed because I gained a lot of growth personally and scientifically. I also met amazing people who I have become friends with and had a lot of great times together. Chakri, Prasanta, Madalina, Sarah, Jos e, Akhil, Guillaume, Yahya, Hezam, Mahdi, Mar, Maroua, Ahlam, and Fadoua, thank you for being good friends and being always present. I had so much fun with you. I will miss you all and I hope we will stay in touch even if I move to the other side of the world.

Finally, I thank my parents who always supported me during my studies since day one. Thank you so much for trusting me, encouraging me and being proud of me. It always pushed me to work more and do my best. Thank you also for the amazing cookies that you sent from Morocco to celebrate my PhD. You were always in my mind even though you were not able to come. Chokran bezzaf. Thank you, Youssef and Laura, for coming from Metz and Strasbourg to celebrate my big day with me. I loved having you here. Thank you for setting up the food and putting up with my stress. I would especially want to thank my brother Youssef for supporting me during the past three years, you were always here to listen to me complain about my simulations and giving me priceless advice.

Of course, I will finish by thanking THE special person in my life who was with me all along this journey and supported me every day. David Browne, an incredible and smart man whose qualifiers are missing to describe him. Thank you for putting up with my

mood swings, stress, and anxiety. Thank you for being always present even though we were thousands of miles away with nine hours' time difference. It meant a lot to me that you came from California to attend my defense, thank you again for all the travels and the adventures we had together, I can assure you that it helped a lot with accomplishing this thesis.

Well if you made it until here, I wish you future PhD student, curious person or my future boss a good read. I hope you will enjoy reading this PhD like I enjoyed writing it.

Table of Contents

Abstract	v
Acknowledgments	vii
1 Introduction	1
1.1 Context and objectives: Bioinspiration applied to ceramics	3
1.2 Scientific program, organization of the project and consortium	4
1.3 Brick and mortar materials and DEM	5
1.4 Graphical outline	7
2 Literature review	9
2.1 Introduction	11
2.2 Brick and mortar materials	12
2.2.1 Natural materials	12
2.2.2 Synthetic materials and fabrication methods	14
2.2.3 Reinforcement mechanisms in brick and mortar (BM) materials	24
2.3 Modeling and performance optimization of brick and mortar materials	30
2.3.1 Analytical models	30
2.3.1.1 Stiffness	31
2.3.1.2 Strength	33
2.3.1.3 Toughness	34
2.3.2 Numerical models	38
2.4 Discrete Element Modeling (DEM)	42
2.4.1 What is DEM?	42
2.4.2 Application of DEM on continuous materials	44
2.5 Outcomes and outlines	47
3 Model development and validation	49
3.1 Introduction	51
3.2 Modeling of a continuous material with DEM	54
3.2.1 Microscopic beam model	54
3.2.2 Fracture criterion	55
3.2.3 DEM simulations	57
3.2.4 Sample generation	58
3.2.5 Elasticity and strength calibration	58
3.3 Modeling a brick and mortar material	62
3.3.1 Representative Volume Element (RVE)	62

TABLE OF CONTENTS

3.3.2	Homogenization procedure	63
3.3.3	Convergence study	64
3.4	Comparison with analytical models	65
3.4.1	Elastic modulus	65
3.4.2	RVE failure	68
3.5	Application to nacre-like alumina	72
3.6	Conclusions	75
4	The influence of interface strength and nano-bridges	79
4.1	Introduction	81
4.2	Discrete model for brick-and-mortar materials	84
4.2.1	DEM framework	84
4.2.2	DEM simulations	86
4.2.3	R-curve computation	86
4.3	Effect of global interface reinforcement via nominal strength	87
4.3.1	Macroscopic strength	87
4.3.2	Toughness	88
4.4	Effect of local interface reinforcement by nano-bridges	92
4.4.1	Macroscopic strength	92
4.4.2	Toughness	93
4.5	Discussion	95
4.6	Conclusions	98
5	Towards more realistic microstructures	101
5.1	Introduction	103
5.2	Effect of a random overlap distribution	104
5.2.1	Simulation conditions	104
5.2.2	Tensile tests	105
5.2.3	Single Edge Notched Tension (SENT) tests	108
5.3	Computation on real microstructures	112
5.3.1	Electron Back-Scattered Diffraction (EBSD) protocol	113
5.3.2	Microstructure analysis	114
5.3.3	Numerical microstructures from the EBSD image	117
5.3.4	Macroscopic strength and toughness	117
5.3.4.1	Strength	117
5.3.4.2	Toughness	120
5.4	Conclusion	126
6	Nacre-like ceramics: compaction and tablet alignment	129
6.1	Introduction	131
6.2	Generation of numerical samples	134
6.3	DEM Simulations: compaction	138
6.4	Tablet orientation	140
6.5	Conclusion	143

7	Conclusion and future work	145
7.1	Conclusion	147
7.2	Future work	149
	Appendices	153
A	Supporting information	155
A.0.1	Contact laws	155
A.0.2	Brick and mortar generation and parameter calibration	156
A.0.3	Crack length determination	158
A.0.4	Generation of microstructures with nano bridges	160
B	Influence of Young modulus ratio on toughness	161
B.1	Crack propagation	161
B.2	Initiation and growth toughness	163
C	FIB-SEM and holotomography images	165
D	Nano-particles volume fraction	169
	Bibliography	171

Chapter 1

Introduction

1.1 Context and objectives: Bioinspiration applied to ceramics

In structural materials, combining high strength and toughness is not usual. Finding a solution to this contradiction is a very important challenge for diverse applications, especially for energy and aeronautics where there is a high demand for strong and damage tolerant refractory materials. In this context, a new project funded by the National French Association of Research (ANR) has been launched in 2016: BiCuIT (Bioinspired Structural Ceramic Composites). In this project, a bio-inspired approach is proposed to design and process a fully ceramic tough composite material that can fulfill the task of combining both high strength and toughness. The main objective of this project is to take the mechanical properties of the nacre-like material developed by [Bouville et al., 2014b] to their optimum. This ceramic-ceramic composite has a brick and mortar (BM) structure inspired by the nacre of seashells. It is composed of 95% of oriented alumina tablets separated by a thin calcium-silicate glass interface and alumina bridges (Fig. 2.9).

A rational control of the architecture and a deep understanding of the process-structure-properties relationships is needed. The newly developed knowledge and techniques could be applied in a close future to industrial materials in order to improve material performances and process efficiency. To reach the project's main objectives, two axes are developed:

- An extensive investigation of the reinforcement mechanisms through characterization (in-situ testing, 3D imaging, Raman spectroscopy) and discrete element simulations of brick and mortar materials, to identify the main parameters responsible for their impressive mechanical properties.
- An improvement of the synthesis of nacre-like alumina, including a precise control of the interface homogeneity and properties. Other routes for tablet alignment should be investigated as well as the introduction and control of residual stresses.

Albeit the current nacre-like ceramics shows an interesting improvement compared to conventional ceramics, the processing and structure still need improvements. The work done by [Bouville et al., 2014b] is only a proof of the concept and the demonstration of the ultimate properties that can be achieved through this approach is still lacking. For example, tablets orientation and nano-particles distribution between tablets are known to be critical for the mechanical performance and can be enhanced via process modifications. In addition, the nature and relative importance of the toughening mechanisms in these all-ceramic composites are still unknown or poorly understood as of today.

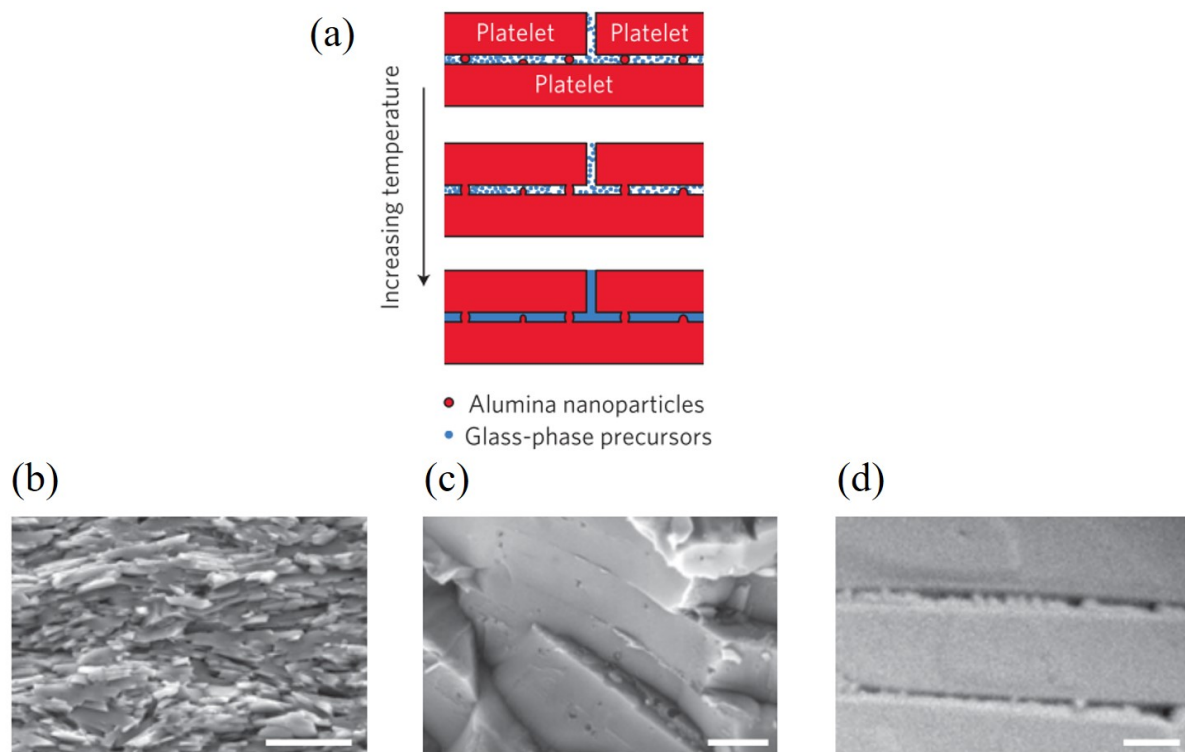


Figure 1.1: Nacre-like alumina. a) A simple scheme with the components of the material. b,c, d) SEM images showing the brick and mortar structure on different scales (scale bars 10 μm (b), 500 nm (c) and 250 nm (d) [Bouville et al., 2014b]).

In addition, the process to obtain the final material is slightly complex and involves multiple steps. Scaling up is therefore very difficult. Also, controlling the tablet alignment is not an easy task as well as the interface distribution.

1.2 Scientific program, organization of the project and consortium

So far, the studied Brick and Mortar (BM) approaches use either an organic or metallic mortar. This project is rather different, the focus here is on ceramic/ceramic composites, where process development, fine morphological and composition characterization, in-situ mechanical testing, and modeling work are combined.

The project is coordinated by The Ceramic Synthesis and Functionalization Laboratory (LSFC) in Saint Gobain Ceramic Research Center. As for the scientific part, one of LSFC main objectives is to simplify the process and scale it up. This allows the processing of bigger samples compare to the old method and easy scale up. More studies on the effect of the new process on the material's structure are in progress. The second objective is to

design and characterize a bi-layer system to achieve a rational design of the composition and structure of the interface.

The second project partner is the Ceramics Institute Research Center (ICER) formerly called SPCTS. The main contribution of this collaborator consists of achieving a more homogeneous and controlled distribution of nano-particles at the interface. Modeling is also part of the program to identify the main parameters that control the adsorption of small particles at the surface of the alumina platelets, and the homogeneity of their distribution.

To have more information on the stress distribution during mechanical testing, the Geology Lab in Lyon (LGL), with expertise in Raman spectroscopy, is performing in-situ mechanical tests using Cr fluorescence spectroscopy to access the local stresses up to 400°C. The micronic spatial resolution of Raman is sufficient to track stress distribution around cracks or indentation tips. Raman spectroscopy will also be used to characterize the bilayer material developed by LSFC lab.

To validate the concepts developed in the project by the other collaborators, Materials, Engineering and Science lab (MATEIS) at INSA Lyon will combine the knowledge of the other tasks to synthesize an optimized nacre-like material and characterize it.

The last collaborator is the SIMAP laboratory where this PhD is conducted. The principal objective of the work done in SIMAP is to develop a numerical model to understand the reinforcement mechanisms and optimize the mechanical properties of nacre-like materials. The numerical model is based on the Discrete Element Method (DEM) code developed in SIMaP laboratory specifically for materials science applications.

1.3 Brick and mortar materials and DEM

Given the many reinforcements mechanisms at play and material parameters controlling them, modeling is an essential tool to orient the design of optimized architectures. Considering the suitability of DEM to model damage, crack propagation and topological modifications (see section 2.4.1), this method was chosen to model the mechanical behavior of nacre-like materials.

As part of the project, DEM simulations are meant to answer some fundamental questions that relates to the concept of BM materials and the reinforcement mechanisms. The first question to be answered is how can toughness arise in materials that comprise only brittle constituents? Also, can we identify the toughening mechanisms and their relative importance in the nacre-like materials? How important is to have a strong interface? Does it affect strength and toughness in a similar way? is there an optimum? Do adding bridges between the tablet improve the mechanical properties? If yes, is there a limit to

this improvement? What are the ideal properties of the interface to maximize the strength and toughness of these materials? Can we link the local crack propagation behavior to the overall mechanical response of the sample? Do alumina nano-particles play a role in tablet alignment?

To answer these questions and more, the work carried out during this PhD will be presented in the form of five chapters. In Chapter 2, the state of the art about natural and synthetic BM materials will be presented. The different reinforcement mechanisms of natural BM materials are listed and described, as well as their effect on the overall mechanical behavior. As for synthetic materials, the focus will be on the different processing routes, their advantages and disadvantages. The analytical and numerical models proposed in the literature to study BM materials are also presented. Lastly, a brief history and description of DEM is proposed, in particular its application to continuous materials.

Chapter 3 will be on the development and the validation of our model against analytical models on a Representative Volume Element (RVE) of a BM material in terms of elasticity and fracture. A simple application is presented to confirm the robustness of the proposed model.

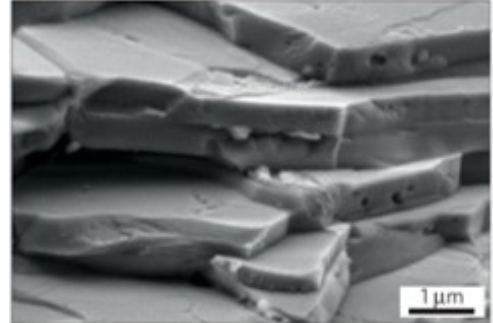
The model is afterwards applied to larger scale microstructures in order to simulate crack propagation over several tablets within a notched geometry and assess toughness. In Chapter 4, the effect of the interface reinforcement (by changing the interface material or by the addition of nanobridges) on composite strength and toughness is studied. Different reinforcement mechanisms are described and two toughness parameters are presented: crack initiation toughness and crack growth toughness. A property map summarizes our findings to design a composite for a given application with the appropriate combination of strength, crack initiation toughness and crack growth toughness.

After working on ideal BM microstructures in Chapter 4. Chapter 5 focuses on the effect of microstructural distributions (i.e. overlap aspect ratio) on the overall mechanical properties. The model is taken a step further to be applied on realistic microstructures, where EBSD images are combined to DEM code. Finally, in Chapter 6, an important step of the process is modeled to study the alignment of the bricks. The uniaxial compaction prior to sintering is modeled to investigate the effect of adding the nano-particles between the tablets on the overall alignment of the resulted material. Conclusions are provided and perspectives are proposed in the last chapter (Chapter 7).

1.4 Graphical outline

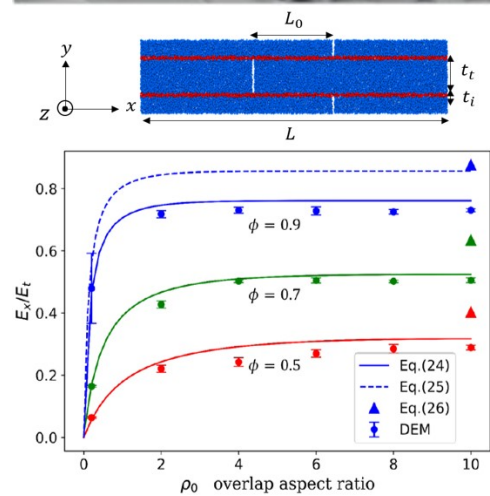
2. Literature review

- Natural BM materials
- Synthetic BM materials
- Analytical and numerical models
- Discrete Element Method



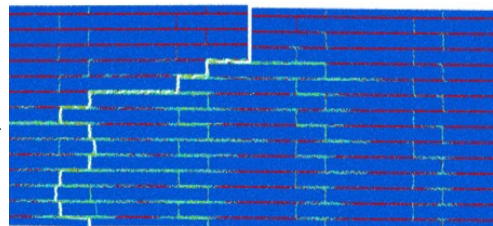
3. Model development and validation

- Simulations at RVE scale
- Comparison with analytical models
- Model application



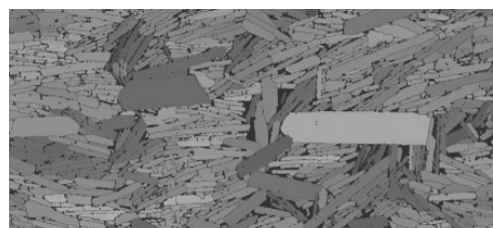
4. Interface reinforcement effects

- Large scale simulations to assess R-curve
- Local (nano-bridges) vs. global interface reinforcement
- Property maps



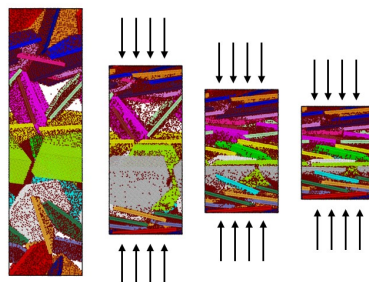
5. Towards more realistic microstructures

- Overlap distributions effect
- DEM and EBSD images



6. Nacre-like alumina and tablet alignment

- Uniaxial compaction
- Nano-particles effect



Chapter 2

Literature review

2.1 Introduction

Having high strength and high toughness simultaneously in structural materials is unusual. Resolving this contradiction is an important challenge for many applications, especially for high temperature applications (energy, aeronautics...) where the quest of strong and damage-resistant refractory materials is very high. In this context, Bouville et al. [Bouville et al., 2014b] have developed a bioinspired approach to design and process fully ceramic tough composite materials that combine both high strength and toughness. The processing of these composites is based on an ice-templating technique (Section.2.2.2), which has been proved remarkably efficient at creating brick and mortar microstructures bio-inspired by the architecture of the nacreous part of seashells [Bouville et al., 2014b]. The objective of this thesis is to bring these nacre-like materials to their optimum behavior through in-depth understanding of reinforcement mechanisms, microstructure and process. These newly developed techniques and knowledge could be very useful to a future industrial application in order to improve material performances and process efficiency.

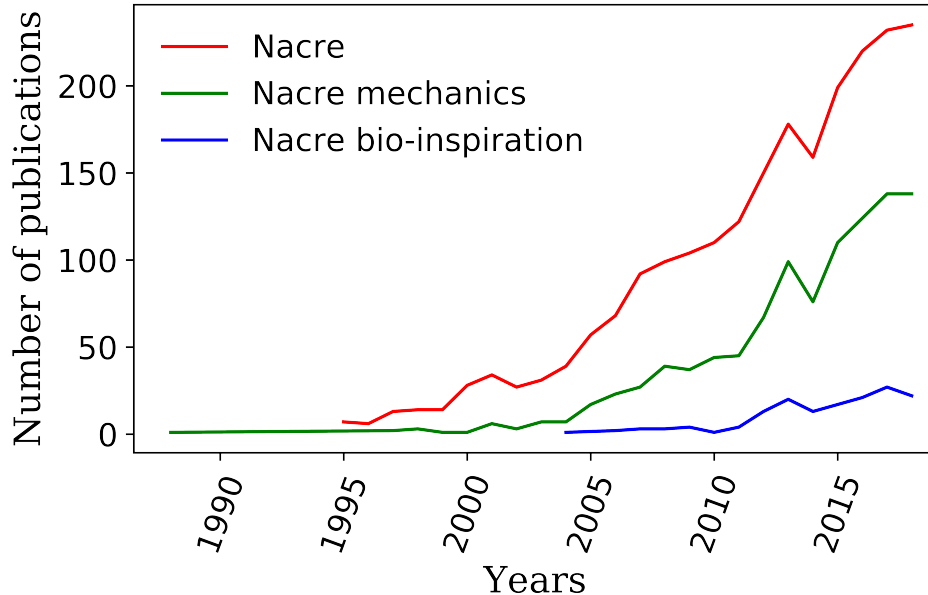


Figure 2.1: Number of scientific publications per year related to the topics relevant to this PhD: nacre, nacre mechanics, and nacre bio-inspiration. The plotted data was taken from web of science.

Due to the impressive mechanical behavior of nacre-like materials and the potential

of bio-inspiration, this research area has been attracting attention since 1997. In fact, the interest in this type of materials has only been increasing over the past years (Fig. 2.1). For example, more than 200 scientific paper were published in 2018 under this topic "nacre". Having this amount of scientific publications is beneficial for the development of these materials, which also means that an exhaustive literature review is difficult to achieve. Here we will focus on the description of brick and mortar materials (natural and synthetic), as well as their impressive reinforcement mechanisms. The analytical and numerical models developed to describe these mechanisms are also presented. Last, Discrete Element Modeling is reviewed as a numerical tool to investigate the link between microstructure and mechanical properties, presented in two subsections. First the DEM method is described then examples of its application on continuous materials are presented.

2.2 Brick and mortar materials

2.2.1 Natural materials

The quest for stronger, tougher and sustainable materials has been an important topic of research for many decades. As most engineering materials sacrifice one or another, researchers strive to overcome these limitations by exploring new materials. Heterogeneity embedded in natural materials engenders outstanding material properties. Natural materials are considered to be very efficient, because of their fulfillment to the complex requirements imposed by their environment using only few basic elements (C, O, H...). Those requirements can be mechanical such as: supporting static and dynamic loads created by the mass of the organism or by the wind load, storing or releasing elastic energy, flexing through large angles, resisting buckling and fracture. Furthermore, natural materials are sustainable, recyclable and also biodegradable, which makes them a model for environmentally conscious engineering.

For practical purposes, natural materials are composites. They are composed essentially from a soft phase (protein) and a stiff phase (minerals) that can form building blocks arranged in a hierarchical manner. For instance, plant cell walls, are composed of cellulose, hemicellulose, pectin and protein and can be lignified, while animal tissues consist largely of collagen, elastin, keratin, chitin and minerals such as salts of calcium or silica. From these constituents, nature succeeded to build a remarkable number of structured composites. Wood and bamboo for example, consist of cellulose fibers in a lignin–hemicellulose matrix, built to hollow prismatic cells of varying wall thickness. Collagen is the basic structural element for soft and hard tissues in animals, such as tendon,

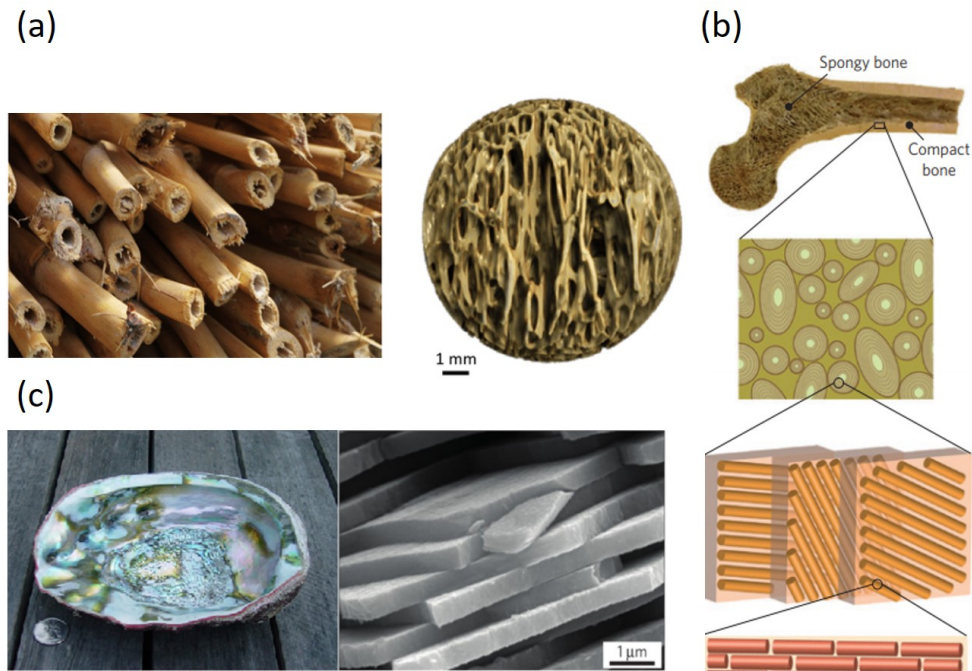


Figure 2.2: Natural structural materials: a) bamboo and its hierarchical structure b) bone showing four levels of hierarchy c) abalone shell and a SEM image of its microstructure. Figures are reproduced from [Ritchie, 2011; Meyers et al., 2008].

	Toughness (MPa.m ^{1/2})	Work of fracture (J.m ²)	Tensile strength (MPa)	Young's modulus (GPa)
Wet nacre	3.7 – 4.5	1034 – 1650	78 – 130	58 – 70
Dry nacre	3.3 – 4.6	437	90 – 167	68 – 90

Table 2.1: Mechanical properties of nacre [Jackson et al., 1988; Currey, 1977; Barthelat et al., 2006].

ligament, skin, blood vessels and muscle. Mechanically speaking, these materials would not have anything special about them when existing as individual blocks, it is thus their structure and arrangement that gives them their striking efficiency.

One of the most remarkable examples is the nacreous part in mollusk seashells, which can reach very high stiffness, strength or toughness simultaneously. Nacre is made of aragonite tablets and proteins arranged in a brick and mortar composite. The architecture of nacre also includes many other structural features defined at different length scales, from the fibril network of the interface to the arrangement of mesolayers [Barthelat et al., 2016]. The high performance of nacre can be attributed to this hierarchical architecture. Aragonite is a brittle ceramic, mineralized by the shell through complex processes [Schäffer et al., 1997]. Because of its high strength and toughness compared to its constituents [Calvert, 1995], nacre has attracted a lot of attention. Several methods were used to characterize the mechanical behavior of nacre: tension [Currey, 1977], shear and four-point bending [Wang et al., 2000b]. Nacre exhibit very important mechanical properties (Fig.2.1), its tensile strength can go up to 167MPa and its toughness to 4.5MPa.m^{1/2}. Compared to engineering materials, the reported values might seem low, but compared to nacre's constituents the improvement of the mechanical properties is extraordinary.

2.2.2 Synthetic materials and fabrication methods

Various processing routes have been developed (mainly in the last decade) to produce synthetic brick and mortar materials. Figure 2.3, shows the main fabrication routes to produce nacre-like materials that we are going to discuss in the following section. A common belief is that some ductility is required at the interface for an efficient toughening of the composite, directing thus research almost exclusively towards ceramic/polymer and ceramic/metal composites. The choice between macroscopic composites, free standing films or coating depends on the final application desired. In this review, we will mainly focus on the methods used for macroscopic composites.

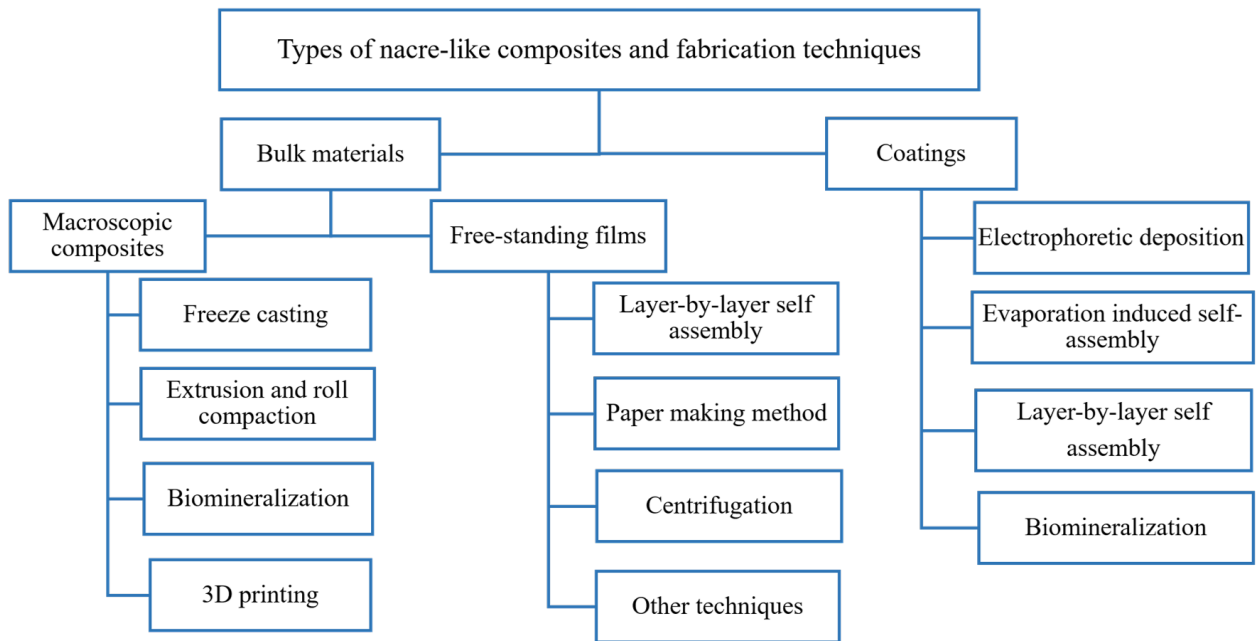


Figure 2.3: A scheme of the essential techniques developed to fabricate nacre-like materials, either as macroscopic composites, free standing films or coatings. Here, only the methods used to produce macroscopic materials are presented, more information can be found in the review done by Corni et al. [Corni et al., 2012].

One of the recent methods to mimic the hierarchical microstructure of nacre is freeze casting, producing hybrid materials with either a lamellar or brick-and-mortar structure [Launey et al., 2009; Munch et al., 2008]. The ceramic bricks are $5\ \mu\text{m}$ to $10\ \mu\text{m}$ thick and $10\ \mu\text{m}$ to $20\ \mu\text{m}$ long. Figure 2.4 shows the process used to produce the lamellar structure. Large porous ceramic scaffolds were prepared from water-based suspension containing sub-micron alumina Al_2O_3 particles and organic additives to control the ice crystal structure, then the suspension is cooled down to $-80\ ^\circ\text{C}$, which allows the lamellae ice to grow directionally and expel alumina particles resulting in a templated ceramic scaffold. Afterwards, the water and the organic additives are eliminated from the samples by freeze drying before the scaffold get sintered. By infiltrating the ceramic scaffold with wax and applying pressure in the perpendicular direction of the lamellae, brick and mortar structure can be produced. A second sintering is then required to eliminate wax and to form bridges between the bricks. The final step consists of infiltrating the scaffold (lamellar or brick and mortar) with polymethyl methacrylate (PMMA), to produce $\text{Al}_2\text{O}_3/\text{PMMA}$ hybrid materials (Fig.2.5). The brick and mortar structure mimic natural nacre on different length scales, with high ceramic content, thin polymer layer and high surface roughness.

The stress-strain curves of the fabricated material are quite similar to those of nacre,

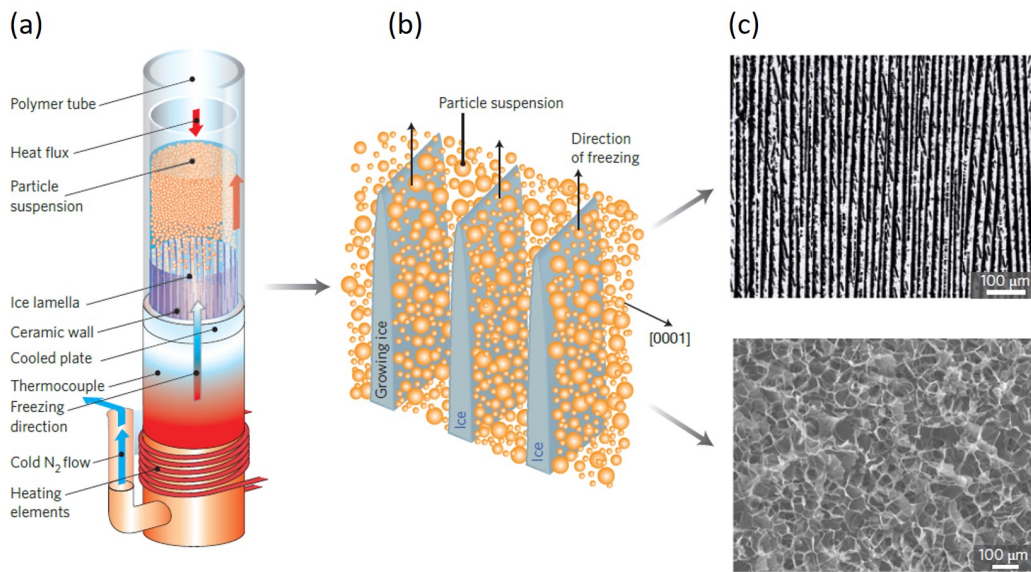


Figure 2.4: a) Directional freezing of ceramic suspensions to form ceramic scaffolds, that can later be used to create layered materials. b) Formation of lamellar ice crystals resulting into the expulsion of the particles. The particles get trapped between the ice crystals and form lamellar material. c) SEM micrographs of the final structure. Figures are adapted from [Deville et al., 2007; Wegst et al., 2010].

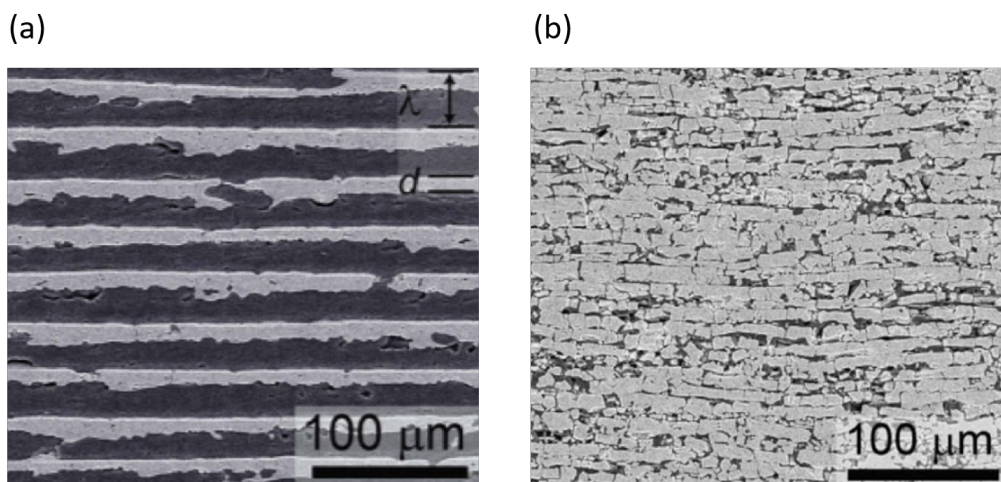


Figure 2.5: a) A SEM image of lamellar structure Al₂O₃ – PMMA produced by freeze casting by Munch et al. , the lighter phase is the ceramic and the darker one is the polymer. b) Brick and mortar structure issued from pressing and sintering the lamellar scaffolds [Munch et al., 2008].

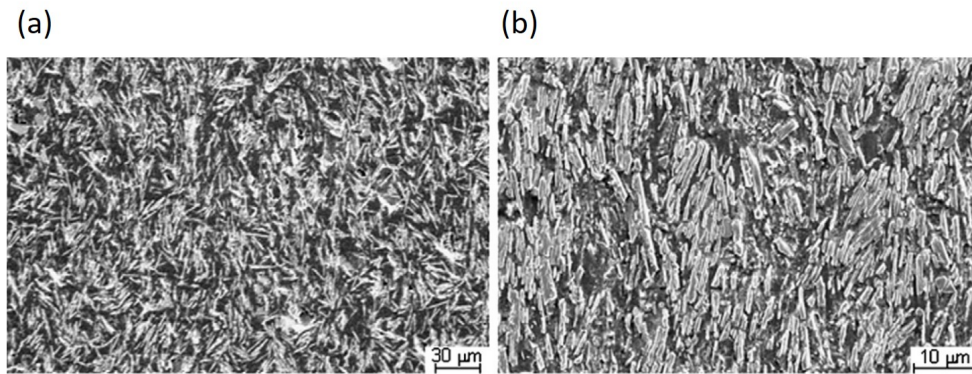


Figure 2.6: A cross section of alumina flakes-epoxy composite a) produced by a simple mixture b) and by HASC. The microstructure is pretty similar to natural nacre, with a thickness close to that of aragonite tablets and a slightly bigger diameter [Oner Ekiz et al., 2009].

the flexural strength was of 210 MPa comparing to 135 MPa for natural nacre, and the fracture toughness as a function of the crack extension surpassed that of natural nacre.

This technique has also been applied to fabricate $\text{Al}_2\text{O}_3/\text{Al}$, $\text{Al}_2\text{O}_3/\text{epoxy}$, hydroxyapatite/ Al , hydroxyapatite/epoxy composites [Munch et al., 2008; Launey et al., 2010], proving the flexibility of the method. The composites in question showed a significant improvement in flexural strength (300 MPa) and toughness ($40 \text{ MPa}\cdot\text{m}^{1/2}$). Although freeze casting showed promising results, scaling -up process seems to be difficult. Another challenge would be how to uniformly infiltrate the polymer in the ceramic scaffold.

Another method to produce nacre like materials is hot press assisted slip casting (HASC), it was used to produce alumina flake-epoxy composites [Oner Ekiz et al., 2009]. The composite is fabricated by mixing manually the components and pouring the mixture into a porous mold, within a steel die, the system is hot pressed at 150°C for 30 minutes afterwards. The pressure applied helps the liquid matrix to flow through the mold, decreasing the matrix content in the composite and aligning the alumina flakes in the perpendicular direction to the pressure direction.

Figure 2.6 shows a cross section of the composite produced by a simple mixture (Fig.2.6.a) and by HASC (Fig.2.6.b), where alumina flakes are more aligned pointing out to the effectiveness of HASC in reinforcing phase alignment as compared to simple mixing. The flexural moduli and strength of the material were quite close to natural nacre 19 – 23 GPa and 135 – 155 MPa respectively. However, the interfacial bonding between the two phases still need to be optimized.

Inspired by a natural process, biomineralization or bottom-up technique is an in-situ experimental method in which the mineralization takes places in vitro from supersaturated solutions in the presence of organic macromolecules which can accelerate or prevent

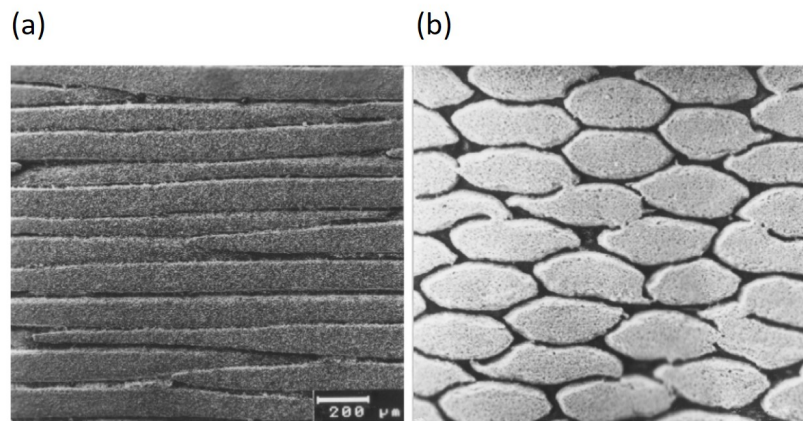


Figure 2.7: Microstructure of Si_3N_4 fibrous monolithic composite Wang et al. [2000a]. a) On both sides of the sample, the fibers are arranged regularly in a uniaxial direction. b) A cross section showing the hexagonal shape of the cells.

crystals growth depending on their concentration.

To prepare a composite using this method, both the macromolecular solution and the supersaturated solution are added up together and left to perform naturally. The choice of the organic template is very important to form the desired inorganic layer [Oaki et al., 2006; Zhang et al., 2004; Xu et al., 1998]. This method, has been widely studied to understand the underlying fundamental processes and was applied to produce bulk materials. However, the process time is quite long, a day or two are needed to produce microscale materials and the mechanical properties are not as good as would be expected from this microstructure.

Another interesting method is the extrusion and roll compaction used by Wang et al. [Wang et al., 2000a] to produce two high toughness ceramics: a fibrous monolithic silicon nitride/boron nitride ($\text{Si}_3\text{N}_4/\text{BN}$) to mimic the behavior of bamboo and laminated $\text{Si}_3\text{N}_4/\text{BN}$ to imitate the behavior of nacre. The ceramic powders, organic binder, plasticizing agents and lubricant are mixed then rolled until obtaining a well rolled mud pie. The mud pie is afterwards extruded using orifices with different diameters, then roll compacted to obtain laminated green bodies or coated to obtain fibers. The final steps consist of drying then hot-pressed sintering.

The composites obtained by this method (Fig.2.7), showed very interesting mechanical properties, especially after adding silicon carbide whiskers to the Si_3N_4 matrix and Al_2O_3 to the BN layers to adjust bonding strength between layers. Toughness and work of fracture reached very high values: $28 \text{ MPa}\cdot\text{m}^{1/2}$ and $4\text{KJ}\cdot\text{m}^{-2}$ respectively. The extrusion and roll compaction method seem to be promising for the production of nacre-like bulk materials with mechanical properties similar to hierarchical natural materials.



Figure 2.8: A SEM micrograph of a printed nacre produced by Yadav et al. using 3D printing method [Yadav et al., 2018].

3D printing technology or additive manufacturing has also been used to produce bioinspired architectural materials. It is defined a method that employs a computer-controlled design followed by the movement of a pattern generating device in the form of ink deposition nozzles or laser writing optics for layer by layer fabrication of materials. Unlike traditional manufacturing methods that encompasses several separate processing techniques (cutting, forming, bending or transforming materials and components for further assembling in one part), 3D printing has the capability of doing it all at once.

One of the pioneers in using 3D printing is Dimas and his coworkers Dimas et al. [2013], where they used photopolymers to produce a nacre like structure composed of simple building blocks. The resulting structure showed a fracture response far higher than its constituents. Still, the lack of control over the manufacturing process makes it hard to synthesize the composites at a finer length scale. Yadav et al. [Yadav et al., 2018] also used 3D manufacturing to prototype molluscan shell architectures (Fig.2.8), where they used a photo-polymer and studied the effect of microstructural manipulation on mechanical and frictional features of the printed molluscan shell.

However, the manufacturing of these composite depends on resolving some technical problems. The materials used in 3D printing/additive manufacturing are rather limited, only a few metals, polymers and a limited number of ceramics can be used to establish structures with features with a size of micrometer/sub micrometer. The difficulty of controlling the surface quality and the microstructure of individual layers is also a problem that may impede the reliable combination of mechanical properties required for the structural application of the finished materials.

Recently, a new bioinspired BM material, nacre-like alumina, has been developed by [Bouville et al., 2014b]. In contrast with metal-ceramic or polymer-ceramic composites,

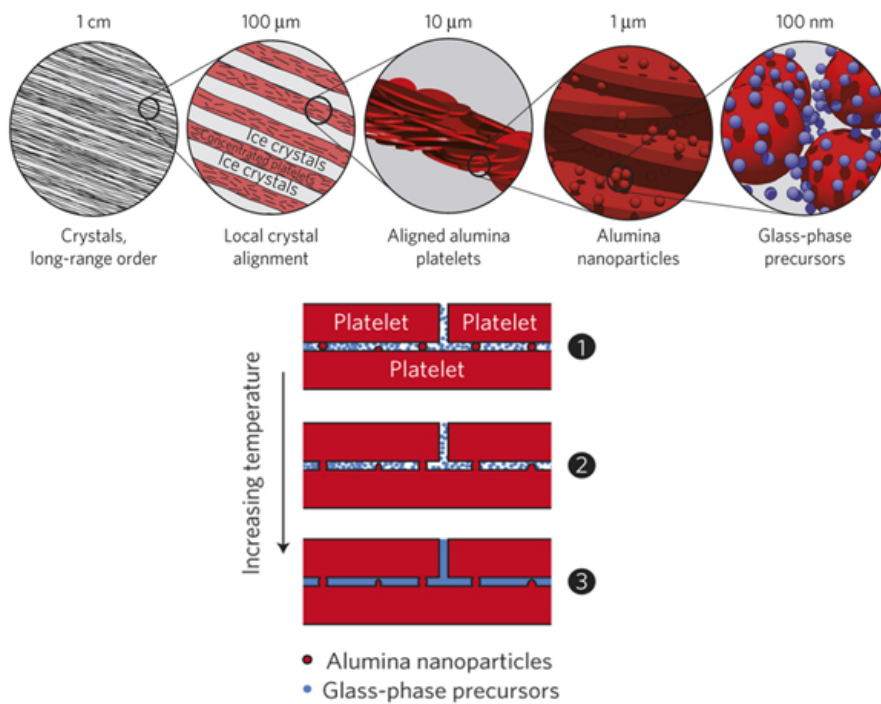


Figure 2.9: A description of the fabrication strategy and structural self-organization in nacre like alumina. Ice crystals grow to trigger the alignment of the alumina tablets, then the nano-particles and the glass precursors get trapped between the tablets. Figures are reproduced from [Bouville et al., 2014b].

this ceramic-ceramic composite can maintain high strength and high toughness at a high temperature 600 °C (Fig.2.10) and keep a high oxidation resistance. The material is composed of brittle constituents only: 98.5 vol. % of alumina tablets with a diameter of 7 μm and a thickness of 500 nm and alumina nano-particles (100 nm), 1.3 vol. % of silica, and 0.2 vol.% of calcia. All the components were incorporated into an initial aqueous suspension that was frozen under flow afterwards. The ice crystals line up in parallel to the direction of the thermal gradient and thus form a template aligning the platelets in the same direction, resulting in a sample of a few centimeters with aligned crystals. The sample is sintered afterwards at high temperature (1500 °C) and high pressure (100 MPa) using the Spark Plasma Sintering (SPS) to prevent grain growth, which is not possible in conventional sintering process. The whole operation was carried out in a cylindrical graphite die closed by two graphite pistons.

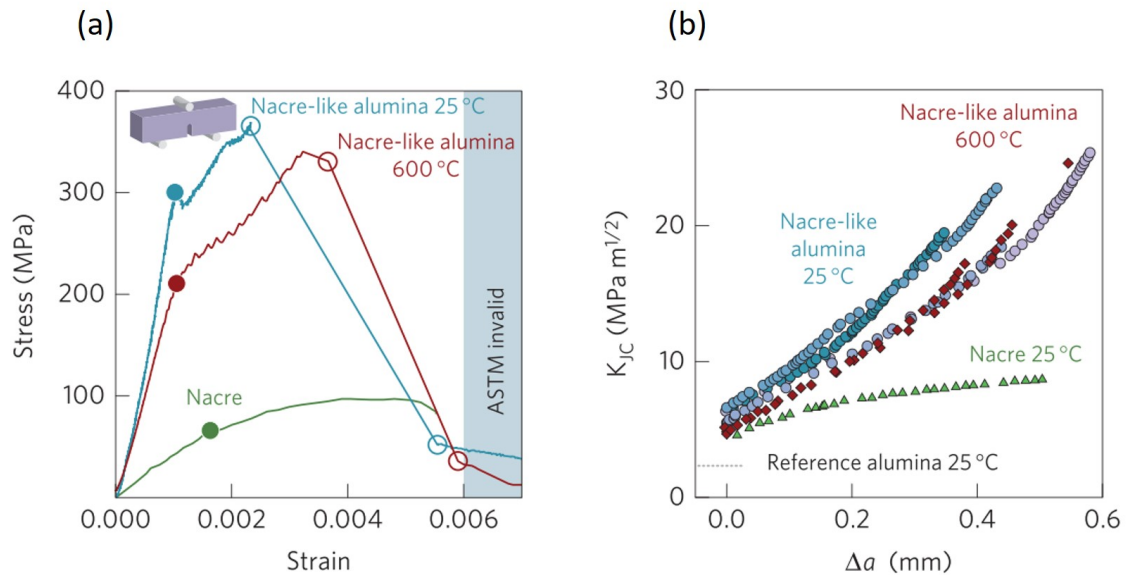


Figure 2.10: Mechanical properties of nacre-like alumina at different temperatures. a) Stress-strain curves. The filled disks show the beginning of stable crack propagation and the circles show the beginning and the end of unstable crack propagation. b) Fracture toughness as a function crack size. Figures are reproduced from [Bouville et al., 2014b].

[Pelissari et al., 2017; Grossman et al., 2017] used Magnetically-Assisted Slip Casting (MASC), to produce nacre-like alumina (NLR/TL). First, suspensions were made by mixing deionized water and alkali-free organic polyelectrolyte as a dispersant, then adding acid boric, the mixture is afterwards sonicated for half an hour. The alumina functionalized tablets are then incorporated in the suspension that was sonicated for 10 minutes. A rheological thickening binder was mixed to the suspensions. The resulting slurries were put on a porous mold under rotating magnetic field to align the alumina tablets. Then,

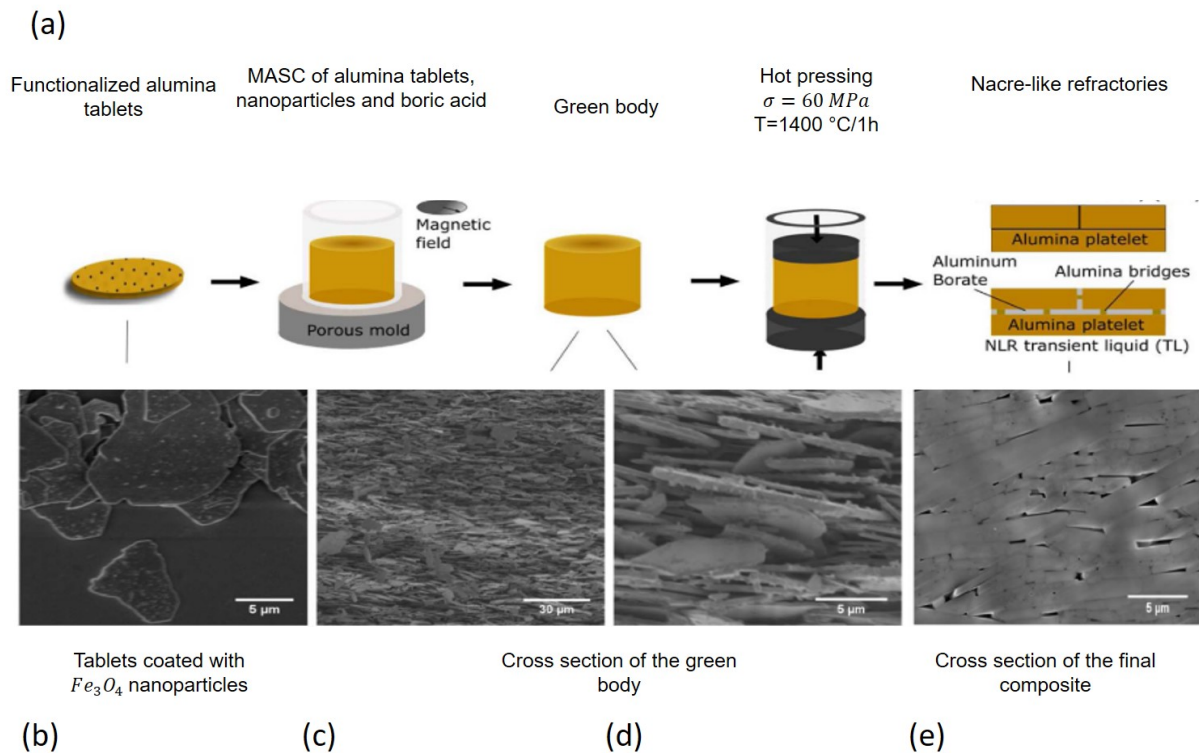


Figure 2.11: (a) Magnetically Assisted Slip Casting (MASC) steps followed to produce nacre-like ceramics. (b–e) SEM micrographs of the materials at different stages of the fabrication: (b) functionalized alumina platelets, (c) and (d) cross-section of green body perpendicular to the platelet alignment, and (e) cross section of the nacre like refractory with transient liquid phase. Figures are reproduced from [Pelissari et al., 2017].

the prepared samples were dried 4h at $60 \text{ }^\circ\text{C}$ and hot pressed.

In contrary to nacre-like alumina produced by freeze-casting and SPS, that was tested at $600 \text{ }^\circ\text{C}$ only, NLR/TL produced by MASC was tested at higher temperatures (up to $1200 \text{ }^\circ\text{C}$) and showed remarkable strength ($\approx 300 \text{ MPa}$) and fracture toughness ($\approx 6 \text{ MPa}\cdot\text{m}^{1/2}$). The MASC (Fig.2.11) processing route allows for the manufacture of ceramics with highly organized textured microstructure at different length scales and is fast, easy and suitable for the production of large samples.

Because of technological restrictions, unclear understanding of the toughening mechanisms and design principles of nacre, only a few bioinspired materials achieved mechanical properties as good as biological materials. Most of the designs developed are only empirical duplications of natural nacre. For the most part, higher tensile strength and stiffness are relatively easy to reach for synthetic materials, but a high toughness and other functions seems to be hard to achieve. As a result, a deeper understanding of the dependence of the remarkable toughness of nacre on its hierarchical structure will be helpful to optimize

the design and manufacturing of new bio-inspired materials.

Fabrication techniques	Materials	Mechanical properties	Challenges	References
Freeze casting + Infiltration	80 vol.% Al_2O_3 20 vol.% $PMMA$ or AL or epoxy	Strength: 210 MPa	Complex infiltration step	[Munch et al., 2008] [Launey et al., 2009]
HASC	60 vol.% Al_2O_3 flake 40 vol.% epoxy	Modulus: 19 – 23 GPa Strength: 133 – 155 MPa	Optimization of interfacial bonding (Al_2O_3 /epoxy)	[Oner Ekiz et al., 2009]
Biom mineralization	–	Modulus 16.1 GPa	Time consuming method	[Oaki et al., 2006] [Zhang et al., 2004] [Xu et al., 1998]
Extrusion and roll compaction	Si_3N_4 – BN with SiC whiskers in the Si_3N_4 matrix	Toughness 28 $MPa.m^{1/2}$ Work of fracture : 4 $KJ.m^{-2}$	Time consuming method	[Wang et al., 2000a]
3D printing	Photopolymers	–	Limited range of materials Limited control over surface quality Limited resolution	[Dimas et al., 2013] [Yadav et al., 2017] [Yadav et al., 2018]
Freeze casting and SPS	98.5 vol.% Al_2O_3 1.3 vol.% SiO_2 0.2 vol.% CaO	Modulus: 290 GPa Strength: 470 MPa Toughness: 22 $MPa.m^{1/2}$	Upscaling	[Bouville et al., 2014b]
MASC	Functionalized alumina tablet Alumina nano particles Boric acid	Strength : $\approx 300 MPa$ Toughness: $\approx 6 MPa.m^{1/2}$	–	[Pelissari et al., 2017] [Grossman et al., 2017]

Table 2.2: A summary of the main different methods to produce synthetic nacre-like materials.

2.2.3 Reinforcement mechanisms in brick and mortar (BM) materials

In fracture mechanics, toughness is defined as the resistance to failure or crack propagation, it is related to the amount of energy required to propagate a crack. The linear-elastic fracture toughness can be described in terms of a critical stress intensity factor K_{IC} at which the crack begins to grow. The fracture behavior can depend strongly on the crack size; a principal manifestation of this dependence is the rising resistance - curve (R-curve) (Fig.2.13) where the force to sustain cracking increases with the crack extension [Launey & Ritchie, 2009].

Reinforcement mechanisms can be divided into two categories; intrinsic and extrinsic mechanisms (Fig.2.12). Intrinsic mechanisms act only ahead of the crack tip and results essentially from plasticity in order to enhance the materials inherent damage resistance, leading to increasing crack-initiation toughness. These mechanisms are active undependably of the crack size or geometry, and they essentially affect its initiation.

In contrary to intrinsic toughening, extrinsic toughening includes microstructural mechanisms acting behind the crack tip to resist its further opening by lowering the stress and strain fields at the crack tip. These mechanisms can occur by fiber bridging, where the fibers hold the two fracture surfaces together after the crack has propagated, or by frictional interlocking between two rough fracture surfaces. It can also be a result of microcracking around the main crack to relieve the stress at the main crack tip. Therefore, extrinsic mechanisms influence only the crack growth and have practically no effect on crack initiation [Ritchie, 2011], which shows that toughening depends on the crack size. Thus, it is common to represent toughness as a function of crack extension (Fig.2.13).

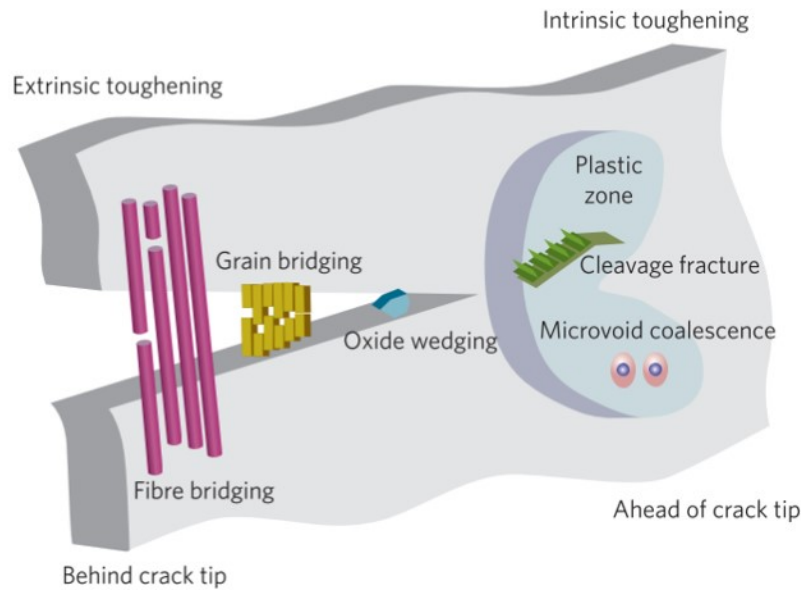


Figure 2.12: A Schematic illustration of intrinsic damage mechanisms: which promote crack propagation and extrinsic crack-tip-shielding mechanisms, which prevents the crack from advancing [Ritchie, 2011].

Based on the operating scale, the structural toughening mechanisms of nacre can be classified, from inter-tablets mechanisms operating at the micrometer scale (crack deflection, bridging, interlocking, etc) to intra-tablets mechanisms at the nano-meter scale:

- **Nano-grains:** Li [Li, 2004] has shown the important role of nano-grains within the tablets to strengthen them, which can improve the overall performance of nacre.
- **Tablet nano-asperities:** Evans et al. and Wang et al. [Evans et al., 2001; Wang et al., 2000b] showed that nano-asperities on the tablets were the reason behind table sliding resistance.
- **Tablet interlocking:** Barthelat et al. [Barthelat et al., 2007], showed that tablet waviness appears as a critical feature that is considered to be responsible for the large inelastic deformations and strength of nacre. It also generates progressive tablet interlocking during tablet sliding and propagates inelastic deformations over large regions of the material.
- **Bridges between tablets:** The bridges formed between the tablets can be considered one of the important features responsible in nacre like materials for high strength and toughness. It was also proven that the size, density and distribution of the nano-bridges affect strength and toughness [Gu et al., 2017; Shao et al., 2014; Grossman et al., 2018].

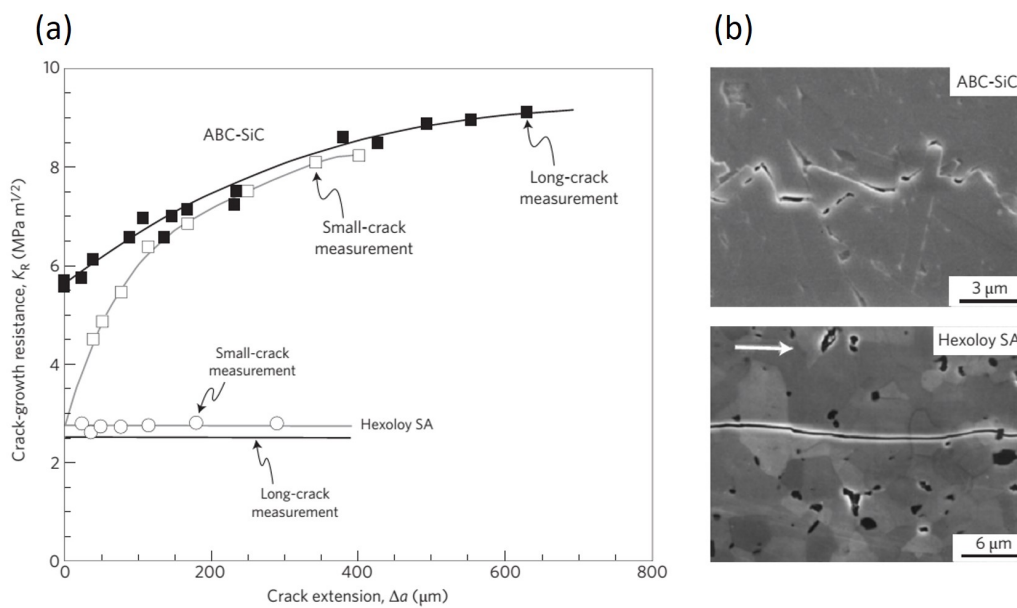


Figure 2.13: : a) An example of a rising crack-resistant curve (R-curve) of ABC/SiC (Silicon carbide, processed with dopants of aluminum, silicon and boron) which can fail intergranularly along the brittle grain-boundary films (extrinsic toughening). b) Commercial SiC hexoloy, fails transgranularly with no extrinsic toughening (no rising R-curve) [Ritchie, 2011].

- **Microcracking:** The presence of multiple microcracks outside the main crack path helps to distribute the microstructural damage in the material. Microcracking, for example, is the preeminent reinforcement mechanism responsible for the high toughness in nacre like-alumina. (Fig.2.14.b).
- **Crack deviation:** The crack avoids the ceramic bricks/tablets and deviates around them resulting into the pull-out of the bricks from the microstructure. Also, the damage ahead from the main crack results into producing elastic bridges, that efficiently bridge the crack (Fig.2.14a) and forces the load to slow down the crack propagation.

Bouville et al. [Bouville et al., 2014b] have reproduced some of these reinforcement mechanisms in their nacre-like alumina Al_2O_3 . The incorporation of alumina nanoparticles at the interface plays an essential role by forming nano-bridges between the tablets and nano-asperities at their surface, providing thus energy dissipation mechanisms during crack propagation by tablet pull-out, bridge breakages, and sliding friction [Grossman et al., 2017]. The extrinsic nature of the reinforcement mechanisms is confirmed by a R-curve behavior [Bouville et al., 2014b].

The combination of the different mechanisms on different length scales in nacre is the

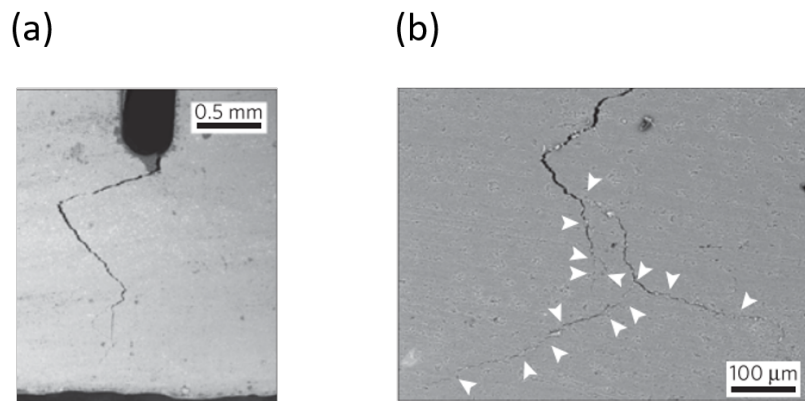


Figure 2.14: Damage resistance in nacre-like alumina, a) shows a long range crack deviation. b) Microcracking and crack bridging at the tip of the main crack/end of the crack path. Figures are reproduced from [Bouville et al., 2014b].

key behind its extraordinary toughness. Biological materials reinforcement mechanisms and their relation with the microstructure can be quite complicated to understand and quantify, therefore modeling can be a good solution to gain a better understanding of these mechanisms and provide helpful guidelines to manufacture synthetic materials.

Nomenclature

Microstructural parameters

ϕ	Tablet volume fraction
ρ	Tablet aspect ratio
ρ_0	Overlap aspect ratio
k	Overlap ratio
L	Tablet length
L_0	Overlap length
t	Thickness

Mechanical properties

ν	Poisson ratio
Σ	Macroscopic strength
Σ_i	Interface shear strength
Σ_t	Tablet tensile strength
E_i	Interface elastic modulus
E_t	Tablet elastic modulus
E_x	Macroscopic axial elastic modulus
E_y	Macroscopic transverse elastic modulus

2.3 Modeling and performance optimization of brick and mortar materials

To aid the comprehension of the mechanical behavior of natural BM materials and the establishment of design guidelines of synthetic BM materials, in particular quantitatively, a variety of models have been developed.

2.3.1 Analytical models

Shear-lag or tension shear-chain (TSC) models have been widely used to model BM models. The term shear lag has been used to describe models that represent fibers as one-dimensional, axial load-carrying springs. Other simplifications can be made, but the common characteristic of shear-lag models is that a three-dimensional fiber is assumed to act like a one-dimensional entity. Shear-lag models of varying degrees of complexity have been used to determine stresses in a broken fiber. The first shear-lag model in the literature was used to determine stresses in a fiber embedded in an elastic matrix [Cox, 1952].

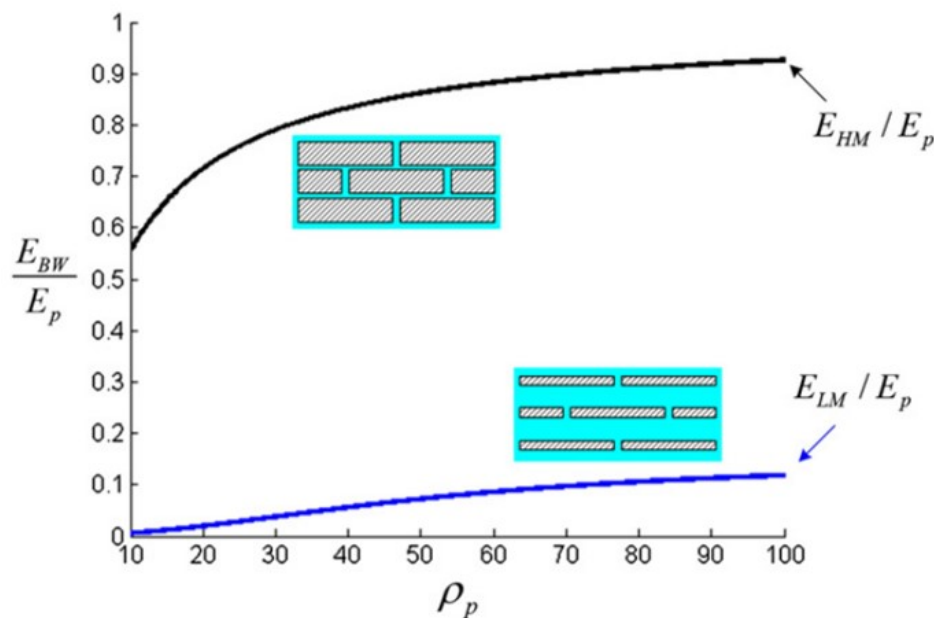


Figure 2.15: The elastic modulus of high and low mineralized staggered bio-composite normalized by the tablet's elastic modulus as a function of the aspect ratio of tablets [Bar-On & Wagner, 2013].

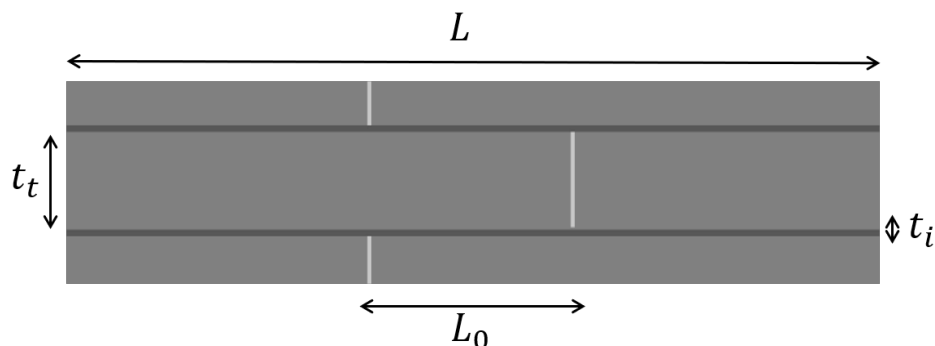


Figure 2.16: Representative Element Volume of nacre composed of two tablets linked with two interfaces and its microstructural parameters.

The following microstructural parameters (Fig.3.5) were used in the description of the models:

- The tablets aspect ratio $\rho = \frac{L}{t_t}$
- The overlap aspect ratio $\rho_0 = \frac{L_0}{t_t}$
- The overlap ratio $k = \frac{L_0}{L}$
- The tablets volume fraction $\phi = \frac{t_t}{t_t+t_i}$

The indexes i and t refer to interface and tablet respectively.

2.3.1.1 Stiffness

Jager and Fratzl [Jäger & Fratzl, 2000] proposed a 2D model with staggered array of tablets that accounts for the increase of stiffness and strength with the amount of mineral in the fibril and the level of staggering. A similar shear-lag model was developed by Kotha et al. [Kotha et al., 2001] on *Pinctada* nacre, where the organic phase is assumed to be elastic. Stress transfer between the tablets is also modeled and analyzed. The model results into a closed form expression that relates the elastic modulus to the material properties of its constituents.

Bar-on et al [Bar-On & Wagner, 2013] also developed a simplified approach to calculate the effective modulus and describe the elastic behavior of a staggered bio-composite. They propose a condensed analytical formula of the modulus. As a conclusion, they find that higher stiffness can be reached by using platelets with higher aspect ratio (Fig.2.15).

Another model predicting stiffness, is the model developed by [Barthelat, 2014]. Both tablets and interfaces are considered linear elastic, the effects of Poisson's ratio are neglected to simplify the calculations. The elastic modulus is presented as a function of

microstructural parameters (Eq.2.1). The tablets are made of a linear elastic and brittle material with

$$\tilde{E}_x = \frac{E_x}{E_t} = \frac{\phi}{1 + \frac{1}{\beta} (\coth(k\beta) + \coth(\beta(1-k)))} \quad \text{with} \quad \beta = \rho \sqrt{\frac{1}{2(1+\nu)} \frac{E_i}{E_t} \frac{\phi}{1-\phi}} \quad (2.1)$$

Begley et al. and Ni et al. [Begley et al., 2012; Ni et al., 2015] studied the load transfer between the tablets at the scale of a Representative Volume Element (RVE) to predict mechanical properties of BM materials. Stiffness (Eq 2.2) was developed as a function of the microstructural parameters and the stiffness ratio (interface/tablet). One of the drawbacks of these models is that they are only valid for sufficiently large values of the tablet volume fraction (typically $\phi > 0.8$). By simplifying the form of Equations (2.1, 2.2) proposed by their authors, one may notice that the two models only differ by a factor of ϕ .

$$\tilde{E}_x = \frac{E_x}{E_t} = \frac{2\beta \sinh[(1-k)\beta] \sinh(k\beta)}{2 \sinh(\beta) + \beta [\cosh(\beta) - \cosh((2k-1)\beta)]} \quad (2.2)$$

BM materials exhibit an anisotropic behavior, but only few models account for it [Bertoldi et al., 2008]. The elastic axial modulus (Eq.2.3) proposed by Bertoldi et al and Ji and gao et al. [Ji & Gao, 2004] is similar to the expression presented by the other models, except for the fact that the expression was developed for a symmetric overlap ($k = 0.5$).

$$\tilde{E}_x = \frac{E_x}{E_t} = \frac{1}{\left(1 + \frac{1-\phi}{\phi}\right) \left(1 + \frac{8}{\rho^2} \frac{1-\phi}{\phi} (1+\nu)\right)} \quad (2.3)$$

The expression of the transverse elastic modulus (Eq.3.27) takes in account the tablet volume fraction, the interface/tablet stiffness ratio and the Poisson ratio.

$$\tilde{E}_y = \frac{E_y}{E_t} = \frac{[1 - \phi(1 - \frac{E_t}{E_i})](1 - \nu^2)}{\Gamma} \quad (2.4)$$

where

$$\Gamma = \phi(1-\phi)(1+\nu)^2 \left[(1-2\nu)\left(1 + \frac{E_t^2}{E_i^2}\right) + 2\frac{E_t}{E_i}\nu^2 \right] + \frac{E_t}{E_i}((1-\phi)^2 + \phi^2)(1-\nu^2)^2 \quad (2.5)$$

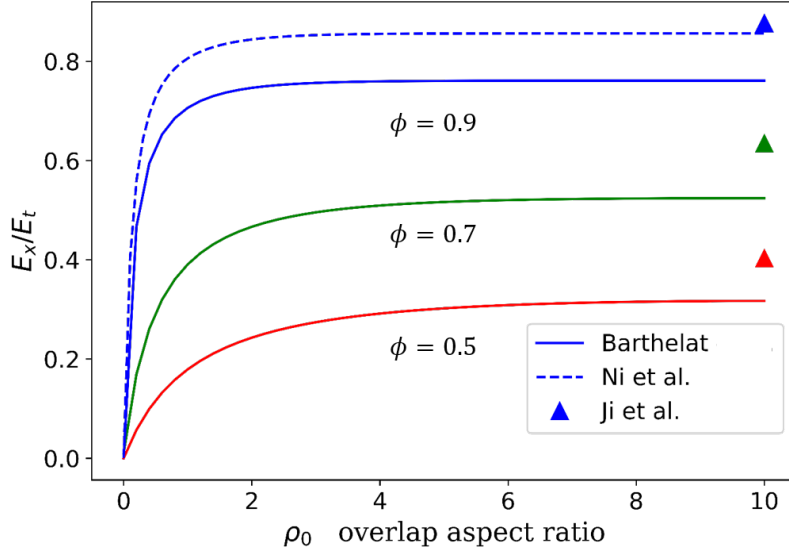


Figure 2.17: The normalized axial elastic modulus of brick and mortar materials as a function of the overlap aspect ratio using the expressions presented in the shear-lag models. The modulus is computed for three different volume fractions.

The tensile strength of the tablets is governed by linear fracture mechanics. The interfaces are considered linear elastic-perfectly plastic and their yielding is governed by Von Mises plasticity.

2.3.1.2 Strength

Jager and Fratzl [Jäger & Fratzl, 2000], Kotha et al. [Kotha et al., 2001] and Barthelat [Barthelat, 2014] also predicted strength as a function of the material's microstructural parameters (Eq.2.6). The tablets are supposed plastic and governed by linear fracture mechanics, and the interface was considered perfectly plastic and its yielding was governed by Von Mises plasticity. However, the assumption used by these models, is that the shear stress is uniform within the interface, which implies a much stiffer tablet than the interface. This is a reasonable assumption for the natural or synthetic nacre with a polymer interface but for an all-ceramic BM material, the stiffness ratio (interface/tablet) is rather close to unity. Only a few models were developed to account for non-uniform shear stress at the interface and can be applied to composites with a stiffness ratio close to unity [Begley et al., 2012; Ni et al., 2015]. Both equations (2.6) [Barthelat, 2014] and (2.7) [Begley et al., 2012] describe failure initiation, but only the second one accounts for the stiffness ratio between the interface and the tablet, through the parameter β .

$$\tilde{\Sigma} = \frac{\Sigma}{\Sigma_t} = \min \left[\rho_0 \phi \frac{\Sigma_i}{\Sigma_t}, \frac{1}{2} \right] \quad (2.6)$$

$$\tilde{\Sigma} = \frac{\Sigma}{\Sigma_t} = \min \left[\frac{\rho \Sigma_i}{\beta \Sigma_t} \tanh(k\beta), \frac{1}{2} \right] \quad (2.7)$$

Gao et al [Gao et al., 2003] introduced an important parameter, which is the critical length scale of the tablets above which the fracture strength is sensitive to the preexisting defect size and the material fails by stress concentration at the head of the crack. Also, when the tablet size is below a critical length scale, the strength of a perfect mineral tablets is maintained despite the existing defects. This critical value has to be chosen to ensure optimum fracture strength and maximum tolerance of flaws.

The nacre-like materials strength was also studied by Bonderer et al [Bonderer et al., 2008], where they showed that the aspect ratio of the tablets strongly affects the material's strength. The tablets aspect ratio should not exceed a certain value imposed by the tablets strength to conserve the ductile behavior.

2.3.1.3 Toughness

To study toughness, some models adopted a simple approach which was based on the calculation of energy absorption. In the model presented by Barthelat the tablets do not absorb energy, which means that the energy absorption decreases linearly as the volume fraction of the tablets increases. In addition, since only a fraction of the interface dissipates energy, larger overlap ratios lead to higher energy dissipation [Barthelat, 2014].

Shao et al. [Shao et al., 2012] have also investigated the toughening mechanisms in nacre by developing a microstructure based fracture mechanics model. By combining shear-lag theory and cohesive zones model, they compared different cohesive laws, they evaluated the contribution of the discontinuous crack bridging of the tablets and found out that the interfacial strength and energy dissipation of the organic phase are the main parameters for the crack bridging toughening effect in nacre.

The analysis done by the authors also showed an important size effect of the tablets on the toughness of nacre and provided an optimal range of thickness and length values. Based on this analysis, an optimal aspect ratio can be determined without difficulty. In this range of values, a larger aspect ratio of tablets would be beneficial for the improvement of the toughening effect of crack bridging. Shao et al. also gave a dimensionless function correlating the steady-state toughening ratio with the sizes of tablets (Fig.2.18) to benefit the optimal design of bio-inspired materials.

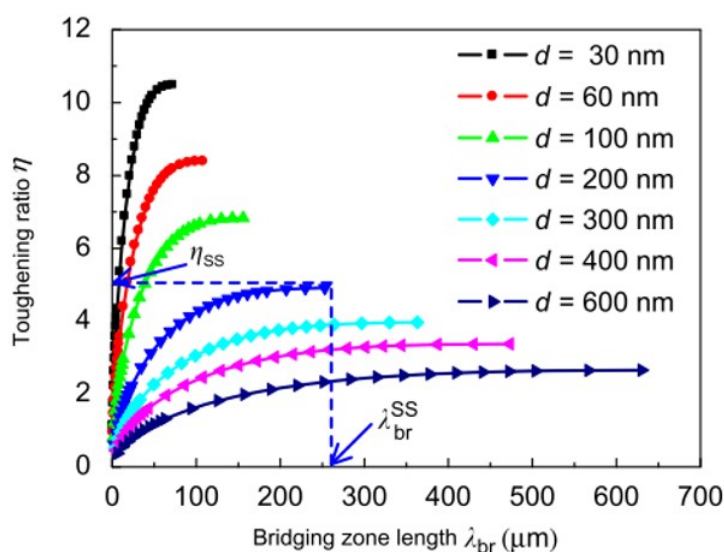


Figure 2.18: : Effects of tablet thickness d on toughness according to [Shao et al., 2012]. The toughening ratio increases with the extension of the bridging zone until reaching a steady state. The plot shows that for a relatively thin tablets, the toughening ratio curve rises more, which mean the thinner the platelets, the higher the fracture toughness.

[Zhang et al., 2011] used a quasi-self-similar model to predict the behavior of hierarchical composites and proved that the composite toughness can be maximized by considering an optimal number of hierarchical levels, however the strength can decrease continuously if additional levels of hierarchy are added.

Considering the contradicting effects on strength and toughness observed in these materials the optimum design requires a compromise. To overcome this problem, Barthelat [Barthelat, 2014] presented a multi-objective optimization methodology where he presented an analytical approach that blends the existing models to provide unified guidelines for optimum designs.

After elaborating a step by step design guidelines, Fig.2.19 can be considered as a framework to help in the process of designing nacre like materials. For example Fig. 2.19.a, b, c) can help select the appropriate tablet volume fraction ϕ that will generate the expected modulus, strength and energy absorption, and by using Fig. 2.19.e, d, we can choose the optimum interface strength and the optimum tablet aspect ratio. All the models presented here are summarized in Table.2.3.

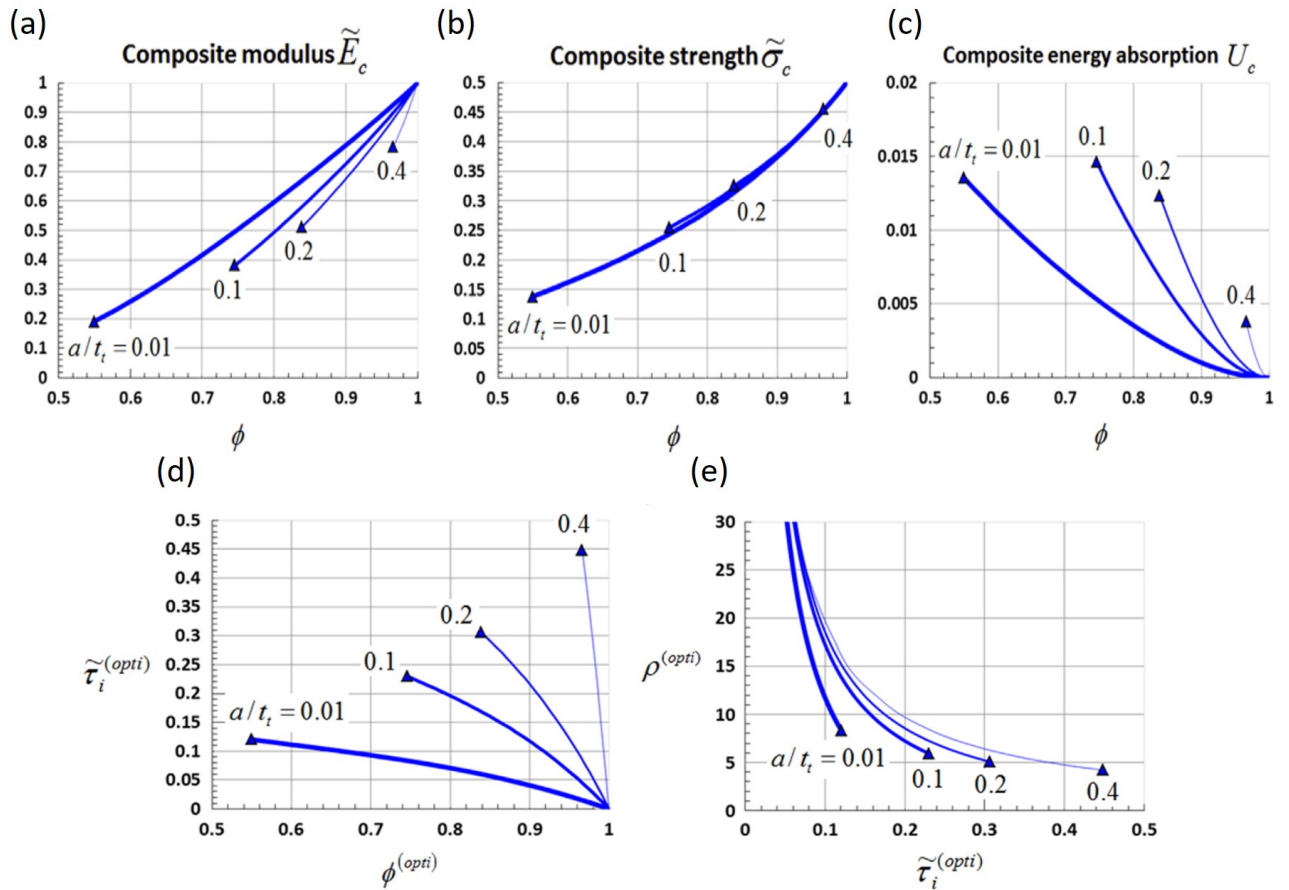


Figure 2.19: : Diagrams used to obtain the optimum design a-b) Optimum strength and stiffness for high tablet volume fraction ϕ c) Optimum energy absorption for high tablet volume fraction ϕ d) Optimum interface shear strength as a function of tablet volume fraction and e) Optimum tablet overlap ratio as a function of interface shear strength. All the curves are given for three different defect sizes a/t_i which is the initial defect size normalized by the tablet thickness. The figures are reproduced from [Barthelat, 2014].

2.3. Modeling and performance optimization of brick and mortar materials

Model	Approach	Predicted properties	Comments	Model limits
[Jäger & Fratzl, 2000]	Shear-lag with uniform shear	Stiffness and strength	Increase of stiffness and strength with level of staggering	Limited values of ϕ , t_t and ρ_0
[Kotha et al., 2001]	Shear-lag with uniform shear	Stiffness and tensile strength	Failure is governed by the organic matrix	Only high values of ϕ
[Gao, 2006]	Shear-lag and cohesive zones model	Strength and toughness	Defect size effects on strength	–
[Bertoldi et al., 2008]	Shear-lag	Stiffness	Including orthotropic and bimodular behavior	Only symmetric overlap $k = 0.5$
[Zhang et al., 2011]	Self-similar mechanical model	Toughness	Optimal level of hierarchy to maximize toughness	Not taking into account interface stress uniformity
[Begley et al., 2012]	Shear-lag with non uniform shear	Stiffness and strength	Accounting for the interface non uniform stress	Only high values of ϕ
[Shao et al., 2012]	Shear-lag and cohesive zones model	Toughness	Optimization of toughness by optimizing tablet size	–
[Bar-On & Wagner, 2013]	Shear-lag with uniform shear	Stiffness	High t_t can lead to high stiffness	Only high values of ϕ
[Barthelat, 2014]	Shear-lag with uniform shear	Stiffness, strength and energy absorption	Design guidelines	–
[Ni et al., 2015]	Shear-lag with non uniform shear	Stiffness and strength	Strength and toughness optimization for a set of microstructural parameters	Only high values of ϕ

Table 2.3: A summary table of analytical models showing the different approaches, their results and limitations.

2.3.2 Numerical models

Several numerical models have been developed to understand the remarkable mechanical properties of nacre and provide design guidelines to fabricate synthetic nacre like materials.

The first approach used was Finite Element Modeling (FEM). One of the premier models developed to describe elastic properties was a 3D model developed by [Katti & Katti, 2001; Katti et al., 2005], where they predicted nacre stiffness. They also studied the effect of mineral bridges on stiffness and concluded that they do not have a major influence on overall stiffness. [Evans et al., 2001] also developed a FEM model to describe the mechanical behavior of nacre, where they showed the influence of the tablets nano-asperities on the inelastic behavior measured in tension along the tablets axis. The study identified the main design principles that govern nacre robustness:

- The non-organic part has a tabular morphology with a tablet size, aspect ratio and topological arrangement chosen to maximize the inelastic strain.
- The wavelengths of the nano-asperities on the tablets provide strain hardening.
- The high adherence and transverse stretch of the organic phase keeps the tablets intact in the regions where the transverse tensile strains are generated.

Another type of models was also used to investigate the mechanical behavior of BM materials, which is the discrete spring network lattice. Nukala et al. [Nukala et al., 2005] developed a model to investigate fracture properties of nacre. The model confirmed that the unique architecture of nacre is behind its high toughness: repeated unfolding of macro molecules in the organic part and the presence of mineral bridges between aragonite tablets. However, how the microscopic mechanisms described in this work contribute to the superior mechanical behavior of nacre is still not clear, which means that it is important to establish a fracture mechanics model that can correlate toughness to its microstructural parameters. [Dimas & Buehler, 2013] also used the discrete spring network lattice approach to develop a meso-scale model to investigate the mechanics of bio-inspired composite materials. By adjusting the constitutive laws of the organic constituent, the authors investigated the fundamental mechanical interactions between the different constituents governing the system (stiffness and fracture resistance) with the objective of providing a simple design guideline for robust composites.

The results presented by Dimas et al. show the importance of the elastic mismatch between the tablets and the organic phase, where they demonstrate that small perturbations in the elastic properties can lead to important shifts in deformation and fracture mech-

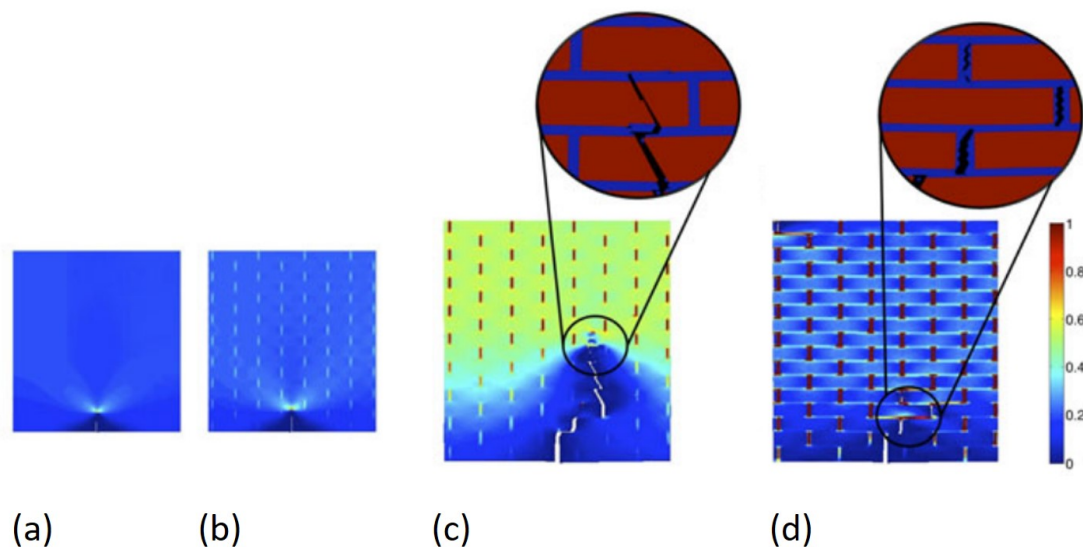


Figure 2.20: : Longitudinal strain fields of the brick and mortar system, (a) bulk material, (b) with a stiffness ratio $E_i/E_t = 0.64$, (c) $E_i/E_t = 0.44$, (d) $E_i/E_t = 0.02$. The interface absorbs the increasing portion of strain as the stiffness ratio decreases which occurs along with a delocalization of stress and strain from the crack tip. (c) Shows a clear transition in the fracture mode (from interface to tablet). Figures are reproduced from [Dimas & Buehler, 2013].

anisms. By tuning the simple elastic interactions, they succeeded to produce a range of composites with high stiffness and toughness that are quite similar to biological materials.

A more recent type of numerical models is based on discrete blocks interacting via cohesive laws established by shear-lag theory. William Pro et al. [William Pro et al., 2015] developed a numerical based model to predict the impact of the tablets shape and alignment on the relationship between macroscopic toughness and inelastic behaviors between the tablets. The method can be used to deal with different shapes and distributions of tablets, it can also predict the effect of material hierarchy. They showed the efficiency and robustness of this approach over finite element models for potential studies of material hierarchy. They also studied the size of the process zone that decreases with the interface ductility (Fig.2.21). However, the computational framework is limited to rigid tablets, which limits its application to synthetic materials with a large mortar/brick modulus ratio and a volume fraction of mortar of about 5%.

Abid et al. [Abid et al., 2018, 2019] studied the effect of microstructure, randomness and interfaces on local strain, failure and toughness. The authors presented each tablet by a node that can only move in the direction of the pulling, the tablets are connected to their neighbors with nonlinear springs (Fig. 2.22). The mechanical behavior of each spring was governed by the shear stress-strain curve shown in Figure 2.22.c, multiplied

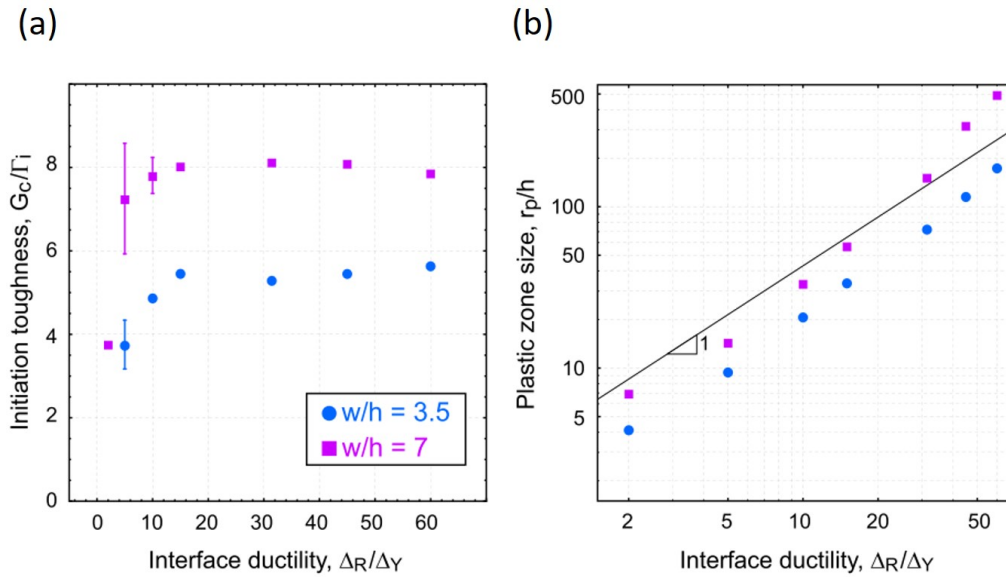


Figure 2.21: a) Effect of interface ductility on macroscopic initiation toughness and (b) effective plastic zone radius at fracture initiation [William Pro et al., 2015]

by the length of the interface. The study showed that statistical variations do not affect stiffness, but effects strength. They also suggested two critical design elements that can delay damage localization and maximize energy dissipation in the composites. The first element is high control over the architecture to minimize statistical variations and the second is having an interface with high deformability and strain hardening.

In another study, same authors [Abid et al., 2019] simulated fracture of staggered composites and studied the combined effects of tablet arrangement, interface properties and statistical variations on fracture mechanics: crack deflection, crack bridging and volumetric process zones of different size and shapes. In this paper, the authors highlighted the efficiency of their approach, especially computationally, as they showed that it can capture the fracture mechanics of large volumes of BM materials under lower computational cost compared to FEM for example. They also observed that crack deflection occurred more in samples with large statistical variations. Similarly to other models, this approach only accounts for rigid tablets. All the numerical models presented here are summarized in Table.2.4.

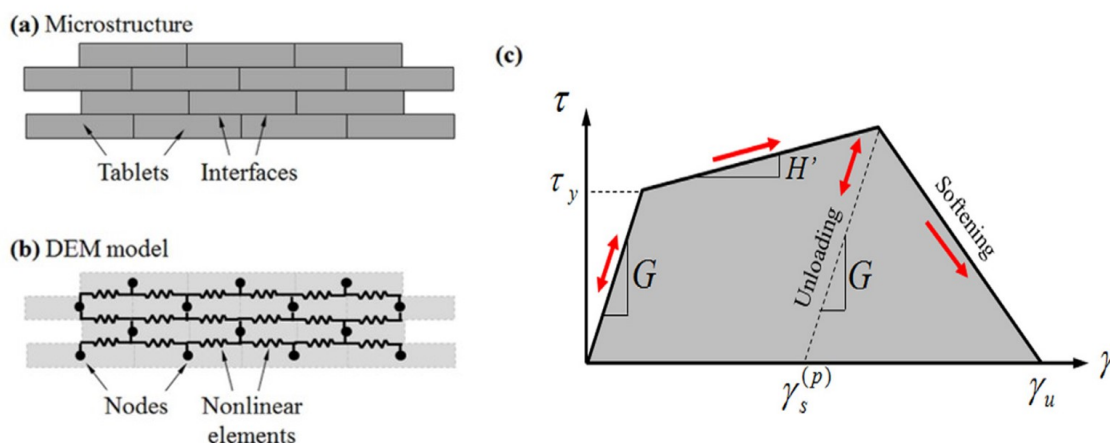


Figure 2.22: (a) A 14 tablet model and (b) corresponding DEM model with rigid tablets and a nonlinear spring at each interface. Tablets and their interfaces are represented by nodes and nonlinear elements respectively. (c) Shear stress-strain curve of individual springs. Figures are adapted from [Abid et al., 2018, 2019].

Model	Approach	Predicted properties	Results	Limits of the model
[Katti & Katti, 2001] [Katti et al., 2005]	FEM	Stiffness	Elastic modulus	No damage/crack propagation
[Evans et al., 2001]	FEM	Strength	ρ , t_t and nano asperities wavelengths optimize strength	–
[Nukala et al., 2005]	Discrete lattice model	Toughness	Nacre's architecture effect on toughness	Lack of comprehension of microstructure contribution to high mechanical properties
[Dimas et al., 2013]	Discrete lattice model	Stiffness and fracture resistance	Elastic mismatch controls fracture mechanisms	–
[William Pro et al., 2015]	Discrete lattice and cohesive laws	Fracture initiation toughness	Tablet shape and alignment on toughness	Rigid tablets
[Abid et al., 2018]	Discrete lattice and Cohesive laws	Stiffness and strength	Statistical variations effects strength but not stiffness	Rigid tablets
[Abid et al., 2019]	Cohesive laws and shear-lag	Toughness	Toughness decreases with the increase of statistical variations	Rigid tablets

Table 2.4: A summary table of all the numerical models presented in this section showing the different methods used, their results and limitations.

2.4 Discrete Element Modeling (DEM)

2.4.1 What is DEM?

Discrete element method was first developed in the 1980's, it is a dynamic Lagrangian method, closely related to the molecular dynamics (MD), that aims to model the collective motion of sets of none-deformable interacting objects, governed by the conservation of momentum [Dubois & Radjai, 2011; Poschel & Thomas, 2005]. At each time step (Fig.2.23), the overlap between objects is detected and used to compute interaction forces [Cundall et al., 1976]. The interactions between these objects are modeled as contact forces and moments. The objects could be of any arbitrary shape (polyhedral objects [Dubois & Radjai, 2011], triangulated bodies [Saeys et al., 2014], superquadratic particles [Stefan et al., 2017], etc..). However, neighbor search and overlap computation are algorithmically and computationally much heavier with arbitrary objects than with spheres.

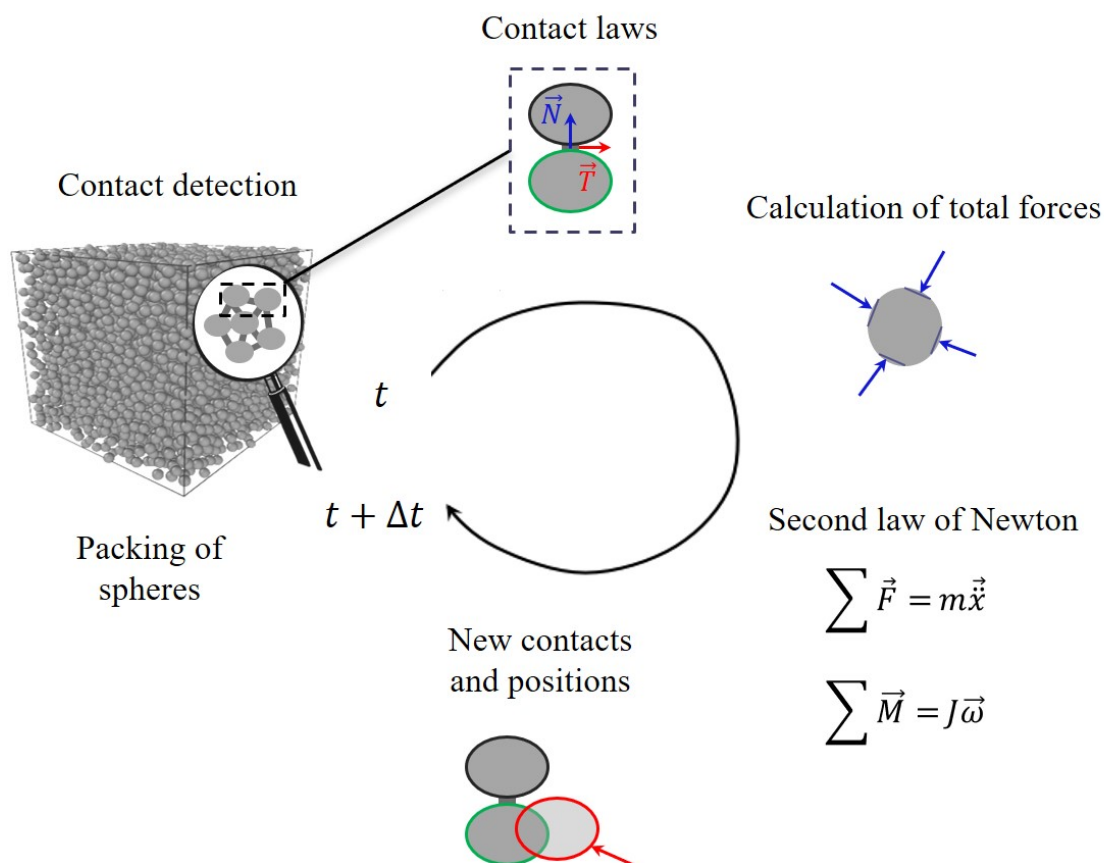


Figure 2.23: Algorithm of the discrete element method

In each modeling context, the compromise between computing efficiency and accurate description can be debated. In our case, our modeling will be based on the use of spheres as

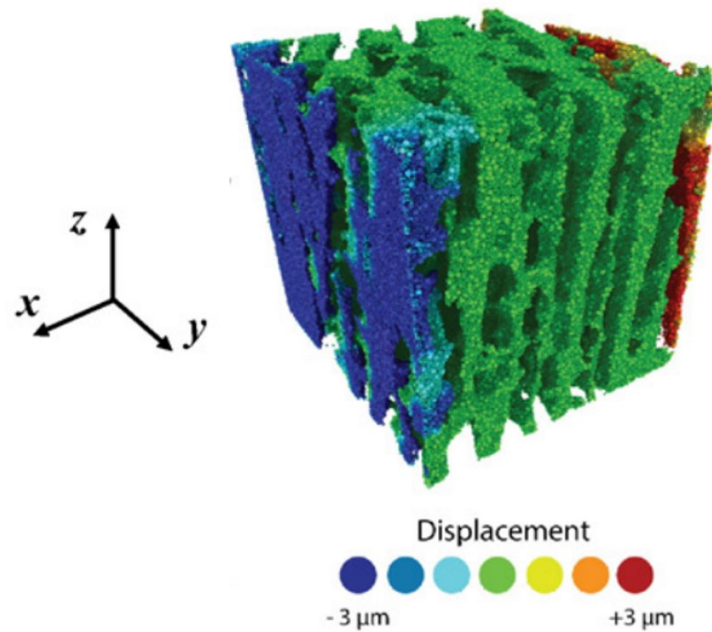


Figure 2.24: Simulation of a longitudinal crushing test of a discrete element packing showing the displacement of particles in the x direction, transverse to the loading axis z . Figures were adapted from [Roussel et al., 2016].

the unit discrete element, favoring computing efficiency and modeling complex shapes with larger collections of spheres that are bonded together. In geomaterials or civil engineering materials the simulation of particles motion is of particular interest. Due to the granular aspect of these materials, DEM simulations were used widely to anticipate landslide events or to model concrete behavior [Camborde et al., 2000]. DEM has been also used to model snow mechanics [Johnson & Hopkins, 2005; Gaume et al., 2015; Burr, 2017]. Numerous DEM applications can be found in materials science to simulate powder processes, such as powder compaction [Martin et al., 2003] or sintering [Martin et al., 2006; Rasp et al., 2013], industrial chemical engineering processes [Zhu et al., 2008; Xu et al., 2011] and also fracture [Roussel et al., 2016] (Fig.2.24).

Recently, DEM has also been used to model continuous materials. These materials start as continuum materials but due to externally applied strains are subjected to fracture and thus exhibit a discrete nature. The topological modifications (branching, bifurcation, new surface generation or crack healing) that come with fracture are difficult to apprehend analytically. Even finite elements would struggle to investigate properly these discrete events, where the volume is meshed and the crack path is predefined, unless using complex approaches such as X-FEM [Moes et al., 1999]. In contrast, thanks to its inherent discrete nature, DEM is well suited for discontinuous problems.

When modeling continuous materials, the particles representing the material have no

clear physical meaning, they are only arbitrary objects discretizing a continuous medium. The DEM description that follows is mostly based on the DEM code dp3D (Discrete Powder 3D), which is developed at SIMaP laboratory and is dedicated mostly to materials science.

2.4.2 Application of DEM on continuous materials

To model the mechanical behavior of continuous media, different constitutive laws such as elasticity, plasticity or fracture were studied in the literature and were transposed to the contact between two particles. The large majority of these models has been derived for spheres and can be easily generalized to the contact between a sphere and a plane or to the contact of two dissimilar spheres with different material properties or different radii.

For example, the elastic contact force between two spherical particles can be derived from Hertz's theory [Hertz, 1882], while the additional effect of surface energy can be accounted for by models derived in the 70's [Johnson et al., 1971; Derjaguin et al., 1994]

DEM simulations of continuum materials need contact laws as they represent the first element of a physically based model. Forces are generated when particles form a contact and since the physics of the problem are often embedded in these forces, a special care must be given to their determination. In other words, the local interactions are responsible for the behavior of the particulate material at the macroscopic scale.

To model the elastic behavior of continuous media (fused silica) using DEM, André et al. [André et al., 2012] developed a hybrid particulate-lattice model using cohesive beam bond (Fig.2.25) elements. They proposed a methodology that tackles two main theoretical difficulties:

- Continuous mechanics laws cannot be used directly with DEM formulation.
- Creation of artificial voids inside the material when using discrete elements.

They also quantified the material's isotropy and performed a calibration process to relate microscopic properties associated to beam elements to expected macroscopic ones and exhibited that DEM is suitable to quantitatively yield the linear elastic behavior of homogeneous continuous media.

However, it was proven that the results presented by André et al. are only valid when a set of geometrical parameters related to the packing are perfectly monitored. In other words, those results are only valid for a specific packing of particles with its own geometrical parameters. To avoid this problem, Kumar et al. [Kumar et al., 2016] presented an abacus (Fig. 2.27) to calibrate microscopic parameters to reach the expected macroscopic

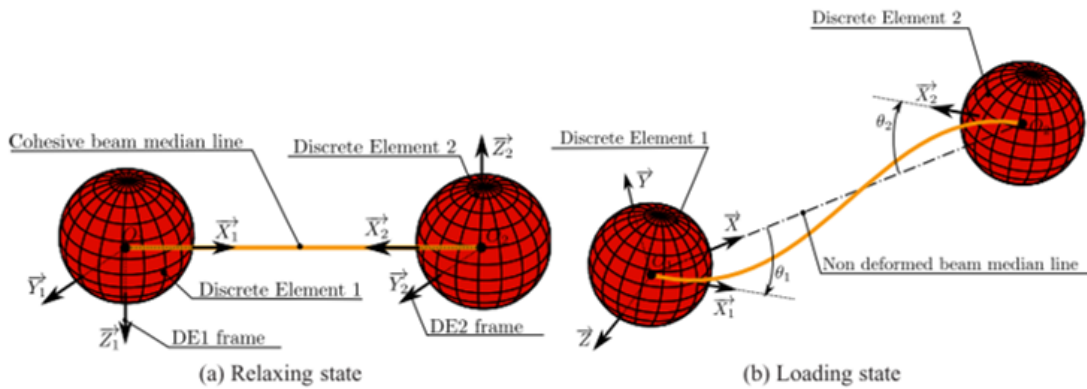


Figure 2.25: Cohesive bond beam configuration: The cohesive beam is represented by its median line. Both cohesive bond ends are fixed to the discrete element centers O_1 and O_2 . Before and after loading states are presented. Figure is adapted from [André et al., 2012].

properties based on different preparation routes. They have shown the important effect of the particles arrangement and packing preparation on the elastic properties (E, ν). Figure 2.27 shows the effect of the preparation of the discrete packing on Young's modulus and Poisson ratio, three preparation routes are studied (Fig.2.26). The main difference between the methods is that the unjammed packing is characterized by a small number of contacts that are very broadly distributed in size, while the jammed packing has a large number of smaller contacts. In this thesis the weakly jammed method is going to be used to generate discrete packings of particles. This method consists of isostatically densifying the packing of particles by moving inwards the periodic bounds. Weak jamming is obtained by imposing a control pressure to the packing, reaching a density of about 0.5. This packing is afterwards densified, using affine displacement to reach the final density of 0.65. This preparation route is considered to be a good compromise because it allows a wider span of attainable Poisson's ratio than the unjammed route but is much less CPU demanding than the jammed route, since densification rates in the low-density domain are much faster than close to the random close packing.

One of the recent approaches to model the elastic behavior of continuous media using DEM has been developed by Leclerc [Leclerc, 2017]. First, they investigated the number of discrete elements to use to prevent discretization effects. Also, they determined the stress fields of a ceramic/metal material and validated them with FEM. Effective elastic properties were determined for a large set of contrast of properties.

André et al. 2013 [André et al., 2013] used DEM to predict fracture. The fracture criterion used was based on the computation of an equivalent stress tensor of each particle, where it was considered that the beam breaks only when the hydrostatic stress is positive

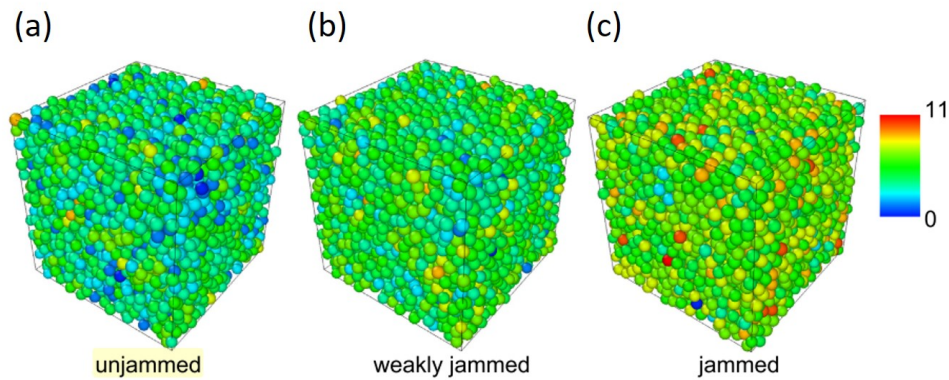


Figure 2.26: Packings for the three preparation routes. The final packing density is 0.65. Colors indicate the number of contacts per particle. Figure is adapted from [Kumar et al., 2016].

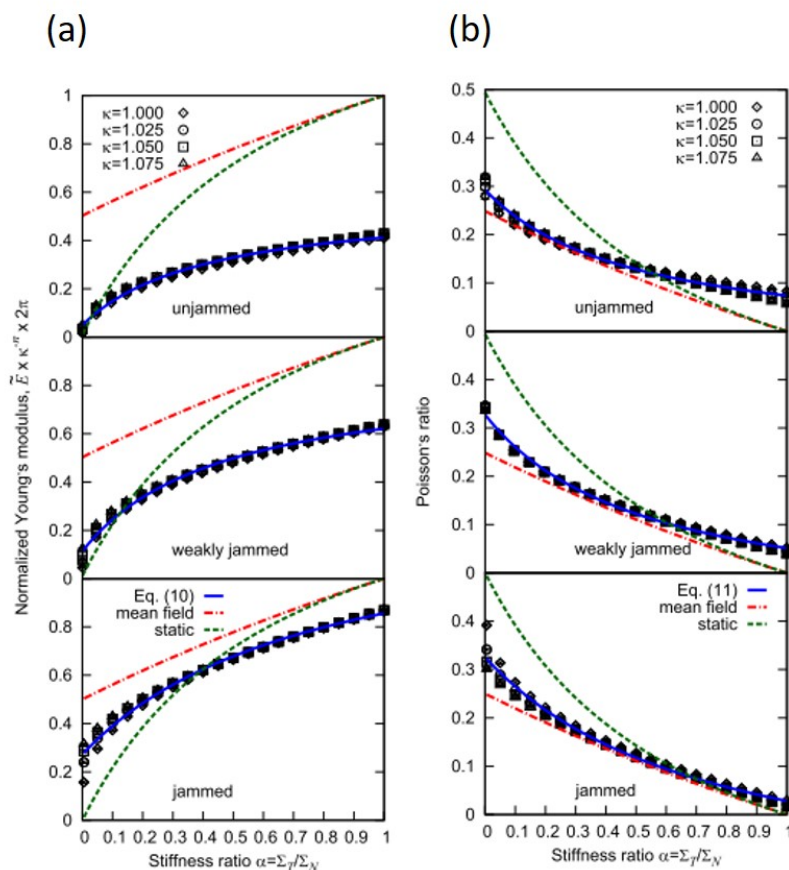


Figure 2.27: Abacus for calibration of microscopic parameters to reach a certain macroscopic behavior. It also shows the effect of the arrangement of the particles and the preparation routes (unjammed, weakly jammed and jammed on the macroscopic response a) Young modulus b) Poisson ratio. Figure is adapted from [Kumar et al., 2016].

and exceeds the microscopic strength obtained by calibration tests.

Numerous authors exhibited the suitability of DEM to simulate the mechanical behavior of heterogeneous media. However, it was only restricted to 2D domains with studies on the damage observed macroscopically during debonding tests [Leclerc et al., 2016]. Maheo et al [Maheo et al., 2015] showed the ability of CBM to simulate cracks in heterogeneous materials using the example of a unidirectional fiber composite. Two fracture criteria were investigated, the breakable bond failure criterion and the removed discrete element failure [Maheo et al., 2015] or the removed beam criterion [André et al., 2013]. Other authors presented a 3D model based on the coupling of DEM and a continuous method called the Constrained Natural Element Method (CNEM) to study the crack propagation in silica under indentation. The idea was to consider a classical approach to model the material in continuous parts introduce DEM where damage and discontinuities occur. [Jebahi et al., 2013] using Arlequin technique [Dhia & Rateau, 2005], which is a technique that offers an extended framework to superpose different models for the design of engineering structures.

Leclerc et al. [Leclerc, 2017] explored the notion of Representative Volume Element (RVE) and the definition of the stress tensor in heterogeneous media in the context of a 2D random particulate composite to prove the suitability of DEM for damage initiation and propagation in heterogeneous media. They also exhibited the influence of variability effects related to the micro-macro scale transition in the discrete element approach on the crack initiation and propagation. The crack propagation is modeled using a fracture criterion that is based on the calculation of the hydrostatic stress. Fracture occurs only when the hydrostatic stress is greater than a certain stress limit, then the cohesive beams related to a specific particle break; the particle does not interact with the other discrete elements.

2.5 Outcomes and outlines

Creating materials with strength and toughness has been a long-sought goal. Conventional engineering materials often face a trade-off between strength and toughness, prompting researchers seeking to overcome these limitations to explore more sophisticated materials, such as composites. Nature exhibits plenty examples of heterogeneous materials that offer outstanding material properties, and many natural materials are widely regarded as examples of high-performing hybrid materials. A classic example is nacre, also known as mother-of-pearl, which boasts a combination of high stiffness, strength, and fracture toughness. Various microstructural features present at various scales contribute to the outstanding performance of nacre. Most of the reinforcement mechanisms operate behind

the crack tip(extrinsic reinforcement) leading to a rising R-curve behavior.

To understand and mimic BM materials, various analytical and numerical models were developed. However, most of the shear-lag models are elastic or elasto-plastic, thus they only account for intrinsic reinforcements. Consequently, an important part of the reinforcement mechanisms is not captured.

In this work we propose an original approach based on Discrete Element Method (DEM) for nacre-like ceramics made of elastic brittle constituents. The model is generic enough to be applicable to all BM materials. DEM first developed for granular materials, has been proven to be very efficient at modeling damage and fracture behavior for composite and continuous materials. In the following chapters, we will present the model development, starting by defining contact laws and calibration, then validation (Chapter 3). Next, we will reveal the critical role of design and the microstructure on strength and toughness of BM synthetic materials by presenting the main parameters for performance optimization (Chapter 4). Afterward, we will head towards more realistic model, taking into account the randomness of the microstructures, the irregularities and initial defects by studying samples issued from the coupling of EBSD micro-graphs of nacre-like alumina and DEM packing (Chapter 5). Lastly, we will determine the effect of alumina nano-particles at the interface on the alignment of the tablets during processing (Chapter 6).

Chapter 3

Model development and validation

In this chapter, the Discrete Element model that we developed to study BM materials is presented as a scientific paper that was published in the *Journal of the Mechanics and Physics of Solids: Elasticity and fracture of brick and mortar materials using discrete element simulations* [Radi et al., 2019a]. First, the contact laws used to describe elasticity and fracture are presented. A random packing of particles connected with bonds is used to model our material, the transition laws between the microscopic and macroscopic parameters, cannot be reached analytically, therefore a calibration process is required to find the appropriate microscopic parameters that fit the wanted behavior of the simulated material at the macroscopic scale. The mechanical response of a BM RVE is then carefully studied and compared to existing analytical shear-lag models. The capacity of this modeling approach to capture damage and crack propagation is highlighted. Finally, as an application example of the model, the optimization of the interface strength of nacre-like alumina is presented. The paper is reported as published with its own introduction that is unavoidably redundant with the present thesis introduction and literature review and may be skipped by the reader.

Contents

1.1	Context and objectives: Bioinspiration applied to ceramics .	3
1.2	Scientific program, organization of the project and consortium	4
1.3	Brick and mortar materials and DEM	5
1.4	Graphical outline	7

Abstract

Natural materials such as bone and the nacre of some seashells are made of relatively weak building blocks and yet often exhibit remarkable combinations of stiffness, strength, and toughness. Such performances are due in large part to their brick and mortar architectures. Many efforts are devoted to translate these design principles into synthetic materials. However, much of the progress is based on trial-and-error approaches, which are time consuming and do not guarantee that an optimum is achieved. Modeling is an appealing alternative to guide the design and processing routes of such materials. However, the current analytical approaches cannot describe the extrinsic toughening mechanisms that takes place during crack propagation and are responsible for the remarkable properties of such materials. Here we show that the Discrete Element Method (DEM) can be used to predict the elastic and fracture behavior of brick and mortar materials and capture non-continuous phenomena such as multi-cracking. In contrast with most analytical shear-lag models, which only predict crack initiation, the model proposed here can also tackle crack propagation. DEM simulations are compared to analytical results with special attention to the shear transfer at the interface. The case of nacre-like alumina–a ceramic/ceramic brick and mortar composite with a brittle interface—is investigated to illustrate the potential of the method. We demonstrate in particular the importance of controlling the interface strength for further optimization of the mechanical properties. This method could be extended to predict and investigate the behavior of brick and mortar composites with a ductile interface, such as polymer/ceramic or metal/ceramic composites.

3.1 Introduction

Structural biological materials often exhibit impressive mechanical properties, such as unique combinations of strength and toughness [Chen et al., 2008]. Nacre, that covers the inside of many seashells species, is a composite which toughness is several orders of magnitude larger than its constituents. Nacre is primarily a hierarchical composite with a brick and mortar (BM) architecture: aligned mineral tablets (bricks) are linked together by a thin organic interface (mortar) providing cohesion and energy dissipation capacity to the material [Jackson et al., 1988; Espinosa et al., 2009]. The architecture of nacre also includes many other structural features defined at different length scales, from the fibril network of the interface to the arrangement of mesolayers [Barthelat et al., 2016]. The high performances of nacre can be attributed to this hierarchical architecture.

Various processing routes have been developed (mainly in the last decade) to produce synthetic BM materials inspired by the structure of nacre [Corni et al., 2012; Zhao &

Guo, 2017]. A common belief is that some ductility is required at the interface for an efficient toughening of the composite, directing thus research almost exclusively towards ceramic/polymer and ceramic/metal composites. A resulting drawback is the inability of these BM composites to sustain harsh environment conditions (high-temperature or oxidative), as well as a moderate strength. Thus, there is still a lack of damage-resistant refractory materials, which current composites cannot fulfill satisfactorily.

Recently, a new bioinspired BM material, nacre-like alumina, has been developed [Bouville et al., 2014b]. In contrast with metal-ceramic or polymer-ceramic composites, this ceramic-ceramic composite can maintain high strength and high toughness at 600°C and keep good oxidation properties. The material is composed of brittle constituents only: 98.5 vol.% of alumina platelets, 1.3 vol.% of silica, and 0.2 vol.% of calcia. In the absence of a ductile interface, the reinforcement mechanisms responsible for the high toughness include microcracking, crack deviation, and crack bridging [Bouville et al., 2014b]. The incorporation of alumina nanoparticles at the interface plays an essential role by forming nano-bridges between the platelets and nano-asperities at their surface, providing thus energy dissipation mechanisms during crack propagation by platelet pull-out, bridge breakages, and sliding friction [Grossman et al., 2017]. The extrinsic nature of the reinforcement mechanisms is confirmed by a R-curve behavior [Bouville et al., 2014b; Launey & Ritchie, 2009]. Further work has extended the compositions [Pelissari et al., 2017] and processing routes [Le Ferrand et al., 2015, 2018] of such materials.

The work by [Bouville et al., 2014b] demonstrates the possibility, using only ceramics constituents, of engineering BM materials with a sufficiently high toughness to avoid catastrophic failure. A good understanding of the reinforcing mechanisms and appropriate modeling is nonetheless necessary to optimize the material microstructure in terms of platelets aspect ratio, interface thickness and interface strength. Such optimization can for example be achieved by a change in composition, or the fine tuning of the amount of nano-bridges.

Modeling the mechanical properties of BM material has been mainly approached by analytical shear-lag models, where the load transfer between tablets is studied at the scale of a Representative Volume Element (RVE). These models come with necessary simplifications which limit their applicability. A common assumption, used for example by [Barthelat, 2014; Zhang et al., 2010], is that shear stress is uniform within the interface, which implies a much stiffer tablet than the interface. This is a reasonable assumption for the natural or synthetic nacles with a polymeric interface but an all-ceramic BM material has a stiffness ratio (interface/tablet) close to unity. Only a few sophisticated models have been developed to account for non-uniform shear and can be applied to composites with a stiffness ratio close to unity [Begley et al., 2012; Ni et al., 2015].

In addition, the majority of analytical models are elasto-plastic and focus only on stiffness, strength, and energy adsorption at the onset of crack propagation. Extrinsic toughening mechanisms that are predominant for nacre-like composite ceramics during crack propagation, are difficult to capture by this class of analytical models. [Sun et al., 2015] have proposed a model for bioinspired carbon nanotube bundles to account for the gradual loss in modulus and strength as the crack propagates. [Song et al., 2016] have used a non-linear shear-lag model to study the progressive failure of interfaces on a laminate with a dozen tablets. As an attempt to model a specific extrinsic mechanism, crack bridging, an interfacial cohesive law has been proposed using analytical approaches [Shao et al., 2012; Barthelat & Rabiei, 2011].

Useful design guidelines and property maps have been derived from these models, and show that optimal combinations of platelet aspect ratio, interface thickness, and yield stress that maximize composite strength and toughness exist [Begley et al., 2012; Barthelat, 2014; Ni et al., 2015]. For example, for a given geometry, increasing the interface yield stress will be beneficial up to the point where the failure mechanism will shift from interface yield to brick failure, thus leading to an optimal interface yield stress [Begley et al., 2012].

Numerical modeling approaches could potentially capture crack propagation and R-curves, i.e. extrinsic toughening mechanisms. FEM has been scarcely used probably due to difficulties to handle topological modifications and a large number of tablets [Bekah et al., 2012; Katti et al., 2005]. Preferred options include discrete methods based on shear-lag description of tablet interactions [William Pro et al., 2015; Abid et al., 2018] or spring lattice models [Sen & Buehler, 2011]. The Discrete Element Method (DEM) based on spherical discrete elements originally designed for granular materials [Cundall & Strack, 1979], [Dubois & Radjai, 2011], [Chareyre, 2019] has probably never been used for BM materials but was successfully used on a layered structure—albeit only in 2D—by [Zhang et al., 2014]. DEM can naturally account for multiple cracking and frictional contacts between the newly created surfaces and thus provide the required ingredients for the explicit modeling of extrinsic reinforcements [Jauffrès et al., 2012; Roussel et al., 2016]. In addition, there is no need to predefine (for mesh refinement purpose for example) the location of the crack path.

The application of DEM to dense materials implies a careful calibration of contact laws to reproduce the macroscopic elastic and fracture behavior [André et al., 2012, 2013; Kumar et al., 2016; Leclerc, 2017]. It is particularly well-suited to model composite materials made of elastic-brittle phases [Maheo et al., 2015].

The present work focuses on the development and validation of DEM simulations for nacre-like ceramics made of elastic brittle constituents but is generic enough to be appli-

cable to all BM materials. The DEM contact laws and the calibration procedure are first described. The mechanical response of a BM RVE is then carefully studied and compared to existing analytical shear-lag models. The capacity of this modeling approach to capture damage and crack propagation is highlighted. Finally, as an application example of the model, the optimization of the interface strength of nacre-like alumina is presented.

3.2 Modeling of a continuous material with DEM

3.2.1 Microscopic beam model

The mechanical behavior of a continuous material is modeled by a network of beams connecting spherical particles of radius R (Fig. A.1. For two particles (labeled 1 and 2), with radii R_1 and R_2 , the effective radius R^* is defined as:

$$R^* = \left(\frac{1}{R_1} + \frac{1}{R_2} \right)^{-1} \quad (3.1)$$

Similarly, a bond between two particles with normal and tangential stiffnesses K_N and K_T carries effective stiffnesses:

$$K_N^* = \left(\frac{1}{K_{N,1}} + \frac{1}{K_{N,2}} \right)^{-1}, \quad K_T^* = \left(\frac{1}{K_{T,1}} + \frac{1}{K_{T,2}} \right)^{-1} \quad (3.2)$$

The normal and tangential stiffnesses K_N^* and K_T^* introduce a size dependence in the model. Thus, we prefer using material parameters $\sigma_N^* = \frac{K_N^*}{2R^*}$ and $\sigma_T^* = \frac{K_T^*}{2R^*}$, which have the unit of stress and allow macroscopic elastic properties to be independent of the sphere size for a given set of microscopic properties σ_N^* and σ_T^* . The normal and tangential forces at the bond scale are thus given by:

$$\mathbf{N} = -4\sigma_N^*R^*\delta_N\mathbf{n} \quad (3.3)$$

$$\mathbf{T} = -4\sigma_T^*R^*\delta_T\mathbf{t} \quad (3.4)$$

where δ_N and δ_T are the normal and the tangential relative displacements between the two particles, and \mathbf{n} and \mathbf{t} are the unit normal and tangential vectors, respectively.

The normal force \mathbf{N} may be attractive or repulsive. Bonds transmit resisting moments M_N and M_T in the normal and tangential directions that oppose the accumulated relative rotations θ_N and θ_T [Potyondy & Cundall, 2004]:

$$M_N = -8\sigma_T^*R^{*3}\theta_N \quad (3.5)$$

$$M_T = -4\sigma_N^*R^{*3}\theta_T \quad (3.6)$$

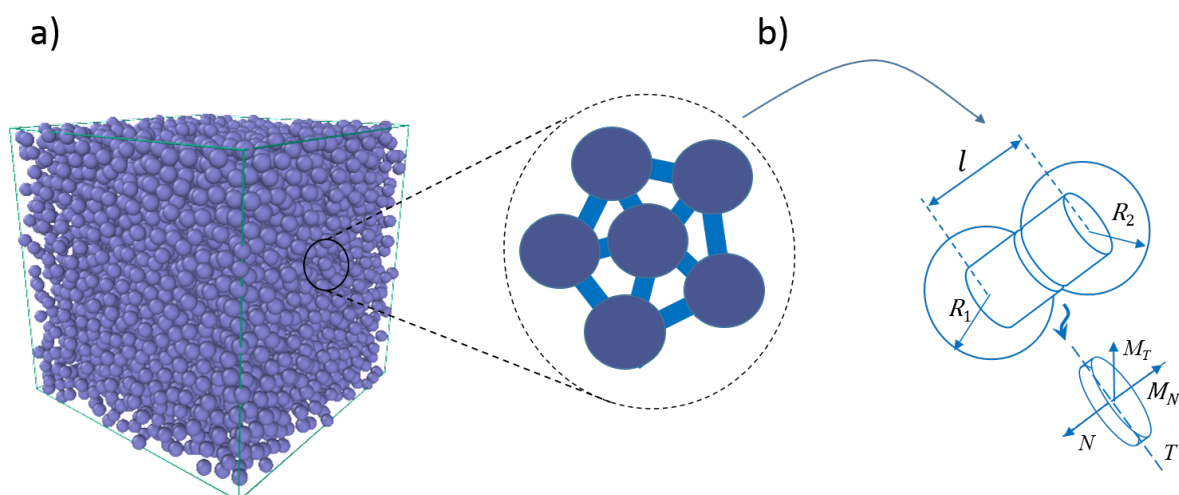


Figure 3.1: From macroscopic to microscopic scale. (a) Random packing of bonded particles representing a continuous material. (b) Two bonded particles of radius R_1 and R_2 transmitting normal/tangential forces and resisting moments.

Note that the formulation in Eqs. (3.5) and (3.6) assumes that the radius of the cylindrical beam bonding the two particles is equal to twice the equivalent radius R^* [Potyondy & Cundall, 2004; Kumar et al., 2016].

The beam model described above associated with the Discrete Element Method (DEM) [Cundall & Strack, 1979] allows the elastic behavior of a continuous material to be represented satisfactorily [Kumar et al., 2016]. In particular, the Poisson effect can be reproduced, although within a limited range of value of the Poisson's ratio ($-0.4 \leq \nu \leq 0.35$). Also, we have shown that the simple bond model proposed here is capable of simulating elastic instabilities such as buckling, without any built-in buckling mechanism artificially introduced in the model [Kumar et al., 2016].

3.2.2 Fracture criterion

The inherent discrete nature of the DEM description of a material provides a natural framework to deal with fracture. Two major approaches exist to model fracture. The first criterion is based on the deletion of a discrete element or the beam connecting the discrete elements when a tensile criterion is satisfied in bonds connected to this element [André et al., 2013; Maheo et al., 2015; Leclerc et al., 2016]. The drawback is that volume conservation is not ensured and that complex strain paths that may lead to crack closure cannot be correctly modeled. The second method, adopted here, consists of the evaluation of the stress (or the strain) within the bond, and the application of a critical stress/strain criterion at the bond level [Potyondy & Cundall, 2004; Carmona et al., 2008]. Once the bond has reached the criterion, the particles and the bond are kept but the bond

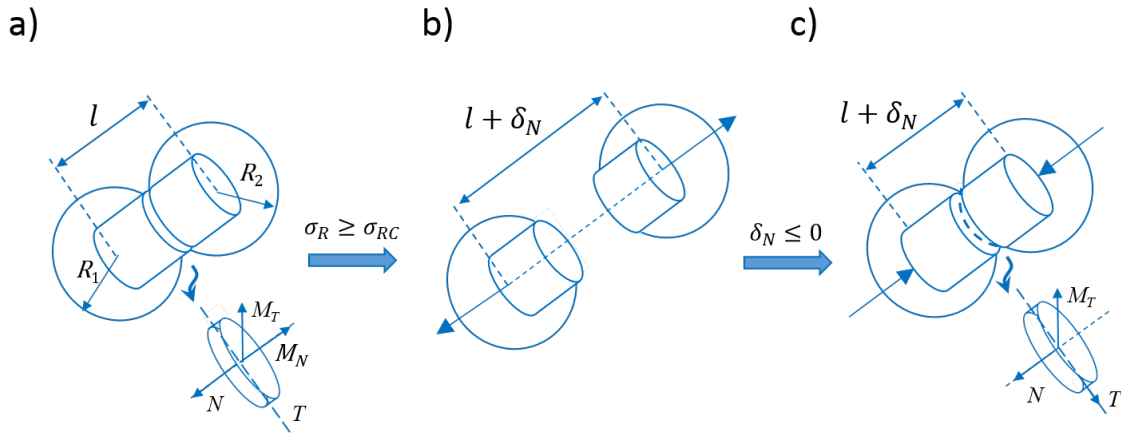


Figure 3.2: Two bonded particles transmitting normal/tangential forces and resisting moments. (a) Unbroken bond. (b) Broken bond. (c) Resumed contact after bond fracture transmitting only compressive forces, friction forces and tangential resisting moment.

behavior is modified as detailed below. The criterion typically involves normal and/or tangent stresses or a combination of both.

In this work we use the Rankine maximum principal stress criterion at the scale of a beam, which is suitable for predicting failure in brittle materials. Rankine criterion states that failure occurs when the maximum principal stress reaches either the uniaxial tension strength, or the uniaxial compression strength. For the beam model, Rankine's equivalent stress is:

$$\sigma_{b,R} = \frac{1}{2} \left(\sigma_{b,N} + \sqrt{\sigma_{b,N}^2 + 4\sigma_{b,T}^2} \right) \quad (3.7)$$

where $\sigma_{b,N} = \frac{N}{4\pi R^2}$ and $\sigma_{b,T} = \frac{T}{4\pi R^2}$ are the normal and the tangential stresses at the bond scale. The bond breaks when the Rankine's equivalent stress $\sigma_{b,R}$ reaches a critical stress σ_{RC} . As demonstrated by [André et al., 2013] this approach may not be relevant for complex triaxial loading such as indentation. However, it should be suitable for the case of BM materials under tensile loading where mainly stress states close to pure tension or pure shear are encountered.

After bond fracture, DEM provides a simple mean to model crack closure if particles resume contact (or if the bond fractured in shear while under compressive stresses, $\sigma_{b,N} < 0$ in Eq. (A.5)). This is accomplished by stating that a broken bond keeps the same normal stiffness as an unbroken bond in compression but cannot transmit any tensile force. The tangential forces transmitted by broken bonds follow the Hertz–Mindlin model in the sticking mode and are limited by Coulomb friction for sliding (friction coefficient μ). Accordingly, broken bonds transmit only resisting moment M_T in the tangential direction but none in the normal direction (Fig. A.2).

3.2.3 DEM simulations

A classical dynamic DEM, as introduced by [Cundall & Strack, 1979], is used in a quasi-static approach within the in-house code dp3D [Martin et al., 2003], to compute the equilibrium positions of particles at each time-step. The code is available for use on request. Strains are first imposed to the sample via periodic conditions or by the use of objects with infinite mass. Particles are displaced in the first half time-step according to the imposed increment in strain following the affine solution (homogeneous deformation of the sample). Contact forces (Eqs. (3.3) and (3.4)) are used to compute the total force acting on each particle. Newton's second law of motion enables the computation of the acceleration and an explicit time-integration scheme is used (velocity-Verlet) to obtain the new position of the particles before a new strain increment is imposed. New contacts and lost contacts are updated at each time-step.

Small enough time-steps and slow enough strain rates are employed to ensure stability and quasi-static equilibrium. More details relative to these aspects can be found in a previous publication [Martin et al., 2003]. Concerning quasi-static conditions, the value of the imposed strain-rate is set at each time-step with consideration to the normalized kinetic energy per particle [Agnolin & Roux, 2007]:

$$\tilde{E}_{kin} = \frac{E_{kin}}{n \max(NR^*)} \quad (3.8)$$

where E_{kin} is the total kinetic energy of the particle system (accounting for rotation and translation terms), n the number of particles and N the normal force (Eq. (3.3)). The strain-rate and the renormalized mass of particles are adapted so that \tilde{E}_{kin} stays reasonably below 10^{-7} all along the simulation to ensure quasi-static conditions [Agnolin & Roux, 2007]. Under such conditions, inertia effects are considered negligible. In particular, we have ensured that bond fracture events, which inevitably release some kinetic energy, do not induce detrimental inertia effects.

Under macroscopic strain, the network of beams, which microscopic interactions have been described above, transmit forces \mathbf{F} at each bond resolved locally into a normal and a tangential component ($\mathbf{F} = \mathbf{N} + \mathbf{T}$). The macroscopic stress tensor resulting from these forces may be computed using Love's formulation [Christoffersen et al., 1981]:

$$\Sigma_{ij} = \frac{1}{V} \sum_{beams} F_i l_j \quad (3.9)$$

where the summation is made on all (intact or broken) beams that transmit forces in the sample volume V , F_i is the i^{th} component of \mathbf{F} , and l_j is the j^{th} component of the branch vector l connecting the centers of two bonded particles (Fig. A.1. A simple dimensional

analysis shows that the use of the microscopic properties σ_N^* and σ_T^* to define material parameters leads, as it should, to a macroscopic response that is independent of the size of the particles that mesh the material.

3.2.4 Sample generation

Samples were generated using periodic conditions on all packings. A gas of nearly monomodal particles (5% dispersion around the average radius R) is first generated by locating particles randomly in a periodic cell. At this stage, particles have no contact and the relative density of the packing is approximately 0.3. By slowly moving inwards the periodic walls, the initial gas of particles is isostatically densified under Hertzian contact law [Martin & Bordia, 2008] (no bonds nor any friction or adhesion between particles during this preparation stage) until a density $D = 0.5$ is obtained. Following the work by [Kumar et al., 2016], we further densify the packing by imposing an affine densification until a final density $D = 0.65$ is reached. This procedure is identical to the so called “weakly jammed” preparation route used by [Kumar et al., 2016].

At this stage, all pairs of particles that are close enough are bonded together to form a continuous material according to the following criteria:

$$\kappa (R_1 + R_2) \geq | \mathbf{l}_{12} | \quad (3.10)$$

where \mathbf{l}_{12} is the branch vector between the center of the pair of particles (Eq. (3.9) and Fig. A.2 and κ is the interaction range. In our case, the interaction range $\kappa = 1.075$ provides enough interlocking between particles as proposed by [Jerier & Molinari, 2012; Scholtès & Donzé, 2013]. We tested previously [Kumar et al., 2016] that this value allows Poisson’s ratios in the [0–0.35] range to be simulated.

In short, a numerical sample is thus meshed with a network of bonds and particles as described above. It is characterized by a particles number n , a relative density D and an average bond number Z_b per particle. Fig. 3.3 summarizes the sample preparation in which a particles gas is densified to form a random packing of particles bonded together.

3.2.5 Elasticity and strength calibration

When using a random packing in DEM to model a continuous material, the relationship between the microscopic interaction laws (bond level) and the macroscopic response (the discrete sample level), cannot be reached analytically. Thus, a calibration process is required to determine the appropriate microscopic parameters that reproduce the material macroscopic behavior [Potyondy & Cundall, 2004; André et al., 2012].

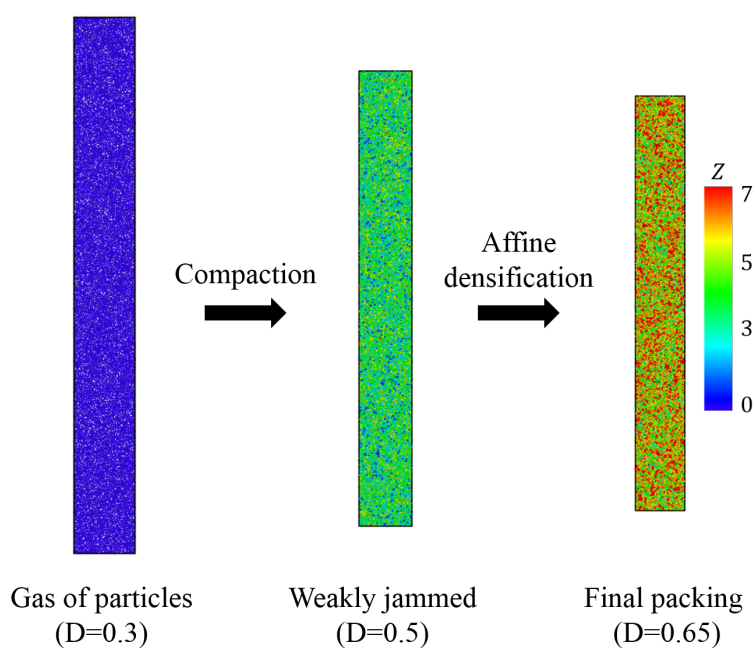


Figure 3.3: Typical evolution of a numerical 3D sample with 20 000 particles during the preparation stage. (a) The initial gas of particles has no contact between particles ($Z = 0$) and a relative density $D = 0.3$. (b) The weakly jammed packing is characterized by an average coordination number $Z = 3.58 \pm 0.02$ and a relative density $D = 0.5$. (c) A final affine densification is imposed ($D = 0.65 \pm 0.01$ relative density) and bonds are installed ($Z_b = 6.65 \pm 0.02$) with an interaction range $\kappa = 1.075$ (Eq. (3.10)).

Moreover, the macroscopic behavior depends on the geometrical arrangement of the discrete network of bonds. To calibrate the microscopic parameters in the contact laws, we rely on the work of [Kumar et al., 2016] who performed extensive quasi-static tensile tests in order to establish relationships between the macroscopic elastic behavior of the packing and the contact stiffnesses for various packing preparations routes. Based on a generalization of the mean field solution, they proposed simple calibration equations to relate the macroscopic elastic response of the packing (the Young's modulus E and the Poisson's ratio ν) to the packing characteristics (Z_b and D), and to the microscopic parameters at the bond scale (σ_N and σ_T). For the simple case of a packing of particles with identical microscopic parameters σ_N and σ_T ($K_{N,1} = K_{N,2}$ and $K_{T,1} = K_{T,2}$ in Eq. (A.2), these equations write:

$$\sigma_N = \frac{E}{Z_b D} \frac{2\pi}{\kappa^m} \frac{4 + a_3\alpha}{a_1 + a_2\alpha} \quad (3.11)$$

$$\sigma_T = \alpha\sigma_N \quad (3.12)$$

with:

$$\alpha = \frac{1 - b_2\nu}{b_1 + b_3\nu} \quad (3.13)$$

where κ is the interaction range (Eq. (3.10)) and m , a_i and b_i are fitted parameters ($m = 2$, $a_1 = 0.42$, $a_2 = 7.45$, $a_3 = 8.68$, $b_1 = 0.55$; $b_2 = 3.02$; $b_3 = 5.75$) for the weakly jammed preparation route [Kumar et al., 2016]. In the next sections we consider that the bricks/tablets and the mortar/interface have different Young moduli but identical Poisson's ratios, $\nu = 0.2$, typical of ceramics.

Rewriting Eq. (3.11), we define a normalized macroscopic Young's modulus \tilde{E} :

$$\tilde{E} = \frac{E}{\sigma_N} = Z_b D \frac{\kappa^m}{2\pi} \frac{a_1 + a_2\alpha}{4 + a_3\alpha} \quad (3.14)$$

which shows, together with Eq. (3.13) that the macroscopic elastic parameters not only depend on the normal and tangential stiffnesses of the bond network but also on the relative density D and on the average bond number Z_b of the particle packing that has been used to construct this network.

Similarly, one may expect that the macroscopic strength Σ of the material defined by the bond network should also depend on D and Z_b . Considering the dependence of the macroscopic elastic behavior on particles arrangement parameters, we thus computed the macroscopic strength for the weakly jammed preparation route.

Five sets of samples with various (Z_b, D) values having a $165R \times 16.5R \times 16.5R$ size in the x , y and z directions, respectively, were generated. For each set, five samples were generated with different initial random seeds. The particles number $n = 7\,000$ was chosen

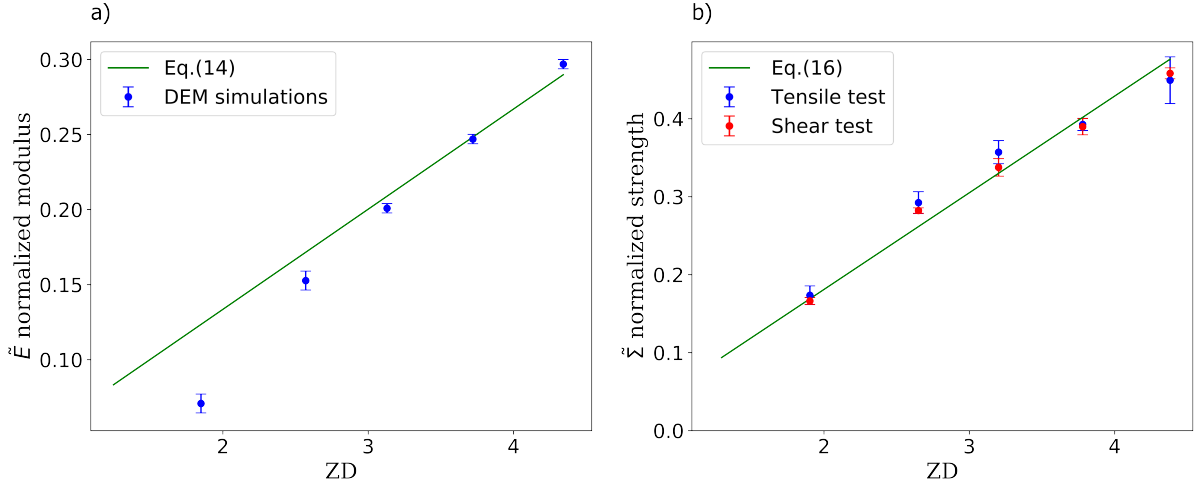


Figure 3.4: Calibration of macroscopic properties of the RVE : (a) Normalized Young's modulus $\tilde{E} = \frac{E}{\sigma_N}$ and Eq. (3.14). (b) Normalized strength $\tilde{\Sigma} = \frac{\Sigma}{\sigma_R}$ calibrated in tensile and shear tests.

large enough to ensure that the convergence of the measured macroscopic property (elastic modulus or strength) is reached [Kumar et al., 2016]. Tensile tests were carried out with periodic conditions and shear tests were carried out with non-periodic conditions. Tensile loading was applied in the x direction while xy pure shear was obtained by enforcing $\sigma_{yy} = 0$ during the computation.

The stress strain curves obtained from the tensile and pure shear tests exhibit a linear behavior followed by brittle fracture. Both elastic constants (E, ν) and strength can be extracted from these simulations. Fig. 3.4a shows the DEM simulation results for the normalized Young's modulus \tilde{E} (Eq. (3.14) versus the product $Z_b D$. The agreement with Eq. (3.14) is reasonable for $Z_b D > 3$.

Fig. 3.4b shows the evolution of the macroscopic strength for different values of the $Z_b D$ product. Similarly to elasticity (Fig. 3.4a), Fig. 3.4b confirms the influence of the packing parameters on the macroscopic strength. After fitting the strength results from tensile and shear tests, a simple common transition law between microscopic and macroscopic strength can be obtained:

$$\tilde{\Sigma} = c_1 Z_b D - c_2 \quad (3.15)$$

where $\tilde{\Sigma} = \frac{\Sigma}{\sigma_{Rc}}$ is the normalized macroscopic strength and $c_1 = 0.124$; $c_2 = 0.067$ are fitted parameters. Eq. (3.15) together with Eqs. (3.13) and (3.14) cannot be considered as calibration equations per se and should only be considered as an approximate tool to compute macroscopic properties from microscopic bond parameters. For small values of the $Z_b D$ product, it is clear that DEM simulations lead to a smaller normalized Young's modulus than predicted by Eqs. (3.13) and (3.14) as the percolation threshold is ap-

proached. Thus, the simple relation proposed by [Kumar et al., 2016] should only be considered as a rough guideline for choosing elastic microscopic parameters in the domain $Z_b D > 3$. In the following, packings characterized by a product $Z_b D = 4.34$ have been used to mesh BM materials. In that case, the following calibration corresponding to our simulations (Fig. 3.4) has been taken for the microscopic parameters:

$$\sigma_N = 3.33E \quad (3.16)$$

$$\sigma_{Rc} = 2.12\Sigma \quad (3.17)$$

3.3 Modeling a brick and mortar material

3.3.1 Representative Volume Element (RVE)

To capture the mechanical behavior of the BM material, we set a 2D periodic Representative Volume Element composed of two tablets and two interfaces. This RVE is classically used in the literature for the development of analytical solutions [Barthelat, 2014; Begley et al., 2012] and finite element simulations [Bekah et al., 2012]. Fig. 3.5 shows a typical periodic configuration of the RVE, discretized with DEM particles. Tablets are connected horizontally by thin (red) interfaces and are separated vertically from each other by free surfaces. Such a model has the advantage of being sufficiently simple to allow for elegant analytical solutions [Barthelat, 2014] while capturing the load transfer from tension in the tablets to shear at the interface.

Using the RVE microstructural parameters and the geometrical parameters specified in Fig. 3.5, we define in accordance with the notations in [Barthelat, 2014], the tablet volume fraction ϕ :

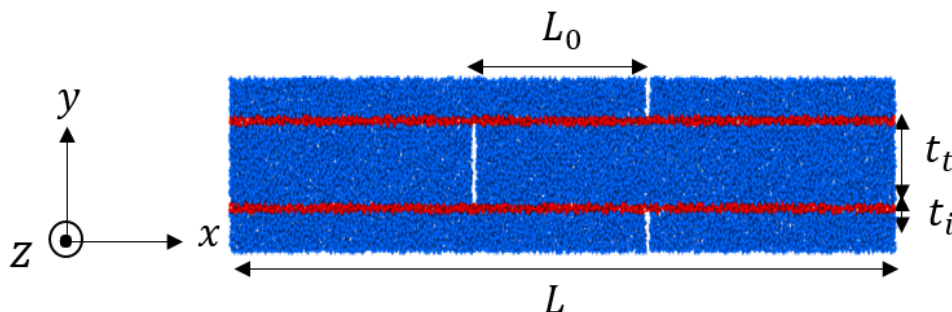


Figure 3.5: Representative Volume Element generated with discrete particles. Red particles mesh interfaces and blue particles mesh tablets. L , L_0 , t and t_i are geometrical parameters characterizing the RVE.

$$\phi = \frac{t_t}{t_t + t_i} \quad (3.18)$$

the tablet aspect ratio ρ :

$$\rho = \frac{L}{t_t} \quad (3.19)$$

the overlap aspect ratio ρ_0 :

$$\rho_0 = \frac{L_0}{t_t} \quad (3.20)$$

and the overlap ratio k :

$$k = \frac{L_0}{L} = \frac{\rho_0}{\rho} \quad \text{with} \quad 0 < k \leq 0.5 \quad (3.21)$$

where subscripts i and t stand for interface and tablet, respectively. For the sake of comparison with existing analytical models [Barthelat, 2014], the vertical interfaces are not filled by DEM particles which means that no stress is carried in the x direction between two tablets. 3D DEM simulations are run in a pseudo 2D configuration with 4 ± 1 particles in the thickness and periodic boundary conditions in all three directions, with $\epsilon_{zz} = 0$ to ensure plane strain conditions.

In the DEM unit cell shown in Fig. 3.5, each phase is represented by a given particle type assigned with microscopic parameters to model its mechanical behavior. These parameters are calibrated independently for the tablet and the interface as described in section 3.2.5.

The stiffness of bonds between interface and tablets particles are treated in series Eq. (A.2). As for fracture, the critical Rankine strength of interface-tablet bonds is dictated by the smallest strength of the interface-interface and tablet-tablet bonds.

3.3.2 Homogenization procedure

To investigate the anisotropic behavior of brick and mortar materials, we performed tensile loadings in both axial and transverse direction. For the axial loading the numerical sample is subjected a macroscopic strain ϵ_{xx} and periodic boundary conditions ($\epsilon_{yy} = 0$) and conversely for the transverse loading. Due to the material's microstructure, the effective elastic tensor is orthotropic [Bertoldi et al., 2008]. In a plane strain configuration the axial and transverse modulus are computed as follows:

$$\tilde{E}_x = \frac{E_x}{E_t} = \frac{1}{E_t} \frac{1}{\epsilon_{xx}} \left(\Sigma_{xx}^{axial} - \left(\frac{\Sigma_{xx}^{transv}}{\Sigma_{yy}^{transv}} \right) \Sigma_{yy}^{axial} \right) \quad (3.22)$$

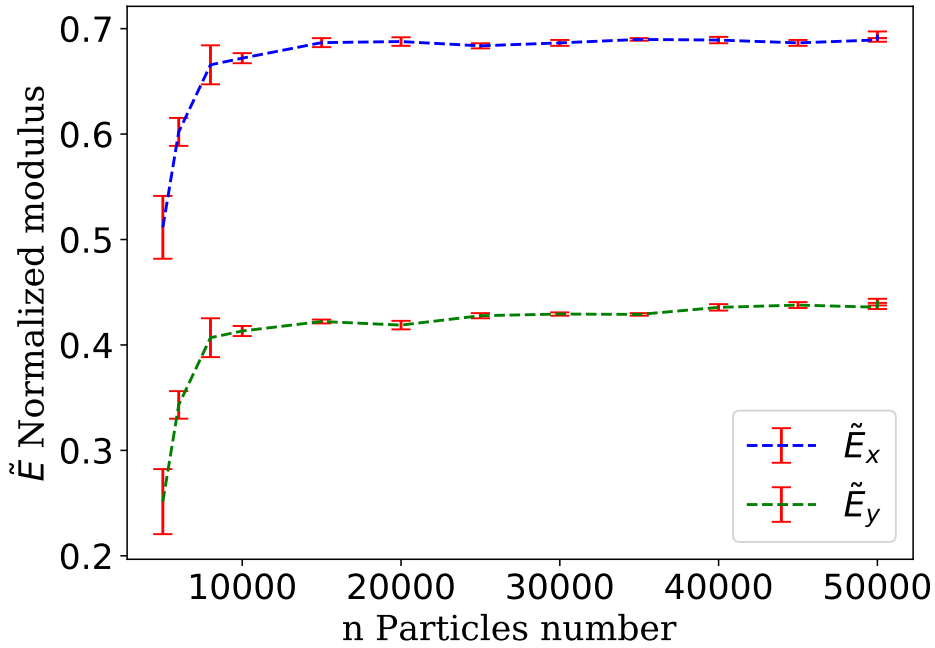


Figure 3.6: Evolution of macroscopic normalized moduli \tilde{E}_x and \tilde{E}_y for the RVE shown in Fig. 3.5 against the particle number n for a constant set of microscopic parameters. Sample characteristics: tablet aspect ratio $\rho = 16$, overlap ratio $k = 0.5$, and $\phi = 0.87$.

$$\tilde{E}_y = \frac{E_y}{E_t} = \frac{1}{E_t} \frac{1}{\epsilon_{yy}} \left(\Sigma_{yy}^{transv} - \left(\frac{\Sigma_{yy}^{axial}}{\Sigma_{xx}^{axial}} \right) \Sigma_{xx}^{transv} \right) \quad (3.23)$$

where *axial* and *transv* stand for axial and transverse loadings, respectively.

3.3.3 Convergence study

We generated thirteen different three-dimensional RVEs with different particles number n to define the minimum number of particles that allows stable macroscopic properties to be obtained with a periodic RVE. More generally, we study in this section the influence of mesh refinement on elastic and fracture properties. For each discrete set with a given number of particles n , five initial samples were generated using different random seeds to compute standard deviations. Each set of particles was generated as described in section 3.2.4. The tablet aspect ratio is $\rho = 16$, the overlap ratio $k = 0.5$ and a tablet volume fraction $\phi = 0.87$. All samples exhibit a size ratio of $80 \times 10 \times 1$ in the three directions. The packing characteristics and the input parameters are reported in Table.1.

Figures 3.6 and 3.7 show the convergence of the elastic moduli and strength as the particle number increases. For a particle number larger than 10 000, the Young's modulus clearly converges with a low standard deviation, which seems inherent to the random discrete nature of the packing used to mesh the RVE. Concerning strength, convergence

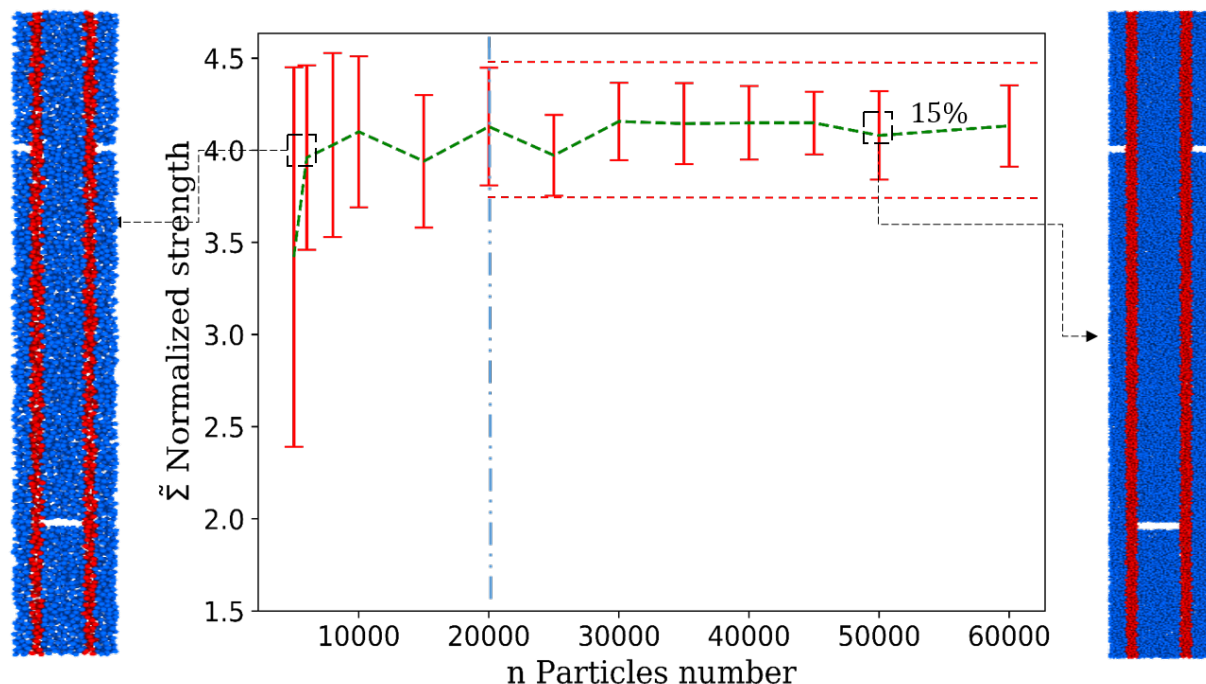


Figure 3.7: Evolution of macroscopic normalized strength $\tilde{\Sigma}$ against particle number n for a constant set of microscopic parameters.

can be considered satisfactory for $n \geq 10\,000$. Hereafter samples are generated with 20 000 particles to ensure that the thinner part of the material (i.e. the interface) contains enough particles (we observed that four particles are sufficient with periodic boundary conditions) to obtain convergence even with a slightly larger tablet volume fractions ϕ .

Interestingly, Fig. 3.6 demonstrates that the RVE exhibits a clear anisotropic elastic response. The axial Young's modulus (E_x) is nearly twice as large as the transverse modulus (E_y). This is generally ignored by analytical models that only consider the axial behavior of the RVE.

3.4 Comparison with analytical models

3.4.1 Elastic modulus

Assuming that there is no vertical interface, i.e. no load transfer in tension between tablets, the classical shear-lag model [Barthelat, 2014; Ni et al., 2015; Ji & Gao, 2004; Begley et al., 2012] leads to the RVE Young's modulus as a function of the Young's modulus of the tablet and the interface. [Barthelat, 2014] proposed:

$$\tilde{E}_x = \frac{E_x}{E_t} = \frac{\phi}{1 + \frac{1}{\beta} (\coth(k\beta) + \coth(\beta(1-k)))} \quad \text{with} \quad \beta = \rho \sqrt{\frac{1}{2(1+\nu)} \frac{E_i}{E_t} \frac{\phi}{1-\phi}} \quad (3.24)$$

[Ni et al., 2015] and [Begley et al., 2012] proposed:

$$\tilde{E}_x = \frac{E_x}{E_t} = \frac{2\beta \sinh[(1-k)\beta] \sinh(k\beta)}{2 \sinh(\beta) + \beta [\cosh(\beta) - \cosh((2k-1)\beta)]} \quad (3.25)$$

and [Ji & Gao, 2004] proposed:

$$\tilde{E}_x = \frac{E_x}{E_t} = \frac{1}{\left(1 + \frac{1-\phi}{\phi}\right) \left(1 + \frac{8}{\rho^2} \frac{1-\phi}{\phi} (1+\nu)\right)} \quad (3.26)$$

where ϕ , ρ , and k are geometrical parameters defined in Eqs. (3.18), (3.19), and (3.21), respectively. The form of Eqs. (3.24) and (3.25) proposed by their authors are reproduced here but one may notice that an analytical simplification of Eq. (3.25) demonstrates that the two models only differ by a factor of ϕ . Note that the model of [Ni et al., 2015] (Eq. (3.25) is only valid for sufficiently large values of the tablet volume fraction (typically $\phi > 0.8$). Also, the model of [Ji & Gao, 2004] has been developed only for a symmetric overlap ($k = 0.5$).

By varying k for $\rho = 20$, Fig. 3.8 shows the evolution of the normalized Young's modulus $\frac{E_x}{E_t}$ against the overlap aspect ratio ρ_0 , which is the parameter controlling the elastic modulus and encompassing both the effects of ρ and k [Barthelat, 2014]. Results for three different tablet volume fractions ϕ are compared to three analytical models [Begley et al., 2012; Barthelat, 2014; Ji & Gao, 2004]. The numerical results were obtained for five realizations and E_x was calculated using the homogenization procedure described in section 3.2. The standard deviation on the normalized Young's modulus was around 4% for high volume tablet fraction showing limited influence of the initial packing arrangement.

A high tablet concentration leads to a high modulus and to less sensitivity to the overlap aspect ratio. Figure 3.8 shows that our simulation results are in good accordance with Barthelat's model. In particular, the region of stiff increase of the E_x/E_t ratio for small overlap aspect ratio is well rendered by this model. The model of Begley exhibits the same kind of transition, in agreement with our simulations, but overestimates the E_x/E_t ratio as compared to our DEM simulation results and Barthelat's model.

As indicated above (Fig. 3.6), the tested RVE exhibits an anisotropic elastic behavior. To validate the elastic modulus in the y direction, we compared it to the analytical model of [Bertoldi et al., 2008], where E_y is given by:

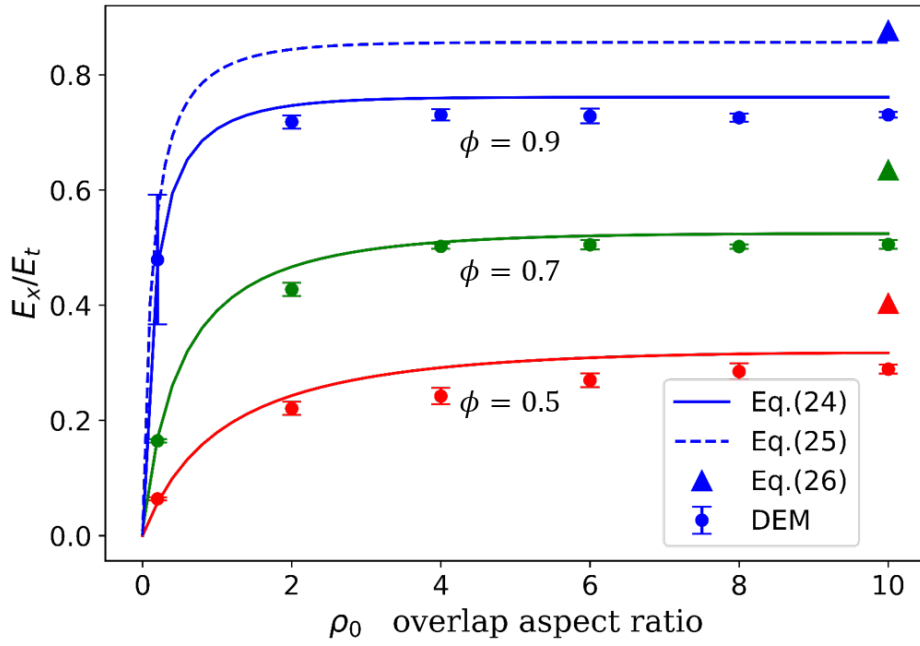


Figure 3.8: Normalized macroscopic Young's modulus $\frac{E_x}{E_t}$ from DEM simulations (bullet symbols) as a function of the overlap aspect ratio for three different tablet volume fractions ϕ with an aspect ratio $\rho = 20$, and a 0.1 Young's modulus ratio ($E_i/E_t = 0.1$). DEM simulation results are compared to three analytical models Eqs. (3.24), (3.25), (3.26) ($\rho_0 = k\rho$)(Eq. (3.21)). Eq. (3.26) is valid only for a symmetric overlap (i.e. $\rho_0 = 10$). Standard deviations are calculated based on five simulations.

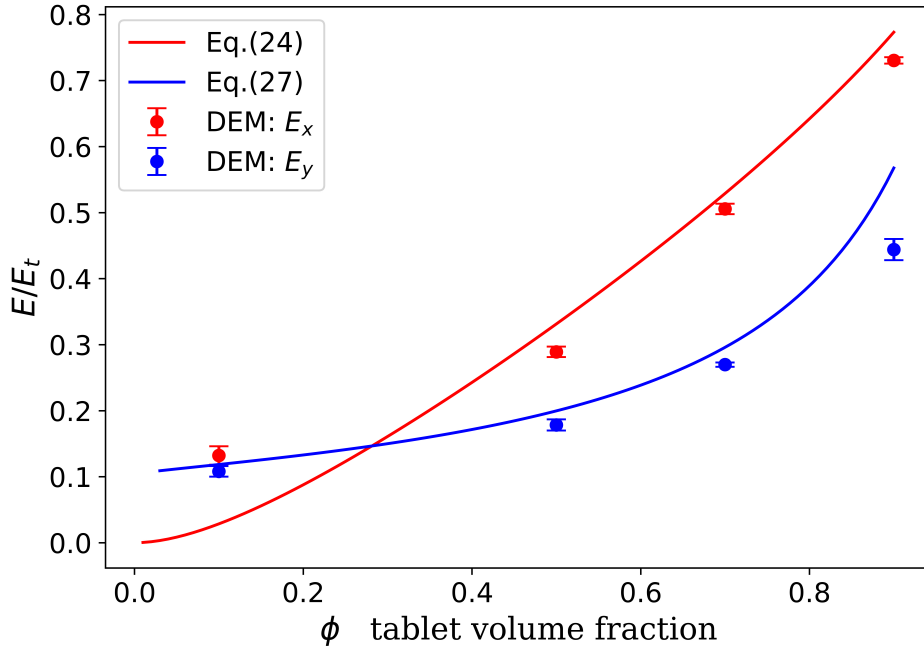


Figure 3.9: Normalized analytical Young's modulus \tilde{E}_x and \tilde{E}_y (Eqs. (3.26) and (3.27) against the tablet volume fraction ϕ with an aspect ratio $\rho = 20$ compared to the DEM results (bullet symbols). The error bars are computed based on five simulations.

$$\tilde{E}_y = \frac{E_y}{E_t} = \frac{[1 - \phi(1 - \frac{E_t}{E_i})(1 - \nu^2)]}{\Gamma} \quad (3.27)$$

where

$$\Gamma = \phi(1 - \phi)(1 + \nu)^2 \left[(1 - 2\nu)\left(1 + \frac{E_t^2}{E_i^2} + 2\frac{E_t}{E_i}\nu^2\right) + \frac{E_t}{E_i}((1 - \phi)^2 + \phi^2)(1 - \nu^2)^2 \right] \quad (3.28)$$

Fig. 3.9 shows that in accordance with Fig. 3.8, Eq. (3.26) overestimates \tilde{E}_x for $\phi \geq 0.5$. Note that analytical models are ill-suited for low tablet volume fractions ($\phi < 0.5$). More interestingly, the DEM simulated \tilde{E}_y is compared to the above analytical model for increasing values of tablet volume fractions ϕ with a symmetric overlap ratio $k = 0.5$ and an overlap aspect ratio $\rho = 20$. \tilde{E}_y values are in quite good agreement with the analytical model on the whole tablet volume fraction domain.

3.4.2 RVE failure

The analytical prediction of the strength of a brick and mortar arrangement has been tackled by numerous authors under various assumptions [Barthelat, 2014; Ni et al., 2015; Begley et al., 2012]. In particular, some authors considered the simplified case of uniform

shear in the interface, which is a valid assumption for a large elastic modulus contrast ($E_i/E_t \ll 0.1$) between interface and tablet (or for an overlap aspect ratio close to unity, which is not of much engineering interest) [Barthelat, 2014]. In that case, the normalized fracture initiation stress writes:

$$\tilde{\Sigma}_{init} = \frac{\Sigma_{init}}{\Sigma_t} = \min \left[\rho_0 \phi \frac{\Sigma_i}{\Sigma_t}, \frac{1}{2} \right] \quad (3.29)$$

where Σ_t and Σ_i are tablet and interface strength, respectively. A critical overlap ratio, $(\rho_0)_c = \frac{\Sigma_t}{2\phi\Sigma_i}$ can be defined to point out when fracture initiation shifts from the interface to the tablet. Note that the fracture initiation stress in Eq.(3.29) does not depend on $\frac{E_i}{E_t}$. The above model, valid for $\frac{E_i}{E_t} \ll 1$, is justified for biological materials or synthetic materials with a polymeric interface. A ceramic/glass or ceramic/ceramic brick and mortar structure will exhibit a markedly larger Young's modulus ratio (typically $\frac{E_i}{E_t} \geq 0.1$). In that case, the model developed by [Begley et al., 2012] and [Ni et al., 2015] that accounts for non-uniform shear in the interface is more appropriate. It writes:

$$\tilde{\Sigma}_{init} = \frac{\Sigma_{init}}{\Sigma_t} = \min \left[\frac{\rho}{\beta} \frac{\Sigma_i}{\Sigma_t} \tanh(k/\beta), \frac{1}{2} \right] \quad (3.30)$$

where β (see Eq. (3.24)) is a parameter that describes the magnitude of the shear transfer in the interface. The models accounting for uniform [Barthelat, 2014] and non-uniform shear transfer [Begley et al., 2012; Ni et al., 2015] are very similar for $\frac{E_i}{E_t} \ll 1$.

To capture the brick and mortar behavior, we apply uniaxial tensile tests along the tablets under periodic conditions on nine RVE's with different overlap aspect ratios ρ_0 for $\rho = 10$, $\phi = 0.87$ and $\frac{\Sigma_t}{\Sigma_i} = 6$. For each RVE, five initial samples were generated using different random seeds to compute standard deviations. Fig. 3.10 shows a typical stress-strain curve. Two points are noteworthy on this curve. The stress Σ_{init} at which we consider that fracture initiates is chosen when 50 bonds are broken (or approximately 0.1% of the total number of bonds). This choice is rather arbitrary but consistent for all tests. Figure 3.10 indicates that this threshold corresponds to the end of a mild damage process that does not affect the linearity of the stress-strain curve, before large damage due to crack propagation that causes a change in slope on the stress-strain curve. The stress Σ_{max} simply defines the maximum stress attained by the sample. The difference between these two stresses gives us information on the extrinsic mechanisms at play after crack initiation.

Figure 3.11a compares analytical models to DEM simulations for fracture initiation (Σ_{init} in Fig. 3.10). The accordance between models and DEM simulations is rather good. In particular, the stress plateau for $\rho_0 > (\rho_0)_c$ is well rendered. For $E_i/E_t = 10^{-3}$, this plateau corresponds to a fracture initiating in the tablets. For lower stiffness contrast,

fracture always initiates in the interface due to larger stress concentration as shear transfer becomes less uniform in the interface [Begley et al., 2012; Ni et al., 2015].

As the crack propagation is not modeled in the analytical models [Begley et al., 2012; Barthelat, 2014; Ni et al., 2015], the stress at crack initiation is considered equal to the maximum stress. However, initiation alone is not enough to characterize the fracture behavior of these brick and mortar materials. Fig. 3.11b shows that indeed when plotting the maximum stress (Σ_{max} in Fig. 3.10), the analytical models that predict only initiation differ markedly from our simulations. A clear difference between Fig. 3.11a and Fig. 3.11b is the role of the stiffness ratio E_i/E_t . The stress at initiation is strongly linked to this ratio, while the maximum stress is weakly related to E_i/E_t (in particular for $E_i/E_t > 0.1$). For a large contrast of Young's modulus ($E_i/E_t = 10^{-3}$), the interface shear stress is uniform which results in very similar values for crack initiation and maximum stresses. However, for a low modulus contrast ($E_i/E_t = 1$), the large stress concentration (non-uniform shear stress) leads to earlier crack initiation, which explains the large difference between stress initiation and maximum stress. After crack initiation in the interface the crack propagates in a stable manner within the interface. Friction and interlocking effects build up rising stresses that ultimately can cause the crack to pass through the tablet leading to a catastrophic failure at approximately half the tablet strength. This explains why most of the data points in Fig. 3.11b fall on a plateau around $0.4\Sigma_t$. Only for low overlap aspect ratio and low stiffness contrast the crack is confined to the interface leading to a lower maximum stress value. We believe that interlocking effects inherent to DEM are realistic for brittle interfaces where newly created rough surfaces may interlock each other and resist to shear loading. The calibration of these mechanisms is possible through modifications of the packing characteristics and the friction law.

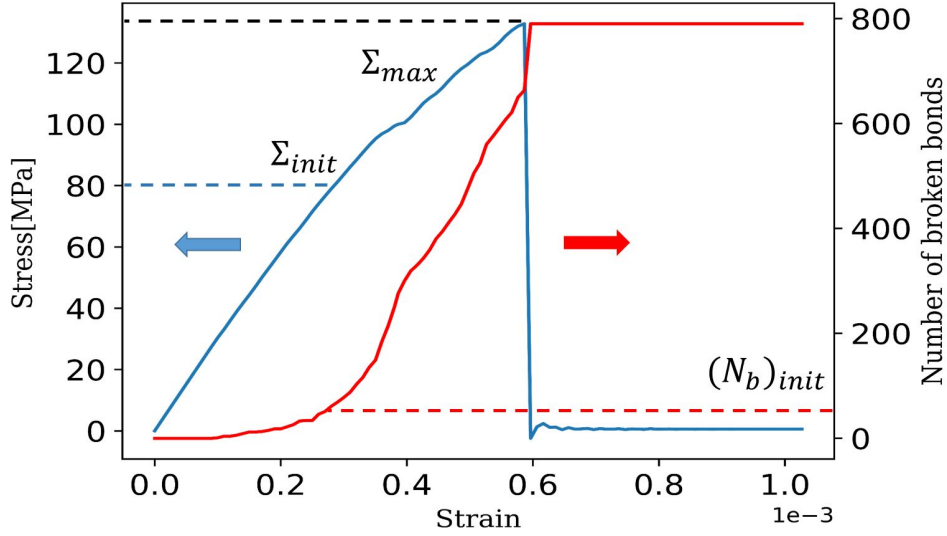


Figure 3.10: Typical stress-strain curve number of broken bonds from a DEM simulation for $\rho_0 = 2.5$ and $\frac{E_i}{E_t} = 0.1$. Two stresses are considered for comparison with analytical models. The fracture initiation stress Σ_{init} corresponds to the stress at which 50 bonds have broken. The strength Σ_{max} corresponds simply to the maximum axial stress.

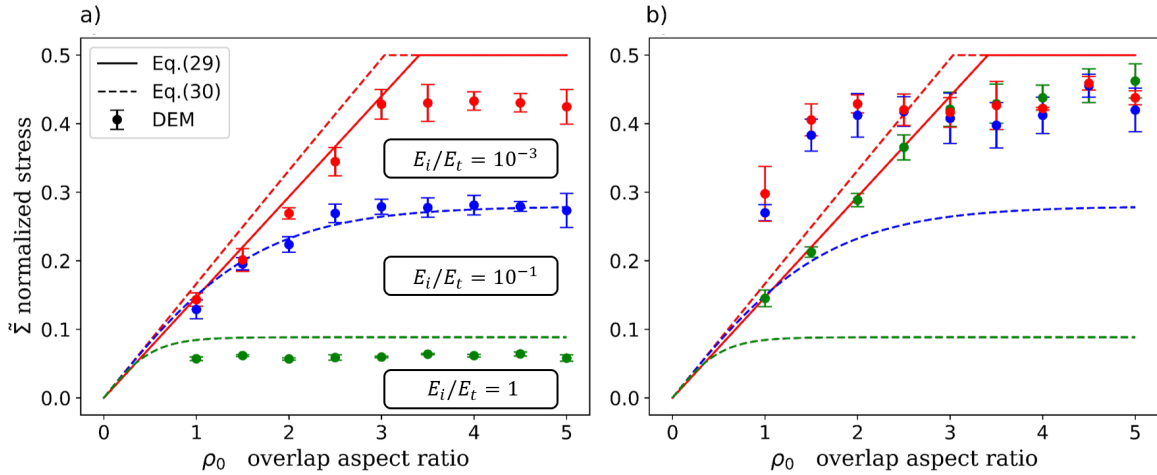


Figure 3.11: Normalized macroscopic stress $\tilde{\Sigma} = \frac{\Sigma}{\Sigma_t}$ of the RVE as a function of ρ_0 for three different stiffness ratios $\frac{E_i}{E_t}$ compared to analytical models [Ni et al., 2015; Barthelat, 2014]. (a) Fracture initiation stress Σ_{init} and (b) Maximum stress Σ_{max} after crack propagation. Eq. (3.29) is only valid for small elastic modulus ratios for which it is very similar to Eq. (3.30).

3.5 Application to nacre-like alumina

To illustrate the potential of the numerical model developed in the previous sections, we apply it to nacre-like alumina. The model microstructural parameters mimic the material described by [Bouville et al., 2014b]. The tablets are made of alumina with a tablet volume fraction $\phi = 0.90$. The aspect ratio is $\rho = 14$, the overlap aspect ratio $\rho_0 = 3.5$ and the overlap ratio $k = 0.25$.

The mechanical properties are those of alumina (the tensile strength of tablets is $\Sigma_t = 5.3$ GPa, [Feilden et al., 2017]). In our case, we consider a tablet/interface stiffness ratio of 0.1. The interface strength Σ_i is left as a parameter as it is the main material parameter that can be tuned experimentally (through composition, residual porosity, ...). To investigate its influence and more generally the influence of the strength ratio between interface and tablet, we generated several samples with interface strengths smaller than the strength of the alumina tablets ($\Sigma_i = [50, 4000]$ MPa).

By applying uniaxial tensile loading as in section 3.3, we obtain stress-strain curves as illustrated in Fig. 4.3. Using the stress/strain curves of each sample, and the number of broken bonds per particle (Fig. 3.13) of three different samples ($\Sigma_i = 200; 1\ 300, 4\ 000$ MPa), three failure behaviors can be distinguished (Fig. 3.14):

- Crack initiation and propagation in the interface (regime 1) for low values of Σ_i .
- Crack initiation at the interface and propagation in the tablet (regime 2) for intermediate values of Σ_i .
- Crack initiation and propagation in the tablets (regime 3) for high values of Σ_i .

The last two regimes lead to an overall brittle behavior of the RVE and are not desirable while the first regime is characterized by interface crack propagation that promotes extrinsic reinforcement through mechanisms such as crack deviation or crack bridging. In addition, for regime 1 the stress does not fall to zero even after complete crack propagation (capping of the number of broken bonds in Fig. 3.13) due to friction and interlocking that keep a non-zero stress level. The failure regime also depends on the overlap aspect ratio ρ_0 : small values of ρ_0 promote regime 1 while large values are associated to regime 3 (Fig. 3.11).

To optimize Σ_i on a quantitative basis, the strength (maximum stress) and the dissipated energy (area under the stress-strain curve) are plotted in Fig. 3.15. As already mentioned, for regime 1 the stress does not fall to zero. The dissipated energy is only computed during crack propagation and does not encompass the energy dissipated by the friction of the broken interfaces after crack propagation (see highlighted area under

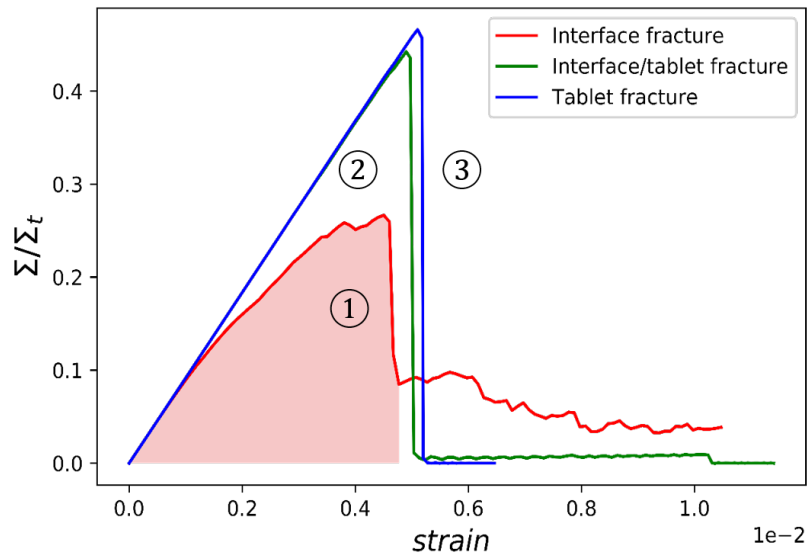


Figure 3.12: Typical stress-strain curves for $\Sigma_i = 200$ MPa, 1 200 MPa and 4 000 MPa. Three fracture regimes can be identified with increasing interface strengths Σ_i : (1) Interface fracture, (2) Interface/tablet fracture and (3) Tablet fracture.

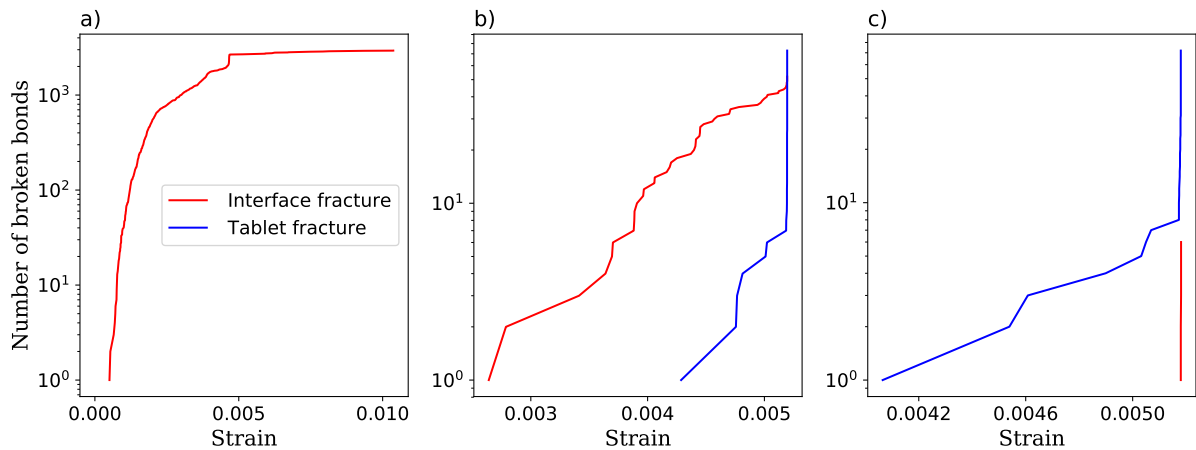


Figure 3.13: Number of broken bonds versus strain for both interface and tablet, where red and blue curves represent the interface and the tablet bonds, respectively. (a) Interface fracture initiation and propagation (b) Interface fracture initiation and tablet fracture propagation (c) Tablet fracture initiation and propagation.

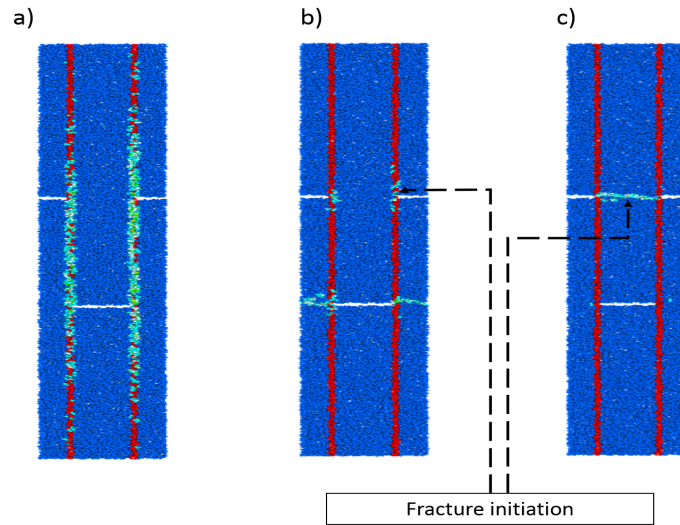


Figure 3.14: The corresponding illustrations of number of broken bonds per particle for the three cases of crack initiation and propagation. (a) Interface fracture initiation and propagation (b) Interface fracture initiation and tablet fracture propagation (c) Tablet fracture initiation and propagation.

curve 1 in Fig. 4.3). The value reported for regime 1 thus corresponds to a lower bound of dissipated energy as friction at broken interfaces may play a non-negligible role in alumina-nacre reinforcement. The examination of the evolution of strength and dissipated energy with increasing Σ_i shows a similar and nearly monotonic behavior that looks disappointing in terms of optimization. Although used by some authors for optimization purposes (e.g. [Barthelat, 2014]), dissipated energy is only a mere indicator of the material fracture toughness. It should be clear that even though they exhibit the largest dissipated energy, samples with large interface strength have a non-desirable brittle behavior, while samples under regime 1 should give rise at a larger scale to extrinsic reinforcement leading to a rising R-curve behavior with high fracture toughness (for sufficiently long cracks). A closer look at Fig. 3.15 and considering the three fracture regimes, show that an interesting optimal value for interface strength maybe found around $0.1\Sigma_t$: both strength and dissipated energy are quite close to the maximal values obtained for large Σ_i and the crack path is still mainly confined within the interface.

The comparison with reported experimental values is also of interest. Two different interface compositions have been processed so far: Calcia/Alumina/Silica glass [Bouville et al., 2014b] and a supposedly stronger Aluminum Borate crystalline phase [Pelissari et al., 2017]. Both authors incorporated alumina nanoparticles in the interface to form strong bridges between the tablets. The reported strength values (assuming a tablet strength of 5.3 GPa, [Feilden et al., 2017] are $\frac{\Sigma}{\Sigma_t} = 0.09$ and $\frac{\Sigma}{\Sigma_t} = 0.13$, respectively. Even taking into account that strength could be overestimated by simulations at a very

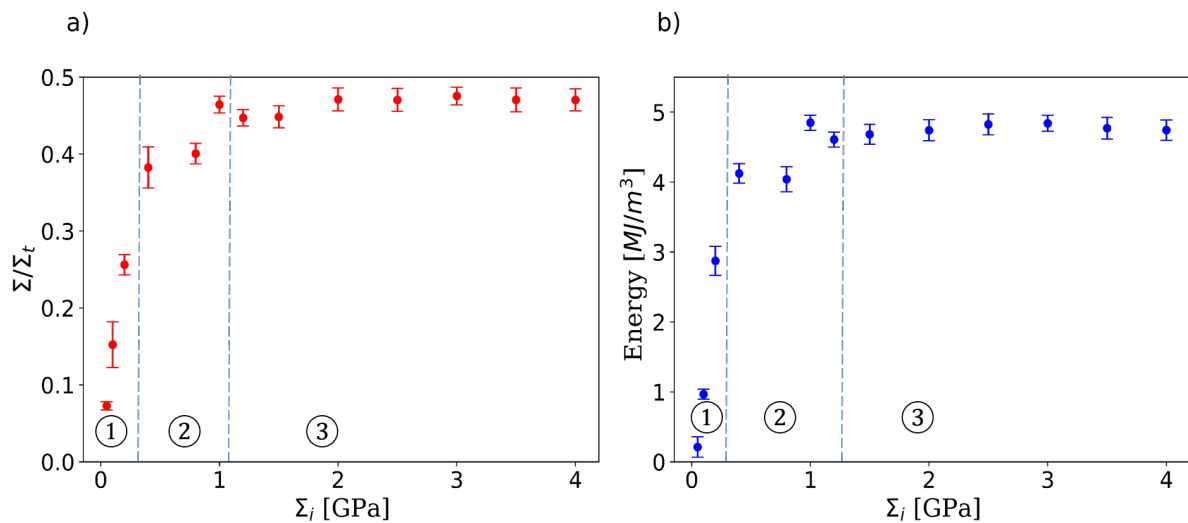


Figure 3.15: (a) Macroscopic strength and (b) fracture energy versus interface strength Σ_i . Standard deviations are calculated from five simulations. Three fracture regimes can be identified with increasing interface strengths Σ_i : (1) Interface fracture, (2) Interface/tablet fracture and (3) Tablet fracture.

small scale [Roussel et al., 2016; Jauffrès et al., 2013], the comparison with simulations shows that the experimental values are still very far from the maximum strength predictions (around $\frac{\Sigma}{\Sigma_t} = 0.4$). It demonstrates that the optimal interface strength has not been reached yet and that the material can still be improved. This is consistent with the concomitant improvement in strength and toughness obtained through the use of a crystalline stronger interface as compared to the original glass interface used by [Bouville et al., 2014b]. The gain in strength may appear a bit low for an interface strengthening of a factor of approximately 4 (~ 200 MPa for aluminum borate, [Ray, 1992], versus ~ 50 MPa for alumina silicate glass, [Cambridge, 2017]). However, one should keep in mind the detrimental effect of increasing the stiffness of the interface to a value close to the platelet's one (Fig.3.11). This is typically what happens when using an aluminum borate interface. The interface strength is thus a key parameter to optimize the mechanical behavior of brick and mortar materials.

3.6 Conclusions

In this work, a numerical model was developed to predict the mechanical response of brick and mortar materials using DEM simulations. Elastic and fracture properties of the components of brick and mortar were calibrated by taking into account the characteristics (average coordination number and packing density) of the particles packing that meshes the material. We have shown that to ensure convergence, care must be taken when

choosing the number of discrete elements that mesh a material.

The comparison of our DEM simulation results to available models in the literature for a standard Representative Volume Element of a brick and mortar materials shows quite good agreement in elasticity, thus giving some confidence in the simulation results. The initiation of fracture is also in good agreement with analytical models. However, predicting fracture initiation alone fall short to model extrinsic reinforcement mechanisms that are responsible for the ability of these materials to prevent catastrophic failure. Indeed, brick and mortar materials mainly develop toughening through crack growth/propagation, after crack initiation. The added value of DEM simulations is their capability to model post-fracture behavior. Most analytical shear-lag approaches on brick and mortar materials [Barthelat, 2014; Begley et al., 2012; Ni et al., 2015] have succeeded in predicting crack initiation but cannot investigate the crack propagation. The topological modifications (branching, bifurcation, new surface generation or crack healing) that come with fracture are indeed difficult to apprehend analytically. Even finite elements would struggle to investigate properly these discrete events. In contrast, DEM, thanks to its inherent discrete nature, is well suited for discontinuous problems.

As an application example of the proposed modeling approach, we choose nacre-like alumina, a ceramic/ceramic composite, and showed that the interface strength can be optimized to maximize strength and toughness. Three crack initiation/propagation regimes were distinguished: interface initiation and propagation (1), interface initiation followed by tablet propagation (2) and tablet initiation and propagation (3). These three regimes are governed by the ratio between the interface strength and the tablet strength. An optimal interface strength value lies at the threshold between regime (1) and (2) where the composite strength is close to its maximum value and the crack still propagates mainly within the interface, thus ensuring the development of extrinsic reinforcement and high toughness.

The geometry of the RVE used here is simple enough to allow comparison with analytical models from the literature and demonstrate the interest of the present approach to model BM materials. However, simulations at a larger scale are required to correctly assess extrinsic toughening through the propagation of cracks amid several tablet layers. This would also allow the study of the effect of material heterogeneities, e.g. in terms of overlap, tablet orientation or tablet aspect ratio. Another point that should be addressed in the future by DEM is the influence of alumina bridges between the tablets that are believed to be an essential ingredient for the exceptional mechanical performances of BM materials [Grossman et al., 2017]. Considering that DEM is based on an explicit scheme, the discrete simulations at a larger scale are anticipated to be CPU intensive. Although parallel computing is available with DEM, a careful strategy will be necessary

for computing large scale problems with millions of particles.

In this work, both materials (interface and tablet) are considered as elastic-brittle. This is because our main interest is in alumina nacre which features porous alumina interfaces that are brittle. Adding some plasticity in the interface behavior will enlarge the domain in which a stable crack can grow without triggering brittle failure. A relatively simple and useful generalization of the model would thus be to consider plastic interactions in the interface to apply DEM to brick and mortar structures with ductile interfaces (metal or polymer). This is possible as DEM is also well suited for tackling plastic deformations [Martin et al., 2003; Martin, 2004].

Chapter 4

The influence of interface strength and nano-bridges

Chapter 4 is an application of the model developed previously on a larger scale, where the effect of the interface on the mechanical behavior of the material is studied. The chapter is based on our scientific paper that was published in Composites Part B: Engineering journal, under the title: "Strength and Toughness Trade-off Optimization of Nacre-like Ceramic Composites" [Radi et al., 2019b]. This paper was submitted with supporting information (SI) describing the contact laws, generation of the numerical microstructures, calibration and details of the crack length computation. Although the first two points have already been covered in Chapter 3, the full SI are reported in Appendix A for completeness. The samples and DEM simulations are outlined, in particular the procedure used to assess the R-curve (Section 4.2). The influence of interface reinforcement on strength and toughness was tested in two manners. First by reinforcing the interface globally by tuning its nominal strength (Section 4.3). Then by reinforcing the interface locally by adding nano-bridges and tuning their density (Section 4.4). Last, a property map that summarizes the obtained results (Section 4.5) to help the design of brick and mortar materials. The paper is reported as submitted with its own introduction that is unavoidably redundant with the present thesis introduction and literature review and may be skipped by the reader.

Contents

- 2.1 Introduction 11**
- 2.2 Brick and mortar materials 12**
 - 2.2.1 Natural materials 12
 - 2.2.2 Synthetic materials and fabrication methods 14
 - 2.2.3 Reinforcement mechanisms in brick and mortar (BM) materials 24
- 2.3 Modeling and performance optimization of brick and mortar materials 30**
 - 2.3.1 Analytical models 30
 - 2.3.2 Numerical models 38
- 2.4 Discrete Element Modeling (DEM) 42**
 - 2.4.1 What is DEM? 42
 - 2.4.2 Application of DEM on continuous materials 44
- 2.5 Outcomes and outlines 47**

Abstract

Bio-inspired by abalone nacre, all ceramic brick-and-mortar composites with impressive mechanical properties have been recently manufactured. Albeit comprising only brittle constituents, extrinsic reinforcement mechanisms impart to these nacre-like ceramics high toughness and non-catastrophic crack propagation properties.

While several models have been developed to understand the mechanical properties of natural and synthetic brick-and-mortar materials, they have always considered a ductile interface and focused mostly on intrinsic toughening mechanisms. Modeling so far has not captured the extrinsic toughening mechanisms responsible for the properties of nacre-like ceramics. Here we show that the Discrete Element Method (DEM) can account for reinforcement mechanisms such as microcracking and crack deflection, and quantitatively assess strength, initiation toughness and crack growth toughness. Two approaches are studied to enhance strength and toughness of nacre-like ceramics, either by reinforcing the interface globally (an increase of the interface strength) or locally (addition of nano-bridges). We combine the results to provide design guidelines for synthetic brick-and-mortar composites comprising only brittle constituents.

4.1 Introduction

The nacreous part of many seashells species is a composite which toughness is several orders of magnitude larger than its components [Chen et al., 2008; Barthelat & Espinosa, 2007]. Nacre has a brick-and-mortar (BM) architecture—aligned mineral tablets (bricks) linked together by a thin organic interface (mortar)—that provides cohesion and energy dissipation capacities to the material [Jackson et al., 1988; Espinosa et al., 2009]. Other structural features are found within the architecture of nacre, from the fibril network of the interface to the arrangement of mesolayers [Barthelat et al., 2016]. The high toughness of nacre can be attributed to different reinforcement mechanisms present at different length scales. Reinforcement mechanisms can be classified as either intrinsic or extrinsic. Intrinsic mechanisms, acting ahead of the crack tip, result mainly from plasticity and are active independently of the crack size or geometry. They essentially affect crack initiation toughness [Ritchie et al., 2009]. In contrast to intrinsic toughening, extrinsic toughening includes microstructural mechanisms that act behind the crack tip to resist its further opening by lowering the stress and strain fields at the crack tip. These mechanisms can occur by fiber bridging, where the fibers hold the two fracture surfaces together after the crack has propagated, or by frictional sliding or interlocking between two rough fracture surfaces. It can also be a result of microcracking around the main crack to relieve the stress at the crack tip. Extrinsic mechanisms influence only the crack

growth [Ritchie, 2011; Feng et al., 2000]. A clear manifestation of this dependence is the rising resistance curve (R-curve) where the force to sustain cracking increases with the crack extension [Launey & Ritchie, 2009; Ritchie, 2011].

Inspired by nature, many synthetic BM materials have been developed [Munch et al., 2008; Oner Ekiz et al., 2009; Zhao & Guo, 2017; Yadav et al., 2017; Niebel et al., 2016; Naglieri et al., 2015]. Because the mortar that provides the necessary plastic deformation in these composites is a metal or a polymer, the composites cannot withstand harsh environmental conditions (high temperatures, oxidation, etc. . .). In contrast, the nacre-like alumina processed by Bouville et al. [Bouville et al., 2014b], Le Ferrand et al. [Le Ferrand et al., 2015] or Pelissari et al. [Pelissari et al., 2017] are only composed of brittle inorganic constituents (e.g. 98.5 vol.% of alumina tablets and nano-particles, 1.3 vol.% of silica and 0.2 vol.% of calcia for the composite developed by Bouville et al.). These ceramic-ceramic composites can thus retain high strength and high toughness at high temperature (600 °C), which makes them very attractive materials for aeronautics, energy, or defense applications. Bouville et al. have reproduced some of the above reinforcement mechanisms (crack deflection, microcracking, tablet pull-out, etc. . .), and showed the essential role of alumina nano-particles at the interface that forms nano-bridges between the tablets, providing energy dissipation mechanisms during crack propagation. Modeling the various mechanisms that explain how a composite which comprises only brittle mineral constituents becomes damage-resistant should help to optimize the material. Indeed, nacre-like ceramics material may still be far from their optimum as only a few microstructural designs have been tested. Adequate modeling should guide microstructural design and help to further improve this material.

The effect of the microstructure on strength and toughness in BM materials with ductile mortar has been approached by several analytic shear-lag models that use a Representative Element Volume (RVE). Stiffness, strength and energy absorption were predicted as a function of microstructural parameters [Kotha et al., 2001; Jäger & Fratzl, 2000; Begley et al., 2012; Barthelat, 2014; Ni et al., 2015], and key parameters were introduced to optimize the material and achieve simultaneously high stiffness, strength and energy absorption [Barthelat, 2014]. Toughening mechanisms such as microcracking, crack deflection, and crack bridging were mainly approached by numerical models as such phenomena are difficult to capture analytically. Early numerical efforts were based on Finite Element Modeling (FEM) [Katti et al., 2005] or discrete lattice [Nukala et al., 2005; Dimas & Buehler, 2013]. More recently, a discrete element approach using rigid brick elements with cohesive zone interactions was developed [William Pro et al., 2015; Abid et al., 2018]. The use of rigid elements is numerically very efficient but implicitly makes the assumption that bricks are unbreakable and that the two constituents have a very

large stiffness contrast. Pro et al. have shown that the plastic zone developing ahead of the crack tip increases with interface ductility [William Pro et al., 2015], and that consequently the modeling of typical natural or synthetic BM materials with ductile interface requires a very large volume. On the contrary, the process zone ahead of the crack tip should be limited to a smaller volume in the case of elastic-brittle interfaces [Abid et al., 2019]. The numerical efficiency of the rigid brick approach has allowed Abid et al. to investigate large volumes and assess the R-curve of BM materials with elastic-softening or elastic-plastic interfaces [Abid et al., 2019]. However, the results and conclusions provided by this type of model cannot be directly transposed to the case of nacre-like ceramic with brittle interfaces and a mild stiffness contrast between the two constituents.

Many authors have underlined the important role of nano-bridges between tablets in natural nacre [Shao et al., 2014; Song et al., 2003] or bio-inspired materials [Naglieri et al., 2015; Grossman et al., 2018, 2017; Gu et al., 2017]. However, the inclusion of nano-bridges in BM analytical or numerical models is scarce [Grossman et al., 2018; Askarinejad & Rahbar, 2014].

Originally designed for granular materials [Cundall & Strack, 1979; Dubois & Radjai, 2011; Chareyre, 2019], and extended more recently to continuous materials [Leclerc, 2017; André et al., 2012, 2013; Kumar et al., 2016] the Discrete Element Method (DEM) based on spherical elements can naturally elucidate topological modifications (crack propagation, multiple cracking, crack branching, etc...), which makes it appropriate to model extrinsic reinforcement mechanisms. Moreover, the crack path location does not need to be predefined in DEM. In contrary to cohesive zones modeling, the crack path location does not need to be predefined in DEM. This means that considering breakable tablets is not more expensive computationally. Also, after fracture, particles may resume contact and interact via frictional contacts. Several studies have proven that DEM is well suited to model the fracture behavior of elastic-brittle materials [André et al., 2013; Maheo et al., 2015; Roussel et al., 2016]. Recently, DEM simulations at the scale of one nacre-like ceramic RVE were successfully validated against existing analytical models in terms of elasticity and strength. The propagation of the crack within the RVE itself was modeled demonstrating the added value of DEM for this problem. Compared to the discrete approach with rigid bricks, the DEM model can capture friction and interlocking effects within an interface and the propagation of the crack to a brick. Fracture surfaces of nacre-like ceramics exhibit broken tablets [Bouville et al., 2014b], demonstrating that the eventuality of brick breakage should be accounted for.

In this work, we use DEM to reproduce extrinsic and intrinsic toughening mechanisms of all-ceramic composites at the scale of a hundred tablets and study the impact of interface reinforcement on strength and toughness. The article is organized as follows. First,

the DEM framework is introduced briefly and the setup of the microstructure and the simulations are outlined. Special attention is given to explain the R-curve computation. Second, the influence of two strategies to reinforce the interface, namely the increase of nominal strength of the interface and the addition of nano-bridges is studied. The capacity of this modeling approach to capture damage and crack propagation is highlighted. The results are then gathered in property maps that provide design guidelines.

4.2 Discrete model for brick-and-mortar materials

4.2.1 DEM framework

To model the mechanical behavior of continuous media with DEM, we consider the material as a random packing of spherical particles bonded by cylindrical beams. The particles here have no physical meaning and should only be regarded as entities of discretization, similar to the mesh in FEM. The DEM formulation and the sample generation procedure are similar to our earlier study on a Representative Volume Element [Radi et al., 2019a]. All DEM simulations are performed with our in-house code dp3D [Martin et al., 2003]. The bonding laws that connect the particles which model both the interface and the tablet are described in section S1 of the Supporting Information (SI) (A). The strength of bonds is dictated by the Rankine criterion.

Figure 4.1 shows a schematic of the typical BM microstructure used in this work. The generation procedure for BM microstructure has been described in earlier works [Kumar et al., 2016; Radi et al., 2019a] and is detailed in section S2 of the SI. A zoom-in (Fig. 4.1) shows the structural parameters of the RVE used. Tablets of length L and thickness t_t are connected horizontally and vertically by thin (red) interfaces with thickness t_i . The BM microstructure is defined by three non-dimensional parameters: the tablet's aspect ratio $\rho = \frac{L}{t_t}$, the overlap ratio $k = \frac{L_0}{L_t}$ and the tablet volume fraction $\phi = \frac{t_t}{t_i+t_t}$. The microstructural parameters used in this study mimic the ceramic material described by Bouville et al. [Bouville et al., 2014b] with an aspect ratio $\rho = 14$ and a tablet's volume fraction $\phi = 0.876$. The tablet volume fraction was chosen to have at least three particles at the interface to ensure convergence [Radi et al., 2019a]. Increasing the tablet volume fraction means increasing the overall number of particles, which leads to prohibitive CPU time. The overlap ratio $k = 0.25$ was chosen under the assumption that there is a uniform distribution over $0 < k < 0.5$.

Tablets and interfaces in the microstructure (Fig. 4.1) are represented by a given particle type assigned with microscopic parameters to model their respective mechanical behavior. The stiffness of bonds that connect interface and tablet particles are treated

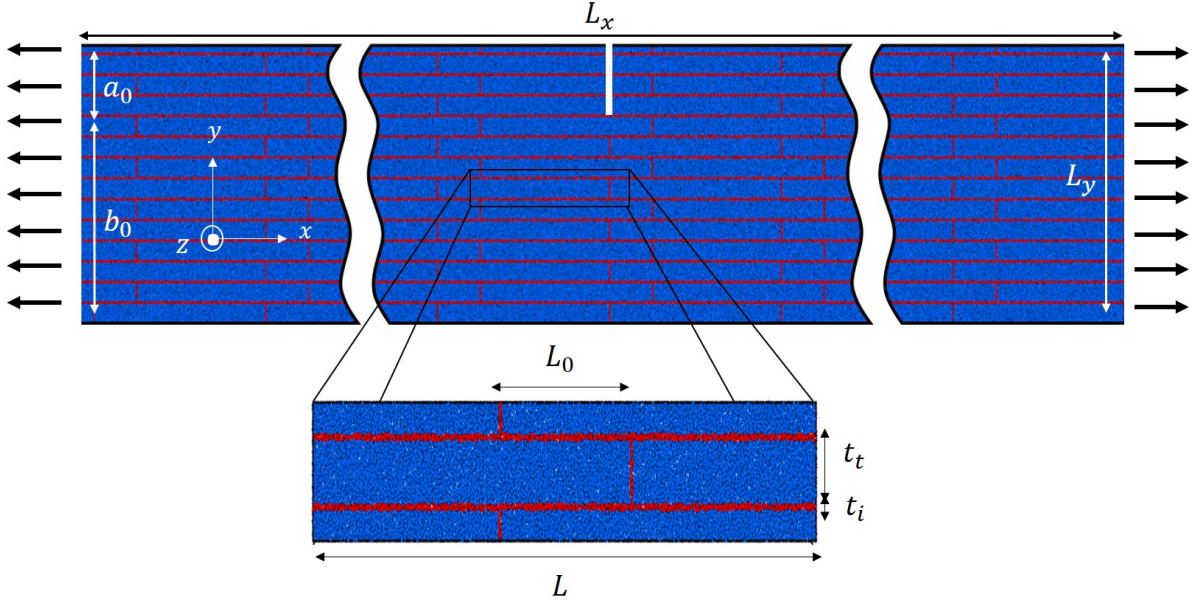


Figure 4.1: Overview of a notched microstructure with staggered tablets (in blue) showing geometry, dimensions ($L_x = 57 \mu\text{m}$, $L_y = 9 \mu\text{m}$), and loading. Similar unnotched samples are used for strength determination. Only half of the volume used in our simulations is represented here. A close-up view shows a representative volume element together with characteristic structural parameters.

in series (see Eq. S2 in section S2 of the SI) and their values are calibrated following the method described in [Kumar et al., 2016]. As for fracture, the strength of bonds at the interface-tablet junction is dictated by the lowest strength (i.e. interface material strength). The microscopic interaction parameters (particle level) are calibrated to attain the macroscopic properties of the interface and of the tablet as detailed in [Radi et al., 2019a]. Table A.1 summarizes the input parameters used in this study. For the Young's moduli, typical value for alumina (tablets), and a lower bound value for an oxide glass (interface) are used. The resulting mechanical macroscopic response of a nacre RVE is comparable in terms of elasticity and stress at crack initiation with existing analytical models, thus validating the DEM approach [Radi et al., 2019a].

	E	ν	Σ
Interface	40 GPa	0.2	0.1 – 2 GPa
Tablet	400 GPa	0.2	4 GPa

Table 4.1: Macroscopic parameters (E Young modulus, ν Poisson ratio, Σ macroscopic strength) used in the simulations. Indicia i and t are used hereafter to refer to the parameters of the interface and tablet, respectively.

4.2.2 DEM simulations

Two types of numerical tests were performed: uniaxial tensile loading of unnotched samples, to study tensile strength and of notched samples (Fig.4.1) to study toughness. The number of particles used to mesh the samples is 1 280 000. This value is based on the discretization convergence study carried out previously [Radi et al., 2019a]. Note that although 2D in its main geometrical features, our model is 3D, with several spheres in the z direction. The size of the samples is $5633 R \times 900 R \times 6 R$ where $R = 10$ nm is the particle radius.

The thickness of a tablet is 500 nm, comparable to the real nacre-like alumina [Bouville et al., 2014b]. Periodic boundary conditions in x and z directions were used with strain-rate imposed in the x direction. Free surface conditions were used in the y direction. Periodic boundary conditions in z correspond to a 2D plane strain configuration and only a few particles in z are required. Due to the periodic conditions in the x direction, crack interaction may arise in case of large crack deviation. The sample was thus chosen long enough in this direction ($\frac{L_x}{L_y} = 6.4$) to retard this artificial effect.

Only one simulation per condition (Σ_i value, Nb value, ...) was conducted. However, we evaluated the reproducibility of the results by generating five different initial random packings for a given typical case and the resulting standard deviation was less than 15%.

4.2.3 R-curve computation

The determination of fracture toughness involves tensile testing along the x axis of the notched microstructure (Fig. 4.1). During simulations, the deformation ϵ_x was progressively increased to propagate a mode I crack through the numerical sample. At every output step i , the number of broken bonds, the projected crack length a_i and the tensile stress are calculated. The procedure to compute a_i is detailed in section S3 of the SI.

To assess the reinforcement that occurs during stable crack propagation, the critical stress intensity factor K_{Ic} versus the projected crack length was calculated (R-curve). Due to the absence of plasticity in our model (all-ceramic composite), the Griffith equation is used [Anderson Ted.L, 2005]:

$$K_{Ic}(a_i) = f\left(\frac{a_i}{L_y}\right)\Sigma(i)\sqrt{L_y} \quad (4.1)$$

where $\Sigma(i)$ is the macroscopic stress and L_y the size of the sample in the y direction. The expression of the function $f\left(\frac{a_i}{L_y}\right)$ depends on the specimen's geometry and the applied loading [Hiroshi et al., 1985]. In our case, the samples are Single Edge Notched Tension

(SENT) and the function $f\left(\frac{a_i}{L_y}\right)$ writes [Anderson Ted.L, 2005]:

$$f\left(\frac{a_i}{L_y}\right) = \frac{\sqrt{2 \tan\left(\frac{\pi a_i}{2L_y}\right)}}{\cos\left(\frac{\pi a_i}{2L_y}\right)} \left[0.752 + 2.02 \left(\frac{a_i}{L_y}\right) + 0.37 \left(1 - \sin\left(\frac{\pi a_i}{2L_y}\right)\right)^3 \right] \quad (4.2)$$

Most models use either the maximum, the minimum, or the average of the values on the R-curve to define toughness [Abid et al., 2019; Davidson & Waas, 2011; Heid-Jorgensen & Budzik, 2018; Hossain et al., 2014]. In this study, we determine for each simulation both the crack initiation toughness $(K_{Ic})_{init}$ and the maximum toughness $(K_{Ic})_{max}$ over the crack resistance curve and calculate the difference ΔK_{Ic} . The maximum critical stress intensity factor $(K_{Ic})_{max}$ is computed within the limit of a chosen value of the projected crack length ($a_i \leq 5 \mu\text{m}$).

As the crack propagation distance is very small (a few micrometers versus a few hundreds of micrometers experimentally), $(K_{Ic})_{max}$ is not representative of a typical crack growth toughness. Indeed, crack growth toughness is potentially much larger after the propagation of the crack over several hundreds of micrometers. Here, ΔK_{Ic} is proportional to the initial slope of the R-curve (Fig. S3.d in the SI) and is thus a more representative measure of the crack growth toughness.

4.3 Effect of global interface reinforcement via nominal strength

4.3.1 Macroscopic strength

Several samples with different interface strength values Σ_i ($\frac{1}{40} \leq \frac{\Sigma_i}{\Sigma_t} \leq \frac{1}{5}$), were used with a fixed tablet strength Σ_t . A typical stress-strain plot is shown in Fig. 4.2a for $\Sigma_i = \frac{\Sigma_t}{8}$ with the axial stress and the total number of broken bonds vs. axial strain. Up to a strain value of $\approx 0.013\%$, the sample exhibits a linear stress-strain behavior characteristic of the elastic behavior of the BM structure prior to any significant fracture event. Between 0.013% and 0.020% strain, the amount of fracture events increases causing the failure of all vertical interfaces. After 0.032% strain, the sample fails in a catastrophic manner. The macroscopic strength Σ is defined by the maximum value of this curve.

The stress-strain responses of all tested samples are shown in Fig. 4.2b. Regardless of the interface strength, the deflection corresponding to the failure of vertical interfaces can be observed on all curves. Both failure stress and strain increase and then reach an asymptotic value at large Σ_i . Albeit slightly lower, the asymptotic strength is comparable to the one predicted by a simple load transfer analysis ($\Sigma = \phi \frac{\Sigma_t}{2} = 0.44\Sigma_t$) [Barthelat,

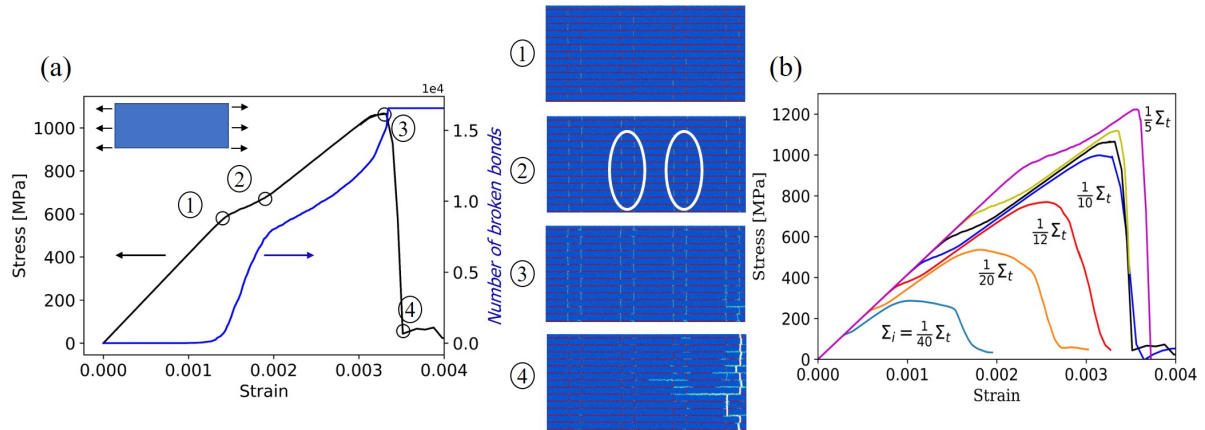


Figure 4.2: a) A typical stress-strain curve along with the number of broken bonds and corresponding snapshots ($\Sigma_i = \frac{1}{8}\Sigma_t$ and $\approx 4\,400\,000$ bonds). (1) End of the elastic domain and failure initiation of vertical interfaces, (2) failure of all vertical interfaces and initiation of crack growth in horizontal interfaces, (3) stress maximum and (4) sample failure. The ellipsoids on the snapshots point to microcracking. b) Stress-strain evolution of unnotched samples with increasing interface strengths.

2014] and simulations at the scale of a RVE [Radi et al., 2019a]. The maximum stress becomes more pronounced (more brittle behavior) as the interface strength approaches the tablet strength. We observed that the crack path goes from a stairway form at low interface strength to a straight one at high interface strength. In that case, we observe that some tablets are fracturing together with interfaces. The transition occurs around $\Sigma_i = \frac{1}{7}\Sigma_t$.

4.3.2 Toughness

Notched samples are used in this section to compute toughness (Fig.4.1). Fig.4.3 exemplifies the crack propagation by displaying the number of broken bonds for increasing strain and the corresponding stress-strain/broken bonds plots. The snapshots describe three characteristic steps in the simulation: (1) damage initiation, (2) maximum stress and (3) complete failure.

The examination of the failure patterns depicted in the snapshots of Fig. 4.3 helps understand the toughening mechanisms. For small interface strength, an overall non-catastrophic failure is observed (Fig. 4.3a). The vertical interfaces tend to fail early creating micro-cracking/multiple cracking [Bouville et al., 2014b; Begley et al., 2012]. This phenomenon occurs ahead of the crack tip and results in crack tip stress relaxation. Microcracking thus leads to an intrinsic reinforcement (as for plasticity in metals) and helps preserve a reasonable crack initiation toughness despite a very weak interface material. The main crack does not propagate through the material in a straight path. Instead,

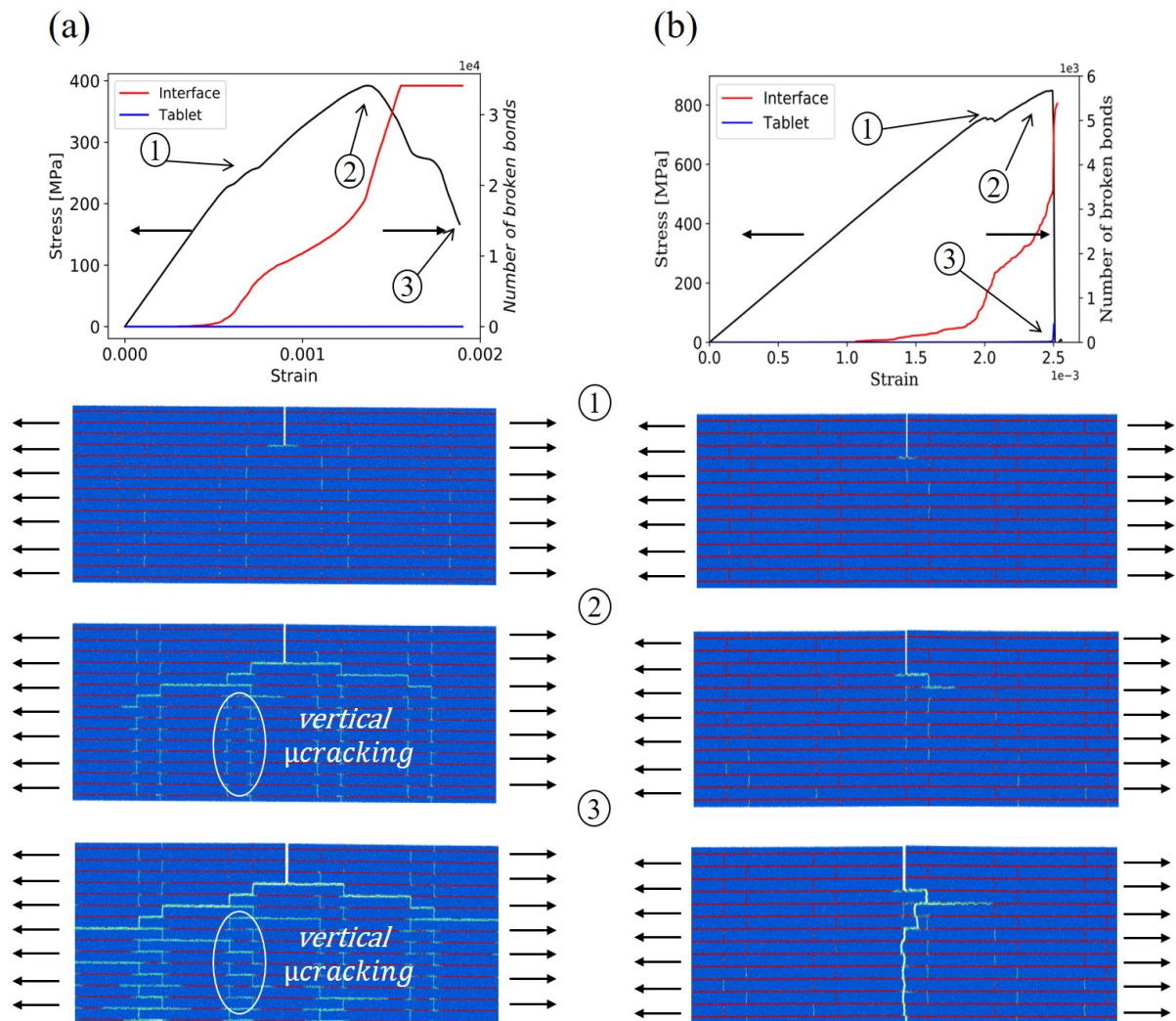


Figure 4.3: Example of a notched sample under uniaxial loading for two different values of interface strength a) $\Sigma_i = \frac{1}{20} \Sigma_t$ and b) $\Sigma_i = \frac{1}{5} \Sigma_t$ with tensile stress-strain curves and broken bonds in both interface and tablets. Corresponding sequences of deformation show (1) damage initiation, (2) maximum stress and (3) material failure.

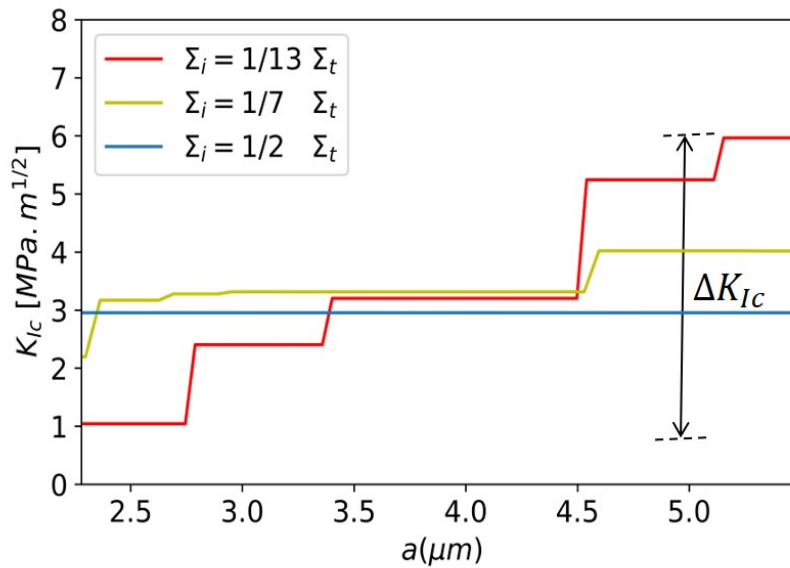


Figure 4.4: Typical crack resistance curves for three interface values representing different behaviors: a rising curve with a staircase pattern for low interface strength, a constant K_{Ic} value for high interface strength and an intermediate case with moderate increase of K_{Ic} .

the crack propagates within the interface and is continually deflected when it encounters a tablet, resulting in a stairway pattern and crack bridging.

For high interface strength (Fig. 4.3b), a higher stress is needed to initiate interface failure, which leads to crack propagation in a straight manner into the material, as it becomes easier to break a tablet than to bypass it. In addition, very little micro-cracking is observed. The resulting crack initiation toughness is large but comes with an unstable crack propagation (Fig. 4.4). Note that in the extreme case of $\Sigma_i = \frac{1}{5} \Sigma_t$, no vertical interface breakage is noticed. In that case, the stress maximum follows damage initiation very closely.

Figure 4.4 shows the resulting R-curve for three typical cases: low, intermediate, and high interface strength. The crack initiation toughness increases with interface strength. The first two cases are characterized by a rising R-curve in the form of a stairway and a relatively low crack initiation toughness. The third case exhibits a flat R-curve and a higher crack initiation toughness. The stairway pattern reveals the propagation of the crack in the interface by finite jumps: horizontal sections of the R-curve correspond to crack propagation in vertical interfaces occurring without any increase in stress (vertical interfaces are already broken) and vertical sections correspond to crack propagation in horizontal interfaces (stress increases but with a constant projected crack length). The length of the steps actually corresponds to a multiple of the platelet thickness. Abid et al. discrete brick model gives rise to very similar stairway R-curves [Abid et al., 2019].

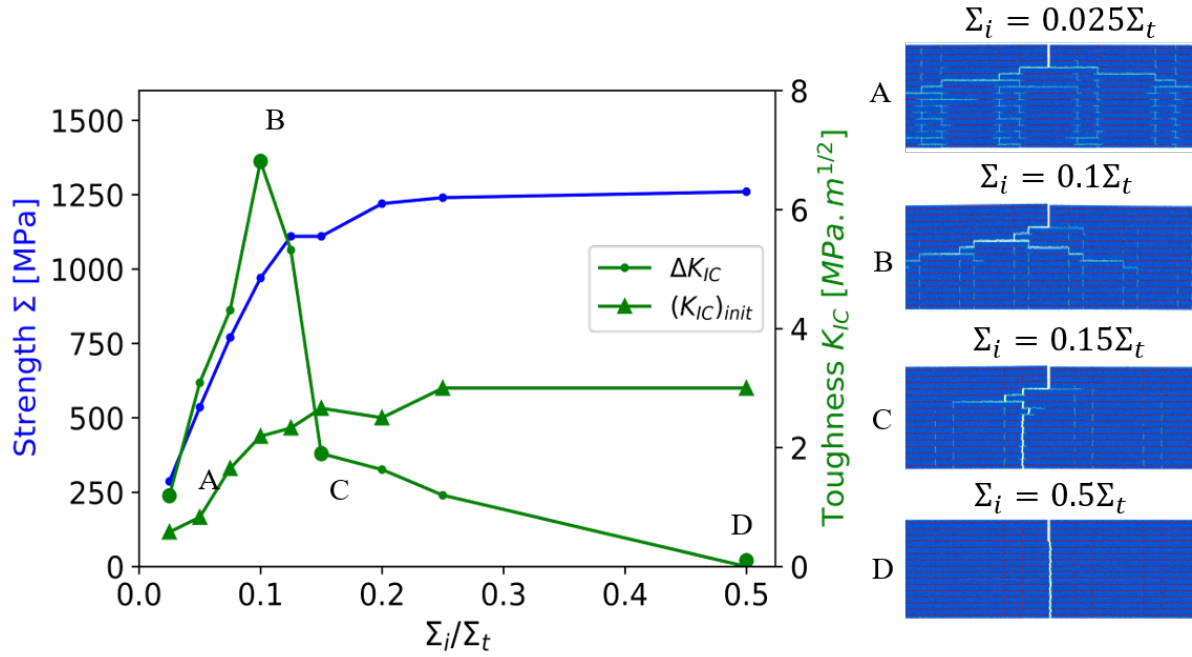


Figure 4.5: Strength, crack initiation toughness, and crack growth toughness for different interface strengths with the crack propagation snapshots. $\Sigma_i = \frac{1}{10}\Sigma_t$ sample exhibits the largest improvement in both strength and toughness.

Fig. 4.5 summarizes the preceding results by plotting strength, crack initiation toughness, and crack growth toughness (ΔK_{IC}) as a function of interface strength. While crack initiation toughness and strength increase in a monotonic manner until they reach an asymptotic value, crack growth toughness reaches a maximum for $\Sigma_i = \frac{1}{10}\Sigma_t$ before decreasing.

Significant amount of microcracking and crack deflection can be noticed in the first two snapshots of Fig. 4.5, which occurs when it is more advantageous for the crack to deviate to reach weaker regions. On the other hand, the last two snapshots of Fig. 4.5 show a brittle behavior with little or no microcracking and limited crack deflection. This could be explained by the high shear strength of the interface that prevents interface damage, and subsequent sliding and friction prior to failure. An interesting configuration is achieved for $\Sigma_i = \frac{1}{10}\Sigma_t$ when the interface strength is high enough to ensure an optimal crack growth toughness combined with a relatively high strength and crack initiation toughness. Further increase of interface strength leads to higher strength but also to brittleness (significant drop of the crack growth toughness).

4.4 Effect of local interface reinforcement by nano-bridges

As demonstrated by evolution in mollusk nacre, nano-bridges represent a simple and potentially efficient route to reinforce locally the interface in a BM structure [Shao et al., 2014]. To test numerically the effect of nano-bridges on our samples, square bridges that span the whole depth of the sample in the z direction were installed in between two adjacent tablets. Nano-bridges have the same mechanical properties as the tablets. Although their geometry is simplistic ($h = d = t_i$, see Fig. S4 of the SI), it gives information on the efficiency of local reinforcement. The average number of nano-bridges per tablet (Nb) in the natural nacre is approximately 40 [Barthelat et al., 2006; Song et al., 2003]. However, the density of nano-bridges in nacre-like alumina [Bouville et al., 2014b] is difficult to assess and not well controlled. In addition, the 2D nature of our model does not allow for a straightforward link between the number of nano-bridges per tablet in experimental conditions (3D) and the number of nano-bridges per tablet length in our simulation. Gu et al. [Gu et al., 2017] have shown that $Nb \approx 9$ is an optimal value for polymer-based 2D BM composites. Here, we choose to vary the number of bridges between $Nb = 3$ and $Nb = 18$ per tablet length. The addition of bridges results in a slightly stiffer composite (2.4 % increase for $Nb = 18$), because of the small increase in stiff material volume fraction.

4.4.1 Macroscopic strength

Using samples depicted in Fig. S4 of the SI with no initial notch, tensile tests were performed on nano-bridge reinforced microstructures. Figs. 4.6a-b show the strain-stress plots of samples for two different interface strengths. Fig. 4.6 a indicates that the number of bridges has a noticeable effect on the curve shape and maximum stress when starting from a low interface strength ($\Sigma_i = \frac{1}{20}\Sigma_t$). The stress deflection that was characteristic of vertical interface failure in the specimen without nano-bridges is much less pronounced when bridges are introduced. More importantly, the maximum stress increases with the number of bridges. For a higher interface strength value (Fig. 4.6.b, $\Sigma_i = \frac{1}{5}\Sigma_t$), the introduction of bridges still has a noticeable influence on strength but its effect is much less pronounced.

Fig. 4.6c aggregates the maximum stress values obtained with increasing Σ_i and increasing Nb . As already noticed for interface reinforcement by nominal strength, all curves converge towards a maximum strength of approximately $0.38 \Sigma_t$, comparable but slightly lower than the load transfer analysis value ($\Sigma = \phi \frac{\Sigma_t}{2} = 0.44\Sigma_t$) [Barthelat, 2014].

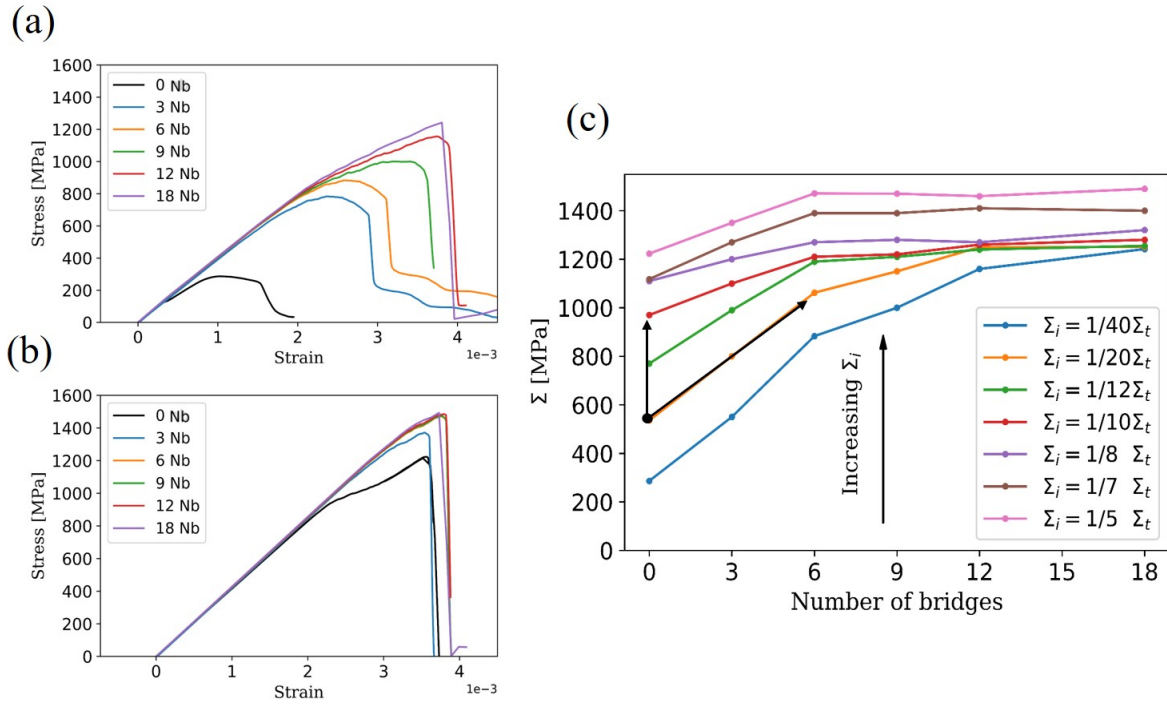


Figure 4.6: Stress-strain response of unnotched samples with various number of bridges per tablet (Nb), for two different interface strengths, a) $\Sigma_i = \frac{1}{20}\Sigma_t$ and b) $\Sigma_i = \frac{1}{5}\Sigma_t$. c) Strength as a function of Nb for increasing interface strengths. The black arrows point to two different paths to obtain the same macroscopic strength either by an increase in Σ_i or the introduction of nano-bridges.

Fig. 4.6c shows that, increasing the number of bridges is equivalent to an increase in interface strength when considering the macroscopic strength.

4.4.2 Toughness

The stress-strain responses of notched samples are presented for two different Nb 's in Fig. 4.7. The $Nb = 6$ case shows the failure of vertical interfaces (vertical microcracking) that immediately transfers damage to the next horizontal interfaces and thus causes horizontal microcracking. The crack path is sinuous and characterized by an irregular surface compared to the 18-bridges sample. The presence of bridges (stiff material, high strength) interrupts the continuity of the interface (soft material, low strength) which allows for a more homogeneous stress distribution that leads to a more progressive failure.

Fig. 4.8.a summarizes the evolution of the crack initiation toughness with the number of bridges. $(K_{Ic})_{init}$ increases with the interface strength and the number of bridges up to $Nb = 18$. Fig. 4.8.a also shows that by reinforcing the interface homogeneously (0 Nb), the maximum value of $(K_{Ic})_{init}$ is close to tablet's toughness (see section S2 of the SI). However, this value is out-passed when adding bridges. In contrast with reinforcement via

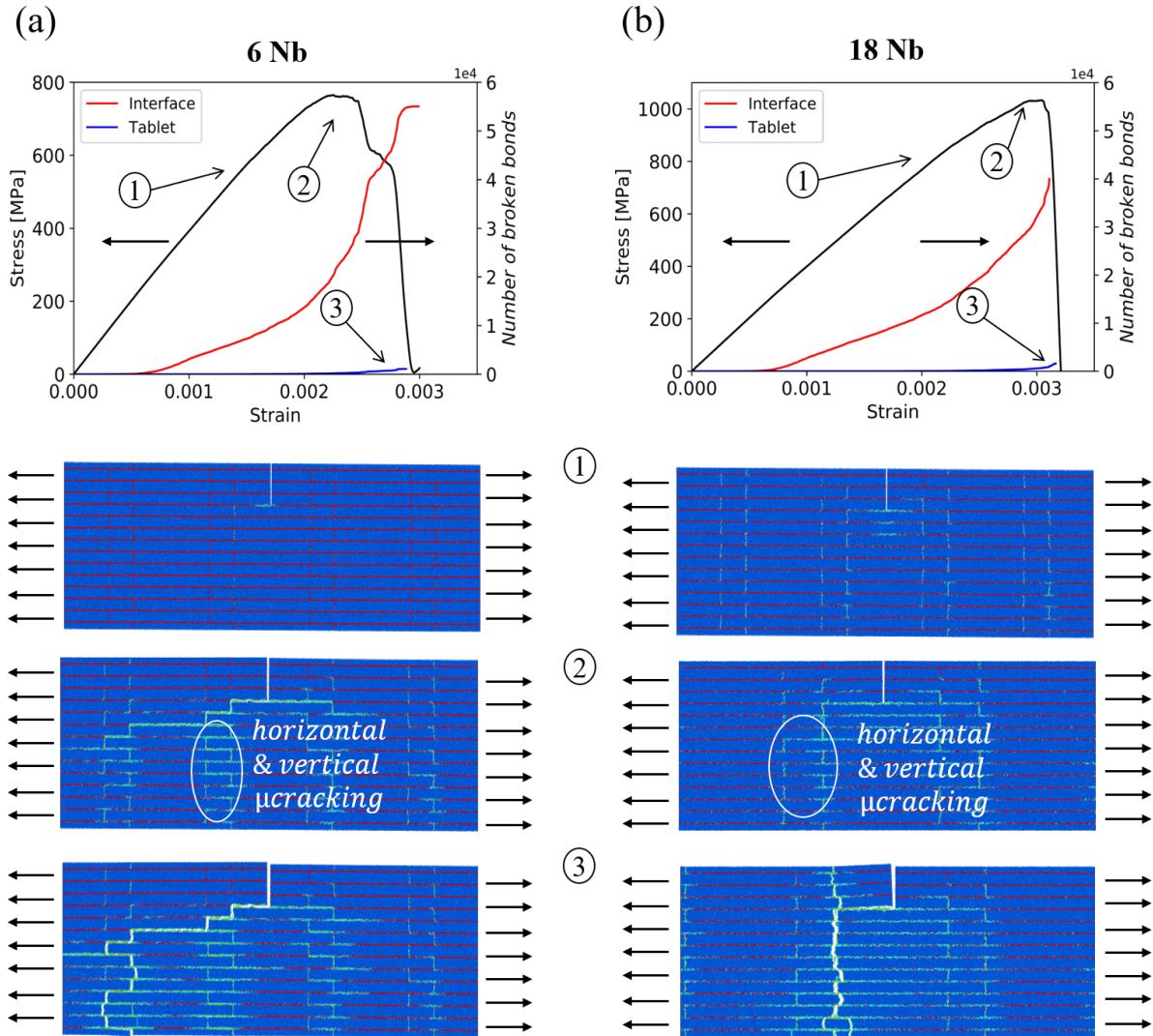


Figure 4.7: An example of a notched sample under uniaxial loading for two different number of bridges per tablet a) 6 *Nb* and b) 18 *Nb* with a fixed interface strength $\Sigma_i = \frac{1}{20}\Sigma_t$. Tensile stress-strain plots and the corresponding sequences of deformation for both simulations with (1) damage initiation, (2) stress maximum, and (3) material failure.

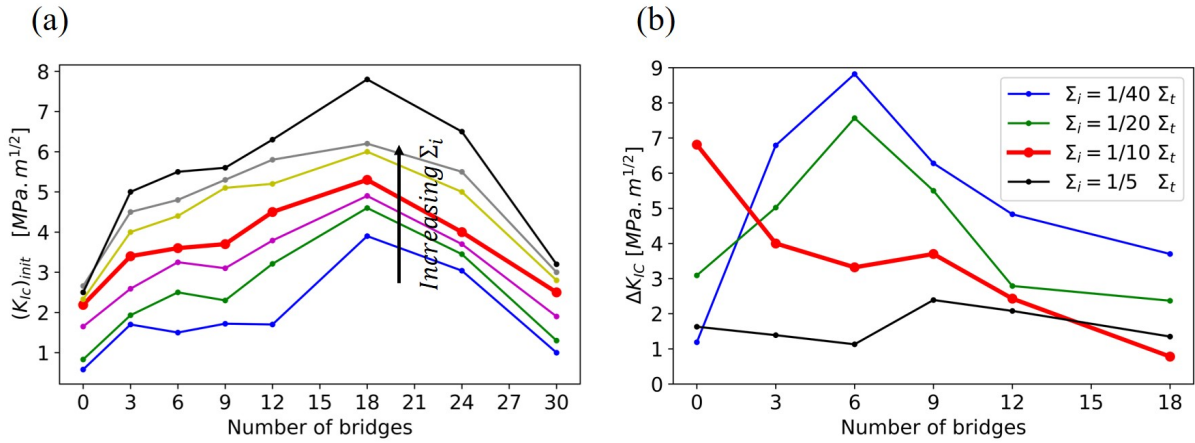


Figure 4.8: Toughness of samples with different Nb compared to without bridges microstructures. a) crack initiation toughness and b) crack growth toughness as a function of Nb for an increasing interface strength. Red bold curves correspond to the optimal (for crack growth toughness) interface strength without bridges.

interface nominal strength where an asymptotic value is reached, the addition of bridges leads to a peak for $(K_{IC})_{init}$ at $Nb = 18$. For larger Nb , $(K_{IC})_{init}$ decreases back to the tablet's value.

Fig. 4.8.b shows the crack growth toughness as a function of the number of bridges for increasing interface strengths. For low interface strength, adding bridges increases crack growth toughness up to a maximum value before decreasing. The maximum value corresponds to a critical number of 6 bridges. For high Σ_i , the addition of bridges decreases the crack growth toughness. For example, adding bridges to the sample with an optimum crack growth toughness (i.e 0 Nb and $\Sigma_i = \frac{1}{10}\Sigma_t$) will only decrease the crack growth toughness value, however it is beneficial for crack initiation toughness (bold red curves on fig. 4.8). The addition of bridges promotes microcracking and in turns an increase of crack growth toughness for low interface strength. However, adding bridges to an already strong interface is not beneficial for crack growth toughness as the interface becomes too strong to deflect efficiently the crack that runs through the tablets.

By adding 18 bridges per tablet the amount of stiff material increases, which means that vertical interfaces failure control the composite strength and the tablets fail immediately upon vertical interface rupture. For that extreme case, the high strength region is associated with a brittle composite response.

4.5 Discussion

The increase of the interface strength and the addition of bridges have a similar effect on strength (Fig. 4.6). In contrast, the interplay of interface strength and additional

bridges is quite different on crack initiation toughness and crack growth toughness. The gain in crack initiation toughness by an increase in Σ_i is larger when starting from a microstructure with bridges than without bridges (Fig. 4.8). Microcracking events, which relax stress at the crack tip, disappear when increasing Σ_i for a sample without bridges. In contrast, we observed that samples with a large number of bridges still exhibit microcracking prior to crack propagation (Fig. 4.7b). More generally, the interface material is damaged but the nano-bridges remain intact while damage diffuses. This is because the stiffness ratio ($\frac{E_i}{E_t} = 0.1$) is lower than the strength ratio ($\frac{\Sigma_i}{\Sigma_t}$) except for $\Sigma_i = \frac{1}{5}\Sigma_t$, where no microcracking is observed. The snapshots in Fig. 4.7b exemplify this phenomena. The crack propagates first at the tip of the notch into an horizontal interface and encounters a bridge with a high stiffness and large strength, which will cause the crack to deviate and propagate vertically into either the interface or the tablet. As for the crack growth toughness, although global or local reinforcement of the interface both leads to a maximum value before a decrease, the value reached via the addition of the optimal number of bridges (6) is slightly higher (9 MPa.m^{1/2} versus 7 MPa.m^{1/2}). While large values of $(K_{Ic})_{init}$ are mainly related to the strength of the interface and micro-cracking development prior to crack propagation, large values of ΔK_{Ic} are also associated to crack deflection by the tablets that is less marked with nano-bridges (Fig. 4.7). The reason that localized reinforcement (addition of bridges) results into better properties than homogeneous reinforcement (increase of interface strength), could thus be explained by the additional horizontal microcracking that was not found in homogeneously reinforced samples, which leads to additional delocalisation of stress. The microcracking that occurs before crack propagation contributes to the high value of crack initiation toughness, while microcracking after crack propagation contribute to high crack growth toughness.

From a practical point of view, starting with a low interface strength, composite strength Σ , initiation toughness $(K_{Ic})_{init}$ and crack growth toughness ΔK_{Ic} of nacre-like alumina can be increased either by an increase of the interface strength or the addition of alumina nano-bridges. For example, starting with $\Sigma_i = \frac{1}{20}\Sigma_t$ and no bridges, the material can be reinforced either by an increase of the interface strength to $\Sigma_i = \frac{1}{10}\Sigma_t$ or by the addition of 6 bridges to reach the same macroscopic strength $\Sigma \approx \frac{1}{4}\Sigma_t$ (see black arrows on Fig. 4.6). These two approaches (increase of Σ_i from $\frac{1}{20}\Sigma_t$ to $\frac{1}{10}\Sigma_t$ or addition of 6 bridges) result in fine approximately in the same ΔK_{Ic} value (7-7.5 MPa.m^{1/2}) and $(K_{Ic})_{init}$ value (2-2.5 MPa.m^{1/2}) (Fig. 4.8). Reaching an optimum crack growth toughness by an homogeneous reinforcement of the interface only, would require a good control over the interface strength, which might seem difficult since the optimum interface strength range is quite narrow (Fig. 4.5). The control of bridges density seems more feasible experimentally. Combining interface strength $\Sigma_i = \frac{1}{40}\Sigma_t$ with 6 Nb, shows an interesting compromise

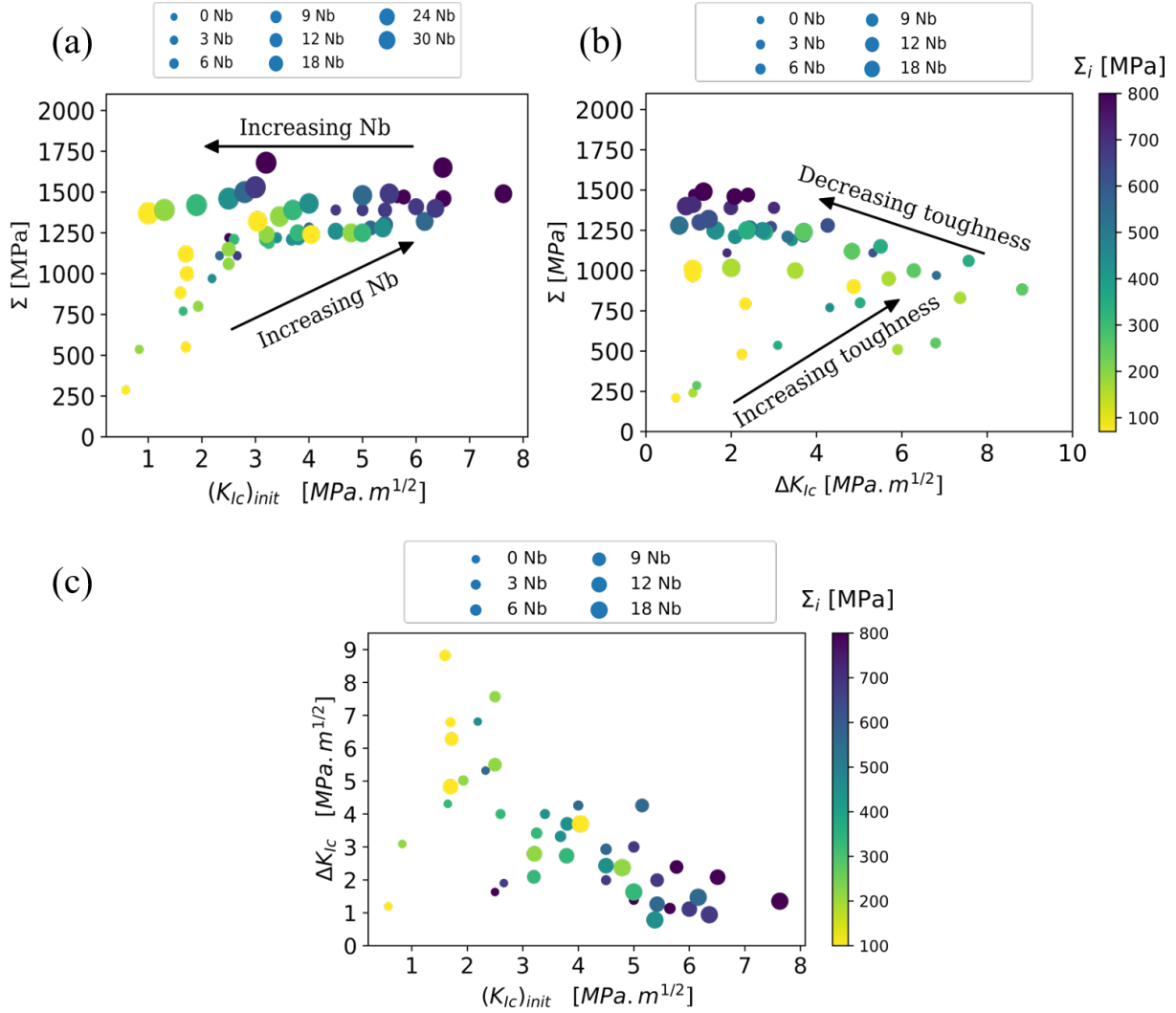


Figure 4.9: Property maps showing the different possible combinations of strength and toughness by variation of either the interface strength or the addition of nano-bridges at the interface. a) crack initiation toughness, b) Crack growth toughness. c) Crack growth toughness versus crack initiation toughness.

between high strength and crack growth toughness (but with a modest $(K_{Ic})_{init}$ value).

The results presented above are gathered in two property maps to help optimize the design of BM materials made of brittle constituents. The first map shows strength versus crack initiation toughness (Fig. 4.9a), where it is evidenced that both high strength and high crack initiation toughness can be reached by an increase of interface strength and the addition of bridges (upper right region of the map). The second map shows strength versus crack growth toughness (Fig. 4.9b). The combination of both high strength and crack growth toughness can be obtained by reaching configurations on the right corner of the map. On the third map ΔK_{Ic} is plotted versus $(K_{Ic})_{init}$ in order to show the difficulty to combine high values for these two properties. By using these property maps,

it is relatively clear how to combine either strength and crack initiation toughness or strength and crack growth toughness, depending on the desired application. When one looks for a combination of high strength and high crack initiation toughness, it is necessary to favour a microstructure with a large number of bridges and high interface strength. Conversely, a microstructure that combines a moderate number of bridges and a moderate interface strength leads to an optimum crack growth resistance. It is worth noting that the largest crack growth toughness value ($9 \text{ MPa}\cdot\text{m}^{1/2}$) is obtained with the addition of bridges and cannot be reached with an increase of the nominal interface strength alone. The more complex case would be to combine high values for all three properties. In that case, a compromise must be found. For example, a microstructure with $N_b=9$ and $\Sigma_i \approx 400 \text{ MPa}$ leads to reasonable values for strength, crack initiation toughness and crack growth toughness (Fig. 4.9c). The few experimental works available in the literature are qualitatively consistent with the presented property maps. For example, Bouville et al. [2014b] nacre-like alumina without nanobridges exhibits a strength comparable to alumina but a very low toughness. In accordance with the property maps, Bouville et al. have shown that the bridges at the interface are essential to reach a high toughness with a low interface strength and Pelissari et al. have shown that the material could be further improved by using a stronger interfaces Pelissari et al. [2017].

4.6 Conclusions

The interface that connects tablets plays an essential role in enhancing the mechanical performance of BM materials made of brittle constituents. In this study, we examined the effect of interface reinforcement on both strength and toughness using DEM simulations, we also proved the efficiency of DEM to reproduce important reinforcement mechanisms (microcracking and crack deflection).

The interface was reinforced using two different methods: either in a homogeneous manner, by an increase of its nominal strength, or by the addition of nano-bridges to the interface. At low interface strength, the un-notched samples were broken by tablets pull-out, whereas for high interface strength, samples were broken following a straight crack. Both reinforcements— increase of interface strength or addition of bridges—resulted in an increase of the overall strength until it reaches an asymptotic value which is in good accordance with analytic or numeric results at the scale of a single RVE [Barthelat, 2014; Radi et al., 2019a].

We distinguished two toughness parameters: crack initiation toughness and crack growth toughness. We showed that the increase of interface strength increases crack initiation toughness until reaching a maximum value. On the other hand, the increase of

the density of alumina nano-bridges improves the crack initiation toughness value [Bouville et al., 2014b; Naglieri et al., 2015] but only to decay after an optimum number of bridges. This result is consistent with the literature [Grossman et al., 2018].

By studying the crack growth toughness, we demonstrate the important role of microcracking and crack deviation in increasing the crack growth toughness. An optimum value of crack growth toughness can be reached by adjusting the interface strength to $\Sigma_i = 0.1\Sigma_t$. This strength ratio is higher than the one used in experimental work [Pelissari et al., 2017; Bouville et al., 2014b], which would indicate that there is room for improvement in the design of BM materials made of brittle constituents.

On a more practical level, increasing the interface strength can be managed by changing the composition of the interface material during processing. A bi-layer system consisting of two sapphire substrates separated by an interface can be considered as a good candidate to tune and determine the interface properties experimentally. However, due to the narrow range of the optimum interface strength, the control seems complicated in practice. Controlling the density of alumina nano-bridges at the interface appears to be more feasible.

The model could be enriched to account for residual stresses within the interface, which are suspected to play an important role in the enhancement of mechanical properties of nacre-like ceramics developed by Pelissari et al. [Pelissari et al., 2017]. Beside, an extension to BM microstructures with ductile interfaces (metal or polymer) is possible by considering plastic interactions at the interface, knowing that DEM is also well-suited for tackling plastic deformations [Martin et al., 2003; Martin, 2004].

Our model has demonstrated its ability to capture complex damage and crack propagation within nacre-like ceramics. The use of this approach to model Ceramic Matrix Composites (CMCs), a class of material with only brittle constituents and similar damage and fracture behavior, could be of high interest.

Given the critical role of design for these materials, a question must be answered: do conclusions based on simulations of ideal microstructures apply to real materials? To answer this question, our next work will consist of making our model more realistic by taking into account randomness and initial defects of the material. This can be achieved by coupling EBSD micro-graphs of nacre-like alumina with DEM.

Chapter 5

Towards more realistic microstructures

Contents

3.1	Introduction	51
3.2	Modeling of a continuous material with DEM	54
3.2.1	Microscopic beam model	54
3.2.2	Fracture criterion	55
3.2.3	DEM simulations	57
3.2.4	Sample generation	58
3.2.5	Elasticity and strength calibration	58
3.3	Modeling a brick and mortar material	62
3.3.1	Representative Volume Element (RVE)	62
3.3.2	Homogenization procedure	63
3.3.3	Convergence study	64
3.4	Comparison with analytical models	65
3.4.1	Elastic modulus	65
3.4.2	RVE failure	68
3.5	Application to nacre-like alumina	72
3.6	Conclusions	75

5.1 Introduction

Using different fabrication techniques (Chapter 2), scientists succeeded in developing nacre-like materials that provide very promising mechanical properties. However, the resulting microstructures are not as perfect as the materials produced by nature and exhibit a significant randomness and defects compared to natural nacre (Fig.5.1). Well aligned periodic materials can be produced only at larger length scales in architectures materials using either manual assembly [Zhu & Barthelat, 2011], 3D printing [Espinosa et al., 2011; Yadav et al., 2018] or laser engraving [Chintapalli et al., 2014].

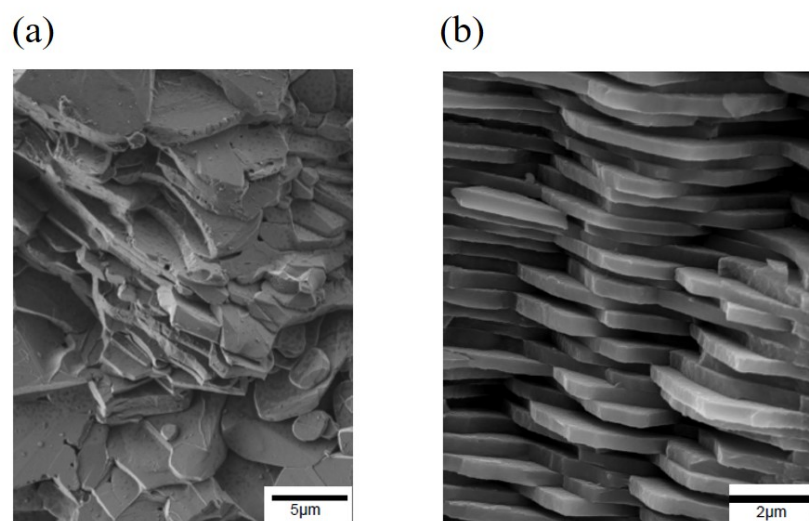


Figure 5.1: SEM micrographs of a) synthetic alumina-nacre and b) natural nacre. (add ref hassan)

Most of the studies conducted on nacre-like materials showed that introducing microstructural variations degrades both strength [Abid et al., 2018] and toughness [William Pro et al., 2015]. Nevertheless, it has been shown that in some configurations, microstructural variations were beneficial. For example, in ductile crack growth, a non-uniform distribution of obstacles leads to higher toughness than when the obstacles are equally distributed [Needleman & Tvergaard, 1991]. For nacre-like materials, a recent study also suggests that some random variations in the microstructure can improve toughness [Abid et al., 2019]. All the studies conducted before were focused on materials with ductile interfaces and the only microstructural variations considered were the overlap and some of the interface properties. Also, most of those models consider that the tablets are rigid, which is a questionable hypothesis in the case of low interface/tablet modulus ratio.

In previous chapters (Chapter 3 and 4), only BM microstructures with a fixed and uniform overlap ratio ($k = 0.25$) were evaluated. In this chapter, more realistic microstructures are considered. First, the effect of the overlap distribution combined with the variation of interface strength on tensile strength, crack propagation and toughness is studied. The results are then compared to the simulations with a uniform overlap distribution conducted in the previous chapter (Chapter 4). Second, a new method is introduced that allows the modeling of more complex/real morphologies of BM materials. Scanning Electron Microscopy images are used as an input for DEM simulations. Tensile tests are performed on both unnotched and single edge notched samples, the simulated behavior is compared to the results obtained using ideal microstructures.

5.2 Effect of a random overlap distribution

5.2.1 Simulation conditions

To evaluate the effect of the overlap aspect ratio ($\rho_0 = \frac{L_0}{t_t}$) distribution, three numerical DEM samples with different overlap distributions are evaluated. A similar method was used by [Abid et al., 2019]. The first step consists of generating three sets of images with different overlap distributions $\frac{\Delta\rho_0}{\tilde{\rho}_0}$, with $\Delta\rho_0$ the standard deviation and $\tilde{\rho}_0$ is the average overlap aspect ratio. Note that the tablet aspect ratio rho is fixed, and the variation of ρ_0 was obtained by varying the overlap ratio k . In comparison to the uniform overlap (Fig. 5.2), the distribution of the vertical interfaces in the non-uniform overlap distributions (the three images at the bottom) is random with a specific standard deviation. The effect of the overlap distribution was investigated from 0 to 0.225, which is in the range of the standard deviations measured on natural nacre [Rabiei et al., 2010]. However, the standard deviations measured in synthetic materials are much higher and difficult to quantify [Bai et al., 2016].

The preparation route of the discrete packings consist of three major steps [Radi et al., 2019a]; first, a random gas of approximately one million monomodal ($\pm 5\%$) particles is generated, with no initial contact between the particles. The gas is afterwards densified from a density of 0.3 to 0.5 by moving inwards the simulation box isostatically. An affine displacement is then imposed to reach a density of 0.65. Note that the density used here is not the material's density, it is the packing density, which is the ratio of the particles and the simulation box volumes. After densification, geometric bonds are added to connect the particles, the average number of contacts per particle is about 6.40. Once the packing is prepared, it is combined with the image generated previously to produce the DEM samples used in this study. Note that all the samples are periodic in the tablet's direction (x axis)

and in the plane direction (z axis) but not in the y axis direction. The microstructural parameters and mechanical properties used in our simulations are summarized in Chapter 3.

<p>Uniform overlap</p> $\frac{\Delta\rho_0}{\widetilde{\rho}_0} = 0$	
<p>Non-uniform overlap</p> $\frac{\Delta\rho_0}{\widetilde{\rho}_0} = 0.025$	
<p>Non-uniform overlap</p> $\frac{\Delta\rho_0}{\widetilde{\rho}_0} = 0.125$	
<p>Non-uniform overlap</p> $\frac{\Delta\rho_0}{\widetilde{\rho}_0} = 0.225$	

Figure 5.2: The four images used in our simulations. The top one is a uniform overlap. Three other overlap distributions $\frac{\Delta\rho_0}{\widetilde{\rho}_0}$ were tested.

5.2.2 Tensile tests

To study the effect of $\frac{\Delta\rho_0}{\widetilde{\rho}_0}$ on tensile strength, quasi-static uniaxial loadings were applied along the tablets on the three non-uniform overlap distributions microstructures. Both the effects of the overlap aspect distribution and the interface mechanical properties (i.e strength) were investigated. The interface strength Σ_i is varied from $\frac{1}{40}\Sigma_t$ to $\frac{1}{5}\Sigma_t$, with $\Sigma_t = 4$ GPa the tablet strength. Only one simulation per set of parameters is presented here. However, to evaluate dispersion of our results, five simulations were conducted for a given case and the dispersion was less than 10% (Fig. 5.3a).

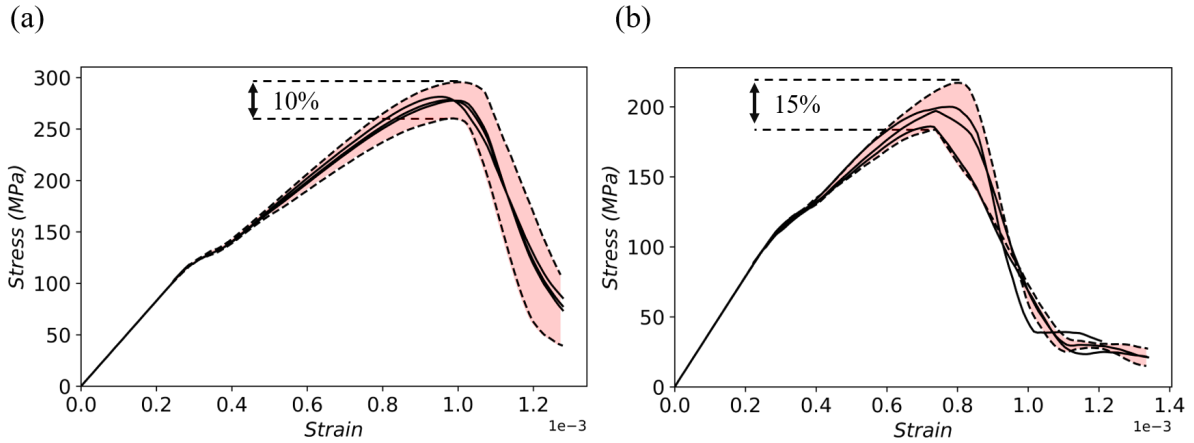


Figure 5.3: Stress-strain curves a given overlap ratio distribution $\frac{\Delta\rho_0}{\tilde{\rho}_0} = 0.025$ showing the dispersion for both a) unnotched and b) notched samples. 5 simulations are reported with plain curves. Dotted curves are mean a) $\pm 5\%$ b) $\pm 7.5\%$.

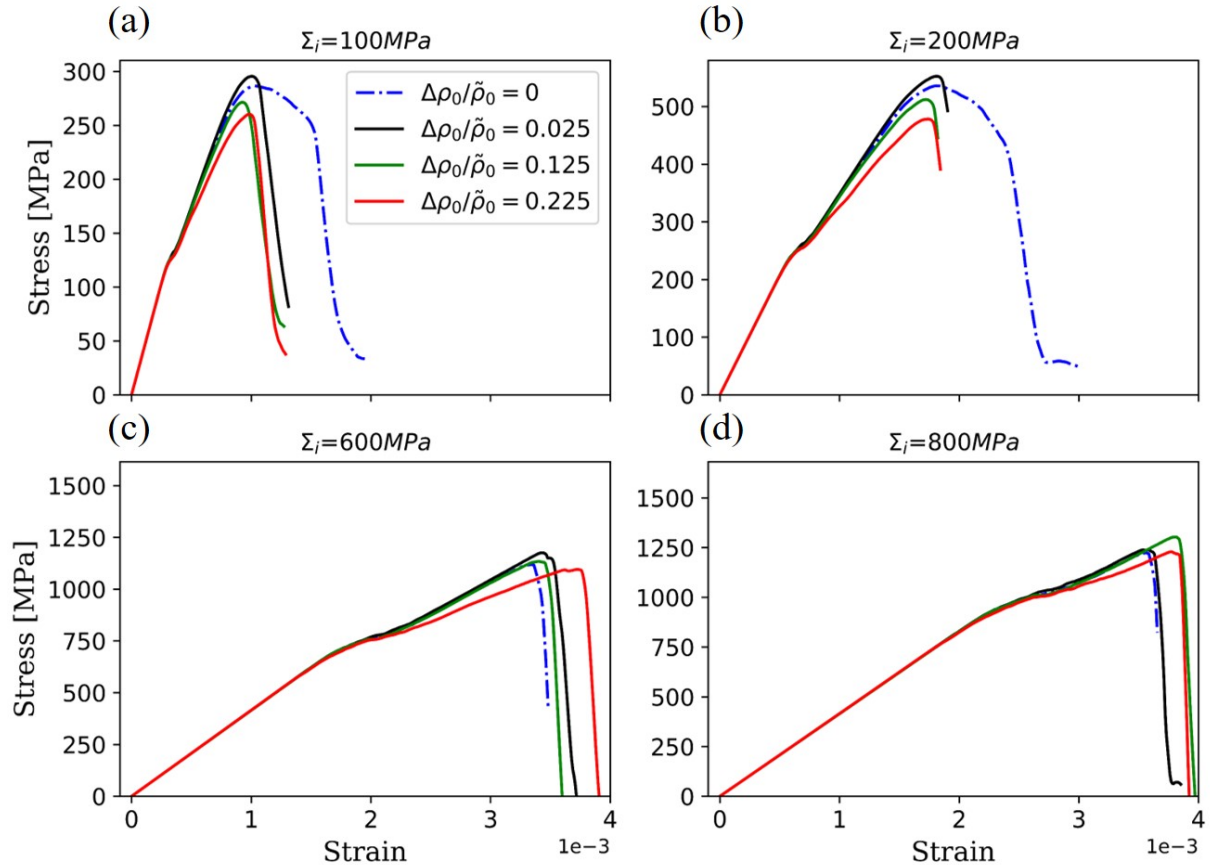


Figure 5.4: Stress-strain plots of the three non-uniform overlap distributions for four different interfaces. All the plots are compared to the uniform overlap distribution tested in the previous chapter ($\frac{\Delta\rho_0}{\tilde{\rho}_0} = 0$).

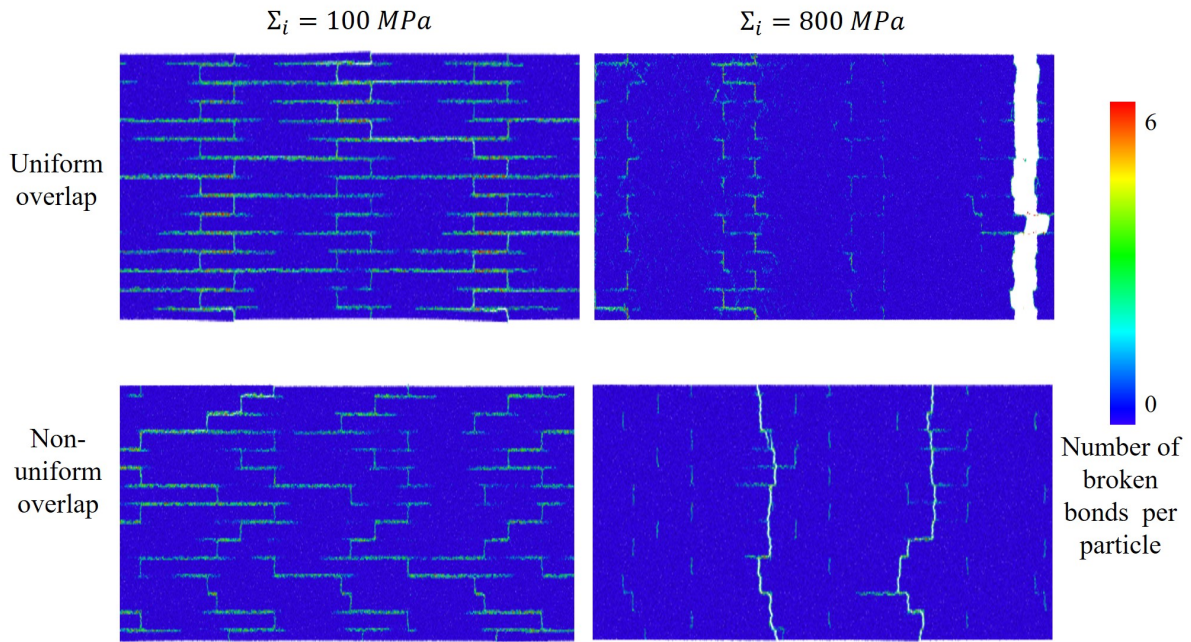


Figure 5.5: Snapshots of the tensile tests performed on uniform and non-uniform overlap distributions for two values of interface strength. The images are taken at after the maximum stress. The color bar indicates the number of broken contacts per particle.

Figure 5.4 shows the mechanical response of the tested samples in terms of stress versus strain. By comparing the non-uniform and the uniform overlap distributions at a high interface strength (Fig.5.4.c and d), we can see that the overlap distribution does not have a significant effect on the shape of the curves or on the cracks formation (Fig.5.5). Vertical interfaces break first in both uniform and non-uniform overlap distributions before the whole sample fails brutally.

At a lower interface strength (Fig.5.4.a and b) we notice that the slight deviation that occurs after the elastic part and which characterizes the initiation of damage, occurs at the same deformation level. Also, the stress-strain curve of the uniform overlap distribution is larger and the damage propagation is more stable. By inspecting the image from the uniform overlap distribution that was taken at the end of the simulation (Fig. 5.5), we can notice that cracks are evenly distributed in the sample which might explain the larger deformation in the x axis direction comparing to other overlap distributions.

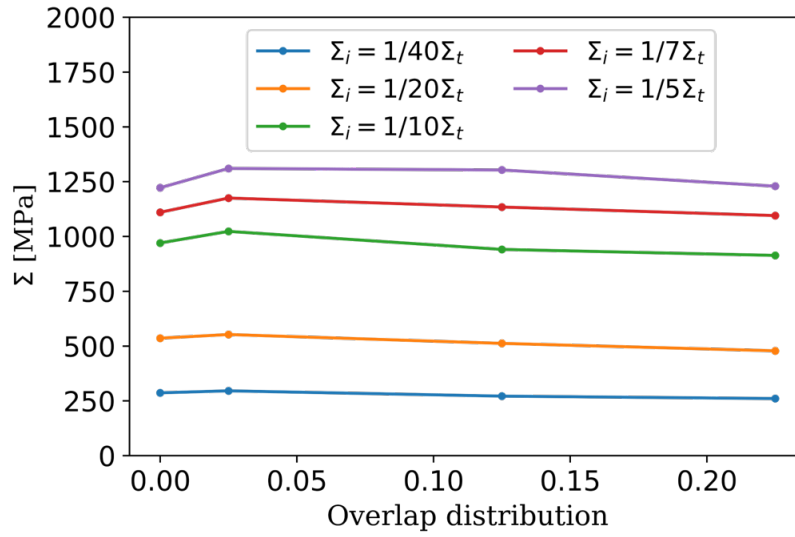


Figure 5.6: Strength versus overlap distributions of the different interface strength values.

Figure 5.6 shows the macroscopic strength versus the overlap distributions for different interface strength values. Here we can see that the macroscopic strength increases as expected with the interface strength for all distributions of the overlap. Moreover, the amount of overlap distribution does not heavily affect the macroscopic strength in these kinds of microstructures, the strength variation for a given interface strength was less than 20%. It is however observed that a small overlap distribution can increase the strength slightly. This effect is more pronounced for the largest interface strength. However, the variation is close to the estimated error bar and is thus not considered as statistically significant.

5.2.3 Single Edge Notched Tension (SENT) tests

The samples tested in this section are all notched and the notch a is $2\ \mu\text{m}$ long (we recall that the sample's length is $57\ \mu\text{m}$ and its thickness is $9\ \mu\text{m}$). Uniaxial loading was applied under the same conditions as in the previous section. The resulting stress-strain curves are presented in Figure 5.7. To evaluate the dispersion of our results, five simulations were conducted for a given case and the dispersion was less than 15% (Fig. 5.3 b). By comparing the maximum stresses of the different overlap distributions along with the interface strength, it is noticeable that the value of the maximum stress decreases with the increase of the overlap distribution value. In other words, increasing the randomness of the overlap position results in a decrease of the maximum stress. As for the shape of the curves, the curves are quite similar (Fig. 5.7), the stairway pattern noticed on some of the curves is due to tablet pullout during crack propagation.

Fig. 5.7 shows a comparison of stress-strain curves between uniform and non-uniform overlaps along with the damage (number of broken bonds and snapshot) for two chosen interface strength (200 and 800 MPa). By comparing Figures 5.8 a and 5.8 b, a few differences can be noticed between uniform and non-uniform overlap distributions. For the uniform overlap distribution (Fig.5.8 a), the stress-strain curve is slightly wider, in other words, the failure is extended on larger strain, which means that the material failure is slightly less catastrophic than the non-uniform distribution (Fig.5.8 b). This could be confirmed by inspecting the attached images. The snapshots are taken after the maximum stress to show the final shape of the main crack and the damage around it. The microcracks in the first image are distributed homogeneously and the main crack is deviated by almost a 90 degrees angle, while in the non-uniform distribution, the main crack is only deviated by approximately 45 degrees. As for higher interface strength, the amount of the stiff material increases and the crack propagates in an approximately straight manner in both overlap distributions.

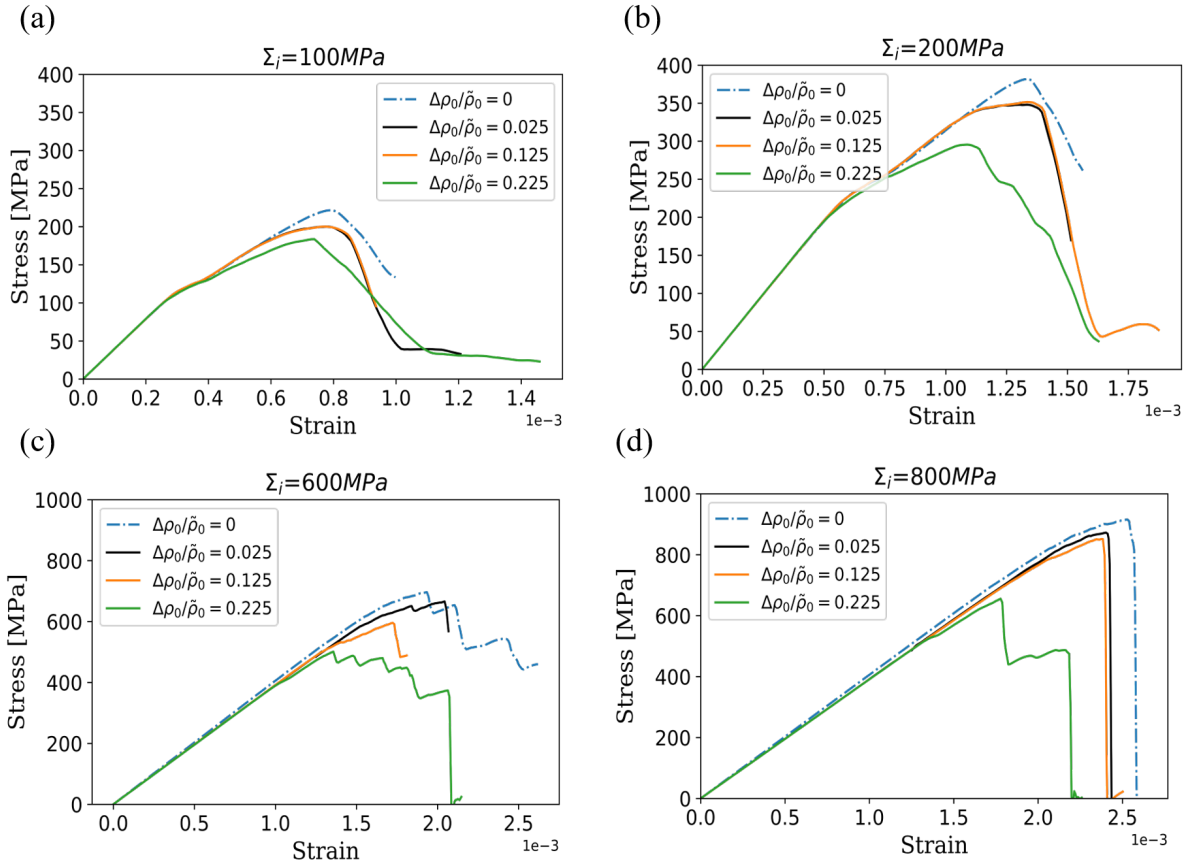


Figure 5.7: Stress-strain curves of single edge notch tests performed on the different overlap aspect ratio distribution samples. Four interface strength values are shown here.

In the previous chapter (Chapter 4), we studied the reinforcement mechanisms of BM materials and showed that breaking the interface or the tablet has an important effect on fracture. In Figure 5.8 the amount of broken bonds during tensile tests is also plotted along with the axial stress and strain. After the elastic part of the curves, the first broken bonds are the interface bonds, this is noticed in all samples regardless of their interface strength or overlap ratio distribution (Fig.5.8). For $\Sigma_i = \frac{1}{20}\Sigma_t = 200$ MPa, and at fracture initiation, indicated by the slight deviation on the stress-strain curve (Fig.5.8 a,b), mainly vertical interfaces are broken (diffuse damage around the crack tip). A first brutal increase of broken bonds is associated with this damage. Interfaces keep breaking gradually until most of the vertical interfaces fail and the damage spread to horizontal interfaces causing the crack propagation. Note that the vertical interfaces behind the crack tip do not break. Meanwhile, the tablet bonds stay intact. Both configurations are similar except the slightly higher amount of broken bonds in uniform overlap. This pattern is noticed for all interface strength values from $\Sigma_i = \frac{1}{80}\Sigma_t$ to $\Sigma_i = \frac{1}{13}\Sigma_t$. As for high interface strength, where the failure is more brittle (Fig.5.8c,d), less interfaces fail before the crack propagates in a straight manner into the tablets. Before crack propagation, the breakage of interfaces is beneficial because it releases the stress around the notch and delays crack propagation. However, if the the number of broken bonds at the interface is high, the intensity of damage increases and the sample becomes less resistant which leads to an early crack propagation.

To describe toughness, R-curves of the different overlap distributions are plotted in Figure 5.9. Two interface values are presented here to illustrate the two main behaviors, stable crack propagation (Fig. 5.9 a) and fragile behavior (Fig. 5.9 b). As mentioned in the previous chapter, the stairway pattern describes the finite jumps that the crack path takes in the interface. The horizontal sections of the curve correspond to the crack propagation in the vertical interfaces that occurs without increasing the stress, while the vertical sections correspond to crack propagation in horizontal interfaces. The length of each step, is equivalent to a multiple of the tablet thickness. The shape of the curves is similar for all the overlap distributions. The R-curves of the uniform overlap are slightly higher than the non uniform overlap distributions, which accordingly leads to slightly higher toughness as reported in Figure 5.10.

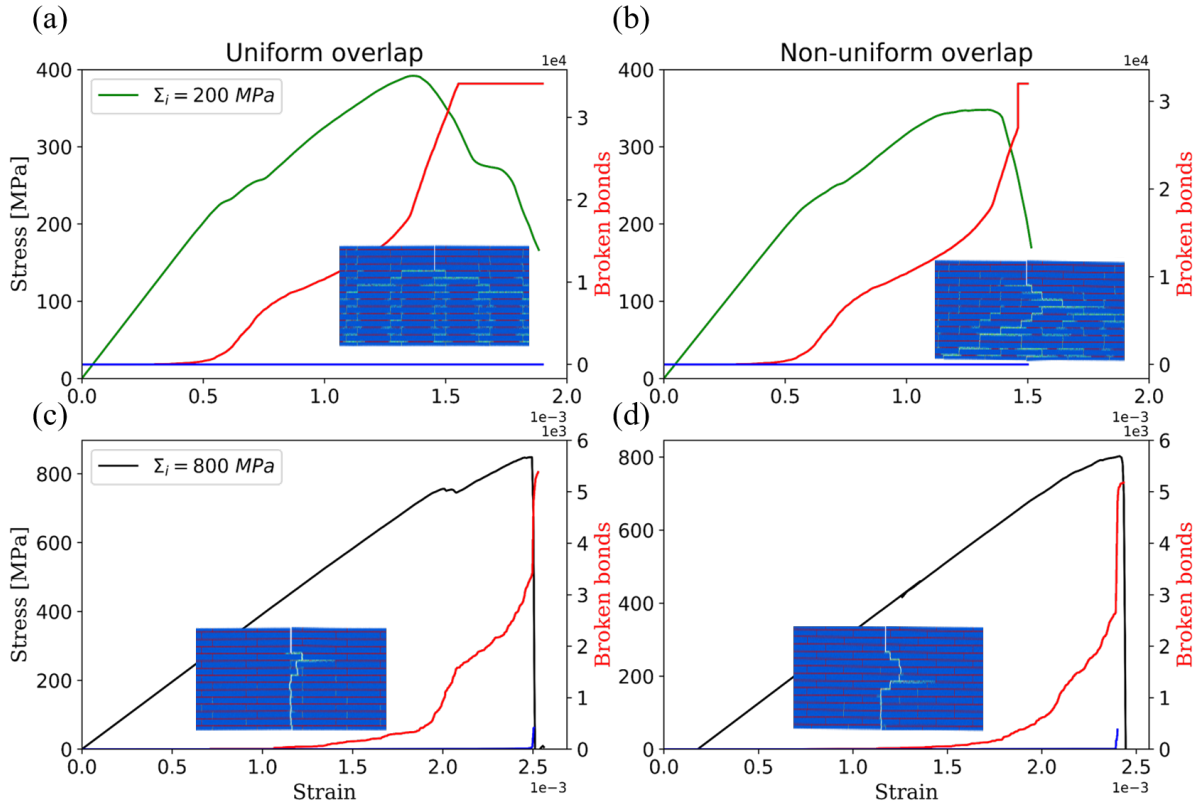


Figure 5.8: Comparison of the samples' final shape after failure for uniform and non-uniform distributions. Both cases of failure are captured here, a,b) stable crack propagation or non-catastrophic failure (green curves) , and c,d) catastrophic failure (black curves). Stress-strain curves are plotted along the number of broken bonds in the interface (red curves) and the tablets (blue curves).

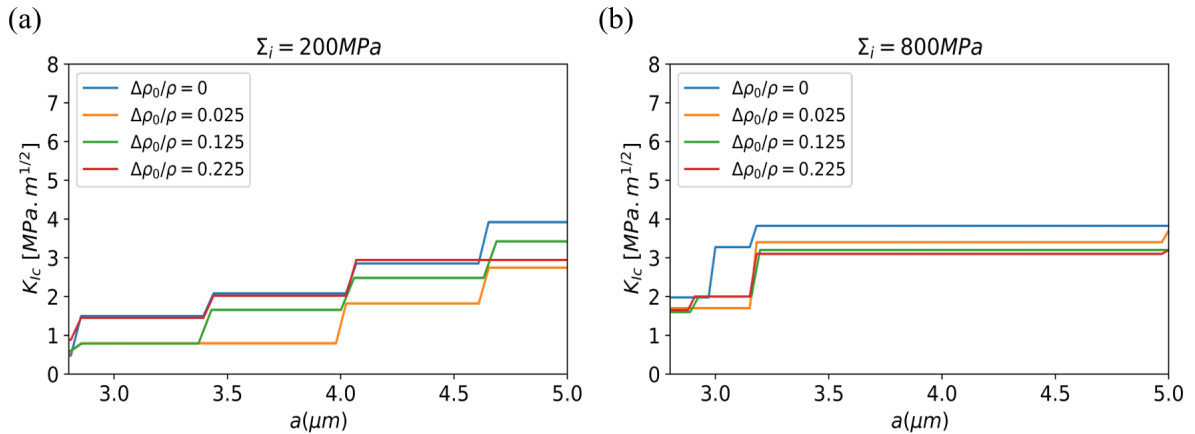


Figure 5.9: R-curve for the four different overlap distributions. Two interface strengths are presented here: a) $\Sigma_i = \frac{1}{20} \Sigma_t$, b) $\Sigma_i = \frac{1}{5} \Sigma_t$.

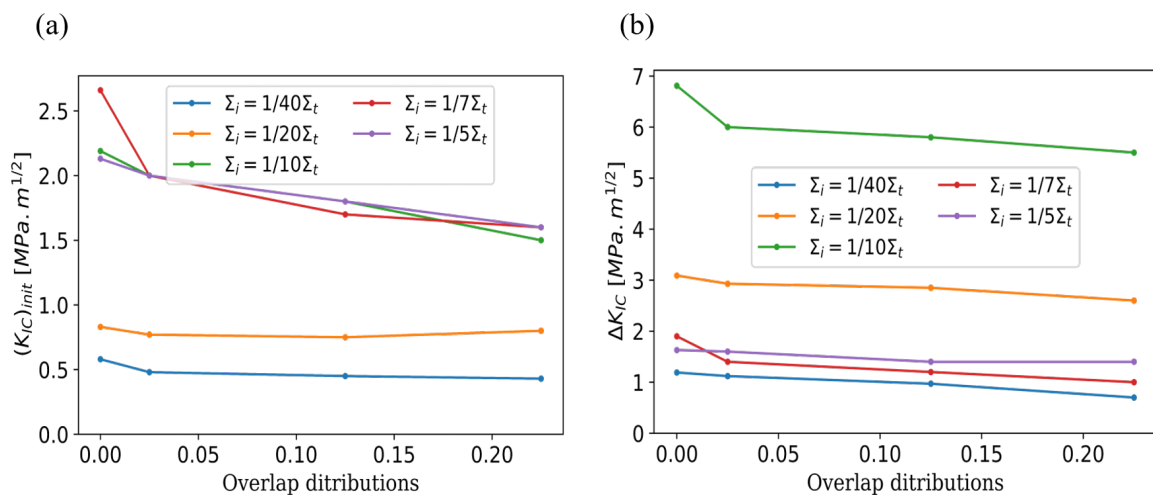


Figure 5.10: Toughness of samples versus overlap aspect ratio distributions for different interface strength values. a) Initiation toughness $(K_{Ic})_{init}$ and b) crack growth toughness ΔK_{Ic} as a function of the interface strength.

In Figure 5.10, both initiation toughness $(K_{Ic})_{init}$ and crack growth toughness ΔK_{Ic} are presented as a function of the overlap distribution. More details about the calculation and R-curve plotting can be found in Chapter 4 and Appendix A. The general trend observed is a decrease of both toughnesses with increasing overlap distribution. The initiation toughness decays up to 26% and crack growth toughness up to 18 %.

5.3 Computation on real microstructures

The preceding section attempted to improve realism in simulations by introducing some deviations in overlap. A natural path to get much closer to real microstructures, is to base our simulations on images taken from actual alumina-nacre microstructures. To obtain alumina-nacre images, we first tried nano-holotomography imaging that was performed at the European Synchrotron Radiation Facility (ESRF) (beamline ID16B). More information on this technique can be found in [Villanova et al., 2014]. The voxel size was of 25 nm giving a field of view of 30 μ m. The images obtained were not usable due to artifacts and the resolution of the images, that made interfaces and tablets not easily recognizable. Another technique that was tried is the Focused Ion Beam milling combined with Scanning Electron Microscopy (FIB-SEM) imaging. The acquisition was performed using a ZEISS NVISION 40, at the Consortium des Moyens Technologiques Communs (CMTC). A 30 KeV ion beam under a normal incidence was used. An important amount of charge effects was noticed which disturbed the sequential slicing and caused the drifting of the ion beam (low efficiency of the milling). The charging effects occurred due to the mate-

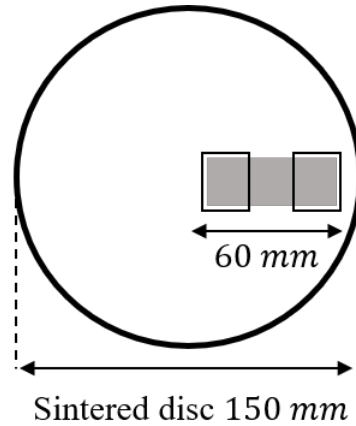


Figure 5.11: Top view of the sintered alumina-nacre disc and the spatial location of the samples.

rial's insulating nature. Due the different problems encountered using the these methods, we decided using Electron Back-scatter Diffraction instead.

5.3.1 Electron Back-Scattered Diffraction (EBSD) protocol

Electron Back-Scattered Diffraction is a scanning electron microscope-based microstructural-characterization technique generally used to study crystalline or polycrystalline materials, to provide information about the structure, crystal orientation, and the phases present in the material. To perform an EBSD analysis, a bar of 60 mm long, 10 mm wide and 10 mm thick was cut from a sintered disc of 150 mm diameter (Fig.5.11). The sides of the specimens were cut to characterize the center of the disc (first black box) and its edge. The obtained sample was 10 mm long, 10 mm wide and 10 mm thick. One of the drawbacks of this method is being a 2D method, however, real 3D DEM (dp3D) modeling of BM materials, if possible, would be very heavy computationally. Consequently, following our previous work on numerically generated microstructures we used the 3D DEM code to perform computation on 2D geometries (pseudo 2D simulations).

The samples are afterwards polished along their thickness face, perpendicularly to the tablets' alignment (area=1 cm) following a two steps polishing procedure. First, the samples are mechanically polished using diamond discs up to 1 μm diamond size. The second step consists of a vibratory polishing using colloidal silica that was applied for 8 hours to reveal the grain boundaries. The final microstructure is presented in Figure 5.12. During polishing some of the small tablets get extracted, which leaves the voids that can be noticed on the images. The main advantage of mechanical polishing compared to ionic milling is that the final surface is much more important. Although the tablets and

interfaces are easily distinguished, we choose to use the index quality map because the binarization was easier.

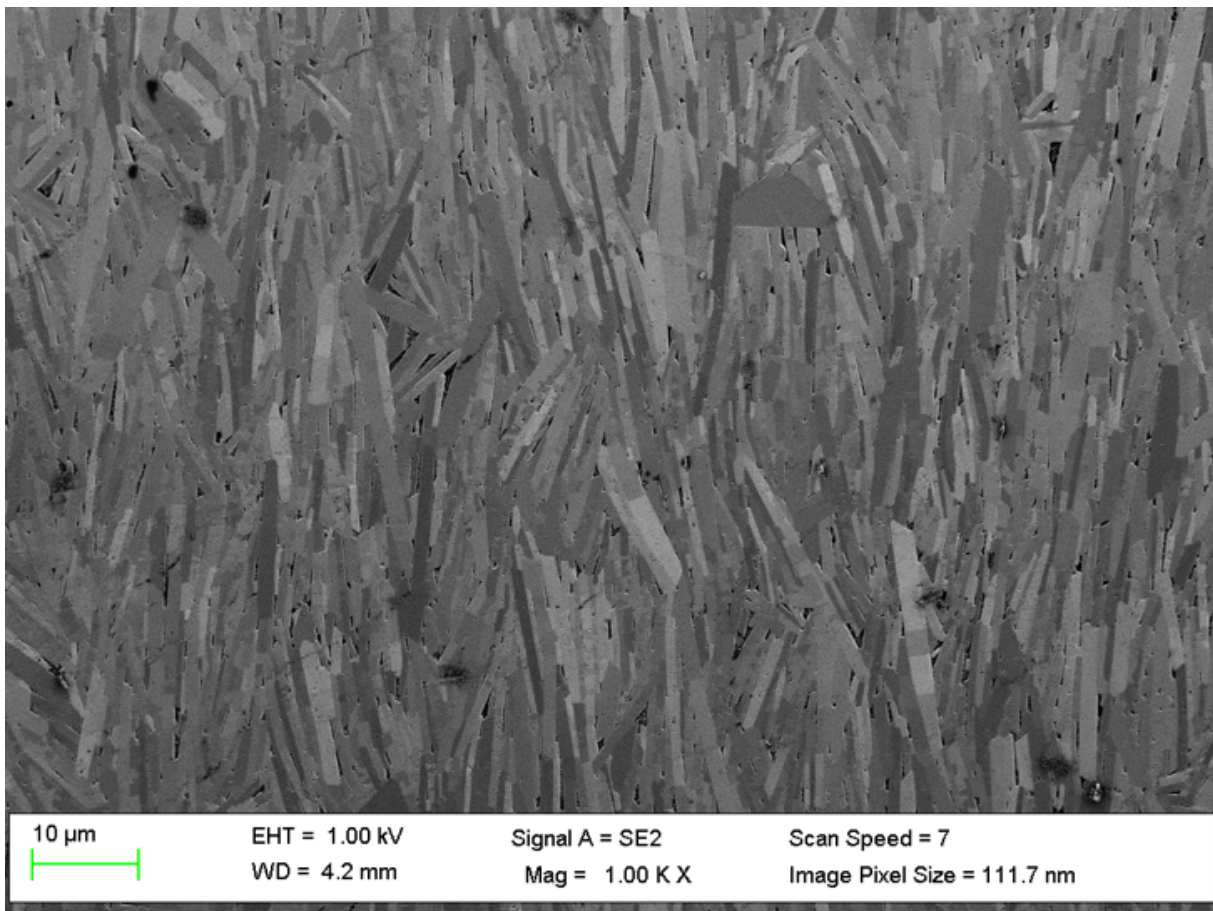


Figure 5.12: A SEM micrograph of the obtained microstructure after the final polishing and before EBSD analysis.

The EBSD acquisition was performed using an Oxford Instruments detector installed in Zeiss Supra 5S SEM microscope at MATEIS laboratory, one of our project partners. During the acquisition, the sample was tilted at 70° to maximize the detection of the diffracted backscattered electrons. An acceleration voltage of 15 Kev and a step size of 80 nm are used for the analysis. In this work we will use the index quality map (Fig.5.13) that displays an excellent contrast between crystalline lamellae (good indexing quality, appears in white to light gray) and interface material (amorphous, no indexing possible, appears in black).

5.3.2 Microstructure analysis

The EBSD image shown in Fig. 5.13 is binarized using a thresholding method. The white refers to the tablets and the black to the interface (Fig.5.14 b). After applying the



Figure 5.13: EBSD analysis of the sample (Index quality map). The image here is rotated compared to the previous figure.

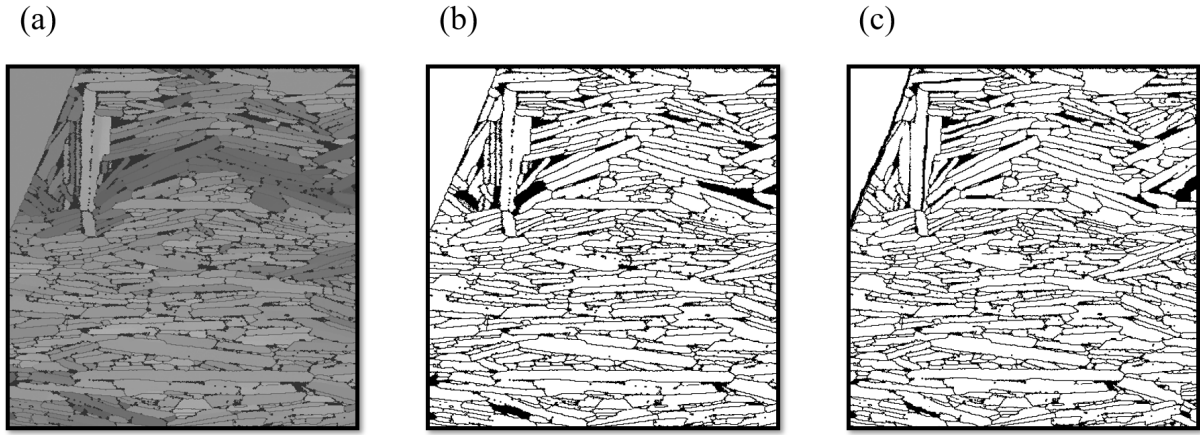


Figure 5.14: An example of image processing. a) Index quality map from EBSD analysis. b) The image after the threshold. c) The final image used with the packing of particles.

	Full image	Microstruc- ture 1	Microstruc- ture 2	Microstruc- ture 3	Microstruc- ture 4
Tablet aspect ratio ρ	13.50	13.48	13.62	13.60	13.52
Tablet volume fraction ϕ	0.851	0.849	0.852	0.851	0.850
Tablet orientation	85 °	87.2 °	83.4 °	83.1 °	86.8 °

Table 5.1: Microstructural parameters issued from the granulometry algorithm for the full image (Fig.5.13) and the sub-images.

threshold, some of the tablets might disappear, that is why a slight manual adjusting is necessary (Fig.5.14 c). Four images with a size of 1053x363 pixels are cut, then duplicated in the z axis direction to create 3D images. To ensure the periodicity of the samples in the x axis direction (along the tablets), a third phase that has a size of 118x363 pixels was added to both edges, the mechanical properties of this phase are the same as the BM material ideal microstructure properties. The final size of each image is 1291x363x8 pixels.

To quantify the microstructural parameters of the images: the tablet's aspect ratio, volume fraction and orientation, we use a granulometry algorithm that was developed by [Boulos et al., 2012]. The microstructure analysis of the whole image (image0) then of each sub-image (image1, image2, image3, image4) reveals the average aspect ratio, the tablet volume fraction $\phi = \frac{t_t}{t_i + t_t}$ and the average tablet orientation along the x axis. The results are summarized in Table. 5.1.

5.3.3 Numerical microstructures from the EBSD image

The three dimensional binarized image is used as a mask on a packing of particles of about 1 million particles, the number of particles was chosen to get at least three particles per interface, the packing of particles has the same aspect ratio as the image used (Section 5.3), with a number of voxels to number of particles ratio of 4. For each particle, the color of the voxel geometrically corresponding to the center defines the material type: tablet or interface. Figure 5.15 shows the four microstructures obtained by combining EBSD images and discrete packings. The samples will be referred to as microstructure 1, 2, 3 and 4, starting from the top of the image. By inspecting the different samples, we can notice the randomness of the tablet aspect ratio, orientation, overlap aspect ratio and the interface thickness.

5.3.4 Macroscopic strength and toughness

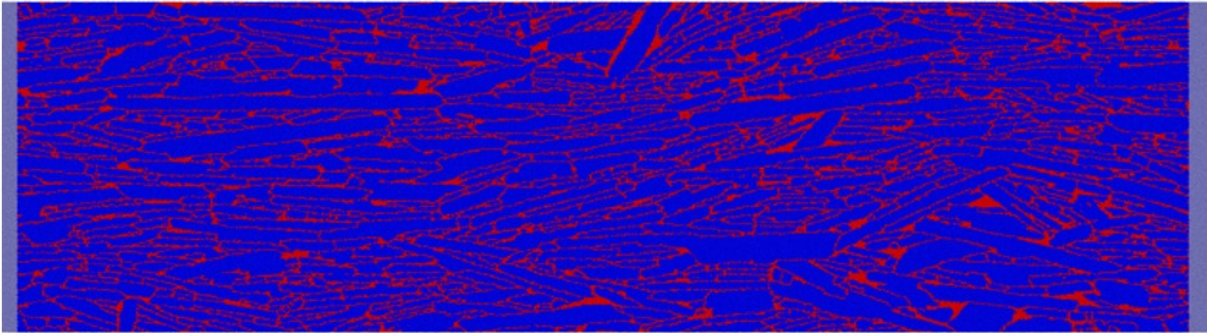
To study the evolution of strength, quasistatic tensile tests under periodic conditions in the x axis direction were applied to the four unnotched samples with varying interface strength. The same tests were performed on notched samples to evaluate toughness.

5.3.4.1 Strength

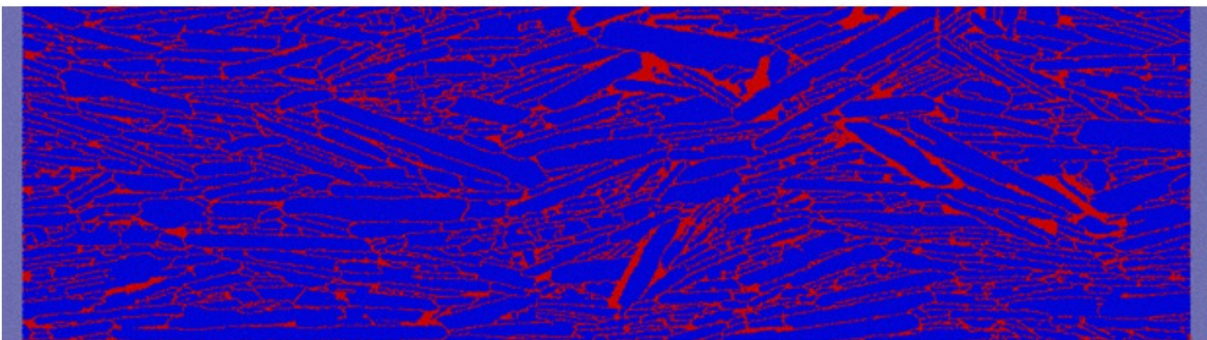
The four samples with different interface strength values Σ_i ($\frac{1}{40} \leq \frac{\Sigma_i}{\Sigma_t} \leq \frac{1}{4}$) were used with a fixed tablet strength $\Sigma_t = 4$ GPa. The macroscopic strength Σ is defined by the maximum value of the stress-strain curves. The stress-strain responses of the tested samples are shown in Fig.5.16. By investigating the curves for a small interface strength ($\leq \frac{1}{10}\Sigma_t$), after the elastic part, the vertical interfaces start to fail. After the maximum value of stress, the curves drop progressively, this is due to the progressive failure of the interface (Fig. 5.17). As for higher interface strengths, the curves show a more brittle failure. The sample breaks into half through a crack that takes the path of the thinner interfaces (Fig. 5.17).

Figure 5.19 is a summary of the preceding curves showing strength as a function of interface strength. While strength increases monotonously and reaches an asymptotic value around $\Sigma_i = \frac{1}{7} \Sigma_t$ in ideal microstructures (Section 5.3.4.2), for real microstructures, the theoretical asymptotic value of $\phi \frac{\Sigma_t}{2}$ is not reached yet for $\Sigma_i = \frac{1}{4} \Sigma_t$. Also, it is interesting to notice that even though the four microstructures are different, we have a similar strength of almost all the interface strengths tested, with an average difference of $\approx 25\%$, except for $\Sigma_i = \frac{1}{40} \Sigma_t$ where the strength is doubled between microstructure1 (maximum value) and microstructure3 (minimum value).

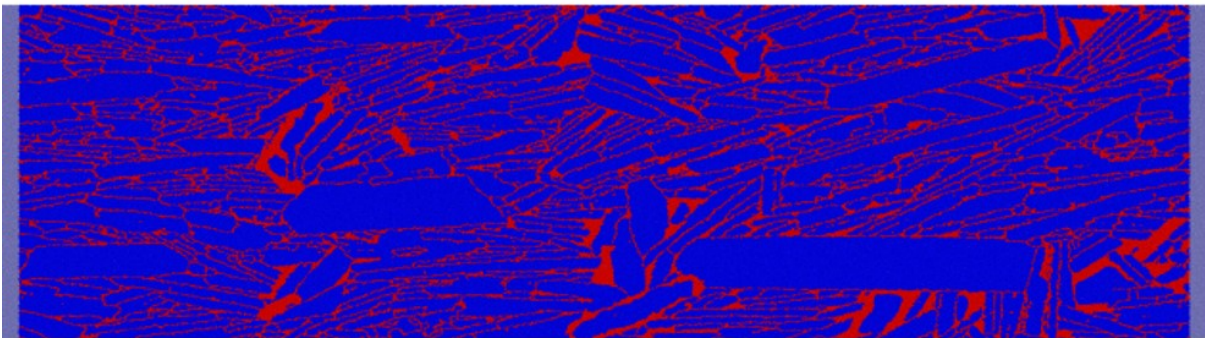
Microstructure 1



Microstructure 2



Microstructure 3



Microstructure 4

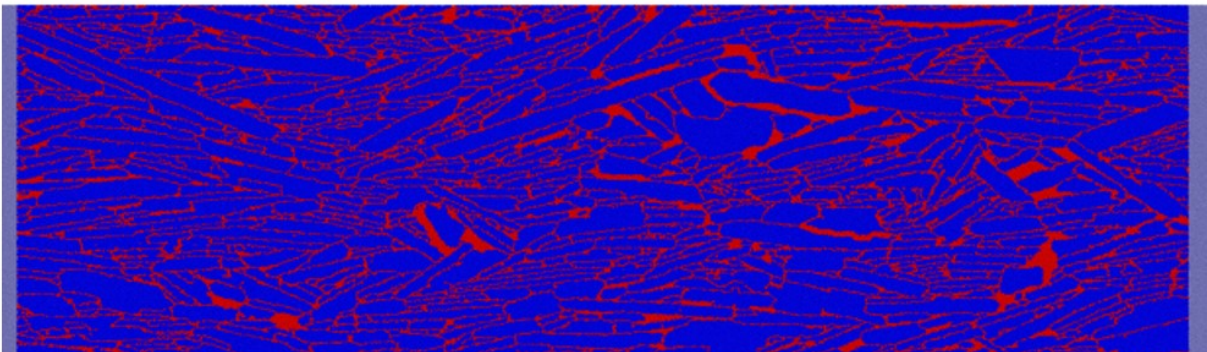


Figure 5.15: Discrete element microstructures from combining EBSD images with discrete element packings.

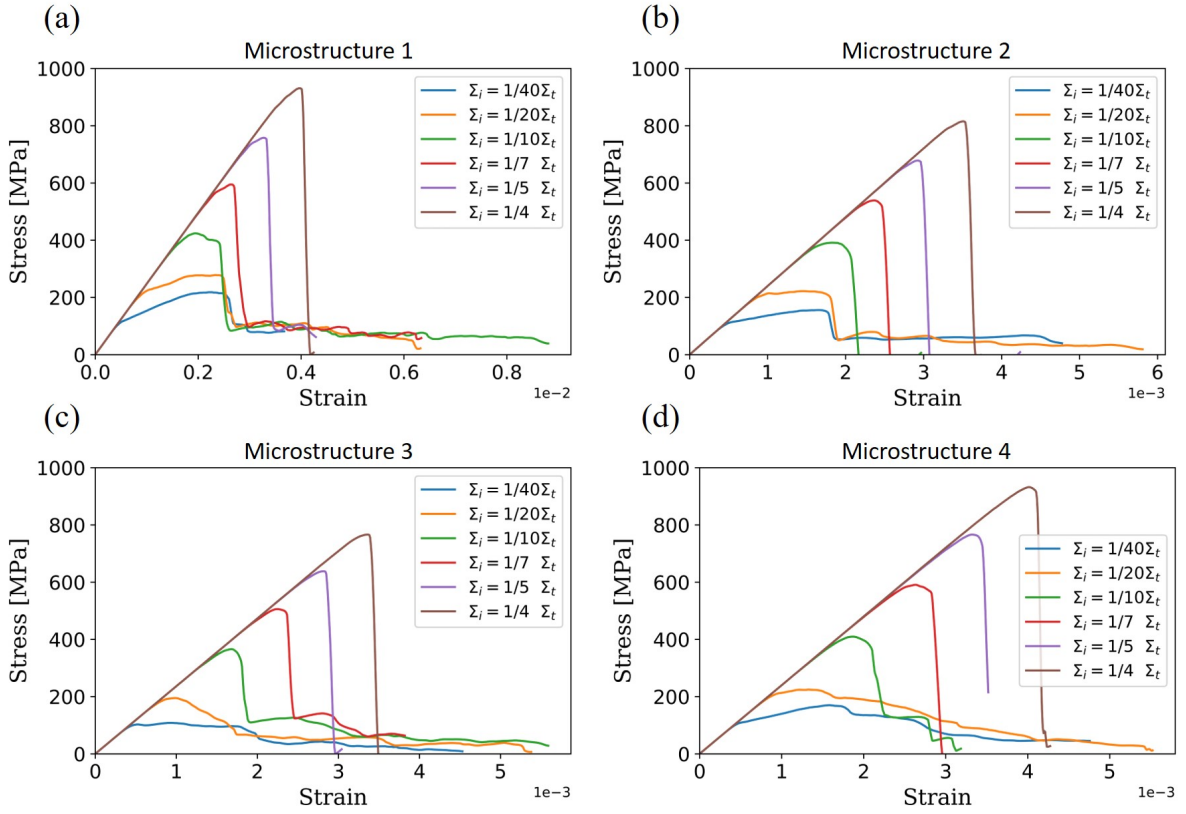


Figure 5.16: Stress-strain curves resulted from tensile tests applied on the four different microstructures.

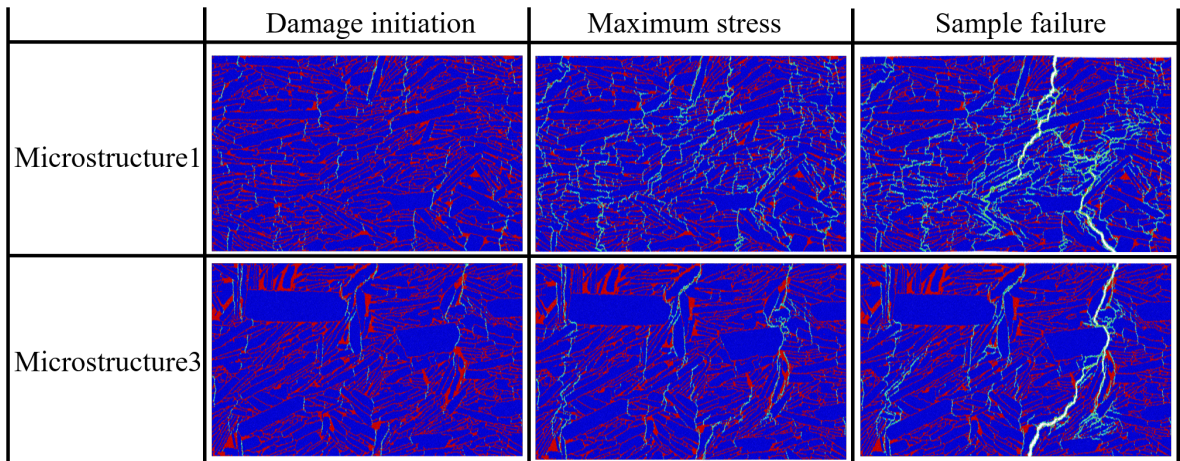


Figure 5.17: Snapshots of the tensile tests performed on microstructure 1 and 3 for a low interface strength ($\Sigma_i = \frac{1}{20} \Sigma_t$).

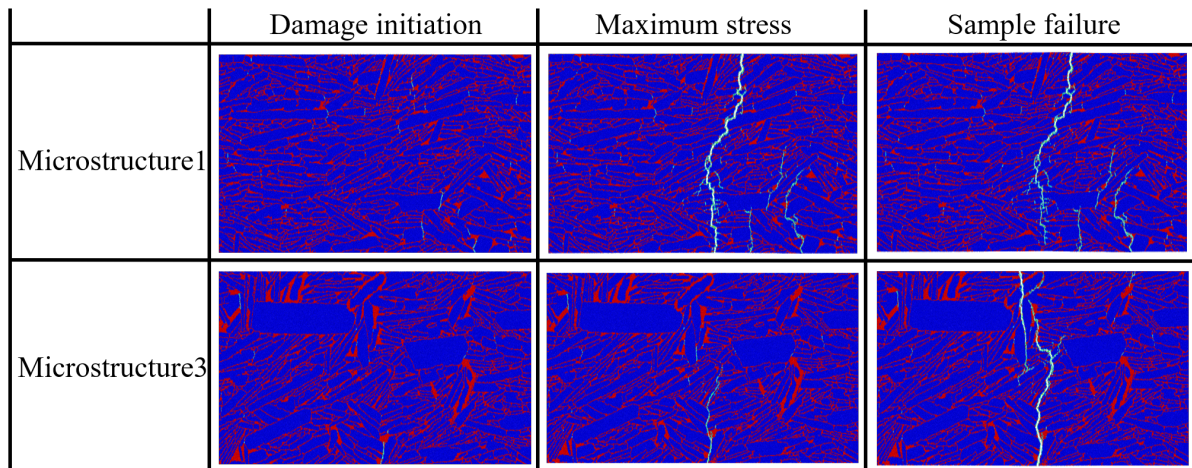


Figure 5.18: Snapshots of the tensile tests performed on microstructure 1 and 3 for a high interface strength ($\Sigma_i = \frac{1}{4} \Sigma_t$).

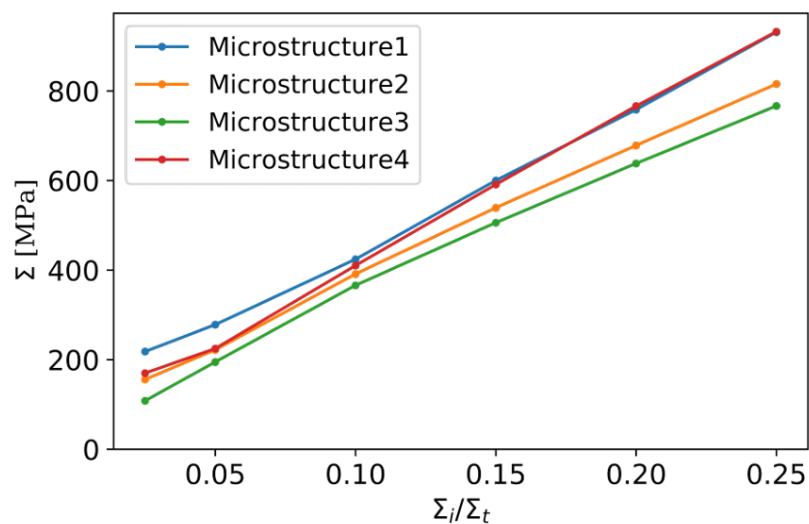


Figure 5.19: Strength of all the tested microstructures for different interface strengths

5.3.4.2 Toughness

The stress-strain evolution before and during crack propagation of the different microstructures is plotted in Figure 5.20. Two types of behaviors are noticed, stable crack propagation and catastrophic failure. The behavior is quite similar to the one observed in ideal microstructures. At lower interface strength (Fig.5.20 a,b,c), an overall non-catastrophic failure is observed. The vertical interfaces fail prior to crack initiation creating microcracking/multiple cracking. However, the deflection noticed on the curves of ideal microstructures that characterizes the vertical interfaces failure is less pronounced

on some microstructures (i.e microstructure2 and 3), this could be explained by the low density of vertical interfaces in this case (Fig.5.15). After reaching the maximum stress, the tablets keep pulling out which is characterized by the bumpy curves at the end of the simulations. Also, one might notice that the maximum stress is higher in microstructures1 and 4 compared to the rest of the microstructures. For higher interface strengths (Fig.5.20 d,f,e), the curves show a fragile behavior for microstructures 1 and 4, but not for microstructures 2 and 3.

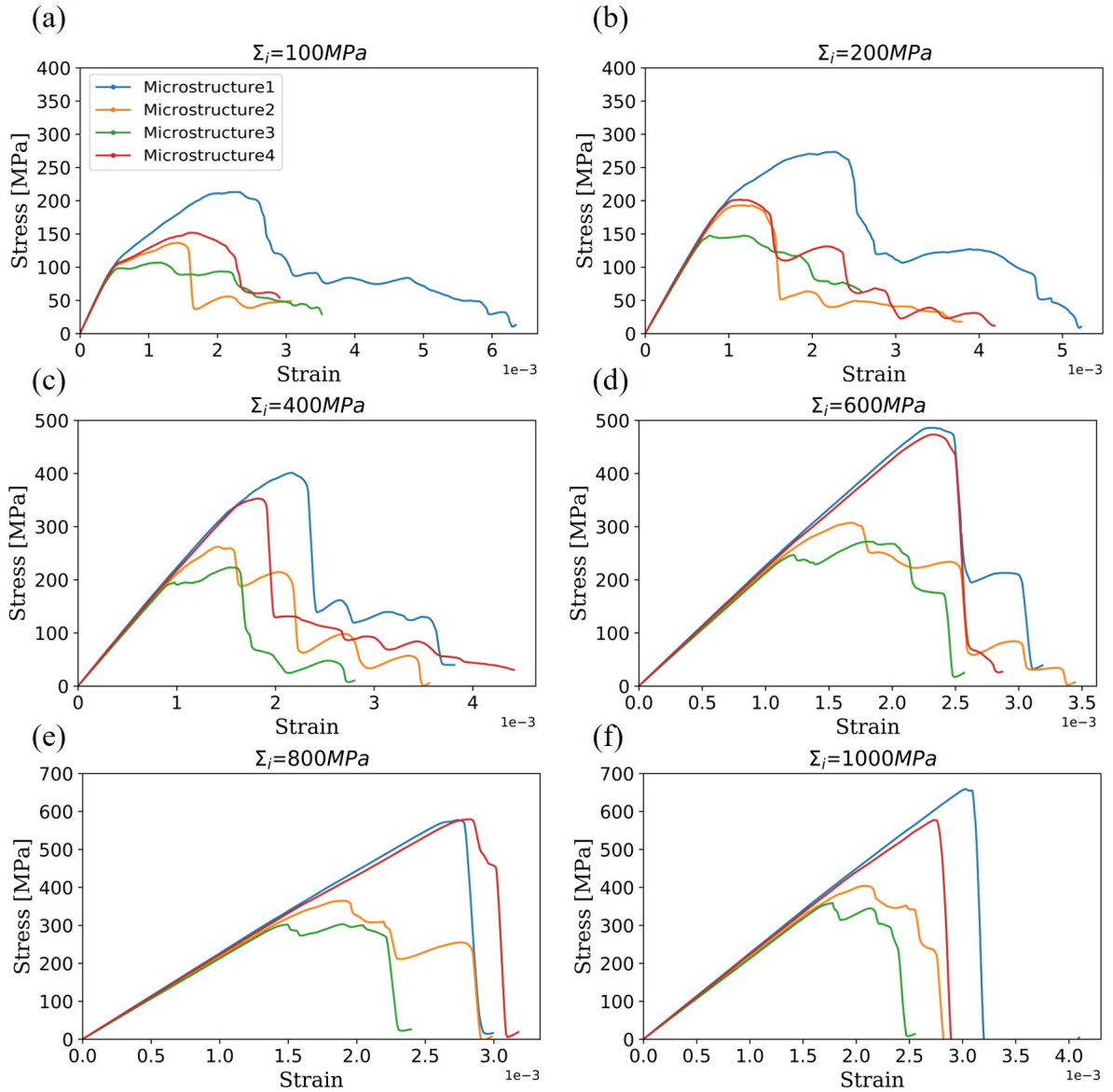


Figure 5.20: Stress-strain plots of single edge notched samples for different interface strength values. a) $\Sigma_i = \frac{1}{40} \Sigma_t$, b) $\Sigma_i = \frac{1}{20} \Sigma_t$, c) $\Sigma_i = \frac{1}{10} \Sigma_t$, d) $\Sigma_i = \frac{1}{7} \Sigma_t$, e) $\Sigma_i = \frac{1}{5} \Sigma_t$, f) $\Sigma_i = \frac{1}{5} \Sigma_t$.

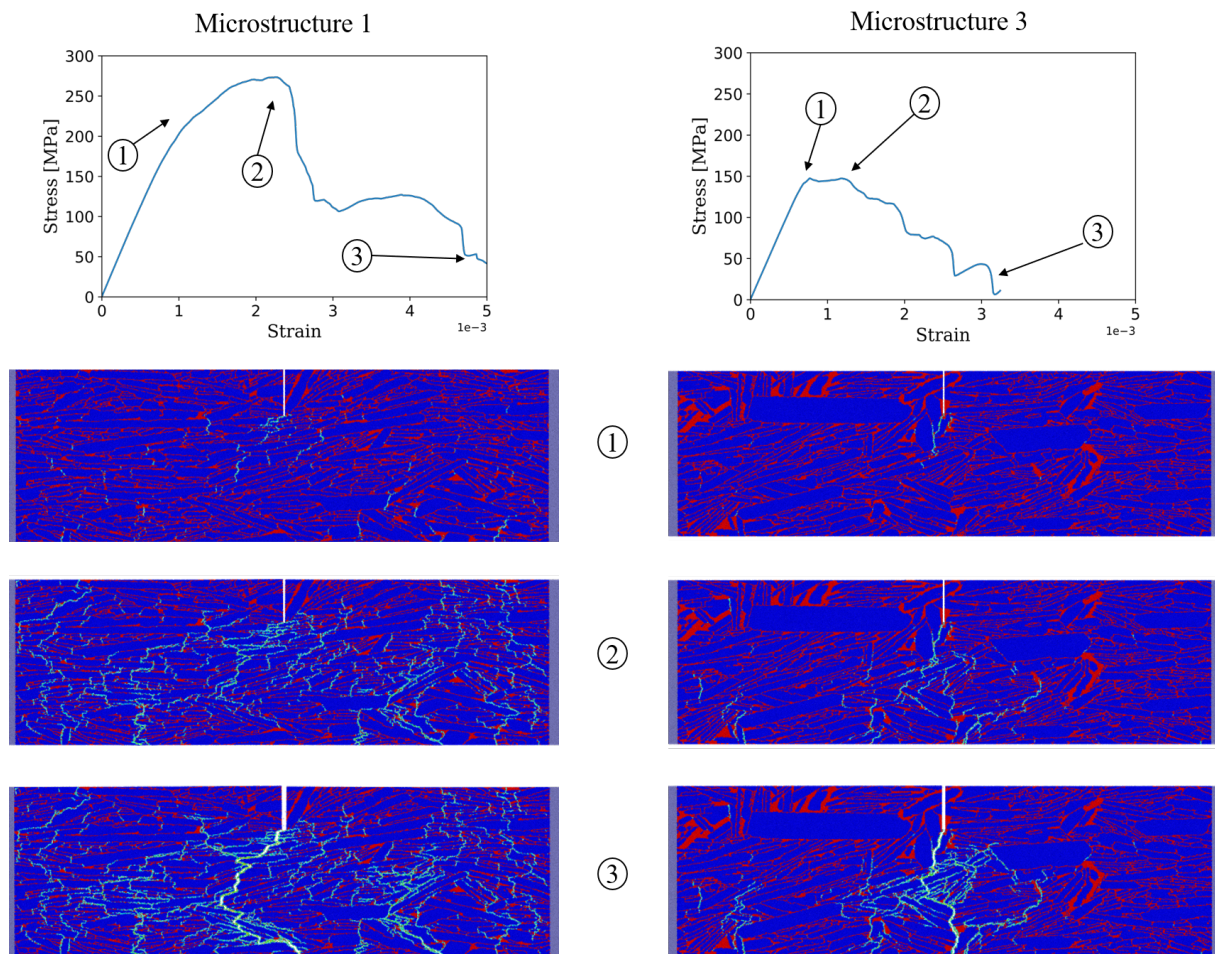


Figure 5.21: Crack propagation illustration in microstructures 1 and 3 for a low interface strength ($\Sigma_i = \frac{1}{20} \Sigma_t = 200$ MPa). Stress-strain curves and snapshots of the three main events during SENT (1) damage initiation, (2) maximum stress and (3) material failure.

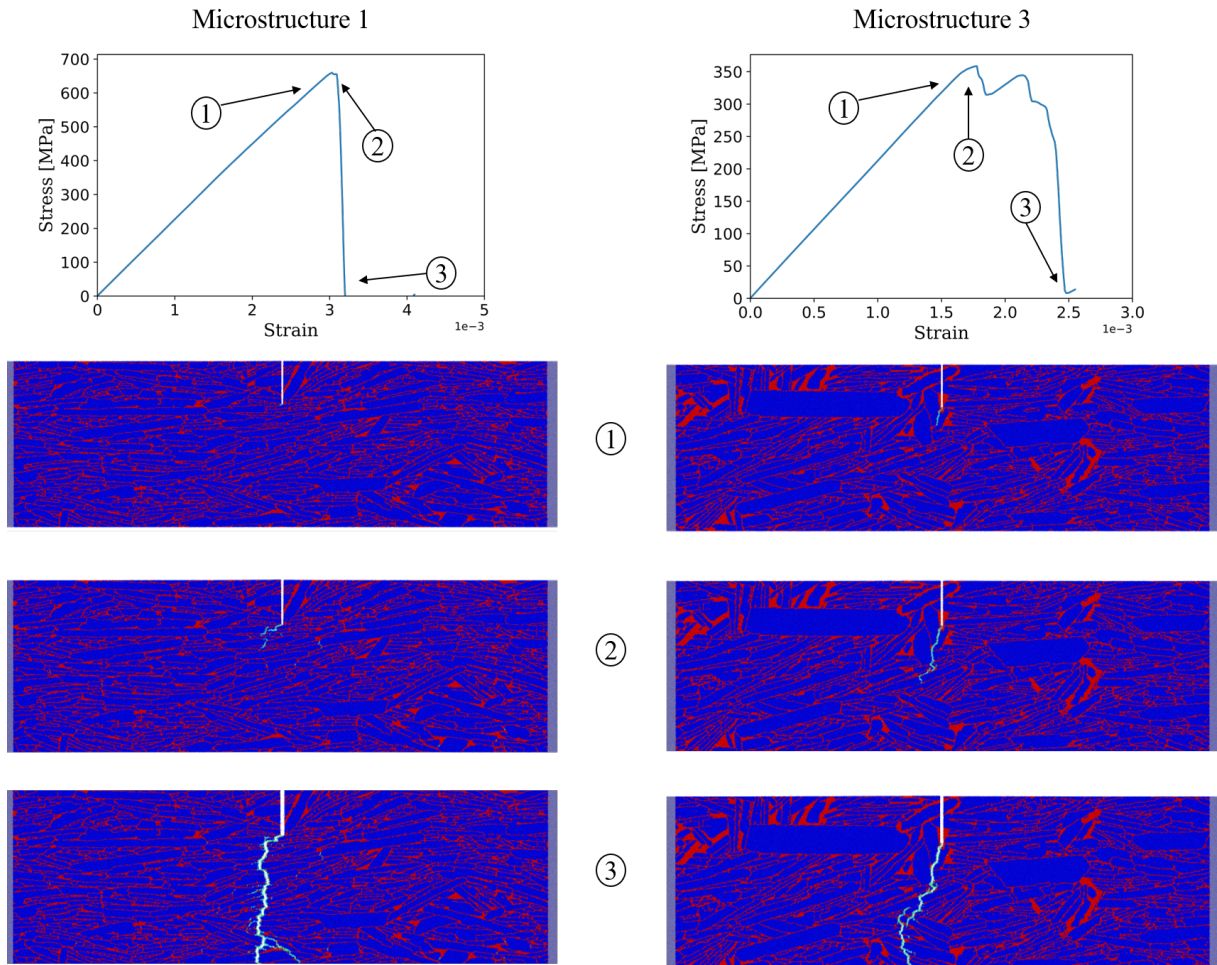


Figure 5.22: Crack propagation illustration in packings 1 and 3 for a high interface strength ($\Sigma_i = \frac{1}{4} \Sigma_t = 1000$ MPa). Stress-strain curves and snapshots of the three main events during SENT (1) damage initiation, (2) stress maximum and (3) material failure.

To understand the influence of the microstructures on crack propagation, we compare the microstructures with the highest and the lowest stresses (microstructure1 and 3). First, for a low interface strength (Fig.5.21) then for a higher interface strength (Fig.5.22). Basically, the same reinforcement mechanisms are noticed as in the ideal microstructures (microstructure0). First, microcracking, which is the breakage of vertical or horizontal interface, participates in stress relaxation at the crack tip. This mechanism helps in preserving reasonable initiation toughness even with weak interfaces. By comparing the microstructures 1 and 3, it is noticeable that more damage/microcracking is present in microstructure1 prior to the crack propagation, while in microstructure3 less interfaces are damaged before crack propagation. This logically leads to a higher initiation toughness for microstructure 1 as observed on the R-curves (Fig. 5.24). We can also notice that damage is, as expected, located in the region of highest mechanical loading, i.e the crack

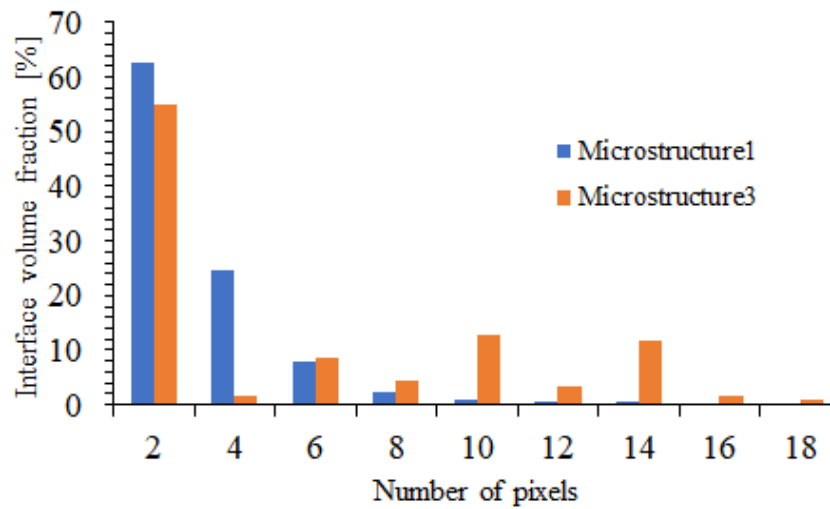


Figure 5.23: Interface volume fraction of the different interfaces thickness for microstructures1 and 3 obtained by a granulometry analysis of the interface phase [Boulos et al., 2012]. The interface thickness is represented by the number of pixels. Here 2 pixels correspond to 100 nm.

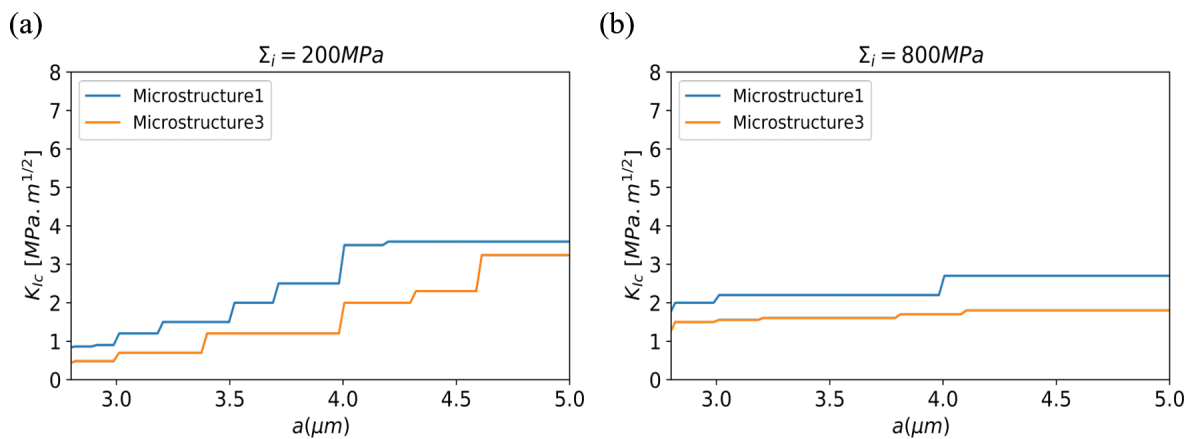


Figure 5.24: Toughness versus crack extension (R-curve) of microstructure1 and 3. a) Low interface strength ($\Sigma_i = \frac{1}{20} \Sigma_t$), b) High interface strength ($\Sigma_i = \frac{1}{5} \Sigma_t$).

tip. It is also interesting to notice that regardless of the interface strength, the order of the maximum stress remains the same (microstructure1 > microstructure4 > microstructure2 > microstructure3). Usually, when the crack starts propagating in the material through the interfaces, it gets deflected when encountering a tablet resulting in a non-straight crack pattern (microstructure1). However, in microstructure3, when the crack passes through the interface, it encounters two non well-oriented tablets that lead to a straighter pattern of the crack. In other words, if the tablet was well-aligned in the x axis direction, the crack would get deviated towards the x axis direction instead of the y axis direction, and would take a less straight pattern, with shorter "steps" on the R-curve (Fig. 5.24). This could explain the lower maximum stress and toughness reached in this microstructure for $\Sigma_i = \frac{1}{20} \Sigma_t = 200$ MPa. The four microstructures have approximately the same tablet volume fraction (± 0.01), however as seen in Fig 5.21, compared to microstructure1, microstructure3 has a less homogeneous distribution of the interface thickness. This could be confirmed by analyzing Figure 5.23. In fact, in microstructure3, a less homogeneous distribution of the interface thickness is noticed and thicker interfaces are present: 10 and 14 pixels which corresponds to 500 nm and 700 nm. Also, the tablets in microstructure1 and 4 have an average orientation of 87° to the y axis, while microstructure2 and 3 have an orientation of 83° (Tab. 5.1). This demonstrates the possible effect of tablet orientation and interface thickness distribution on the overall behavior of this type of microstructures.

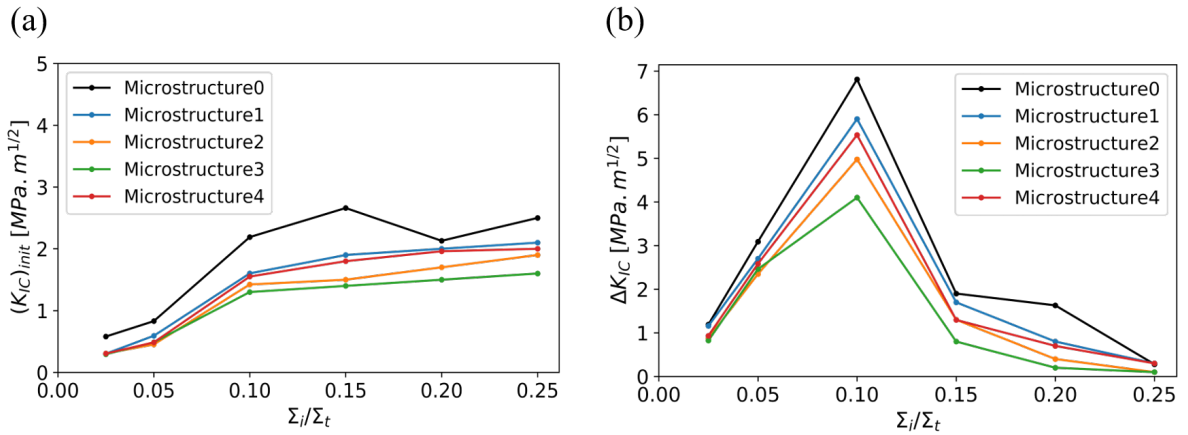


Figure 5.25: Toughness of the four samples with different interface strengths, compared to the ideal microstructure referred to as microstructure0. a) initiation toughness and b) crack growth toughness.

As for higher interface strengths (Fig. 5.22), the stress needed to start the interface failure is much higher. Before crack propagation, less vertical interfaces fail as the interface strength gets higher compared to low interface strength, which leads to less stress

relaxation at the crack tip, resulting in a straight crack that goes through the whole sample including tablets. Reaching a lower stress in microstructure3 could also be explained by the large distribution of interface thickness and the tablet orientation. Note that the aspect ratio and the tablet volume fraction of the four microstructures are similar. The initiation toughness resulted from this configuration is higher but leads to unstable crack propagation. As the interface strength increases, less and less vertical interfaces break. In that case, the stress maximum follows damage initiation very closely.

As a summary, Fig. 5.25 shows the initiation toughness $(K_{Ic})_{init}$ and the crack growth toughness ΔK_{Ic} of the different samples as a function of interface strengths compared to the ideal microstructures (microstructure0, $\phi = 0.87$ and $\rho_0 = 3.5$). Initiation toughness increases in a monotonic manner to reach a maximum value. From microstructure1 to microstructure3, the initiation toughness decreases by about 20%. The ideal microstructure (microstructure0) exhibits a larger $(K_{Ic})_{init}$ (+27%) but within the same range. Thus, it shows that the ideal microstructure, although a rough simplification of the real microstructure, can be used for optimization.

As mentioned in the previous chapter, the crack here propagates in a very small region compared to what is done experimentally, this means that $(K_{Ic})_{max}$ is not quite representative of a typical crack growth toughness. Therefore, $\Delta K_{Ic} = (K_{Ic})_{max} - (K_{Ic})_{init}$ which represents the initial slope of R-curve, is more representative of crack growth toughness. In Figure 5.25 b, crack growth toughness increases to reach an optimum value at $\Sigma_i = \frac{1}{10} \Sigma_t$ and decreases afterwards. It is interesting to notice that the optimum value of crack growth toughness is reached at the same interface strength as the ideal microstructure (microstructure0). Similarly, to initiation toughness, microstructures2 and 3 have lower crack growth toughness values than the rest of the microstructures. By comparing microstructure1 and 3, the crack growth toughness drops by 27%. Due to the size of the samples used here, the resulted values of crack growth toughness from this study should not be compared directly to experimental work where the crack propagation length is 3 microns in this work versus, several hundreds in typical Single Edge Notch Beam tests.

5.4 Conclusion

Microstructural variations have an important role in the BM materials behavior. In the literature, the overlap aspect ratio is presented as a key parameter in the optimization of the mechanical behavior.

Here, we studied the effect of the overlap aspect ratio distribution on strength, initiation toughness and crack growth toughness. Three different overlap distributions were tested and compared to the uniform overlap distribution. For strength, the difference

between the distributions was not very important. However, for toughness, a slight difference in the crack path was noticed, especially for low interface strengths, the crack was less deviated compared to the uniform overlap, which explain the slightly lower crack growth toughness. We also showed how vertical microcracking affects toughness. Although statistical variations were proved to degrade the overall mechanical properties, here we showed that their effect is minor on strength but more pronounced on initiation toughness and crack growth toughness.

More realistic microstructures were tested to extend our model. In this chapter we introduced a new method to study the mechanical behavior of synthetic nacre-like materials by combining EBSD micrographs with Discrete Element simulations. First, we presented the protocol for the images preparation, then the samples were tested for both strength and toughness. The results were then compared to the ideal microstructure. This method allows to perform more accurate tests and closer results to what is done experimentally but, in less time and effort. The simulations presented here provided information unattainable by experiments such as the crack path, the interface strength impact, the tablet orientation and the interface thickness distribution impact on the mechanical behavior of nacre-like materials.

Chapter 6

Nacre-like ceramics: compaction and tablet alignment

Contents

4.1	Introduction	81
4.2	Discrete model for brick-and-mortar materials	84
4.2.1	DEM framework	84
4.2.2	DEM simulations	86
4.2.3	R-curve computation	86
4.3	Effect of global interface reinforcement via nominal strength	87
4.3.1	Macroscopic strength	87
4.3.2	Toughness	88
4.4	Effect of local interface reinforcement by nano-bridges	92
4.4.1	Macroscopic strength	92
4.4.2	Toughness	93
4.5	Discussion	95
4.6	Conclusions	98

6.1 Introduction

The outstanding mechanical properties of nacre are attributed to the highly regular brick and mortar arrangement of the constituent phases which combine the compliance of the organic matrix (proteins such as beta chitin and lustrins) with the strength of the inorganic platelets (aragonite- CaCO_3). Similarly, the possibility to align and organize the tablets in bulk brick and mortar materials offers interesting possibilities for the design and discovery of materials and architectures exhibiting novel functional properties. The quality of the final material, and in particular its mechanical response, depends largely on the quality of the alignment of the constituents as mentioned in Chapter 5.

Several attempts have been described in the literature to manufacture composites with a high degree of tablets alignment using different manufacturing techniques, carrying out HASC (Hot press Assisted Slip Casting), which consists of mixing the components manually and pouring the mixture into a porous mold, within a steel die, then hot pressing the system [Oner Ekiz et al., 2009]. This technique provides good alignment of alumina flakes, however, the interfacial bonding between the two phases still need improvement. Another technique called Magnetically-Assisted Slip Casting (MASC) was used, where magnetic field is used to align alumina tablets. The method shows promising results but due to the complexity of the process, scaling up is not easy [Oner Ekiz et al., 2009; Grossman et al., 2017; Pelissari et al., 2017]. The alignment of the tablets was also proven to have an important effect on the thermal properties of BM materials. Several strategies based on the application of electric [Fujihara et al., 2012] or magnetic field [Lin et al., 2013; Cho et al., 2010] were developed to align the tablets in order to improve thermal properties (i.e thermal diffusivity). A new strategy was developed by Bouville et al., where freezing under flow and field-assisted sintering (FAST) were used to prepare a highly textured alumina [Bouville et al., 2014a]. The principle of that technique was to directionally freeze a well-dispersed flowing system. The system contains elementary building blocks such as anisotropic alumina platelets (with high shape factor), alumina nanoparticles and glass-phase nanoprecursors and to use the ice crystals growth as a driving force for the creation of a long-range order and for the local self-assembly of the particles between the crystals. In their work, they compared two structures, a controlled architecture processed by using ice-templating and a homogeneous composite obtained by simply mixing the components. The first structure revealed a thermal diffusivity almost three times greater than the homogeneous composite. Compared to the other methods mentioned before, ice-templating proved to be comparatively much more efficient. Also, ice-templating is able to align particles in much more concentrated suspensions, almost 20 vol.%, compared to less than 5 vol.% for the other methods. However, while these techniques are well known

and commonly used in the lab scale, their application on an industrial scale remains difficult. To overcome the limitations that come with these techniques especially in terms of sample size and productivity, instead of ice-templating, uniaxial pressing is considered in the BICUIT project, which is a relatively simpler process that can be successfully used for the elaboration of alumina-based samples with a nacre-like microstructure. The main steps of the process are represented in Fig.6.1. First, the aqueous colloidal suspension containing all the precursors is prepared following the protocol described in [Bouville et al., 2014a]. The slurry is then quenched in liquid nitrogen, permitting the freezing of the spatial distribution of the slurry, and leading to a homogeneous solid-state system. The last step consists of the pressure assisted hot sintering of the freeze-dried powder. Most of the tablet's alignment occur at the solid state, before the appearance of the liquid phase formed by the glass-phase precursors.

The role of nano-particles in the high temperature sintering of the composite is fairly understood. However, the role of nano-particles in the alignment of tablets during compaction is unknown. Intuitively, one might expect that their presence may help platelet alignment by hindering the blockage of platelets through arching effects. Here we use DEM simulations to provide some insights on this issue.

First, we will describe the scheme to generate the numerical samples and the model setup. Then, we will compare the orientation of the tablets before and after compaction using two structures: tablets with nano-particles on their surface and tablets without any nano-particles and analyze the differences.

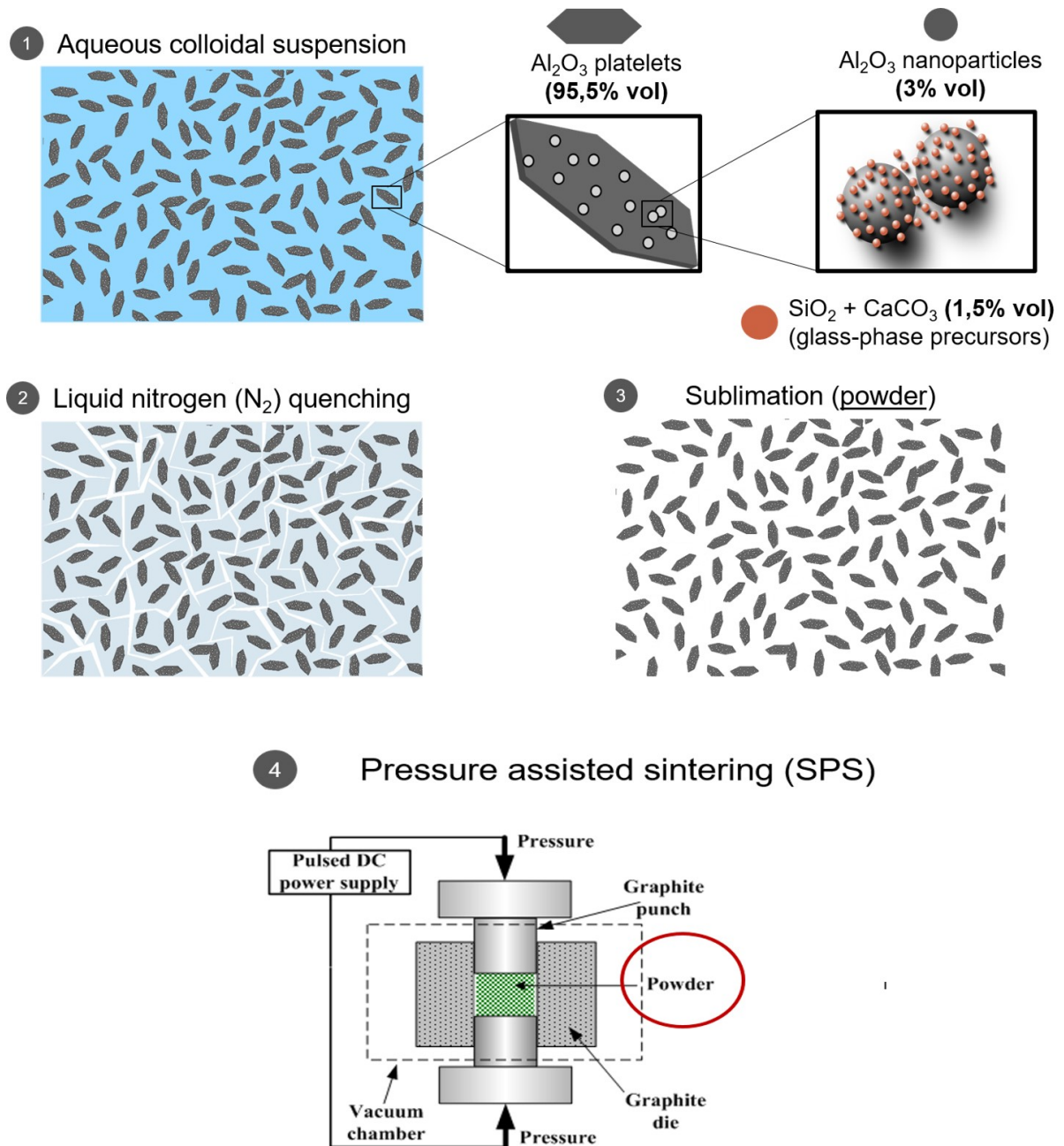


Figure 6.1: Simplified scheme describing the process to produce large nacre-like samples using pressure assisted sintering. Courtesy of LSFC laboratory.

6.2 Generation of numerical samples

In this section we describe the scheme to prepare numerical samples used in discrete element simulations. The numerical sample is made of tablets that should mimic the real tablets observed by SEM (Fig. 6.2). We start by generating tablets from an organized crystalline cube of particles with a radius of $0.05\ \mu\text{m}$. This initial block is then carved into a hexagonal shape (Fig.6.2) to match the shape and the microstructural parameters (the tablet radius R and thickness t_t). For simplicity, all numerical tablets have the same shape. The parameters used are reported in Table 6.1.

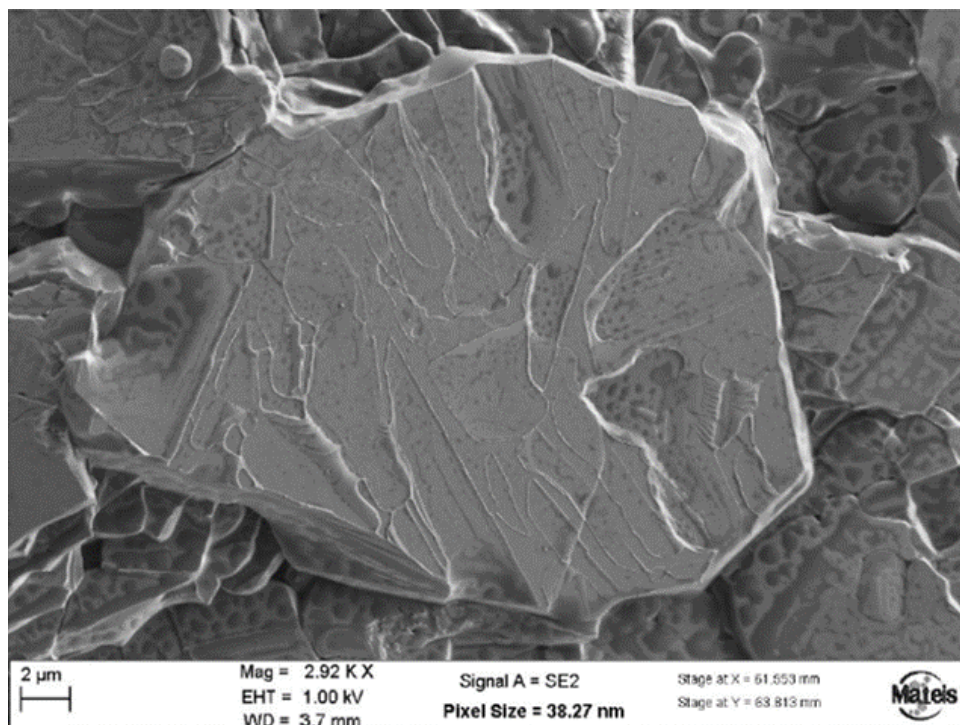


Figure 6.2: SEM micrograph of nacre-like alumina showing the hexagonal shape of an individual tablet. Courtesy of LSFC laboratory.

The number of particles used for each tablet is 6670 particles. Note that at this step, no bonds, nor any friction or adhesion are considered between the particles. The packing is afterwards densified by imposing an affine densification [Kumar et al., 2016]. Afterwards, all pairs of particles that are close enough are linked together by rigid bonds to form a continuous material. The tablets here are non-deformable entities that we call clumps. Clumps are clusters of connected particles in which interactions between particles are not calculated (Fig.6.3). This means that the number of calculated interactions is much smaller than problems where full clusters are used instead, which leads to faster computation. However, this means that we do not have access to the stress inside the

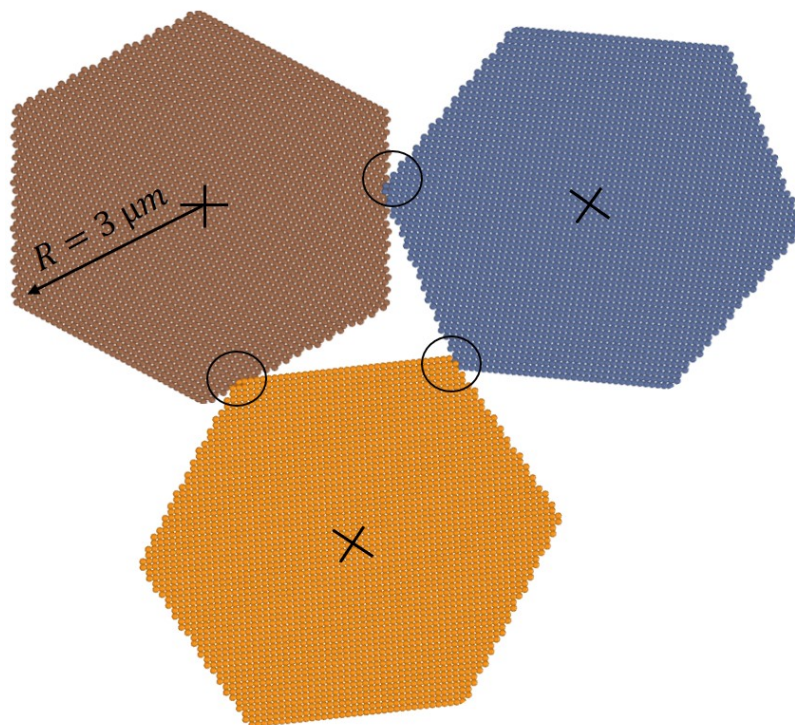


Figure 6.3: A scheme of three clumps interacting through three contacts (black circles). Here the interactions are not calculated inside the clumps. Instead, the total forces and moments are calculated at the center of gravity of the clumps (black cross).

tablets when compacting clumps together. Thus, fracture of platelets is not possible with the clump methodology as we do not compute internal forces in the cluster. This may be a crude approximation for situations where a tablet is blocked (arching). Still, microstructural observations of alumina nacre after SPS would indicate that platelet fracture is not common because the alumina tablets are added at the end of the milling cycle to avoid any excessive breakage due to friction and shocks with the milling media.

After processing the tablets, a random gas of 20 identical tablets with random orientations was generated (Fig.6.4). The necessary precautions were taken to not over represent an orientation [Néda et al., 1999]. The tablets are located randomly in the simulation box with no initial contact between them. The simulation box is periodic on all three axes such that when a tablet sticks outside the periodic cell through a given face, it interacts with the rest of the tablets on the opposite face.

The second step consists of adding the nano-particles to the surface of the tablets. To calculate the amount of nano-particles to add to the samples, we based our calculations

on nacre-like alumina composition (98.5 vol.% alumina, including 3.5 vol.% of alumina-nano particles with a radius of 100 nm and 1.5 vol.% of silica and calcia with a radius of 20 nm) [Bouville et al., 2014a]. In our simulations, we consider that silica and calcia nano-particles have the same size as the alumina particles to avoid too CPU intensive simulations. This leads to a 5 vol.% of nano-particles with a size of 100 nm. The number of nano-particles added to each packing of tablets was calculated using the volume fraction ϕ_{nano} and the radius of nano-particles R_{nano} and the tablet volume V_t (Eq.(6.1) and Tab. 6.1). The particles were then added geometrically to the surface of the tablets.

To make the nano-particles stick to the tablets, we use an adhesive model. The interaction between nano-particles and tablets is governed by the DMT model [Derjaguin et al., 1994], which adds a tensile force to the standard repulsive Hertzian force. The tensile force writes: $N_t = \frac{2}{\pi}wR^*$ where w is the work of adhesion (twice the surface energy) and R^* is the effective radius (see Eq. (3.1) in Chapter 3). A value of γ_s was chosen but has no real physical meaning since the size of the particles comprising the tablets does not reflect the correct adhesive interaction. Still, The DMT model which works under the important assumption that deformation fields are given by Hertz theory [Derjaguin et al., 1994] allows for the adhesion of the nano-particles on the surface of tablets. An additional step was necessary to reach the equilibrium position of nano-particles on the tablets. Initially, the nano-particles are deposited with a relative indentation of $\frac{\delta_N}{R} = 10^{-9}$. The equilibrium of the tablets with nano-particles was done for 2000 time steps and a surface energy $w = 2\gamma_s = 2J.m^{-2}$. Also, we have observed that during densification some nano-particles detach from the tablet's surface but return on the tablets at the end of the densification.

$$N_{nano} = \frac{\phi_{nano}}{1 - \phi_{nano}} N_t V_t \frac{1}{\frac{4}{3}\pi R_{nano}^3} \quad (6.1)$$

Number of tablets N_t	Tablet radius R (μm)	Tablet thickness t_t (μm)	Tablet volume (μm^3)	Nano-particle volume fraction (ϕ_{nano})
20	3	0.5	6.43	5%

Table 6.1: Microstructural parameters used in the generation of the initial discrete packings

After adding nano-particles to the tablet surfaces, the gas is densified. The evolution from a random gas to a dense packing is a CPU time consuming process, that is why the

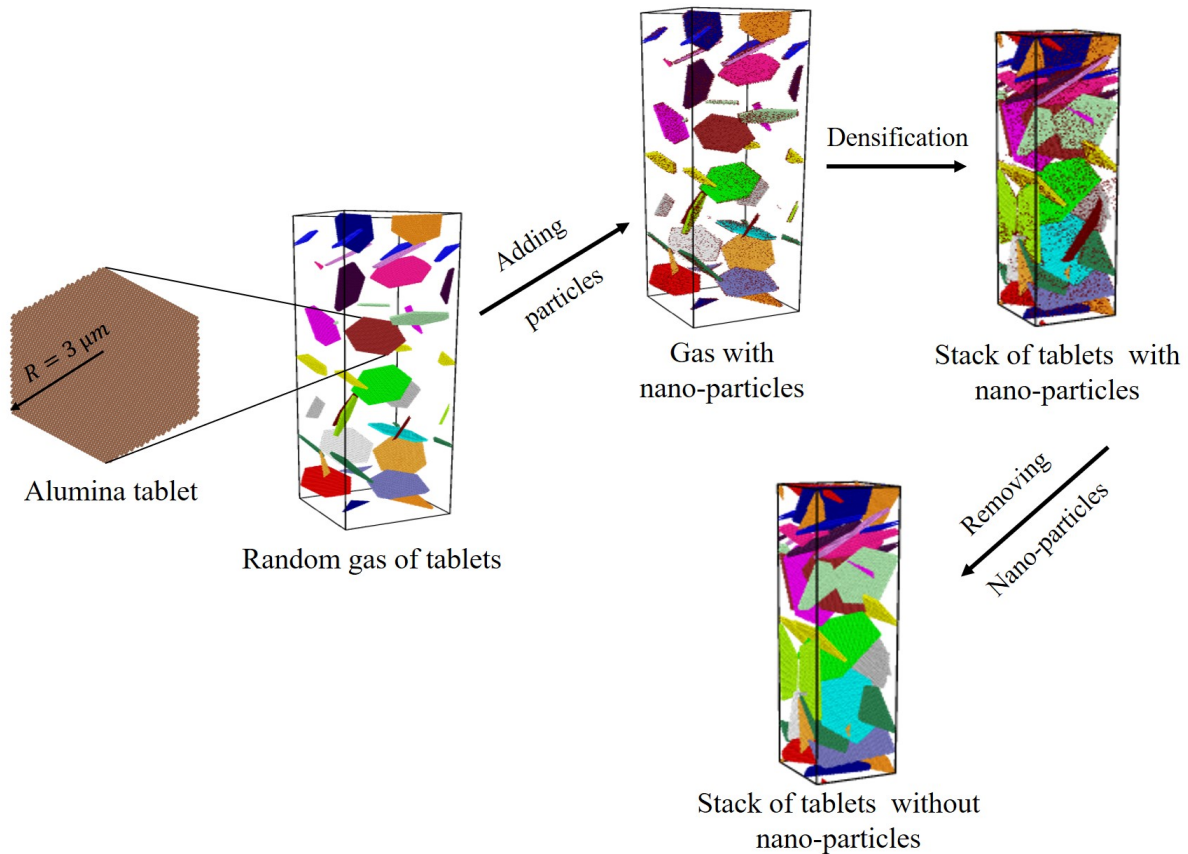


Figure 6.4: Typical evolution of numerical 3D samples with 20 tablets during the preparation stage. The initial gas of tablets has no contact between tablets and an initial density of 0.032. Nano-particles are added and the gas is then densified to obtain a packing of a density of 0.1. The nano-particles are removed to create identical samples but without nano-particles.

densification is conducted in two steps; first the gas is densified at high densification rate up to the creation of the first contact between the tablets, then the gas is isostatically densified under a prescribed very low pressure ($P=0.02$ MPa) by decreasing the size of the simulation box, leading to tablet rearrangement. The macroscopic stress tensor in the packing is calculated using the Love's formulation (see (Eq. 3.9) in Chapter 3). [Christoffersen et al., 1981].

Following the procedure described above, the first type of microstructures (tablets with nano-particles on the surface) was generated. The second type of microstructures was created by simply removing the nano-particles. A set of ten samples of each type was generated using ten different initial random seeds.

6.3 DEM Simulations: compaction

The stacks of tablets that were prepared in the preceding section were submitted to compaction with a slow constant strain rate ($\dot{\epsilon} = 10^{-5}$) to approach quasi-static conditions. The compaction was carried in the z axis direction to reach a final density of 0.6 which corresponds to the density of the material right before sintering. A small adhesion was kept between the tablets and the nano-particles to ensure their attachment to the surface.

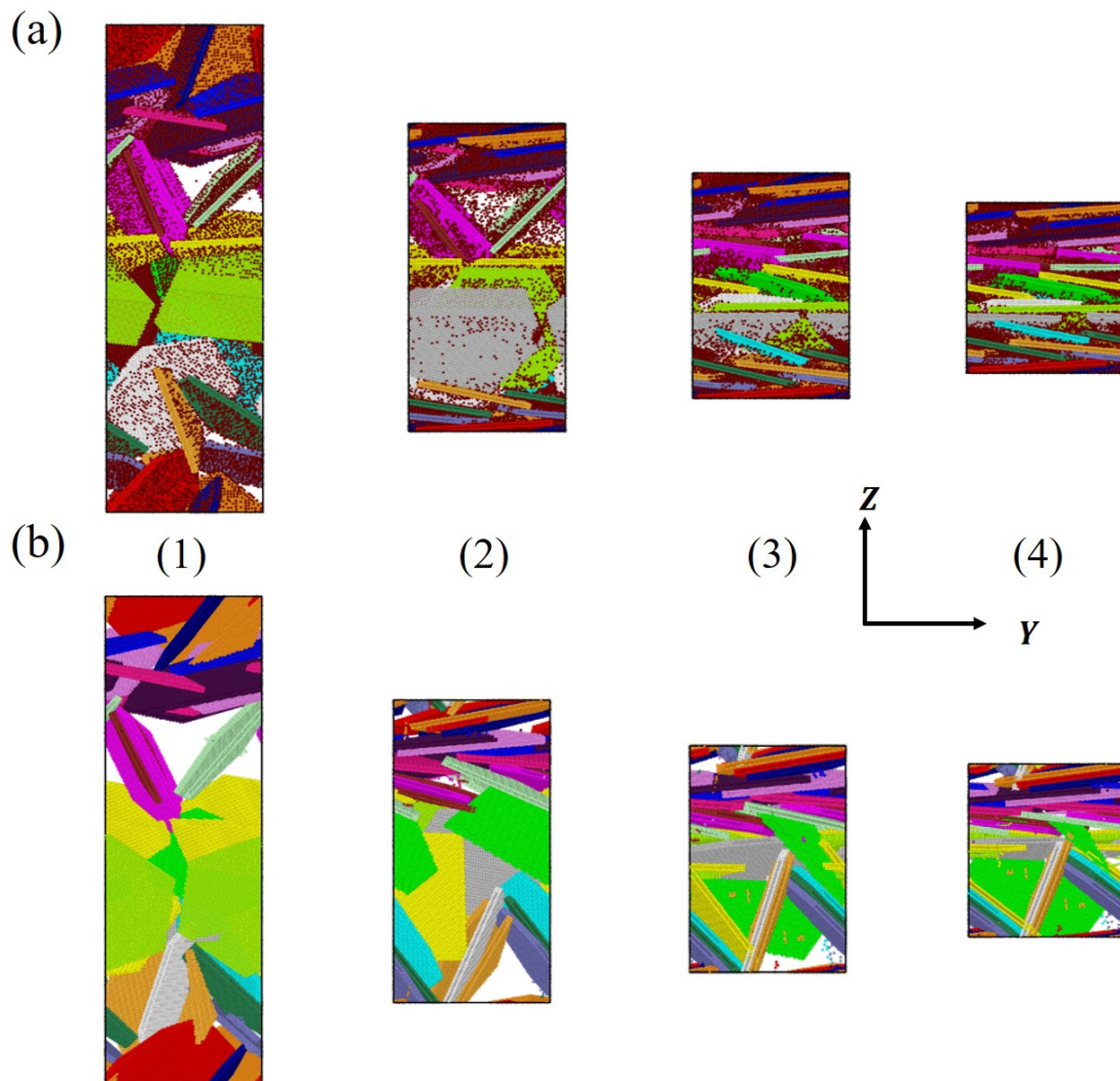


Figure 6.5: Sample evolution during uniaxial compaction of the two types of microstructures: a) with nano-particles and b) without nano-particles.

Figure 6.5 depicts four typical views of two packings of random tablets submitted to compaction. The packings 6.5.a and 6.5.b represent the material in the two studied

cases: with nano-particles and without nano-particles with the same initial geometrical configuration for the tablets. At stage (1) the tablets are randomly orientated. From stage (1) to (2), the compaction in the z axis direction offers some possibility for the tablets to rearrange. At a larger relative density, stage (3) shows the tablet's normal vector starting to align with the z axis direction. Stage (4) shows the final structure at a density of 0.6. It is interesting to note that a few tablets stayed blocked parallel to the compaction direction in the sample without nano-particles. We can observe that the same tablets were more easily aligned in the sample with nano-particles. This could be explained by the fact that the nano-particles have a ball-bearing effect. In other words, when a vertical tablet is in contact with a horizontal one, the nano-particles on the surface reduce rotational friction and help the vertical tablet to lay on top of the neighboring tablet. Still, we have observed in a few instances that even with nano particles, some tablets could be stuck parallel to the compaction direction.

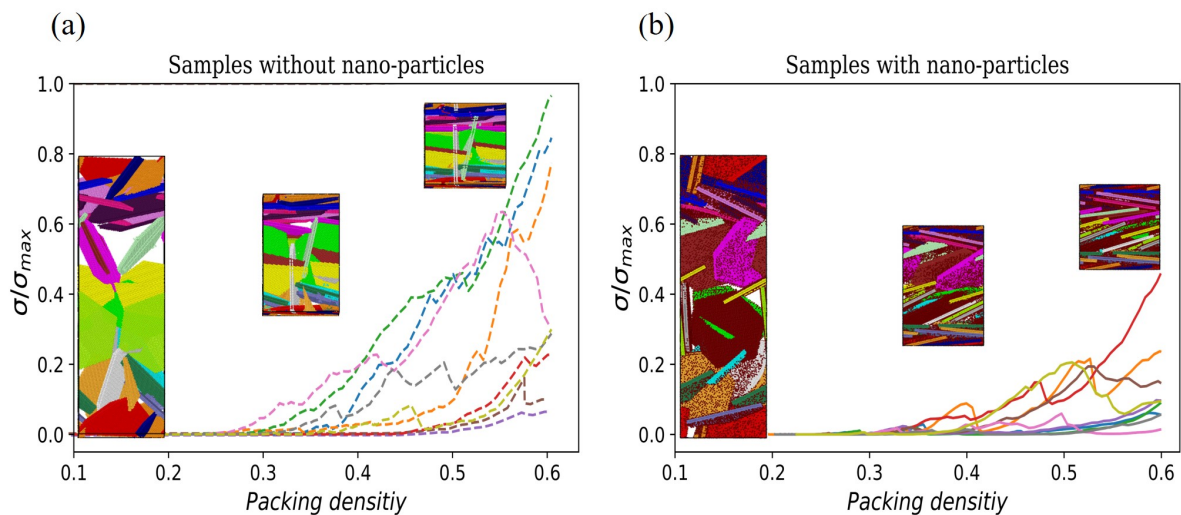


Figure 6.6: Evolution of the normalized axial stress as a function of the packing density for ten simulations for both microstructure types a) without nano-particles and b) with nano-particles. The axial stress is normalized by the maximum stress of the compacted the without nano-particles compacted samples.

Figure.6.6 shows the evolution of the normalized axial stress in the compaction direction as a function of the relative density of the ten samples used. The axial stress presented here has no physical meaning as discussed in the section describing the clumps method (Section 6.2). The stress here is normalized by the maximum stress value of the compacted without nano-particles samples to make the comparison between the two types of samples easier. The stress-density curves of the samples with no nano-particles are globally higher than the samples with nano-particles. In both plots we can notice

that the stress-density curves are scattered. By looking at the curves, we can notice some stress peaks followed by stress decrease. This can be explained by the unblocking of some tablets that get stuck vertically between two other horizontal tablets.

No friction was introduced at tablet/tablet contacts and at tablet/nano-particle contacts. This is because the non-smooth nature of the tablet's surface made of spheres provides already some friction.

6.4 Tablet orientation

During the compaction of the samples with nano-particles, an interesting phenomenon was noticed in some of the sandwiched tablets. The vertical tablet between the two horizontal tablets sweeps the nano-particles from the surface of the tablets that it is in contact with. One might think that this could affect the alignment of the concerned tablets. In reality, it does not, because with several tablets put together in the simulation box, the missing amount of particles from one surface is compensated by the other particles on the second surface. However, this phenomenon affects the homogeneity of the final sample. We have attempted to characterize this phenomenon on a simplified configuration with only three tablets. In this configuration, a nearly vertical tablet is sandwiched in between two horizontal ones for which a vertical motion is imposed. As seen in figure 6.7, a larger quantity of nano-particles is located on the edge of the tablets compared to the opposite edge. Also, the sandwiched tablet brushes particles off the surface of the horizontal tablets, creating a clean surface without nano-particles. This phenomenon (very much emphasized in this specific configuration), illustrates how the dispersion of nano-particles may become non-homogeneous as compaction progresses.

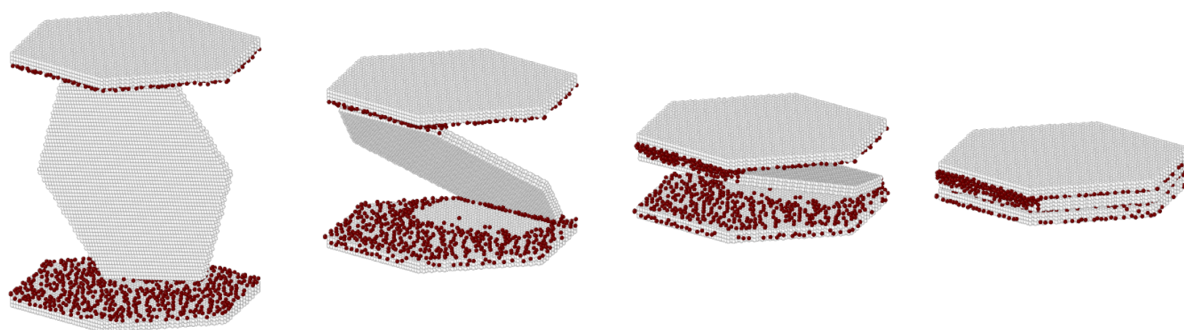


Figure 6.7: Snapshots of a sandwiched tablet under uniaxial compaction between two tablets. Progressively nanoparticles are swept away from the surface.

As mentioned in the previous section, two types of microstructures were generated to study the effect of nano-particles between tablets on their alignment during compaction:

samples without nano-particles and others with nano-particles. To follow the evolution of the orientation of the tablets, we measure the angle θ between the normal vector \mathbf{n} to the tablet and the compaction axis z . When $\theta = 0$, it means that the tablet is perpendicular to the compaction direction, thus well aligned. Figure 6.8 shows the orientation of the tablets in the form of pole figures and the number of occurrence histograms. The pole figures were obtained by projecting the normal vector to each tablet on the xy -plane. Before compaction, for both types of samples, the tablet normal vector projections are uniformly dispersed on the pole figure, and the angle θ is distributed from 0 to 90 degrees (Fig.6.8b). This means that the tablets are randomly oriented, which is confirmed by the histogram showing the number of tablets for each orientation.

During compaction, we can see that tablet orientations are less random and that the tablets started aligning along the z axis. By analyzing the pole figure of the samples without nano-particles (Fig.6.8c), it is noticeable that the density of normal vectors that are parallel ($\theta = 0$) to the loading axis is higher than before compaction. However, by looking to the with nano-particles samples pole figure (Fig.6.8d), this density is much higher. In other words, the amount of well aligned tablets is larger in the compacted samples with nano-particles than the samples that does not contain any nano-particles. It was also noticed that the tablets that contain larger quantities on their surface are well aligned compared to the ones who have less nano-particles.

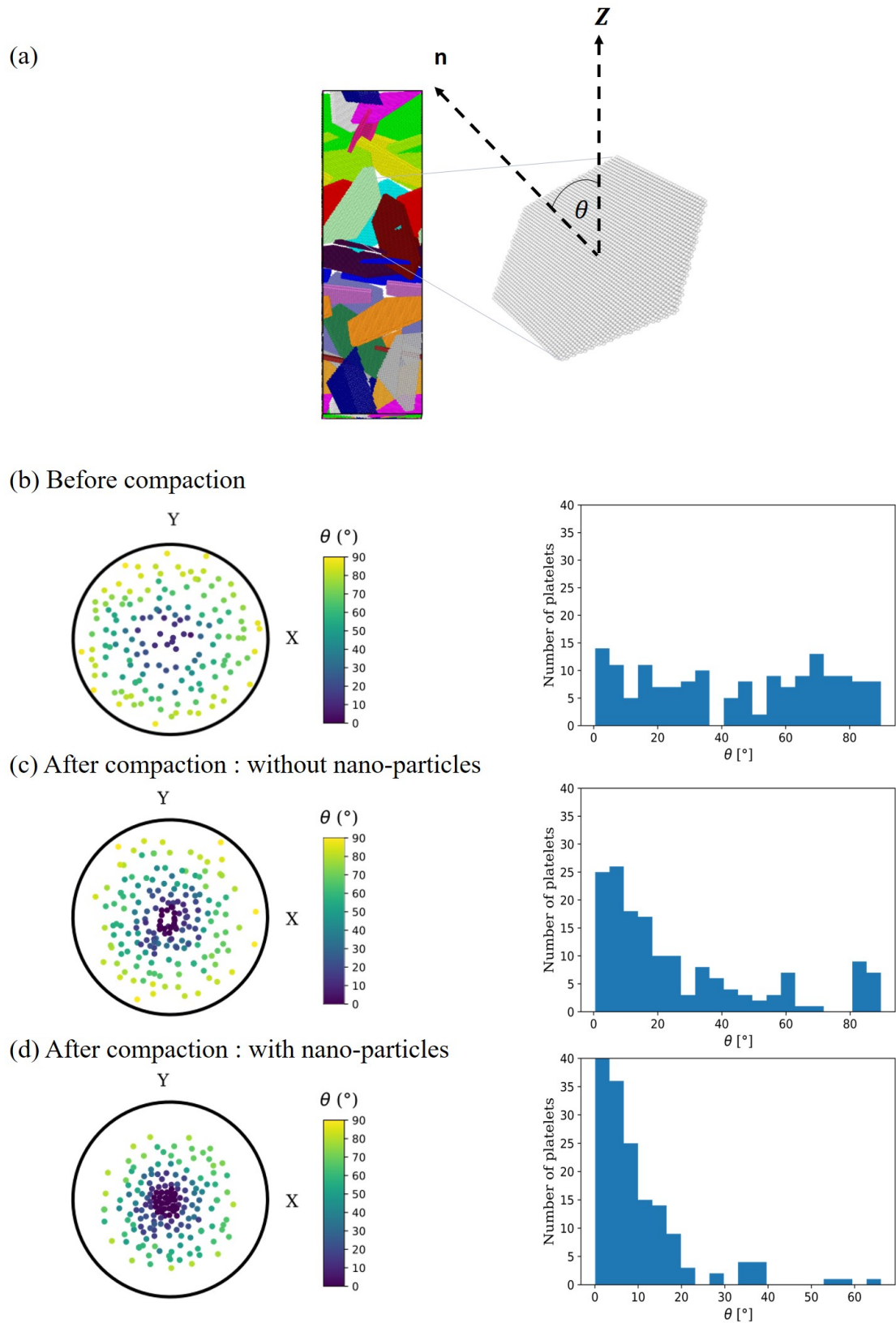


Figure 6.8: a) One of the packings of tablets with a zoom-in on one tablet and the normal vector to it \mathbf{n} . The angle θ between the compaction axis z and \mathbf{n} of each tablet describes its orientation b) before compaction and c, d) after compaction for both types of samples.

6.5 Conclusion

Given the importance of tablets alignment in nacre-like alumina, in this chapter, one of the synthesis steps of nacre-like alumina contributing to alignment is studied: the uniaxial compaction of alumina tablets. First, a brief review of literature is presented to underline the relationship between the process and tablet alignment. Afterwards, 10 numerical microstructures with 20 randomly oriented tablets were generated then compacted to reach a given density. Two types of microstructures were tested and compared, microstructures containing tablets with nano-particles and others without nano-particles on their surface. The evolution of the alignment of tablets in nacre-like alumina during compaction was followed. We showed that the compaction of samples with nano-particles resulted in more well aligned tablets than the samples without any nano-particles on the surface of the tablets. This is attributed to the role of nano-particles as they have a ball-bearing effect between the tablets. Apart from the alignment, an interesting phenomenon was reported: during compaction an important amount of nano-particle gets swiped by the perpendicular tablet to the surface which might case a non-homogeneous distribution of nano-particles on the final materials. Even though the alignment degree of tablets is quite good after the solid-state compaction (i.e. before the apparition of the liquid phase), the actual process developed by LSFC provides further alignment during subsequent liquid phase sintering step. Even though the alignment of tablets obtained by compaction and is not as good as superlattices that were obtained by sedimentation [Henzie et al., 2012], it was proven that the resulted mechanical properties are slightly better (A study in progress at LSFC). More tests are needed to prove the improvement of the mechanical properties as a function of the tablet alignment. Also, in this model, the tablets used are considered unbreakable, an assumption that works in this case but might not be quite realistic for other materials or methods.

Chapter 7

Conclusion and future work

Contents

5.1	Introduction	103
5.2	Effect of a random overlap distribution	104
5.2.1	Simulation conditions	104
5.2.2	Tensile tests	105
5.2.3	Single Edge Notched Tension (SENT) tests	108
5.3	Computation on real microstructures	112
5.3.1	Electron Back-Scattered Diffraction (EBSD) protocol	113
5.3.2	Microstructure analysis	114
5.3.3	Numerical microstructures from the EBSD image	117
5.3.4	Macroscopic strength and toughness	117
5.4	Conclusion	126

7.1 Conclusion

Understanding the reinforcement mechanisms and their relationship with the microstructure and the mechanical properties of BM materials is essential to the development and optimization of tough and strong bio-inspired materials. The literature review presented in this work depicted the various reinforcement mechanisms in natural and synthetic BM materials. Fabrication methods and their advantages and disadvantages were presented.

Up to now, most of the models developed to study BM material are analytical and performed on representative volume element. The few numerical models developed, considered rigid tablets, plastic interfaces, and a large stiffness contrast between the tablets and the interface. This thesis aimed to develop a model applicable to all-ceramic BM material (i.e. tablet breakage allowed, brittle interfaces and small stiffness contrast). The model will allow an in-depth understanding of the reinforcement mechanisms present during crack propagation as well as the optimization of the mechanical properties (strength and toughness). For these purposes, the discrete element method was selected, as it is an adequate numerical tool to account for topological modifications and fracture.

First we developed the numerical model based on a basic representative volume element [Radi et al., 2019a]. Elasticity and fracture of the interface and tablets were calibrated by taking into account the characteristics of the packing that meshes the samples. We have also shown the importance of choosing carefully the number of discrete elements to ensure a good compromise between CPU time and model accuracy.

The DEM model was compared to analytical models in the literature and showed a good agreement in elasticity and fracture initiation. Thanks to the inherent discrete nature of DEM, the present model has the ability to account for friction and interlocking effects during crack propagation (post fracture initiation behavior) and extrinsic reinforcement mechanisms which are responsible for the capacity of these materials to prevent catastrophic failure. As an example, the model is applied to nacre-like alumina RVE. It is shown that an appropriate tuning of the interface strength is important to optimize the material mechanical properties.

In order to assess the toughness in the form of a R-curve and study the reinforcement mechanisms, simulations at the scale of a hundred tablets were conducted. The focus was set on the effect of two strategies to reinforce the interface, either in a homogeneous manner, by an increase of its nominal strength, or by the addition of nano-bridges to the interface. The DEM simulations revealed quite interesting information about strength and toughness, where both reinforcement methods increased strength until reaching an asymptotic value. As for toughness, two main parameters were distinguished: crack initiation toughness and crack growth toughness. It has been shown that by increasing

the interface strength, crack initiation toughness increases to a maximum asymptotic value. However, increasing the density of nano-bridges at the interface improves initiation toughness but only to decrease after a maximum with a high nano-bridges density. As for crack growth toughness, the important role of microcracking and crack deviation in increasing the crack growth toughness was demonstrated. An optimum value was found by setting the interface strength at $\Sigma_i = 0.1\Sigma_t$. This value is higher than what is used in experimental work, which proves that there is room for improvement. An optimum number of nano-bridges was also identified, around 6 per tablet. In order to help the material scientist to design optimized nacre-like ceramics, property maps linking strength, initiation toughness and crack growth toughness to interface strength and amount of nano-bridges are presented.

Only ideal microstructures were simulated so far and the question of the influence of variability (hardly avoidable on a real system) should be investigated. The effect of overlap distribution on strength and toughness was studied and we showed that adding distribution did not degrade significantly strength. As for toughness, a slight difference in the crack path was noticed, where the crack was less deviated for non-uniform overlaps compared to uniform overlaps. The overall toughness (crack initiation toughness and crack growth toughness) decreased with the increase of the overlap distribution. To account for the distributions of the tablets orientation, interface thickness and other structural features, we presented a new method that combines EBSD micrographs with DEM discrete packings to obtain realistic structures. The simulations performed using real microstructures can provide information unattainable by experiments. For example, the crack path or the interface strength impact on the different mechanical properties. The results of the simulations performed on the EBSD microstructures were compared to the ideal BM sample studied in Chapter 4 showing a non negligible decrease of mechanical properties between ideal and real microstructures.

The last part of this thesis was about simulating a part of the synthesis of nacre-like alumina: uniaxial compaction. To study the effect of nano-particles on tablet alignment, the evolution of the orientation of tablets in nacre-like alumina during compaction was followed. The compaction of samples with nano-particles resulted in more well aligned tablets than the samples without any nano-particles on the surface of the tablets. This is attributed to the role of nano-particles as they have a ball-bearing effect between the tablets.

7.2 Future work

Several paths for future work can be considered to complement the results on the mechanical behavior of BM materials obtained throughout this thesis. Some suggestions and guidance are proposed in the following.

First, the model developed in this thesis could be extended to BM microstructures with ductile interfaces (metal or polymer), this is possible by considering plastic interactions at the interface, knowing that DEM is also well-suited for tackling plastic deformations [Martin et al., 2003; Martin, 2004]. With such a model, the interface could deform elastically and plastically, then damage before fracture. This would generalize the interaction model proposed here which simply takes into account elasticity and brittle failure. The advantage would be to be able to broaden the applications of DEM to BM composites with a metallic or polymeric interface or to natural nacre.

The model developed for ideal microstructures accounted efficiently for reinforcement mechanisms. One of the short terms objectives could be the quantification of reinforcement mechanisms such as microcracking and crack deflection. As mentioned in the literature, the fracture resistance does not simply depend on the maximum stress or strain but also depends on the pervasive presence of microcracks and their size [Launey & Ritchie, 2009]. For example, by determining the density of microcracking before and after crack propagation we could figure out how much of this microcracking is actually responsible for stress release at the crack tip. Another mechanism that can be quantified is the crack deflection. By measuring the angle between the crack and its projected length we can track the evolution of the crack deflection and see by how much the crack deflects for a set of parameters for example. As a validation, damage can be quantified experimentally and compared with the numerical model, either by using acoustic emission [Kim & Weiss, 2003], or by using a data fusion approach (acoustic emission and digital image correlation) [Vanniamparambil et al., 2014].

Introducing a controlled amount of compressive residual stresses (relying on coefficient of thermal expansion mismatch) has proved successful to improve the toughness of ceramics and layered ceramics [Chang et al., 2014] (Fig. 7.1). Therefore, accounting for residual stresses within the interface in our model could be of an interest.

Coupling DEM and EBSD images showed promising results. The realistic microstructures studied here were taken from one sample only. Using images from different samples with varying microstructures must provide more information about the crack path, and the influence of the microstructure on the mechanical behavior. By using these images, different microstructural parameters, such as the volume fraction, the tablet aspect ratio, the distribution of interface thickness, can be tailored to reach the optimum mechanical

properties. Also, we can add microstructural defects (i.e. porosities), control their density and quantify their effect on the overall mechanical behavior. The idea would consist of starting from a realistic microstructure obtained by EBSD and numerically manipulating the image incrementally to explore the effect of a given parameter (volume fraction, the tablet aspect ratio, the distribution of interface thickness, tablet orientation, ...) on the mechanical response.

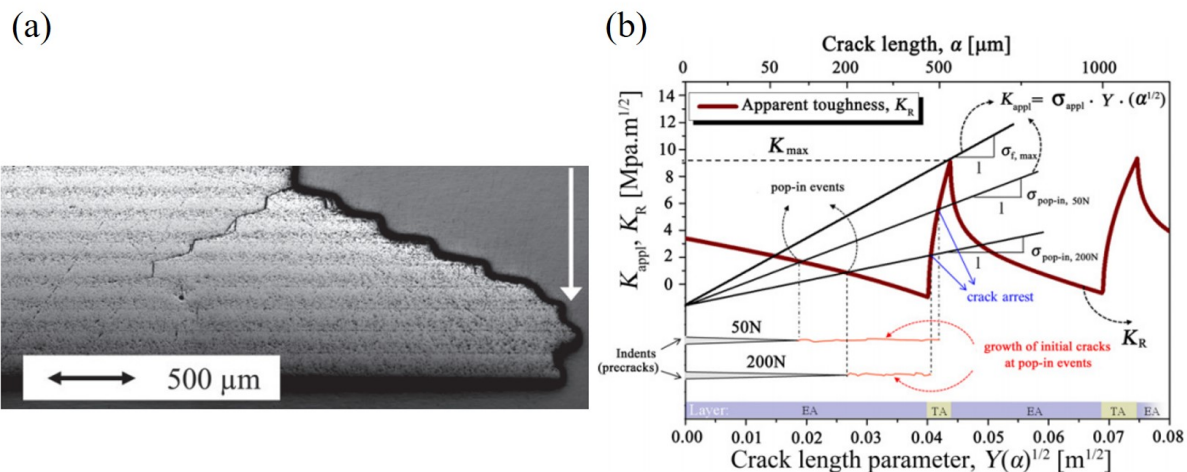


Figure 7.1: Toughness increase in layered ceramics after introducing compressive residual stresses. a) Optical micrographs of the composite bend bars post fracture [Pavlacka et al., 2013]. The arrow indicates the transverse direction b) Stress intensity factor (K_{appl}) and calculated material fracture toughness (K_R) as a function of the crack length for indented composite [Chang et al., 2014].

Because of the strong and directional bonding between the constitutive atoms in ceramics, they present a high fusion temperature and thus high thermal stability. It has been proved that nacre-like alumina has very interesting mechanical properties at high temperatures. By using DEM we could study the effect of the microstructure on the thermal properties of nacre-like alumina. Recently, the in-house code dp3D used in this PhD has been developed so as to implement heat conduction and thermal expansion. Resistance to thermal shock and/or to thermal fatigue could thus be carried out.

Bouville et al [Bouville et al., 2014a] showed the importance of tablet alignment on thermal properties (i.e. thermal diffusivity). In Figure 7.2, the relative improvement of the thermal diffusivity between aligned tablets composites and randomly aligned composites for different processing methods is presented. Therefore, it could be interesting to enrich the model by evaluating the resulting thermal diffusivity of the aligned tablets by uniaxial compaction.

In the dp3D code (and in most DEM code), the unit particle is a sphere. Thus, the alumina tablets were described here as a set of bonded spheres. This has the advantage

of simplicity for contact detection and distance calculation. However, it has the drawback of a very coarse description of the tablet's surface. In particular, the rounded shape of the protruding spherical particles provides an artificial frictional surface, which may not be realistic. This could be prevented by increasing the number of spheres but at the cost of prohibitive CPU time for simulations. Arbitrary shaped 3D particles using level set functions as a geometric basis (LS-DEM) have been proposed. One of the advantages of this method is its computationally time-efficient framework compared to full field methods (e.g. Finite Element Method). Also, LS-DEM can reproduce and capture macroscopic and microscopic behavior in a similar manner as experiments (Fig.7.3) [Kawamoto et al., 2018].

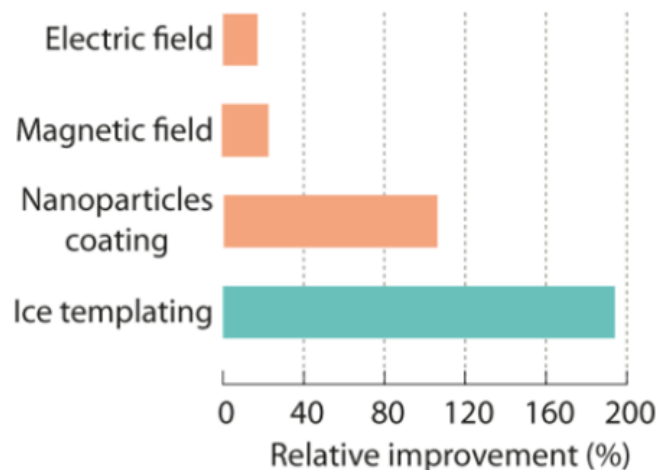


Figure 7.2: Comparison of the relative improvement of the thermal properties of BM materials, where the tablet were aligned using different methods: electric field, magnetic field (with or without super paramagnetic nano-particles coating) and ice templating [Bouville et al., 2014a].

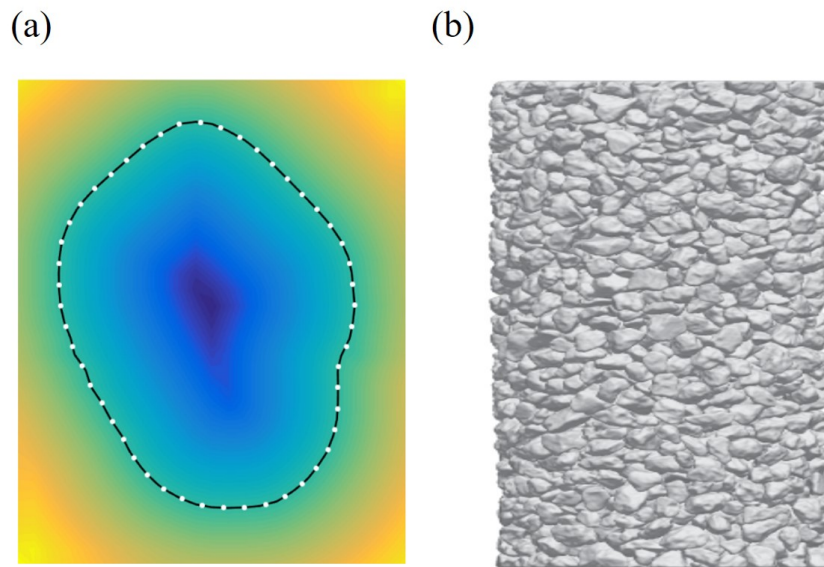


Figure 7.3: a) An example of boundary node discretization with nodes in white seeded on the grain surface. b) A virtual level set function representation of a specimen [Kawamoto et al., 2018].

Appendices

Appendix A

Supporting information

A.0.1 Contact laws

To model the mechanical behavior of continuous media with DEM, we consider the material as a random packing of spherical particles of radius R connected with cylindrical beams (Fig. A.1). An effective radius R^* of two particles with radii R_1 and R_2 is introduced:

$$R^* = \left(\frac{1}{R_1} + \frac{1}{R_2} \right)^{-1} \quad (\text{A.1})$$

Similarly, the effective normal K_N and tangential K_T stiffnesses at the bond level are defined from particle's stiffness:

$$K_N^* = \left(\frac{1}{K_{N,1}} + \frac{1}{K_{N,2}} \right)^{-1}, \quad K_T^* = \left(\frac{1}{K_{T,1}} + \frac{1}{K_{T,2}} \right)^{-1} \quad (\text{A.2})$$

To avoid dependence of the macroscopic elastic response on particle's size, we introduce material parameters $\sigma_N^* = \frac{K_N^*}{2R^*}$ and $\sigma_T^* = \frac{K_T^*}{2R^*}$ which render macroscopic elastic properties independent of the sphere size for a given set of microscopic properties σ_N^* and σ_T^* . At the bond scale, the normal and tangential forces are given by:

$$\mathbf{N} = -4\sigma_N^* R^* \delta_N \mathbf{n} \quad , \quad \mathbf{T} = -4\sigma_T^* R^* \delta_T \mathbf{t} \quad (\text{A.3})$$

with δ_N and δ_T the normal and the tangential relative displacements between the two particles, and \mathbf{n} and \mathbf{t} the unit normal and tangential vectors, respectively.

Resisting moments M_N and M_T are transmitted by bonds in normal and tangential directions opposing the accumulated relative rotations θ_N and θ_T [Potyondy & Cundall, 2004]:

$$M_N = -8\sigma_T^* R^{*3} \theta_N \quad , \quad M_T = -4\sigma_N^* R^{*3} \theta_T \quad (\text{A.4})$$

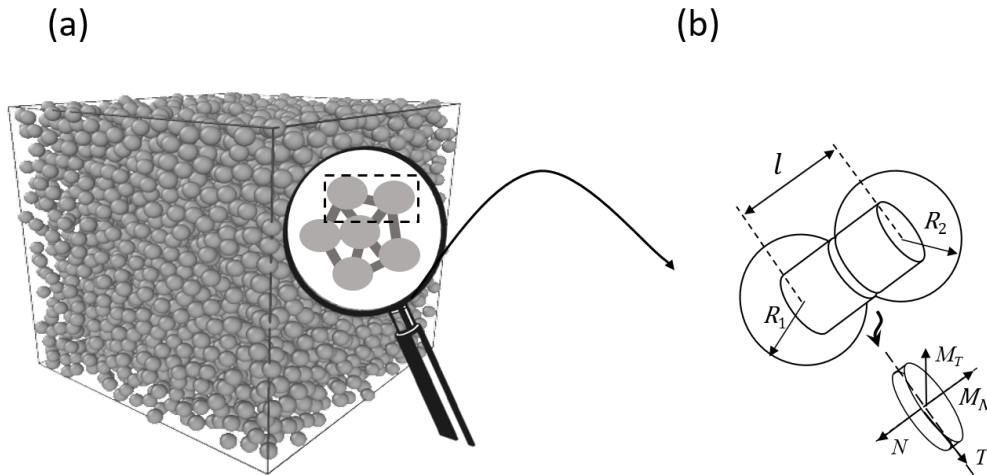


Figure A.1: From macroscopic to microscopic scale. (a) Random packing of bonded particles representing a continuous material. (b) Two bonded particles of radius R_1 and R_2 transmitting normal/tangential forces and resisting moments.

The DEM beam model described above allows the elastic behavior of a continuous material to be represented satisfactorily [Kumar et al., 2016].

Bonds fracture when the maximum principal stress Rankine criterion is satisfied at the beam scale. The criterion states that failure occurs when the maximum principal stress reaches the material strength. In the framework of DEM with bonded contacts, Rankine's equivalent stress is defined as follows:

$$\sigma_{b,R} = \frac{1}{2} \left(\sigma_{b,N} + \sqrt{\sigma_{b,N}^2 + 4\sigma_{b,T}^2} \right) \quad (\text{A.5})$$

with $\sigma_{b,N} = \frac{N}{4\pi R^{*2}}$ and $\sigma_{b,T} = \frac{T}{4\pi R^{*2}}$ the normal and the tangential stresses at the bond level. The bond breaks when the Rankine's equivalent stress $\sigma_{b,R}$ reaches a critical stress σ_{Rc} to be calibrated.

After fracture, broken bonds keep the same normal stiffness as unbroken bond in compression but cannot transmit any tensile force. The tangential forces transmitted by broken bonds follow the Hertz–Mindlin model in the sticking mode and are limited by Coulomb friction for sliding with a friction coefficient μ . As for resisting moments, only tangential moments M_T are transmitted after bond fracture to account for bending (Fig. A.2).

A.0.2 Brick and mortar generation and parameter calibration

Samples were created following three steps:

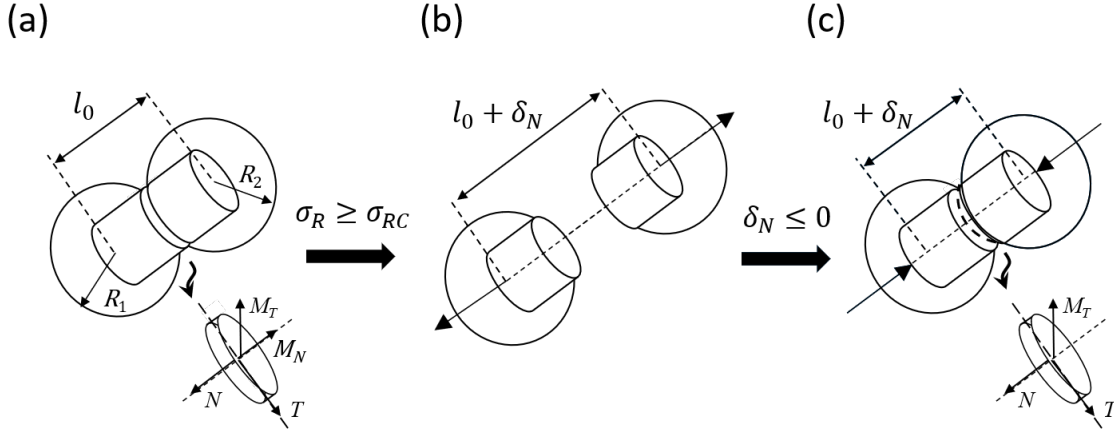


Figure A.2: Two bonded particles transmitting normal/tangential forces and resisting moments with l_0 the initial center to center distance. (a) Unbroken bond. (b) Broken bond. (c) Resumed contact after bond fracture transmitting only compressing forces, friction forces and tangential resisting moment.

- Generating a random gas of nearly monomodal spherical particles with 5% dispersion around the average radius R with a low relative density ($D = 0.3$).
- Densifying the gas isostatically under Hertzian contact law to reach a density $D = 0.5$.
- Imposing an affine densification [Kumar et al., 2016] to reach a density $D \approx 0.65$.

At this stage, particles are bonded together with an interaction range of 1.075 [Kumar et al., 2016] leading to an average bond number of 6.77 per particle. Each phase (tablet and interface) is then attributed a material with microscopic parameters that after calibration mimic the elastic and fracture properties of the given phase (Table A.1).

For notched sample, the centered notch was created across the direction of the tablets by simply removing the discrete elements along the crack line with a length of $a_0 = \frac{1}{5} L_y$ and a width of $4R$. The notch tip is always located into the interface. We tested configurations with the notch tip located in the tablet, without observing any noticeable difference in the macroscopic results.

In DEM, it has been demonstrated that the stress intensity factor K_{Ic} scales with \sqrt{R} [Potyondy & Cundall, 2004]. In this work, R was chosen according to a convergence study to ensure a good compromise between accuracy and CPU time ($R = 10\mu\text{m}$). The resulting toughness for the tablet material is $(K_{Ic})_t = 2.7 \text{ MPa}\cdot\text{m}^{1/2}$, although not equal it is close to the value for dense alumina ($3.5 \text{ MPa}\cdot\text{m}^{1/2}$). The interface material toughness is given by the ratio of strength between tablet and interface: $(K_{Ic})_i = \frac{\Sigma_i}{\Sigma_t} (K_{Ic})_t$.

	Microscopic parameters			Macroscopic properties		
	σ_N^*	σ_T^*/σ_N^*	$\sigma_{b,R}$	E	ν	Σ
Interface	3.33 E	0.21	0.212 Σ	400 GPa	0.2	0.1 – 2 GPa
Tablet	3.33 E	0.21	0.212 Σ	40 GPa	0.2	4 GPa

Table A.1: Microscopic bond parameters (Eq. (A.2)) and macroscopic parameters (E Young modulus, ν Poisson ratio, Σ macroscopic strength) used in the simulations. Indexes i and t refer to the parameters related to the interface and the tablet, respectively.

Particular care must be taken to ensure quasi-static conditions while loading samples in the explicit scheme used in DEM. Thus, the strain rate is decreased before crack propagation to counterbalance the kinetic energy added to the system when the crack starts propagating. The axial stress is calculated in the simulated volume using the Love formula [Christoffersen et al., 1981]:

$$\Sigma_{ij} = \frac{1}{V} \sum_{contacts} F_i l_{pq,j}, \quad (\text{A.6})$$

where the summation is made on all contacts and where V is the sample volume, F_i is the i^{th} component of the total contact force (with normal and tangential terms given by Eqs. (A.3)), and $l_{pq,j}$ is the j^{th} component of the l_{pq} vector connecting the centers of two particles p and q .

A.0.3 Crack length determination

To calculate the projected crack length a_i , we consider the projected length on the y axis. Using the open visualization tool Ovito [Alexander, 2010], we established a procedure to isolate the propagating crack as a cluster of particles pertaining to a given crack, then follow the y coordinate of the endpoint particle as a function of the deformation.

A selection of the particles with at least one broken bond per particle is first carried out. Among this selection, particles are grouped in clusters where two particles are considered to pertain to a given crack when their center to center distance is lower than a certain cutoff distance (here set to $4R$). The main crack is considered to be the largest cluster and the end point particle y -coordinate leads to the a_i value. Therefore, the projected crack length is obtained at every output step i as a function of strain and stress. The crack propagation initiation is considered after the first step, on the a_i versus strain plot (Fig. A.3) which can be considered as a crack tip damage (thickness $\leq t_i$) but not as crack propagation.

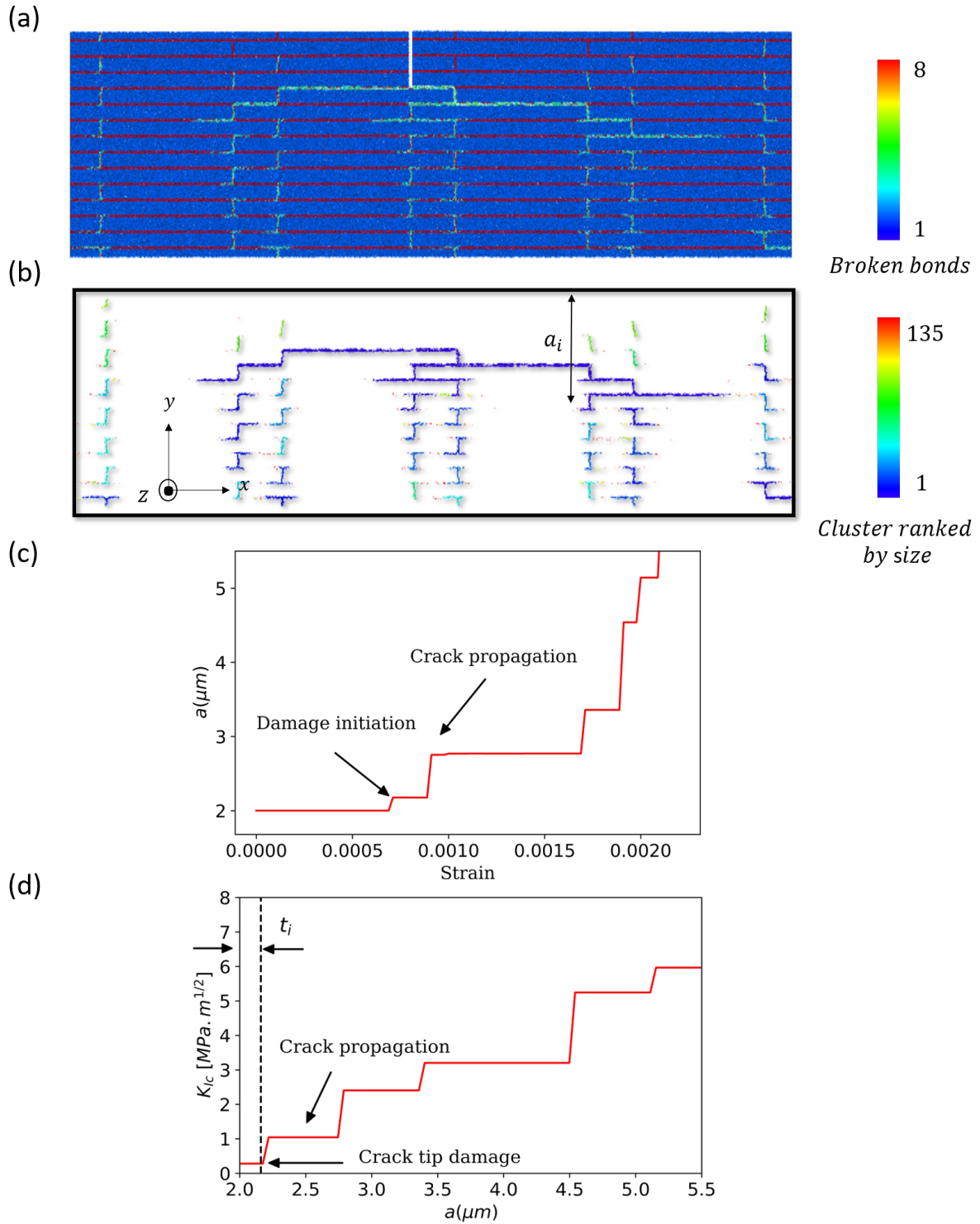


Figure A.3: a) Snapshot showing crack propagation during the tensile loading of a notched sample. b) Cluster selection. In this case, 135 clusters were determined and classified by size. Cluster number 1 is the largest and represents the main crack. c) Crack size propagation with strain exhibiting a step-wise increase. d) R-curve.

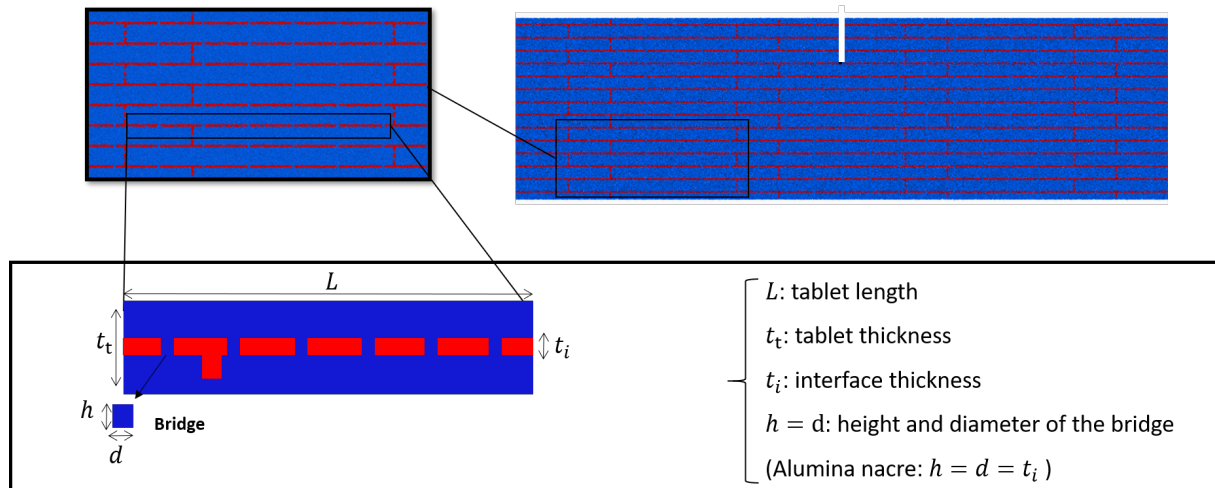


Figure A.4: A notched sample with nano-bridges (in blue) connecting two tablets through the interface. A zoom-in shows the distribution and geometry of nano-bridges. Nano-bridges are introduced both at horizontal and vertical interfaces.

A.0.4 Generation of microstructures with nano bridges

To test numerically the effect of nano-bridges on our samples, cubic bridges that span the whole depth of the sample in the z direction were installed in between two tablets. Their geometry is simplistic and their size is given in Fig. A.4 ($h = d = t_i$). They have the same mechanical properties as the tablets. The average number of nano-bridges per tablet (Nb) in the natural nacre is approximately 40 [Barthelat et al., 2006; Song et al., 2003]. However, the density of nano-bridges in nacre-like alumina is difficult to assess and not well controlled to date.

Appendix B

Influence of Young modulus ratio on toughness

B.1 Crack propagation

Several analytical models [Barthelat, 2014; Begley et al., 2012; Ni et al., 2015] developed on a representative element volume showed that the interface/tablet Young modulus E_i/E_t has an effect on the overall strength. In fact, by increasing E_i/E_t , the strength decreases. To evaluate its influence on toughness, three samples with different Young modulus ratio were created following the procedure described in Chapter 4. The rest of the mechanical and structural properties are similar to the ideal BM microstructures created in Chapter 4. A uniaxial test in the tablet direction was performed under periodic conditions and three modulus ratios were evaluated ($E_i/E_t = 0.001$, $E_i/E_t = 0.1$ and $E_i/E_t = 1$).

Figure B.1 shows the stress-strain of the three samples tested. For a large contrast of Young's modulus ($E_i/E_t = 0.001$), crack initiation happens earlier and the maximum stress is higher and the crack initiation occurs later compared to the other configurations. Also, less microcracking is noticed and the crack propagates in the form of a straight stairway, where the crack passes through the interface till material failure.

As for a low modulus contrast, we notice that the maximum stress decreases. More microcracking occurs and the crack deviates further. The large stress concentration (non-uniform shear stress) leads to earlier the interface the crack propagates in a regular manner within the interface. Friction and interlocking effects build up rising stresses.

Figure B.2 confirms what have been said in the previous paragraph, from a low modulus contrast, the maximum stress increases up to 30 %. However it is noticed that the crack propagation is less stable for higher modulus contrast.

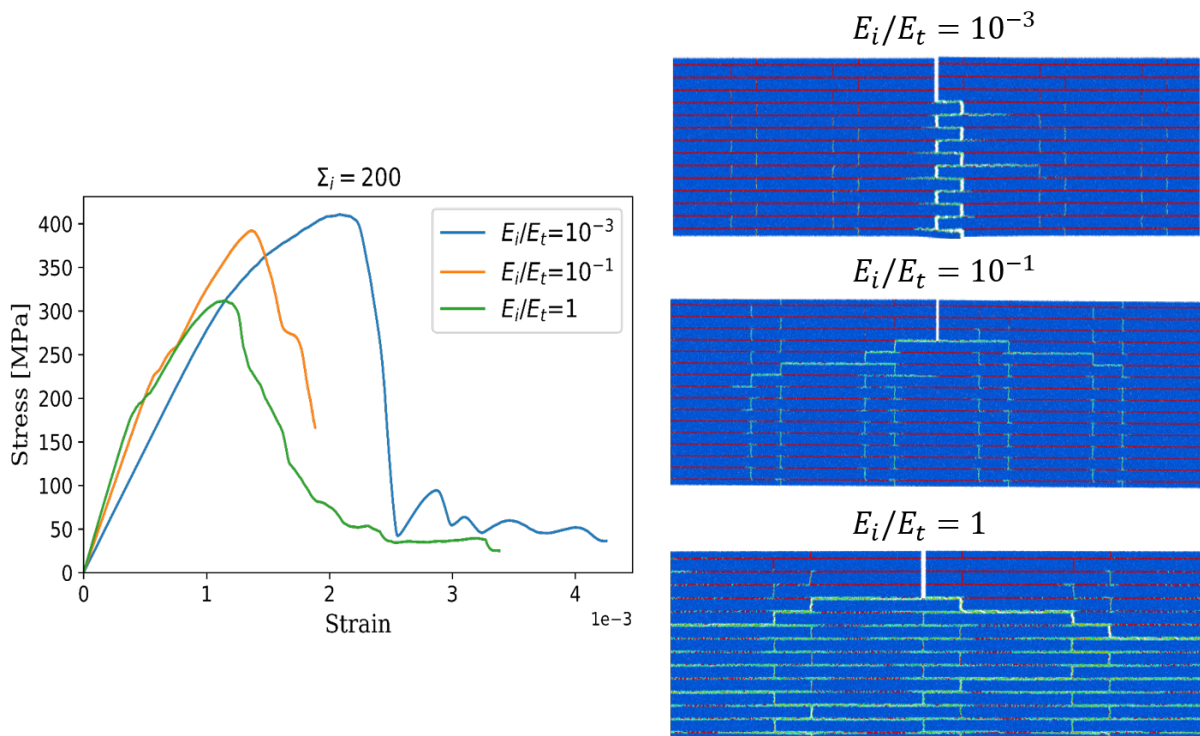


Figure B.1: Stress-strain curves of three notched samples for a given interface strength $\Sigma_i = \frac{1}{20}\Sigma_t = 200$ MPa and three different interface/tablet Young modulus ratios, and the corresponding snapshots of the final shape of the crack path.

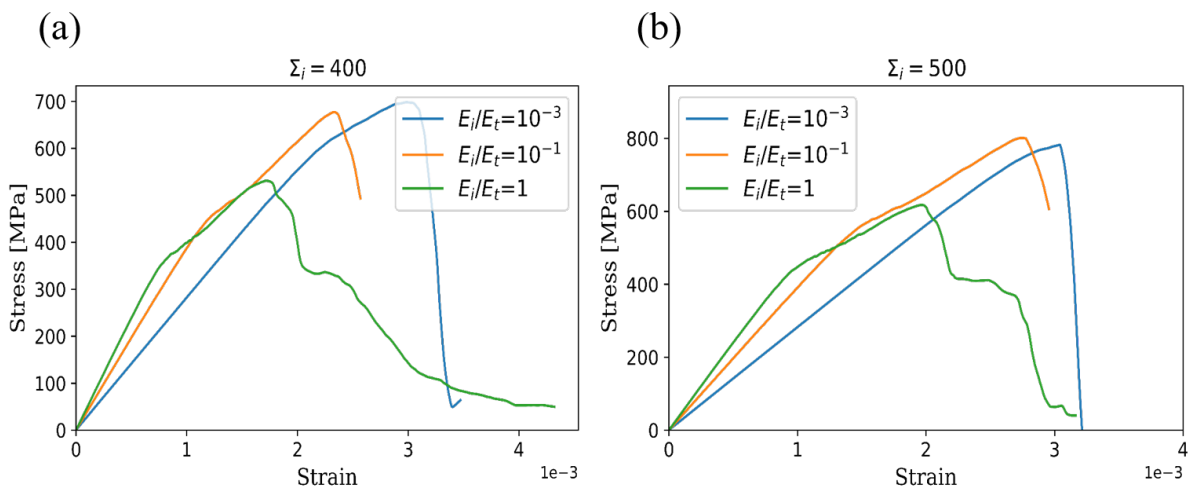


Figure B.2: Stress-strain curves of the three modulus ratios for $\Sigma_i = \frac{1}{10}\Sigma_t = 400$ MPa and $\Sigma_i = \frac{1}{8}\Sigma_t = 500$ MPa.

B.2 Initiation and growth toughness

Figure B.3 depicts the crack initiation toughness $(K_{Ic})_{init}$ and the crack growth toughness ΔK_{Ic} of the different modulus ratios. Both $(K_{Ic})_{init}$ and ΔK_{Ic} increase with the decrease of the modulus contrast.

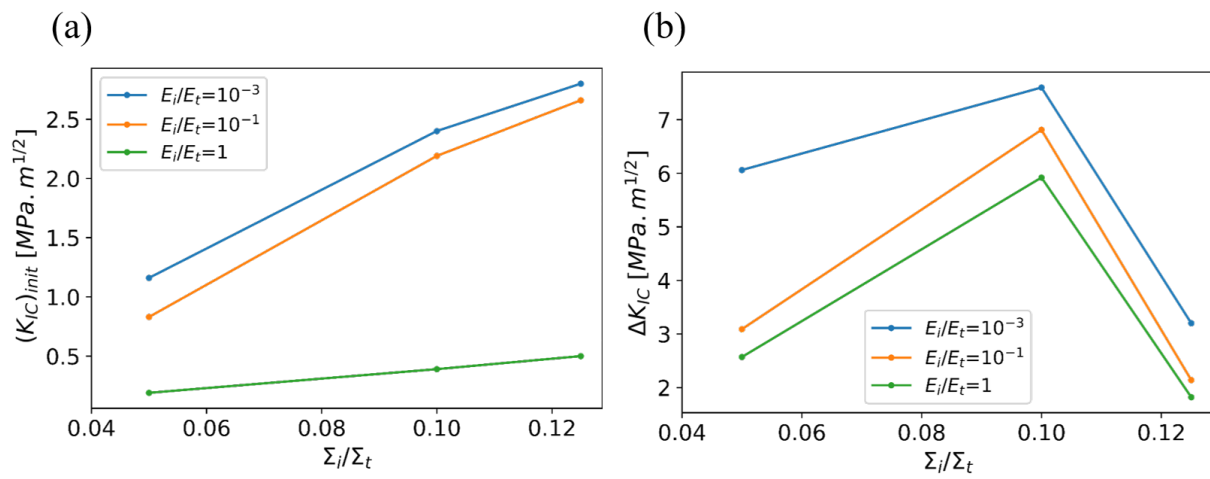


Figure B.3: Crack initiation toughness and crack growth toughness of the three modulus ratios versus the interface strength.

Appendix C

FIB-SEM and holotomography images

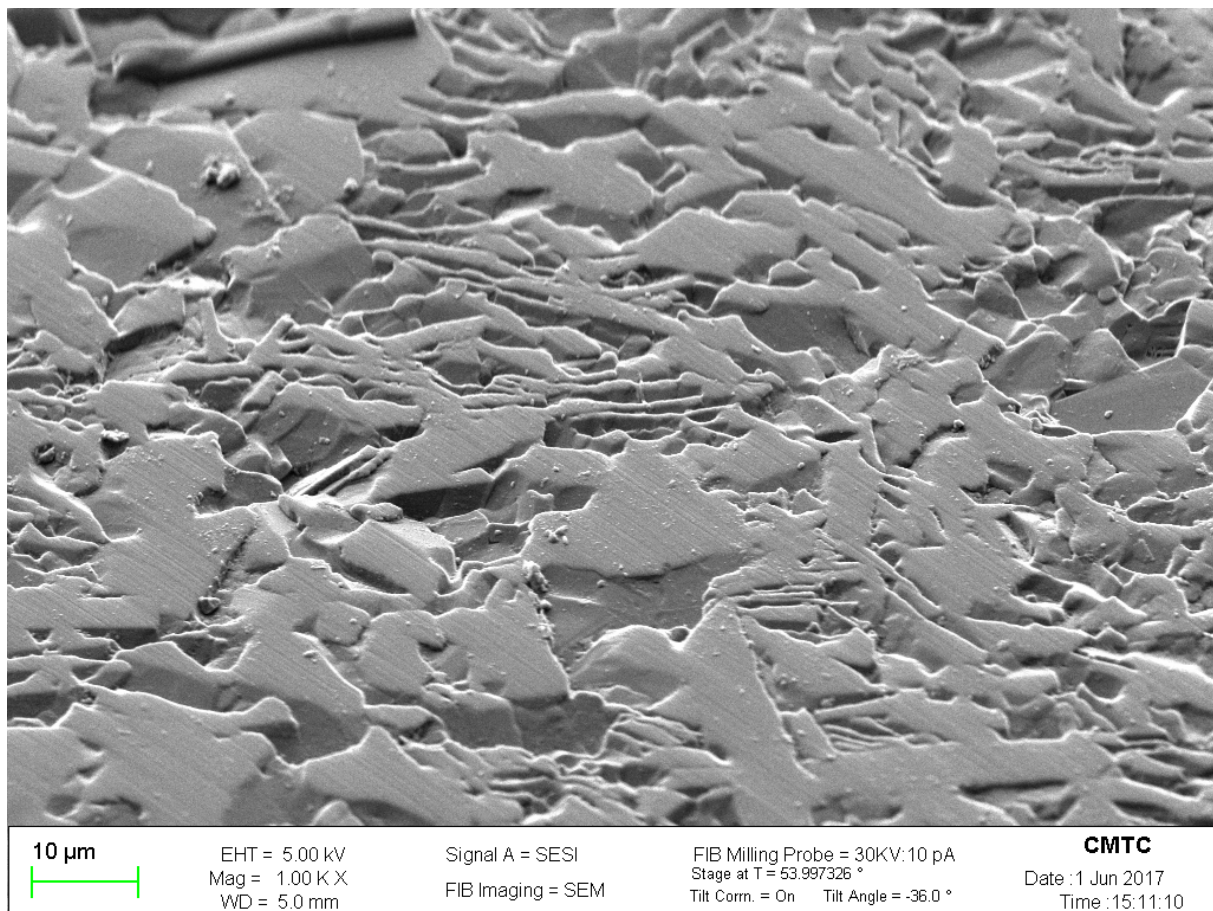


Figure C.1: The coated region for FIB-SEM milling.

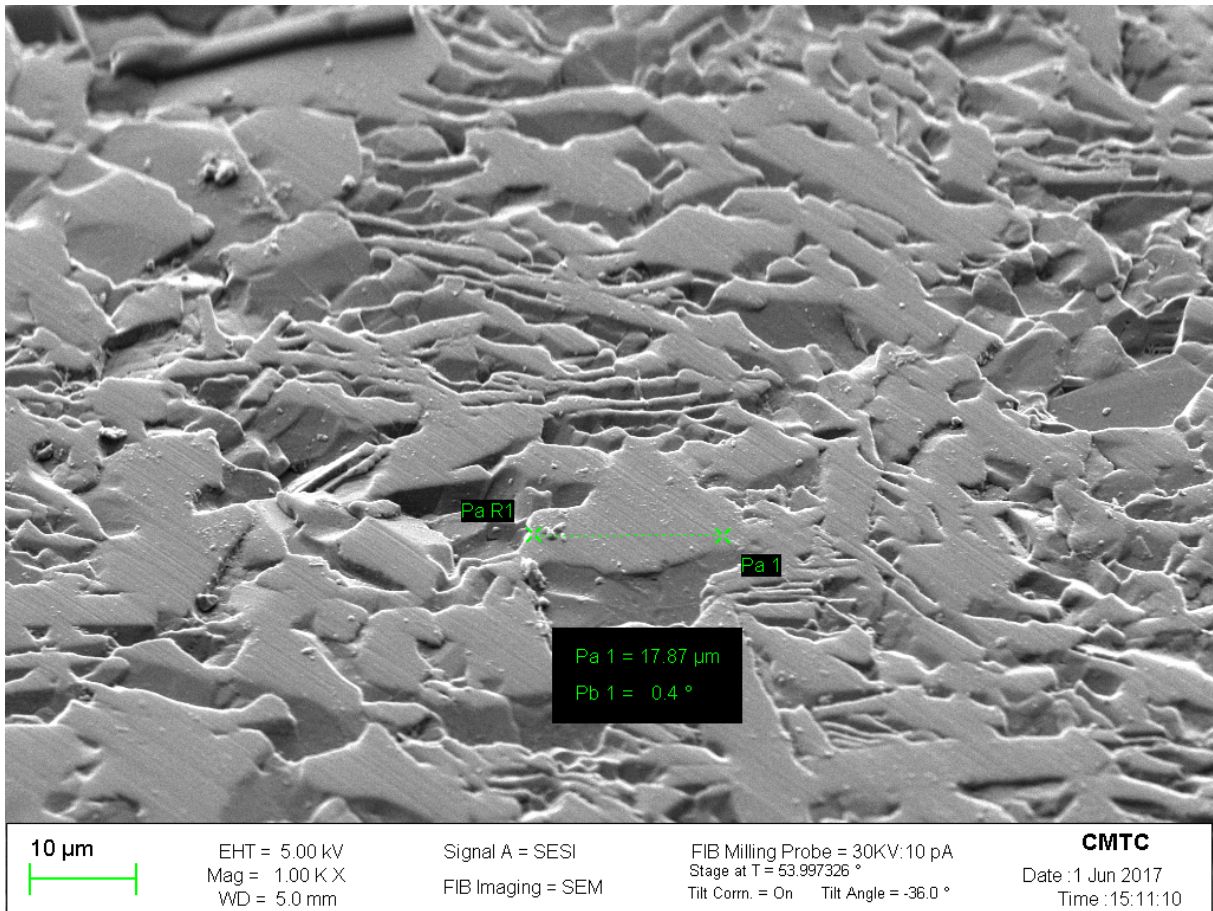


Figure C.2: FIB-SEM milling in the coated region.

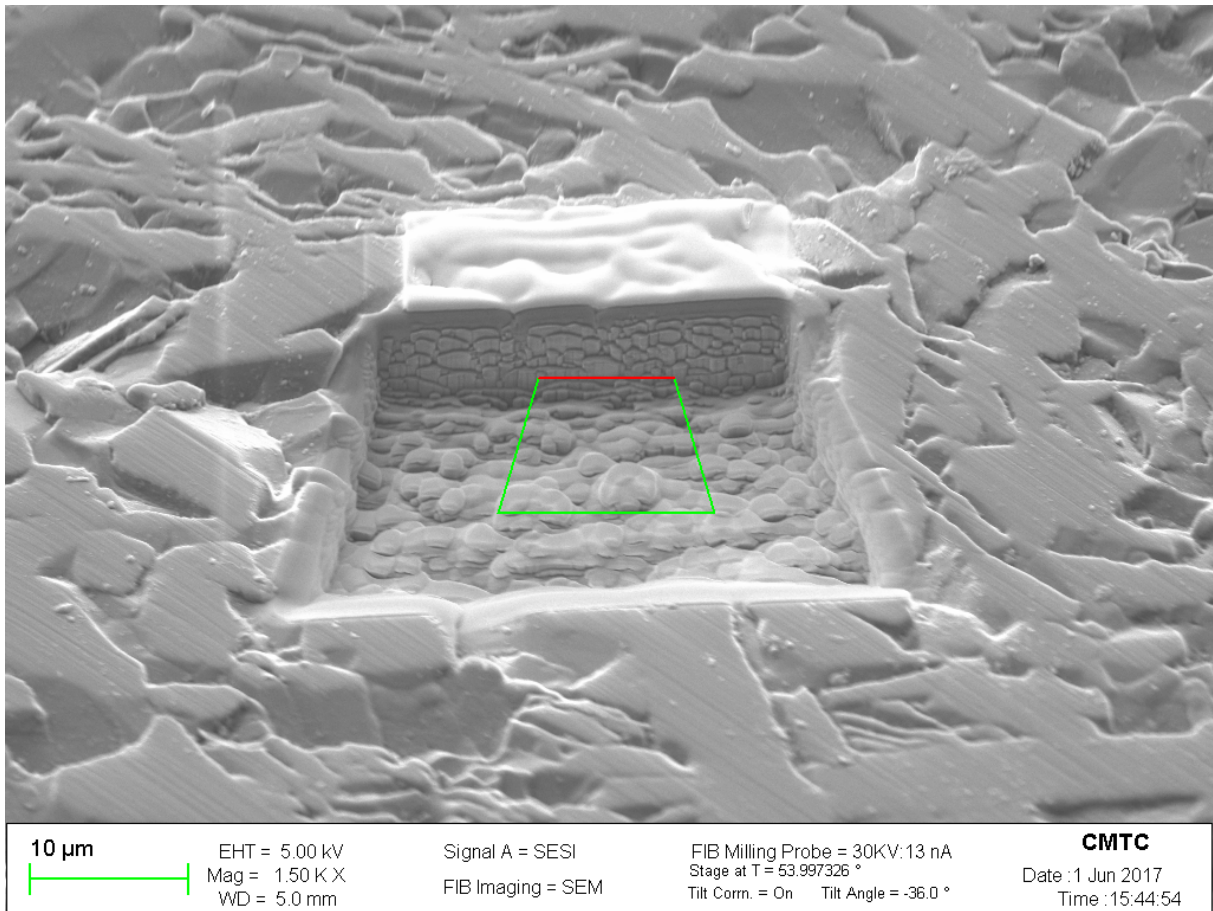


Figure C.3: The final FIB-SEM milling. The BM structure is not distinguishable.

Appendix D

Nano-particles volume fraction

In Chapter 6, we studied the effect of nano-particles on the alignment of tablet during compaction and proved its positive influence. Here we compare two volume fractions of nano-particles (Fig. D.1), the primary results showed that the effect on tablet alignment is minor. However, the normalized axial stress is higher for the 3% volume fraction samples.

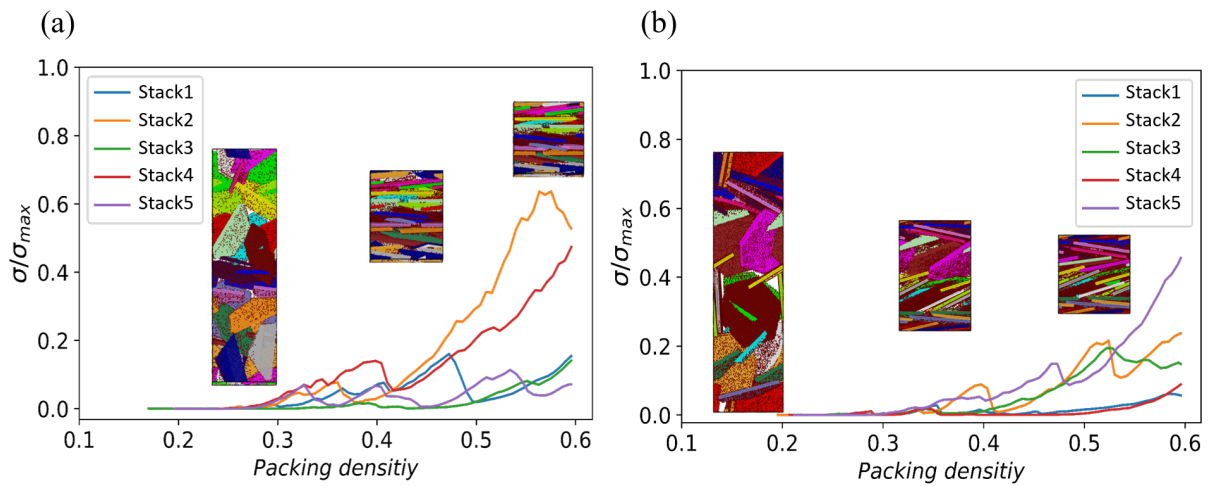


Figure D.1: Normalized stress as a function of the tablet stack density for two nano-particles densities. a) 3% and b) 5%.

Bibliography

Bibliography

- Abid, N., Mirkhalaf, M., & Barthelat, F. (2018). Discrete-element modeling of nacre-like materials: Effects of random microstructures on strain localization and mechanical performance. *Journal of the Mechanics and Physics of Solids*, 112, 385–402. (Cited on pages 39, 41, 53, 82, and 103.)
- Abid, N., Pro, J. W., & Barthelat, F. (2019). Fracture mechanics of nacre-like materials using discrete-element models: Effects of microstructure, interfaces and randomness. *Journal of the Mechanics and Physics of Solids*, 124, 350–365. (Cited on pages 39, 40, 41, 83, 87, 90, 103, and 104.)
- Agnolin, I. & Roux, J. N. (2007). Internal states of model isotropic granular packings. I. Assembling process, geometry, and contact networks. *Physical Review E - Statistical, Nonlinear, and Soft Matter Physics*, 76, 061302. (Cited on page 57.)
- Alexander, S. (2010). Visualization and analysis of atomistic simulation data with OVITO- the open Visualization Tool. (Cited on page 158.)
- Anderson Ted.L (2005). *Fracture Mechanics TextBook*. Ttaylor and Francis, third edit edition. (Cited on pages 86 and 87.)
- André, D., Iordanoff, I., Charles, J.-l., & Néauport, J. (2012). Discrete element method to simulate continuous material by using the cohesive beam model. *Computer Methods in Applied Mechanics and Engineering*, 213-216, 113–125. (Cited on pages 44, 45, 53, 58, and 83.)
- André, D., Jebahi, M., Iordanoff, I., Charles, J.-l., & Néauport, J. (2013). Using the discrete element method to simulate brittle fracture in the indentation of a silica glass with a blunt indenter. *Computer Methods in Applied Mechanics and Engineering*, 265, 136–147. (Cited on pages 45, 47, 53, 55, 56, and 83.)
- Askarinejad, S. & Rahbar, N. (2014). Toughening mechanisms in bioinspired multilayered materials. *Journal of The Royal Society Interface*, 12(102), 20140855–20140855. (Cited on page 83.)

- Bai, H., Walsh, F., Gludovatz, B., Delattre, B., Huang, C., Chen, Y., Tomsia, A. P., & Ritchie, R. O. (2016). Bioinspired Hydroxyapatite/Poly(methyl methacrylate) Composite with a Nacre-Mimetic Architecture by a Bidirectional Freezing Method. *Advanced Materials*, 28(1), 50–56. (Cited on page 104.)
- Bar-On, B. & Wagner, H. D. (2013). New insights into the Young’s modulus of staggered biological composites. *Materials Science and Engineering C*, 33(2), 603–607. (Cited on pages 30, 31, and 37.)
- Barthelat, F. (2014). Designing nacre-like materials for simultaneous stiffness, strength and toughness: Optimum materials, composition, microstructure and size. *Journal of the Mechanics and Physics of Solids*. (Cited on pages 31, 33, 34, 35, 36, 37, 52, 53, 62, 63, 65, 66, 68, 69, 70, 71, 74, 76, 82, 87, 92, 98, and 161.)
- Barthelat, F. & Espinosa, H. D. (2007). An experimental investigation of deformation and fracture of nacre-mother of pearl. *Experimental Mechanics*, 47(3), 311–324. (Cited on page 81.)
- Barthelat, F., Li, C. M., Comi, C., & Espinosa, H. D. (2006). Mechanical properties of nacre constituents and their impact on mechanical performance. *Journal of Materials Research*, 21(8), 1977–1986. (Cited on pages 13, 92, and 160.)
- Barthelat, F. & Rabiei, R. (2011). Toughness amplification in natural composites. *Journal of the Mechanics and Physics of Solids*, 59(4), 829–840. (Cited on page 53.)
- Barthelat, F., Tang, H., Zavattieri, P. D., Li, C. M., & Espinosa, H. D. (2007). On the mechanics of mother-of-pearl: A key feature in the material hierarchical structure. *Journal of the Mechanics and Physics of Solids*, 55(2), 306–337. (Cited on page 25.)
- Barthelat, F., Yin, Z., & Buehler, M. J. (2016). Structure and mechanics of interfaces in biological materials. *Nat. Rev. Mater.*, 1(4), 16007. (Cited on pages 14, 51, and 81.)
- Begley, M. R., Philips, N. R., Compton, B. G., Wilbrink, D. V., Ritchie, R. O., & Utz, M. (2012). Micromechanical models to guide the development of synthetic ‘brick and mortar’ composites. *Journal of the Mechanics and Physics of Solids*, 60(8), 1545–1560. (Cited on pages 32, 33, 37, 52, 53, 62, 65, 66, 68, 69, 70, 76, 82, 88, and 161.)
- Bekah, S., Rabiei, R., & Barthelat, F. (2012). The Micromechanics of Biological and Biomimetic Staggered Composites. *Journal of Bionic Engineering*, 9(4), 446–456. (Cited on pages 53 and 62.)

- Bertoldi, K., Bigoni, D., & Drugan, W. J. (2008). Nacre: An orthotropic and bimodular elastic material. *Composites Science and Technology*, 68(6), 1363–1375. (Cited on pages 32, 37, 63, and 66.)
- Bonderer, L. J., Studart, A. R., & Gauckler, L. J. (2008). Bioinspired Design and Assembly of Platelet Reinforced Polymer Films. *Science*, 319(5866), 1069–1073. (Cited on page 34.)
- Boulos, V., Fristot, V., Houzet, D., Salvo, L., & Lhuissier, P. (2012). Investigating performance variations of an optimized GPU-ported granulometry algorithm. *Conference on Design and Architectures for Signal and Image Processing, DASIP*, (pp. 36–41). (Cited on pages 116 and 124.)
- Bouville, F., Maire, E., & Deville, S. (2014a). Self-assembly of faceted particles triggered by a moving ice front. *Langmuir*, 30(29), 8656–8663. (Cited on pages 131, 132, 136, 150, and 151.)
- Bouville, F., Maire, E., Meille, S., Stevenson, A. J., & Deville, S. (2014b). Strong, tough and sti bioinspired ceramics from brittle constituents. *Nature Materials*, 13(March), 1–7. (Cited on pages 3, 4, 11, 19, 20, 21, 23, 26, 27, 52, 72, 74, 75, 82, 83, 84, 86, 88, 92, 98, and 99.)
- Burr, A. (2017). *Investigation of pore closure during polar firn densification Étude de la fermeture des pores lors de la densification du névé polaire*. PhD thesis, Grenoble Alpes. (Cited on page 43.)
- Calvert, P. (1995). Biomimetic ceramics and hard composites. In *Biomimetic Design and Processing of Materials*. AIP PRESS. (Cited on page 14.)
- Camborde, Mariotti, & Donzé (2000). Numerical study if rock and concrete behavior by discrete element modelling. *Computers and Geotechnics*, 27, 225–247. (Cited on page 43.)
- Cambridge, M. G. D. (2017). Ces edupack database. (Cited on page 75.)
- Carmona, H. A., Wittel, F. K., Kun, F., & Herrmann, H. J. (2008). Fragmentation processes in impact of spheres. *Physical Review E - Statistical, Nonlinear, and Soft Matter Physics*, 77(5), 1–10. (Cited on page 55.)
- Chang, Y., Bermejo, R., & Messing, G. L. (2014). Improved fracture behavior of alumina microstructural composites with highly textured compressive layers. *Journal of the American Ceramic Society*, 97(11), 3643–3651. (Cited on pages 149 and 150.)

- Chareyre, B. (2019). *The Discrete Element Method for Granular Solids*. ISTE Press - Elsevier, 1st editio edition. (Cited on pages 53 and 83.)
- Chen, P.-Y., Lin, a. Y. M., Lin, Y.-S., Seki, Y., Stokes, a. G., Peyras, J., Olevsky, E. a., Meyers, M. A., & McKittrick, J. (2008). Structure and mechanical properties of selected biological materials. *J. Mech. Behav. Biomed. Mater.*, 1(3), 208–26. (Cited on pages 51 and 81.)
- Chintapalli, R. K., Mirkhalaf, M., Dastjerdi, A. K., & Barthelat, F. (2014). Fabrication, testing and modeling of a new flexible armor inspired from natural fish scales and osteoderms. *Bioinspiration & biomimetics*, 3(9). (Cited on page 103.)
- Cho, H.-B., Tokoi, Y., Tanaka, S., Suzuki, T., Jiang, W., Suematsu, H., Niihara, K., & Nakayama, T. (2010). Facile Orientation of Unmodified BN Nanosheets in polysiloxane/BN Composite Films Using a High Magnetic Field. *Journal of Materials Science*, 46, 2318–2323. (Cited on page 131.)
- Christoffersen, J., Mehrabadi, M. M., & Nemat-Nasser, S. (1981). A Micromechanical Description of Granular Material Behavior. *Journal of Applied Mechanics*, 48(2), 339. (Cited on pages 57, 137, and 158.)
- Corni, I., Harvey, T. J., Wharton, J. A., Stokes, K. R., Walsh, F. C., & Wood, R. J. K. (2012). A review of experimental techniques to produce a nacre-like structure. *Bioinspiration & Biomimetics*, 7(3), 031001. (Cited on pages 15 and 51.)
- Cox, H. L. (1952). The elasticity and strength of paper and other fibrous materials. *British journal of applied physics*, 3(72). (Cited on page 30.)
- Cundall, P. A. & Strack, O. D. L. (1979). A discrete numerical model for granular assemblies. *Géotechnique*, 29(1), 47–65. (Cited on pages 53, 55, 57, and 83.)
- Cundall, R. B., Rudham, R., & Salim, M. S. (1976). Photocatalytic oxidation of propan-2-ol in the liquid phase by rutile. *Journal of the Chemical Society, Faraday Transactions 1*, 72, 1642. (Cited on page 42.)
- Currey, J. D. (1977). Mechanical Properties of Mother of Pearl in Tension Articles citing this article. *Proc.R.Soc.Lond.B.*, 196, 443–463. (Cited on pages 13 and 14.)
- Davidson, P. & Waas, M. (2011). Non-smooth mode I fracture of fibre-reinforced composites: an experimental, numerical and analytical study. *Philosophical Transactions of the Royal Society A: Mathematical, Physical and Engineering Sciences*, (pp. 1942–1965). (Cited on page 87.)

- Derjaguin, B. V., Muller, V. M., & Toporov, Y. P. (1994). Effect of contact deformations on the adhesion of particles. *Progress in Surface Science*, 45, 131–143. (Cited on pages 44 and 136.)
- Deville, S., Saiz, E., & Tomsia, A. P. (2007). Ice-templated porous alumina structures. *Acta Materialia*, 55(6), 1965–1974. (Cited on page 16.)
- Dhia, H. B. & Rateau, G. (2005). The Arlequin method as a flexible engineering design tool. *International Journal for Numerical Methods in Engineering*, 62(11), 1442–1462. (Cited on page 47.)
- Dimas, L. S., Bratzel, G. H., Eylon, I., & Buehler, M. J. (2013). Tough composites inspired by mineralized natural materials: Computation, 3D printing, and testing. *Advanced Functional Materials*, 23(36), 4629–4638. (Cited on pages 19, 23, and 41.)
- Dimas, L. S. & Buehler, M. J. (2013). Tough and stiff composites with simple building blocks. *Journal of Materials Research*, 28(10), 1295–1303. (Cited on pages 38, 39, and 82.)
- Dubois, F. & Radjai, F. (2011). *Discrete-element Modeling of Granular Materials*. Wiley, wiley edition. (Cited on pages 42, 53, and 83.)
- Espinosa, H. D., Juster, A. L., Latourte, F. J., Loh, O. Y., Gregoire, D., & Zavattieri, P. D. (2011). Tablet-level origin of toughening in abalone shells and translation to synthetic composite materials. *Nature Communications*, 2(1), 173–179. (Cited on page 103.)
- Espinosa, H. D., Rim, J. E., Barthelat, F., & Buehler, M. J. (2009). Merger of structure and material in nacre and bone - Perspectives on de novo biomimetic materials. *Progress in Materials Science*, 54(8), 1059–1100. (Cited on pages 51 and 81.)
- Evans, a. G., Suo, Z., Wang, R. Z., Aksay, I. a., He, M. Y., & Hutchinson, J. W. (2001). Model for the robust mechanical behavior of nacre. *Journal of Materials Research*, 16(09), 2475–2484. (Cited on pages 25, 38, and 41.)
- Feilden, E., Giovannini, T., Ni, N., Ferraro, C., Saiz, E., Vandeperre, L., & Giuliani, F. (2017). Micromechanical strength of individual Al₂O₃ platelets. *Scripta Materialia*, 131, 55–58. (Cited on pages 72 and 74.)
- Feng, Q., Cui, F., Pu, G., Wang, R., & Li, H. (2000). Crystal orientation, toughening mechanisms and a mimic of nacre. *Materials Science and Engineering C*, 11, 19–25. (Cited on page 82.)

- Fujihara, T., Cho, H., Nakayama, T., Suzuki, T., Jiang, W., Suematsu, H., Kim, H. D., & Niihara, K. (2012). Field-Induced Orientation of Hexagonal Boron Nitride Nanosheets Using Microscopic Mold for Thermal Interface Materials. *Journal of the American Ceramic Society*, 95, 369–373. (Cited on page 131.)
- Gao, H. (2006). Application of fracture mechanics concepts to hierarchical biomechanics of bone and bone-like materials. *International Journal of Fracture*, 138(1-4), 101–137. (Cited on page 37.)
- Gao, H., Ji, B., Jager, I. L., Arzt, E., & Fratzl, P. (2003). Materials become insensitive to flaws at nanoscale: Lessons from nature. *Proceedings of the National Academy of Sciences*, 100(10), 5597–5600. (Cited on page 34.)
- Gaume, J., Van Herwijnen, A., Chambon, G., Birkeland, K. W., & Schweizer, J. (2015). Modeling of crack propagation in weak snowpack layers using the discrete element method. *Cryosphere*, 9(5), 1915–1932. (Cited on page 43.)
- Grossman, M., Bouville, F., Erni, F., Masania, K., Libanori, R., & Studart, A. R. (2017). Mineral Nano-Interconnectivity Stiffens and Toughens Nacre-like Composite Materials. *Advanced Materials*, 29(8), 1–7. (Cited on pages 21, 23, 26, 52, 76, 83, and 131.)
- Grossman, M., Bouville, F., Masania, K., & Studart, A. R. (2018). Quantifying the role of mineral bridges on the fracture resistance of nacre-like composites. *PNAS*, 50(June), 24–28. (Cited on pages 25, 83, and 99.)
- Gu, G. X., Libonati, F., Wettermark, S. D., & Buehler, M. J. (2017). Printing nature: Unraveling the role of nacre’s mineral bridges. *Journal of the Mechanical Behavior of Biomedical Materials*, 76(May), 135–144. (Cited on pages 25, 83, and 92.)
- Heid-Jorgensen, S. & Budzik, M. K. (2018). Effects of bondline discontinuity during growth of interface cracks including stability and kinetic considerations. *Journal of the Mechanics and Physics of Solids*, 117, 1–21. (Cited on page 87.)
- Henzie, J., Grünwald, M., Widmer-Cooper, A., Geissler, P. L., & Yang, P. (2012). Self-Assembly of Uniform Polyhedral Silver Nanocrystals into Densest Packings and Exotic Superlattices. *Nature Materials*, 11, 131–137. (Cited on page 143.)
- Hertz, H. (1882). Ueber die Berührung fester elastischer Körper. *J reine angew Math*, 92, 156–171. (Cited on page 44.)
- Hiroshi, T., C, P. P., & George, I. R. (1985). *The stress analysis of cracks handbook*. Unknown, asme press edition. (Cited on page 86.)

- Hossain, M. Z., Hsueh, C., Bourdin, B., & Bhattacharya, K. (2014). Effective toughness of heterogeneous media. *Journal of the Mechanics and Physics of Solids*, 71, 15–32. (Cited on page 87.)
- Jackson, A. P., Vincent, J. F. V., & Turner, R. M. (1988). The Mechanical Design of Nacre. *Proceedings of the Royal Society B: Biological Sciences*, 234(1277), 415–440. (Cited on pages 13, 51, and 81.)
- Jäger, I. & Fratzl, P. (2000). Mineralized collagen fibrils: A mechanical model with a staggered arrangement of mineral particles. *Biophysical Journal*, 79(4), 1737–1746. (Cited on pages 31, 33, 37, and 82.)
- Jauffrès, D., Liu, X., & Martin, C. L. (2013). Tensile strength and toughness of partially sintered ceramics using discrete element simulations. *Engineering Fracture Mechanics*, 103, 132–140. (Cited on page 75.)
- Jauffrès, D., Martin, C. L., Lichtner, A., & Bordia, R. K. (2012). Simulation of the elastic properties of porous ceramics with realistic microstructure. *Modelling and Simulation in Materials Science and Engineering*, 20(4), 045009. (Cited on page 53.)
- Jebahi, M., André, D., Dau, F., Charles, J. L., & Iordanoff, I. (2013). Simulation of Vickers indentation of silica glass. *Journal of Non-Crystalline Solids*, 378, 15–24. (Cited on page 47.)
- Jerier, J. F. & Molinari, J. F. (2012). Normal contact between rough surfaces by the Discrete Element Method. *Tribology International*, 47, 1–8. (Cited on page 58.)
- Ji, B. & Gao, H. (2004). Mechanical properties of nanostructure of biological materials. *Journal of the Mechanics and Physics of Solids*, 52(9), 1963–1990. (Cited on pages 32, 65, and 66.)
- Johnson, Langstreth, K., Kendall, K., & Roberts, A. D. (1971). Surface energy and the contact of elastic solids. *Proceedings of the royal society of London. A. mathematical and physical sciences*, (pp. 301–313). (Cited on page 44.)
- Johnson, J. B. & Hopkins, M. A. (2005). Identifying microstructural deformation mechanisms in snow using discrete-element modeling. *Journal of Glaciology*, 51(174), 432–442. (Cited on page 43.)
- Katti, D. & Katti, K. (2001). Modeling microarchitecture and mechanical behavior of nacre using 3D finite element techniques Part I Elastic properties. *Journal of Materials Science*, 6, 1411–1417. (Cited on pages 38 and 41.)

- Katti, K. S., Katti, D. R., Pradhan, S. M., & Bhosle, A. (2005). Platelet interlocks are the key to toughness and strength in nacre. *Journal of Materials Research*, 20(05), 1097–1100. (Cited on pages 38, 41, 53, and 82.)
- Kawamoto, R., Andò, E., Viggiani, G., & Andrade, J. E. (2018). All you need is shape: Predicting shear banding in sand with LS-DEM. *Journal of the Mechanics and Physics of Solids*, 111, 375–392. (Cited on pages 151 and 152.)
- Kim, B. & Weiss, W. J. (2003). Using acoustic emission to quantify damage in restrained fiber-reinforced cement mortars. *Cement and Concrete Research*, 33(2), 207–214. (Cited on page 149.)
- Kotha, S. P., Li, Y., & Guzelsu, N. (2001). Micromechanical model of nacre tested in tension. *Journal of Materials Science*, 36(8), 2001–2007. (Cited on pages 31, 33, 37, and 82.)
- Kumar, R., Rommel, S., Jauffrès, D., Lhuissier, P., & Martin, C. L. (2016). Effect of packing characteristics on the discrete element simulation of elasticity and buckling. *International Journal of Mechanical Sciences*, 110, 14–21. (Cited on pages 44, 46, 53, 55, 58, 60, 61, 62, 83, 84, 85, 134, 156, and 157.)
- Launey, M. E., Munch, E., Alsem, D. H., Barth, H. B., Saiz, E., Tomsia, A. P., & Ritchie, R. O. (2009). Designing highly toughened hybrid composites through nature-inspired hierarchical complexity. *Acta Materialia*, 57(10), 2919–2932. (Cited on pages 15 and 23.)
- Launey, M. E., Munch, E., Alsem, D. H., Saiz, E., Tomsia, A. P., & Ritchie, R. O. (2010). A novel biomimetic approach to the design of high-performance ceramic - Metal composites. *Journal of the Royal Society Interface*, 7(46), 741–753. (Cited on page 17.)
- Launey, M. E. & Ritchie, R. O. (2009). On the fracture toughness of advanced materials. *Advanced Materials*, 21(20), 2103–2110. (Cited on pages 24, 52, 82, and 149.)
- Le Ferrand, H., Bouville, F., Niebel, T. P., & Studart, A. R. (2015). Magnetically assisted slip casting of bioinspired heterogeneous composites. *Nat. Mater.*, 14(September), 1–17. (Cited on pages 52 and 82.)
- Le Ferrand, H., Bouville, F., & Studart, A. (2018). Design principles for textured multi-layered composites using magnetically assisted slip casting. *arXiv:1808.01327*, (pp. 1–20). (Cited on page 52.)

- Leclerc, W. (2017). Discrete Element Method to simulate the elastic behavior of 3D heterogeneous continuous media W. *International Journal of Solids and Structures*. (Cited on pages 45, 47, 53, and 83.)
- Leclerc, W., Haddad, H., & Guessasma, M. (2016). International Journal of Solids and Structures On the suitability of a Discrete Element Method to simulate cracks initiation and propagation in heterogeneous media. *International Journal of Solids and Structures*, 108, 98–114. (Cited on pages 47 and 55.)
- Li, X. (2004). Nanoscale structural and mechanical characterization of natural nanocomposites: Seashells. *Jom*, 59(3), 71–74. (Cited on page 25.)
- Lin, Z., Liu, Y., Raghavan, S., Moon, K., Sitaraman, S. K., & Wong, C. (2013). Magnetic Alignment of Hexagonal Boron Nitride Platelets in Polymer Matrix: Toward High Performance Anisotropic Polymer Composites for Electronic Encapsulation. *ACS Applied Materials & Interfaces*, 5, 7633–7640. (Cited on page 131.)
- Maheo, L., Dau, F., André, D., Charles, J. L., & Iordanoff, I. (2015). Composites : Part B A promising way to model cracks in composite using Discrete Element Method. *Composites Part B*, 71, 193–202. (Cited on pages 47, 53, 55, and 83.)
- Martin, C. L. (2004). Elasticity, fracture and yielding of cold compacted metal powders. *J. Mech. Phys. Solids*, 52, 1691–1717. (Cited on pages 77, 99, and 149.)
- Martin, C. L. & Bordia, R. K. (2008). Influence of adhesion and friction on the geometry of packings of spherical particles. *Phys. Rev. E*, 77, 31307. (Cited on page 58.)
- Martin, C. L., Bouvard, D., & Delette, G. (2006). Discrete element simulations of the compaction of aggregated ceramic powders. *Journal of the American Ceramic Society*, 89(11), 3379–3387. (Cited on page 43.)
- Martin, C. L., Bouvard, D., & Shima, S. (2003). Study of particle rearrangement during powder compaction by the Discrete Element Method. *Journal of the Mechanics and Physics of Solids*, 51, 667–693. (Cited on pages 43, 57, 77, 84, 99, and 149.)
- Meyers, M. A., Chen, P.-Y., Lin, A. Y.-M., & Seki, Y. (2008). Biological materials: Structure and mechanical properties. *Progress in Materials Science*, 53(1), 1–206. (Cited on page 13.)
- Moes, N., Dolbow, J., & Belytschko, T. E. D. (1999). A Finite Element Method for Crack Growth Without Remeshing. *International Journal for Numerical Methods in Engineering*, 46(February), 131–150. (Cited on page 43.)

- Munch, E., Launey, M. E., Alsem, D. H., Saiz, E., Tomsia, A. P., & Ritchie, R. O. (2008). Tough, bio-inspired hybrid materials. *Science*, 322(5907), 1516–1520. (Cited on pages 15, 16, 17, 23, and 82.)
- Naglieri, V., Gludovatz, B., Tomsia, A., & Ritchie, R. (2015). Developing strength and toughness in bio-inspired silicon carbide hybrid materials containing a compliant phase. *Acta Materialia*, 98, 141–151. (Cited on pages 82, 83, and 99.)
- Néda, Z., Florian, R., & Brechet, Y. (1999). Reconsideration of continuum percolation of isotropically oriented sticks in three dimensions. *Physical Review E - Statistical Physics, Plasmas, Fluids, and Related Interdisciplinary Topics*, 59(3), 3717–3719. (Cited on page 135.)
- Needleman, A. & Tvergaard, V. (1991). An analysis of dynamic, ductile crack growth in a double edge cracked specimen. *International Journal of Fracture*, 49(1), 41–67. (Cited on page 103.)
- Ni, Y., Song, Z., Jiang, H., Yu, S. H., & He, L. (2015). Optimization design of strong and tough nacreous nanocomposites through tuning characteristic lengths. *Journal of the Mechanics and Physics of Solids*, 81, 41–57. (Cited on pages 32, 33, 37, 52, 53, 65, 66, 68, 69, 70, 71, 76, 82, and 161.)
- Niebel, T. P., Bouville, F., Kokkinis, D., & Studart, A. R. (2016). Role of the polymer phase in the mechanics of nacre-like composites. *Journal of the Mechanics and Physics of Solids*, 96. (Cited on page 82.)
- Nukala, P. K. V., Zapperi, S., & Āimunović, S. (2005). Statistical properties of fracture in a random spring model. *Physical Review E - Statistical, Nonlinear, and Soft Matter Physics*, 71(6), 1–11. (Cited on pages 38, 41, and 82.)
- Oaki, Y., Kotachi, A., Miura, T., & Imai, H. (2006). Bridged nanocrystals in biominerals and their biomimetics: Classical yet modern crystal growth on the nanoscale. *Advanced Functional Materials*, 16(12), 1633–1639. (Cited on pages 18 and 23.)
- Oner Ekiz, O., Dericioglu, A. F., & Kakisawa, H. (2009). An efficient hybrid conventional method to fabricate nacre-like bulk nano-laminar composites. *Materials Science and Engineering C*, 29(6), 2050–2054. (Cited on pages 17, 23, 82, and 131.)
- Pavlacka, R., Bermejo, R., Chang, Y., Green, D. J., & Messing, G. L. (2013). Fracture behavior of layered alumina microstructural composites with highly textured layers. *Journal of the American Ceramic Society*, 96(5), 1577–1585. (Cited on page 150.)

- Pelissari, P. I., Bouville, F., Pandolfelli, V. C., Carnelli, D., Giuliani, F., Luz, A. P., Saiz, E., & Studart, A. R. (2017). Nacre-like ceramic refractories for high temperature applications. *Journal of the European Ceramic Society*, 38(4), 2186–2193. (Cited on pages 21, 22, 23, 52, 74, 82, 98, 99, and 131.)
- Poschel, T. & Thomas, S. (2005). Computational granular dynamics: models and algorithms. *Springer*. (Cited on page 42.)
- Potyondy, D. O. & Cundall, P. A. (2004). A bonded-particle model for rock. *International Journal of Rock Mechanics & Mining Sciences* 41, 41, 1329–1364. (Cited on pages 54, 55, 58, 155, and 157.)
- Rabiei, R., Bekah, S., & Barthelat, F. (2010). Failure mode transition in nacre and bone-like materials. *Acta Biomaterialia*, 6(10), 4081–4089. (Cited on page 104.)
- Radi, K., Jauffrès, D., Deville, S., & Martin, C. L. (2019a). Elasticity and fracture of brick and mortar materials with discrete elements simulations. *Journal of the Mechanics and Physics of Solids*, 126, 101–116. (Cited on pages 49, 84, 85, 86, 88, 98, 104, and 147.)
- Radi, K., Jauffrès, D., Deville, S., & Martin, C. L. (2019b). Strength and toughness trade-off optimization of nacre-like ceramic composites. *Composites Part B*, (pp. 107699). (Cited on page 79.)
- Rasp, T., Kraft, T., & Riedel, H. (2013). Discrete element study on the influence of initial coordination numbers on sintering behaviour. *Scripta Materialia*, 69(11-12), 805–808. (Cited on page 43.)
- Ray, S. P. (1992). Preparation and Characterization of Aluminum Borate. *Journal of the American Ceramic Society*, 75(9), 2605–2609. (Cited on page 75.)
- Ritchie, R. O. (2011). The conflicts between strength and toughness. *Nature Materials*, 10(11), 817–822. (Cited on pages 13, 24, 25, 26, and 82.)
- Ritchie, R. O., Buehler, M. J., & Hansma, P. (2009). Plasticity and toughness in bone. *American Institute of Physics*. (Cited on page 81.)
- Roussel, D., Lichtner, A., Jauffrès, D., Villanova, J., Bordia, R. K., & Martin, C. L. (2016). Strength of hierarchically porous ceramics: Discrete simulations on X-ray nanotomography images. *Scripta Materialia*, 113, 250–253. (Cited on pages 43, 53, 75, and 83.)

- Saeys, W., Vanmaercke, S., Van Liedekerke, P., Van Oosterwyck, H., Odenthal, T., Keresztes, J., Ramon, H., Tijskens, E., & Smeets, B. (2014). Modeling contact interactions between triangulated rounded bodies for the discrete element method. *Computer Methods in Applied Mechanics and Engineering*, 277, 219–238. (Cited on page 42.)
- Schäffer, T. E., Ionescu-Zanetti, C., Proksch, R., Fritz, M., Walters, D. A., Almqvist, N., Zaremba, C. M., Belcher, A. M., Smith, B. L., Stucky, G. D., Morse, D. E., & Hansma, P. K. (1997). Does Abalone Nacre Form by Heteroepitaxial Nucleation or by Growth through Mineral Bridges? *Chemistry of Materials*, 9(8), 1731–1740. (Cited on page 14.)
- Scholtès, L. & Donzé, F.-V. (2013). A DEM model for soft and hard rocks: Role of grain interlocking on strength. *Journal of the Mechanics and Physics of Solids*, 61(2), 352–369. (Cited on page 58.)
- Sen, D. & Buehler, M. J. (2011). Structural hierarchies define toughness and defect-tolerance despite simple and mechanically inferior brittle building blocks. *Scientific Reports*, 1, 1–9. (Cited on page 53.)
- Shao, Y., Zhao, H. P., & Feng, X. Q. (2014). Optimal characteristic nanosizes of mineral bridges in mollusk nacre. *RSC Advances*, 4(61), 32451–32456. (Cited on pages 25, 83, and 92.)
- Shao, Y., Zhao, H. P., Feng, X. Q., & Gao, H. (2012). Discontinuous crack-bridging model for fracture toughness analysis of nacre. *Journal of the Mechanics and Physics of Solids*, 60(8), 1400–1419. (Cited on pages 34, 35, 37, and 53.)
- Song, F., Soh, A. K., & Bai, Y. L. (2003). Structural and mechanical properties of the organic matrix layers of nacre. *Biomaterials*, 24, 3623–3631. (Cited on pages 83, 92, and 160.)
- Song, Z. Q., Ni, Y., Peng, L. M., Liang, H. Y., & He, L. H. (2016). Interface failure modes explain non-monotonic size-dependent mechanical properties in bioinspired nanolaminates. *Scientific Reports*, 6(December 2015), 1–9. (Cited on page 53.)
- Stefan, P., Alexander, P., & Kloss, C. (2017). Models, algorithms and validation for open-source DEM and CFD-DEM. *Computational Particle Mechanics*, 4, 101–118. (Cited on page 42.)
- Sun, X., Zhang, Z., Xu, Y., & Zhang, Y. (2015). An elastic model for bioinspired design of carbon nanotube bundles. *Acta Mechanica Sinica/Lixue Xuebao*, 31(2), 205–215. (Cited on page 53.)

- Vanniamparambil, P. A., Bolhassani, M., Carmi, R., Khan, F., Bartoli, I., Moon, F. L., Hamid, A., & Kontsos, A. (2014). A data fusion approach for progressive damage quantification in reinforced concrete masonry walls. *Smart Materials and Structures*, 23(1). (Cited on page 149.)
- Villanova, J., Cloetens, P., Suhonen, H., Laurencin, J., Usseglio-Viretta, F., Lay, E., Delette, G., Bleuet, P., Jauffrès, D., Roussel, D., Lichtner, A. Z., & Martin, C. L. (2014). Multi-scale 3D imaging of absorbing porous materials for solid oxide fuel cells. *Journal of Materials Science*, 49(16), 5626–5634. (Cited on page 112.)
- Wang, C., Huang, Y., Zan, Q., Guo, H., & Cai, S. (2000a). Biomimetic structure design - a possible approach to change the brittleness of ceramics in nature. *Materials Science and Engineering C*, 11(1), 9–12. (Cited on pages 18 and 23.)
- Wang, R., Suo, Z., Evans, A., Yao, N., & Aksay, I. a. (2000b). Deformation mechanisms in ice. *Princeton press*, 08544, 2485–2493. (Cited on pages 14 and 25.)
- Wegst, U. G., Schecter, M., Donius, A. E., & Hunger, P. M. (2010). Biomaterials by freeze casting. *Philosophical Transactions of the Royal Society A: Mathematical, Physical and Engineering Sciences*, 368(1917), 2099–2121. (Cited on page 16.)
- William Pro, J., Kwei Lim, R., Petzold, L. R., Utz, M., & Begley, M. R. (2015). GPU-based simulations of fracture in idealized brick and mortar composites. *Journal of the Mechanics and Physics of Solids*, 80, 68–85. (Cited on pages 39, 40, 41, 53, 82, 83, and 103.)
- Xu, G., Yao, N., Aksay, I. A., & Groves, J. T. (1998). Biomimetic Synthesis of Macroscopic-Scale Calcium Carbonate Thin Films. Evidence for a Multistep Assembly Process. *Journal of the american chemical society*, 120(46), 11977–11985. (Cited on pages 18 and 23.)
- Xu, J., Qi, H., Fang, X., Lu, L., Ge, W., Wang, X., Xu, M., Chen, F., He, X., & Li, J. (2011). Quasi-real-time simulation of rotating drum using discrete element method with parallel GPU computing. *Particuology*, 9(4), 446–450. (Cited on page 43.)
- Yadav, R., Goud, R., Dutta, A., Wang, X., Naebe, M., & Kandasubramanian, B. (2018). Biomimicking of Hierarchical Molluscan Shell Structure Via Layer by Layer 3D Printing. *Industrial and Engineering Chemistry Research*, 57(32), 10832–10840. (Cited on pages 19, 23, and 103.)

- Yadav, R., Naebe, M., Wang, X., & Kandasubramanian, B. (2017). Review on 3D Prototyping of Damage Tolerant Interdigitating Brick Arrays of Nacre. *Industrial and Engineering Chemistry Research*, 56(38), 10516–10525. (Cited on pages 23 and 82.)
- Zhang, S., Zhang, J., Zhang, Z., Dang, H., Liu, W., & Xue, Q. (2004). Preparation and characterization of self-assembled organic–inorganic nacre-like nanocomposite thin films. *Materials Letters* 58, 58, 2266–2269. (Cited on pages 18 and 23.)
- Zhang, W., Telle, R., & Uebel, J. (2014). ScienceDirect R-curve behaviour in weak interface-toughened SiC-C laminates by discrete element modelling. *Journal of the European Ceramic Society*, 34, 217–227. (Cited on page 53.)
- Zhang, Z., Zhang, Y.-W., & Gao, H. (2011). On optimal hierarchy of load-bearing biological materials. *Proceedings of the Royal Society B: Biological Sciences*, 278(1705), 519–525. (Cited on pages 35 and 37.)
- Zhang, Z. Q., Liu, B., Huang, Y., Hwang, K. C., & Gao, H. (2010). Mechanical properties of unidirectional nanocomposites with non-uniformly or randomly staggered platelet distribution. *Journal of the Mechanics and Physics of Solids*, 58(10), 1646–1660. (Cited on page 52.)
- Zhao, H. & Guo, L. (2017). Nacre-Inspired Structural Composites: Performance-Enhancement Strategy and Perspective. *Adv. Mater.*, 29(45), 1702903. (Cited on pages 51 and 82.)
- Zhu, D. & Barthelat, F. (2011). A novel biomimetic material duplicating the structure and mechanics of natural nacre. *Conference Proceedings of the Society for Experimental Mechanics Series*, 2, 181–187. (Cited on page 103.)
- Zhu, H. P., Zhou, Z. Y., Yang, R. Y., & Yu, A. B. (2008). Discrete particle simulation of particulate systems: A review of major applications and findings. *Chemical Engineering Science*, 63(23), 5728–5770. (Cited on page 43.)